L'UNIVERSITE DES SCIENCES ET TECHNOLOGIES DE LILLE

ECOLE DOCTORALE "SCIENCES POUR L'INGENIEUR"

THESE

pour l'obtention du titre de

DOCTEUR

DE L'UNIVERSITE DES SCIENCES ET TECHNOLOGIES DE LILLE

Discipline : Mécanique

Présentée par

Hossam KAMAL IBRAHIM ABDELHAMID

Prédiction numérique de l'écoulement d'un fluide viscoélastique autour d'un cylindre non confiné

Thèse dirigée par:

G. MOMPEAN	Professeur, Université de Lille1, Villeneuve d'Ascq
H. NAJI	Maître de Conférence - HDR, Université de Lille1, Villeneuve d'Ascq

Soutenue le juin 2008 devant le jury composé de:

A. MEZRHAB	Professeur, Université Mohammed 1er, Maroc	Rapporteur
J-R CLERMONT	Directeur de Recherche, Laboratoire de Rhéologie, Grenoble	Rapporteur
D. LEGENDRE	Professeur, ENSEEIHT - INP, Toulouse	Examinateur
L. THAIS	MCF-HDR, Université de Lille1, Villeneuve d'Ascq	Examinateur

L'UNIVERSITE DES SCIENCES ET TECHNOLOGIES DE LILLE

ECOLE DOCTORALE "SCIENCES POUR L'INGENIEUR"

THESIS

submitted to obtain the degree of

DOCTEUR

DE L'UNIVERSITE DES SCIENCES ET TECHNOLOGIES DE LILLE

Discipline: Mechanical engineering

Presented by

Hossam KAMAL IBRAHIM ABDELHAMID

Numerical prediction of a viscoelastic fluid flow past a non-confined cylinder

Under supervision of:

G. MOMPEAN	Professeur, Université de Lille1, Villeneuve d'Ascq
H. NAJI	Maître de Conférence - HDR, Université de Lille1, Villeneuve d'Ascq

Defended in June 2008 before the jury:

A. MEZRHAB	Professeur, Université Mohammed 1er, Maroc	Reporter
J-R CLERMONT	Directeur de Recherche, Laboratoire de Rhéologie, Grenoble	Reporter
D. LEGENDRE	Professeur, ENSEEIHT - INP, Toulouse	Examiner
L. THAIS	MCF-HDR, Université de Lille1, Villeneuve d'Ascq	Examiner

Résumé

Ce travail a pour principal objectif la prédiction numérique de l'écoulement laminaire bidimensionnel d'un fluide viscoélastique autour d'un cylindre en milieu non confiné. La méthode des volumes finis en coordonnées orthogonales généralisées est ici adoptée pour résoudre les équations de conservation. Le modèle constitutif pour le fluide est de type Phan-Tien Tanner simplifié (S-PTT). Afin de stabiliser l'algorithme de résolution, le schéma dit "Elastic Viscous Split Stresses" (EVSS) est utilisé.

Le code de calcul mis au point a été validé dans le cas de l'écoulement newtonien. Les résultats obtenus corroborent ceux de la littérature. Ensuite, ce code a été appliqué au cas d'un écoulement viscoélastique autour d'un cylindre non confiné. Dans ce cas, l'analyse a été réalisée pour différents nombres de Reynolds ($\mathrm{Re} \leq 200$) et pour différents nombres de Deborah (0.0~0.25). Aussi, les caractéristiques principales de l'écoulement (les contraintes d'extra tension viscoélastiques, la première différence des contraintes normales et les champs de pression, de vitesses et de rotation) ont été présentées et commentées. Enfin, les évolutions de nombre de Strouhal, de la traînée et de la portance sont montrées.

Abstract

The two-dimensional viscoelastic incompressible flow past a non-confined cylinder is numerically simulated. The governing equations are stated in the generalized orthogonal coordinate system and the finite volume method is used to descritize them. For the viscoelastic constitutive equation, the simplified Phan-Thien-Tanner (S-PTT) model is employed. The quadratic scheme QUICK is applied to evaluate the convection terms. In order to enhance the stability of the computations, the Elastic Viscous Split Stress (EVSS) formulation is used to decompose the stress tensor.

The developed code was validated for the Newtonian flow. Then the code is applied to predict the viscoelastic flow past a non-confined cylinder. Concerning this case, analysis was carried out for different Reynolds ($\mathrm{Re} \leq 200$) and Deborah (0.0~0.25) numbers. The studied flow fields are the extra-shear stress, the first normal stress difference, the pressure field, the vorticity, and the velocity. Also, the results for the Strouhal number, the drag and the lift coefficient are presented and commented.

Remerciements

Je tiens à remercier, tout d'abord, Allah tout puissant de m'avoir donné la patience, la force et la volonté d'accomplir ce travail.

Je remercie chaleureusement Monsieur le Professeur Gilmar MOMPEAN directeur de ma thèse et Monsieur Hassan NAJI codirecteur de ma thèse qui ont dirigé mes travaux de thèse et qui m'ont constamment suivi au cours de ces trois années. Leur expérience, leurs conseils et leur compétence m'ont été précieux.

Je remercie sincèrement Monsieur le Professeur Ahmed MEZRHAB de l'Université Mohammed 1er, Oujda, Maroc et Monsieur le Professeur Jean-Robert CLERMONT de l'Université de Grenoble d'avoir accepté d'être rapporteurs du présent mémoire en un temps si court, malgré leur notoriété et leurs emplois du temps chargés.

Merci à Monsieur le Professeur Dominique LEGENDRE de l'université de Toulouse pour sa présence au sein du jury.

A Monsieur Laurent Thais, merci de m'avoir aidé et supporté pendant ma thèse et d'avoir accepté de faire partie du jury.

Je tiens à exprimer ma reconnaissance particulière à Monsieur l'Attaché de Défense auprès de l'ambassade d'Egypte et son équipe de travail pour l'autonomie qu'ils m'ont accordée et la confiance qu'ils m'ont témoigné.

Je remercie tout particulièrement tous mes professeurs à l'Ecole Militaire Polytechnique d'Egypte et je leur exprime toute ma reconnaissance et mon amitié pour leur soutien et les précieux conseils qu'ils m'ont apportés et pour l'aide qu'ils m'ont fourni pendant toute ma carrière.

Cette thèse est dédiée à ma chère Maman, à l'âme de mon cher Papa , mon adorable épouse, à mes guerriers Omar et Abdallah, à mes princesses Alia et Norhan et à mon aimable sœur qui avec leur extraordinaire amour et leur incroyable patience m'ont permis d'obtenir tout ce que j'ai.

KAMAL, Hossam

Table of Contents

LIST OF FIGURES III

LIST OF TABLES VII

LIST OF SYMBOLS VIII

INTRODUCTION 1

1. Motivation and methodology 1

2. Outline of the thesis 3

CHAPTER 1: LITERATURE REVIEW 5

1.1. INTRODUCTION 5

1.2. FLOW PAST A CYLINDER IN NEWTONIAN FLUIDS 5

1.3. VISCOELASTIC FLUID MODELS 8

1.3.1 Brief history 8

1.3.2 Upper Convected Maxwell (UCM) and Oldroyd-B models 10

1.3.3 Phan-Thien/Tanner (PTT) model 11

1.3.4 Giesekus model 13

1.3.5 Finitely Extensible Nonlinear Elastic (FENE) family of models 13

1.3.6 Other models 15

1.4. NUMERICAL WORK 15

1.5. EXPERIMENTAL WORK 18

1.6. SUMMARY OF THE LITERATURE SURVEY 20

CHAPTER 2: THEORETICAL STUDY 21

2.1. CONSERVATION EQUATIONS 21

2.2. THE CONSTITUTIVE EQUATION 22

2.3. TRANSFORMATION TO GENERAL ORTHOGONAL COORDINATES 26

2.3.1 Coordinate transformation 26

2.3.2 Governing equations in generalized orthogonal coordinate 30

2.4. STRESS SPLITTING SCHEME 31

2.5. SUMMARY OF THE THEORETICAL STUDY 32

CHAPTER 3: NUMERICAL METHODOLOGY 33

3.1. THE FINITE VOLUME METHOD (FVM) 33

3.2. SPATIAL DISCRETIZATION 35

3.3. TIME DISCRETIZATION 40

3.4. SOLUTION DOMAIN, BOUNDARY AND INITIAL CONDITIONS 42

3.5. GRID GENERATION AND OPTIMISATION 43

3.5.1 Grid generation 43

3.5.2 Mesh optimization 47

3.6. SUMMARY OF NUMERICAL METHODOLOGY 52

CHAPTER 4: RESULTS AND DISCUSSION 53

4.1. OVERVIEW 53
4.2. RESULTS FOR NEWTONIAN FLUID 54
4.3. VISCOELASTIC RESULTS 57
4.3.1 Extra-Shear Stress 58
4.3.1.a Influence of Reynolds number on the extra-shear stress 58
4.3.1.b Influence of Deborah number on the extra-shear stress 63
4.3.2 Normal stress difference 68
4.3.2.a Influence of Reynolds number on the normal stress difference 69
4.3.2.b Influence of Deborah number on the normal stress difference 74
4.3.3 Pressure distribution 80
4.3.3.a Influence of Reynolds number on the pressure 80
4.3.3.b Influence of Deborah number on the pressure 87
4.3.4 Vorticity 94
4.3.4.a Influence of Reynolds number on the vorticity 94
4.3.4.b Influence of Deborah number on the vorticity 99
4.3.5 Velocity profile 105
4.3.5.a Influence of Reynolds number on the flow velocity 105
4.3.5.b Influence of Deborah number on the velocity field 114
4.3.6 Strouhal number 122
4.3.7 Drag Force 124
4.3.8 Lift Force 129

CHAPTER 5: CONCLUSIONS & PERSPECTIVES 131

5.1. CONCLUSIONS 131
5.2. PERSPECTIVES 134

APPENDIX: FLOWCHART OF THE DEVELOPED CODE 135

REFERENCES 137

List of Figures

Figure 1.1 Regimes of flow around a smooth, circular cylinder in steady current (source: Sumer and Fredsøe [2]) 7

Figure 1.2 The dumbbell model 9

Figure 2.1 Cartesian and generalized orthogonal coordinate systems 27

Figure 3.1 Notation for points and distances for pressure velocity control volumes 36

Figure 3.2 Schematic drawing showing the domain solution limits and boundary conditions 43

Figure 3.3 Control volume notation for 3D and 2D cases 43

Figure 3.4 Control volume for calculating scalar quantities (solid colour and capital letters) and control volume for evaluating vector components (hatched and dotted colours with small letters) 44

Figure 3.5 Generated orthogonal grid: (a) the whole grid, (b) zoomed view around the cylinder 46

Figure 3.6 Effect of changing the time step on (a) vertical velocity, (b) drag coefficient and (c) lift coefficient 51

Figure 3.7 Values of non-dimensional quantities for different number of points on cylinder 52

Figure 4.1 Velocity field for a Newtonian fluid flow at: (a) Re = 4, (b) Re = 40, and (c) Re = 47 56

Figure 4.2 Longitudinal and cross sections, and streamlines used to quantify the results. 57

Figure 4.3 Extra-shear stress distribution for De = 0.15 at (a) Re = 40, (b) Re = 60, and (c) Re = 100 59

Figure 4.4 Zero-extra-shear stress contour at De = 0.15 for Re=40 and 45. 60

Figure 4.5 Zero-extra-shear stress contour at De = 0.15 for Re=80, 100 and 125. 61

Figure 4.6 Extra-shear stress magnitudes at De = 0.15 for Re = 40, 60, and 80 along : (a) section S1, (b) section S2, and (c) streamline SLd. 62

Figure 4.7 Extra-shear stress contours for Re = 40 and different Deborah numbers 63

Figure 4.8 Extra-shear stress magnitude for Re = 40 at different Deborah number along (a) section S1 and (b) streamline SLu 64

Figure 4.9 Extra-shear stress at Re = 47 with: (a) De = 0.05, (b) De = 0.15, and (c) De = 0.25 65

Figure 4.10 Extra-shear stress contour at Re = 47 for De = 0.05, 0.15, and 0.25 with indication of asymmetry reduction 66

Figure 4.11 Extra-shear stress magnitudes for Re = 47 along: (a) section S1, (b) section S2 and (c) streamline SLu 67

Figure 4.12 Extra-shear stress magnitudes for Re = 47 at: (a) section S3 and (b) section S4 68

Figure 4.13 First normal stress difference distribution for De = 0.15 at: (a) Re = 45, (b) Re = 80 and (c) Re = 150 70

Figure 4.14 Zero-normal stress difference contour for De = 0.15 at Re = 40 and 45 71

Figure 4.15 Zero-normal stress difference contour for De = 0.15 at Re = 80, 100 and 125 71

Figure 4.16 Normal stress difference magnitudes for De = 0.15 at: (a) section S3 and (b) section S4. 72

Figure 4.17 Normal stress difference magnitudes for De = 0.15 at: (a) section S1, (b) section S2, and (c) streamline SLu. 73

Figure 4.18 Normal stress difference distribution for Re = 40 at: (a) De = 0.1 and (b) De = 0.2 74

Figure 4.19 Zero-normal stress difference contour for Re = 40 75

Figure 4.20 Normal stress difference values for Re = 40 along: (a) section S1 and (b) streamline SLu 76

Figure 4.21 Normal stress difference distribution for Re = 47 at: (a) De = 0.05, (b) De = 0.15 and (c) De = 0.25 77

Figure 4.22 Zero-normal stress difference contour for Re = 47 at De = 0.05, 0.15 and 0.25 78

Figure 4.23 Normal stress difference magnitudes for Re = 47 along: (a) section S1, (b) section S2, and (c) streamline SLu 79

Figure 4.24 Pressure distribution for viscoelastic fluid at De=0.1 for: (a) Re = 40, (b) Re = 60, and (c) Re = 100 81

Figure 4.25 Pressure contours for viscoelastic fluid at De = 0.1 for Re = 35, 40, and 45. 82

Figure 4.26 Pressure contours for viscoelastic fluid having De = 0.1 for Re = 80, 100, and 125 83

Figure 4.27 Magnitudes of pressure for De =0.1 and different Re at: (a) section S3 and (b) section S4 83

Figure 4.28 Pressure for De =0.1 and different Re along: (a) section S1, (b) section S2 and (c) streamline SLu 84

Figure 4.29 Normalized pressure over the cylinder surface for De=0.15 and different Reynolds numbers 85

Figure 4.30 Shift of separation point with increased Reynolds number 86

Figure 4.31 Wake angle versus Reynolds number for different Deborah numbers 86

Figure 4.32 Effect of fluid elasticity on pressure contours at Re = 40 with De = 0.0, 0.1, and 0.15 88

Figure 4.33 Magnitudes of the normalized pressure at Re = 40 on (a) section S1 and (b) streamline SLu. 88

Figure 4.34 Effect of fluid elasticity on pressure distribution at Re= 60 (a) De = 0.0, (b) De = 0.05, and (c) De = 0.15 90

Figure 4.35 Effect of fluid elasticity on pressure contours at Re=60 and different Deborah numbers 91

Figure 4.36 Effect of Deborah number on the separation point at Re= 60. 91

Figure 4.37 Wake angle versus the Deborah number for different Reynolds number. 92

Figure 4.38 Normalized pressure at Re = 60 on (a) section S1, (b) Streamline SLd, (c) section S3, and (d) section S4. 93

Figure 4.39 Normalized vorticity profile for De = 0.15 at: (a) Re = 40, (b) Re = 80 and (c) Re = 150 95

Figure 4.40 Zero-vorticity contour for De = 0.15 at (a) Re = 35, 40, and 45, and (b) Re = 80, 100, and 125. 96

Figure 4.41 Normalized vorticity values for De = 0.15 at (a) Section S3 and (b) Section S4 97

Figure 4.42 Normalized vorticity values for De = 0.15 along (a) Section S1, (b) Section S2 (c) Upper streamline SLu 98

Figure 4.43 Vorticity profile for Re = 45 with (a) De = 0.0, (b) De = 0.1 and (c) De = 0.2 100

Figure 4.44 Zero-vorticity contours for Re = 40 with different Deborah number 100

Figure 4.45 Vorticity profile for Re = 100 with (a) De = 0.0, (b) De = 0.05 and (c) De = 0.15 101

Figure 4.46 Vorticity profile for Re = 100 with (a) De = 0.0, (b) De = 0.05 and (c) De = 0.15 102

Figure 4.47 Magnitudes of vorticity for Re = 100 at (a) Section S1 and (b) Upper streamline SLu 103

Figure 4.48 Magnitudes of vorticity for Re = 100 at (a) Section S1 and (b) Upper streamline SLu 104

Figure 4.49 Normalized velocity for viscoelastic fluid with De=0.1 at: (a) Re = 35, (b) Re = 60, and (c) Re = 125 106

Figure 4.50 Contour of unit normalized velocity for De = 0.15 at: (a) Re = 35, 40 and 45 and (b) Re = 80, 100, and 125. 107

Figure 4.51 Velocity magnitudes for De = 0.15 at Re =40,60, and 100 along the streamline SLu 107

Figure 4.52 Velocity magnitudes for De = 0.15 at: (a) section S1, (b) section S2, (c) section S3, and (d) section S4 108

Figure 4.53 Time history of vertical velocity component for De=0.1 at (a) Re = 40, (b) Re = 50, and (c) Re = 100 110

Figure 4.54 Amplitude of vertical velocity fluctuations versus Reynolds number for different Deborah numbers 111

Figure 4.55 Rise time of velocity fluctuations versus Reynolds number for different Deborah numbers 112

Figure 4.56 Roshko number versus Reynolds number for different Deborah numbers with comparison to the formula of Pipe & Monkewtiz [58] 113

Figure 4.57 Normalized velocity profile for Re = 45 at (a) De = 0.0, (b) De = 0.2 115

Figure 4.58 Effect of fluid elasticity on velocity contours for Re<Recr 115

Figure 4.59 Normalized velocity field for Re = 100 at (a) De = 0.0, (b) De = 0.1, and (c) De = 0.15 117

Figure 4.60 change of velocity contours with the Deborah number at Re = 60. 118

Figure 4.61 Normalized velocity magnitudes for Re = 60 at (a) Section S3 and (b) Section S4 118

Figure 4.62 Normalized velocity values for Re = 60 at (a) Section S1 and (b) Upper streamline SLu 119

Figure 4.63 Amplitude of vertical velocity fluctuations versus Deborah number for different Reynolds numbers 120

Figure 4.64 Rise time of velocity fluctuations versus Deborah number for different Reynolds numbers 121

Figure 4.65 Strouhal number versus Reynolds number for different Deborah numbers. 123

Figure 4.66 Strouhal number versus Deborah number for different Reynolds numbers. 123

Figure 4.67 Average drag force coefficient versus Deborah number for different Reynolds numbers 126

Figure 4.68 Root mean square drag force coefficient versus Deborah number for different Reynolds numbers 126

Figure 4.69 Time history of the drag at Re = 100 for different Deborah number 127

Figure 4.70 Average drag force coefficient versus the Reynolds number for different Deborah number 128

Figure 4.71 Average root mean square drag force coefficient versus the Reynolds number for different Deborah number 128

Figure 4.72 Root mean square of the lift coefficient versus the Deborah number for different Reynolds number 129

Figure 4.73 Root mean square of the lift coefficient versus the Reynolds number for different Deborah number 130

List of Tables

Table 2.1 Different fluid models obtained by changing the constitutive equation parameters β, ε, and ξ 25

Table 3.1 Variables of the generalized transport equation and their corresponding quantities in the governing equations. 34

Table 3.2 characteristics of the computational meshes. 48

Table 3.3 computational characteristics of meshes. 48

Table 3.4 Comparison of non-dimensional quantities for different mesh grids. 49

Table 3.5 Running time for different time steps. 50

Table 3.6 Relative change of values of non-dimensional quantities for different time steps. 50

List of Symbols

Latin symbols:

$\mathbf{A}$	general tensor
$\mathrm{d}A$	infinitesimal area
B	bottom face of the control volume
C_{bp}	average base pressure coefficient
C_d	average drag coefficient
C_{l-rms}	root mean square lift coefficient
$\mathbf{D}$	rate of deformation tensor
D	cylinder diameter
De	Deborah number
E	east face of the control volume
$\vec{F}$	total force exerted on the cylinder
$\vec{F}_1$ and $\vec{F}_2$	forces of the spring on the two beads of the dumbbell (Figure 1.2)
F_D	drag force
F_L	lift force
f	frequency of vortex shedding.
$\mathbf{g}$	metric tensor
h	downstream point on the x-axis (Figure 4.2)
H_i^j	stretching factors
h_i	scale factors
I	identity matrix
$\lvert J \rvert$	Jacobian of coordinate transformation
k	stiffness constant of the dumbbell spring (Figure 1.2)
M_i	mesh grid
m_1 and m_2	two beads of mass of the dumbbell (Figure 1.2)
mem	quantity of total used memory by the code
N	north face of the control volume
N_1	first normal stress difference
$\overline{N}_1$	dimensional value of the first normal stress difference
N_2	sconde normal stress difference
N_c	total number of nodes
N_{cyl}	number of nodes on the cylinder
$\hat{n}$	outward unit vector
P	pressure
P_n	normalized values of pressure
$\mathbf{Q}$	the end-to-end vector of the polymer chain
Q, and Q_0	finite constant representing the fully stretched length of the molecules
R	cylinder radius

Re	Reynolds number:
R_{sk},	the Roshko number
r	coordinate in the standard polar coordinates
$\vec{r}_1$ and $\vec{r}_2$.	position vectors of the two masses of the dumbbell (Figure 1.2)
S	south face of the control volume
$S_{i,j}^{nm}$	physical surface area of the control volume face
Str	Strouhal number
S1 and S2	two longitudinal sections (Figure 4.2)
S3 and S4	two cross sections (Figure 4.2)
SLu and SLd	two streamlines (Figure 4.2)
S_Φ	source term
$\delta s_{\min/\max}^{i}$	minimum and maximum side lengths of control volumes.
T	top face of the control volume
t_0	typical time scale of the flow
t_{comp}	the total computation time
Δt	time step
U_0	the free-upstream velocity
V^i	the physical volume of the control volume
$V_{\min/\max}^{i}$	minimum and maximum areas of control volumes
dV	infinitesimal volume
$\breve{\mathbf{v}}\left(\breve{v}_i\right)_{i=1,2,3}$	physical velocity field
$\mathbf{v}$	velocity field
W	west face of the control volume
Wi	Weissenberg number
x	horizontal position
dx_{rq}	physical distances between successive nodes
Y	function of material properties
y	vertical position
z	lateral coordinate

Greek symbols:

α	a parameter representing the dimensionless “mobility factor”
β	retardation ratio.
$\dot{\gamma}$	typical shear rate of the flow
Γ	time parameter.
δ_{ij}	Kronecker delta.
ε	material parameter related to its elongation behaviour.
dζ_i	infinitesimal physical distances in curvilinear coordinates
η_0	total viscosity
η_p	the polymer-contributed viscosity
η_N	Newtonian solvent viscosity

η_m	molecular contributed viscosity.
η_{m0}	zero-shear rate molecular contributed viscosity.
Θ	coefficient of the transported variable
θ	angle coordinate of the standard polar coordinates
θ_w	wake angle
Λ	coefficient fo the transported variable
λ	characteristic time constant (fluid relaxation time)
μ	parameter relating different viscosities
ν	fluid kinematic viscosity
ξ	material parameter related to its elongation behaviour.
ρ	fluid density
$\mathbf{\Sigma}$	purely elastic stress
$\boldsymbol{\tau}$	viscoelastic stress tensor
$\bar{\tau}_{12}$	calculated value of extra-shear stress
Φ	transported quantity
ϕ	velocity potential
$\vec{\psi}(\psi_1,\psi_2)$	generalized orthogonal coordinate system.
ψ	stream function of the potential flow past a cylinder
$\vec{\omega}.$	vorticity
$\bar{\omega}$	dimensional value of vorticity

Abbreviations and operators

2D	two-dimensional
3D	three-dimensional
AESM	algebraic extra-stress model
CFD	Computational Fluid Dynamics
CS	control surface
CV	control volume
DEVSS	discrete elastic viscous split stress formulation
EVSS	Elastic-Viscous Stress Splitting formulation
FDM	Finite Difference Method
FENE	Finitely Extensible Nonlinear Elastic
FENE-P	FENE model with Peterlin's closure
FENE-L	FENE model with Lielens's closure
FENE-CR	FENE model with Chilcott and Rallison's closure
GLS3	three-field velocity-pressure-stress Galerkin/Least-Squares
LDPE	low density polyethylene
PDF	probability distribution function
PTT	Phan-Thien/Tanner model
QUICK	Quadratic Upstream Interpolation Scheme for Convective Kinematics
UCM	Upper Convected Maxwell model
"$\breve{}$"	physical components in the curvilinear coordinates
∇	vector differential operator

INTRODUCTION

Turning mining waste into paste wins prize

A chemical engineer, whose work in fluid mechanics is reducing the environmental impact of mining, has been awarded Australia's premier national award for scientific achievement. Professor David Boger of the University of Melbourne was awarded the Prime Minister's Prize for Science. Boger says his research has allowed some mines to convert their waste into a paste-like form that is less mobile and thus is less of a threat to the environment. His key contribution to science has been in the understanding of how "non-Newtonian" fluids behave.

ABC Science Online - Wednesday, 5 October 2005

In the last two decades, the interest in studying non-Newtonian fluids has increased. This is mainly due to their wide use in chemical process industries, food industry, construction, petroleum engineering, power technology, and many commercial and technological applications. Important examples of this type of fluids are slurries, ceramics, toothpaste, gels, various kinds of mineral oils, some types of suspensions, etc. Modelling the dynamics of such fluids in processes such as pipelining, extrusion, emulsification, etc., is often a delicate and challenging task, leading to mathematical problems of relevant difficulty. Viscoelastic fluids represent a category of non-Newtonian fluids. These fluids exhibit not only viscous, but also elastic behaviour (including memory effects), which is not encountered in simple Newtonian fluids such as water or air.

1. Motivation and methodology

The numerical simulation of viscoelastic fluid flow is a rich research area because of the need to understand the viscoelastic fluid behaviour in many engineering problems. Besides, the flow past a curved obstacle is one of the daily encountered problems in many applications. This work deals with the simulation of a viscoelastic fluid flowing past a non-confined cylinder. The viscoelastic fluid is described by a differential constitutive equation devised the Phan-Thien-Tanner (PTT) model [1]. To

carry out the simulation of this flow domain, the obstacle is assumed as a long cylinder placed inside the domain. The presence of such an obstacle exhibits some important changes in the flow field. One of these changes is the occurrence of the von Kármán vortex street phenomenon, beyond a critical Reynolds number, which is a repeating pattern of swirling vortices induced by the unsteady separation of flow over bluff bodies. On the other hand, it is known that the addition of small amounts of polymer to a Newtonian fluid can drastically change the properties of flows. However, these modifications such as the drag reduction effect or the suppression of small-scale fluctuations are still not well understood. Indeed, the link between these two phenomena remains especially unclear. Hence, simulating the viscoelastic fluid flow past a cylinder can be useful to better understand these phenomena.

In viscoelastic fluid mechanics, a considerable amount of work deals with the viscoelastic fluid flow past a cylinder. However, most of these works have considered the problem of the cylinder placed symmetrically between two plates or inside a channel. This is the well-known confined cylinder problem. The blockage ratio defines the ratio of the cylinder diameter to the distance between the two plates (or the channel height). It is noted that the problem of a confined cylinder with blockage ratio of 0.5 has been dealt with extensively, while the problem of non-confined cylinder is almost unexplored. Up to our knowledge, no work is found simulating the PTT fluid flow past a non-confined cylinder.

The presence of an obstacle inside the solution domain poses great complexity on the discretization technique. The usual Cartesian discretization of the domain fails to trace the curved profile of the obstacle. Polar and spherical coordinate systems may represent a solution but they face another problem in defining flat domain boundaries. Non-structured grids arise as an acceptable substitution for those traditional systems. However, this technique of space discretization has heavy complexity and computational cost. In the present study, the generalized orthogonal coordinate system is adapted to express the governing equations. This system of coordinates allows avoiding the problems of the traditional coordinate systems with a light computational cost.

The numerical approach is based on the Finite Volume Method (FVM) which is applied to descritize the governing equations. This method is very widely used in Newtonian fluid mechanics. Viscoelastic fluid mechanics was investigated, at early beginnings, by structural engineers so the Finite Element Method (FEM) is still dominating the field. With the introduction of FVM, viscoelastic fluid simulation has benefited from the simplicity and accuracy of this method. The implementation of the FVM in non-Newtonian fluid simulations is rapidly growing. Other methods (like Spectral Methods SM, Finite Difference Method FDM, and Boundary Element Method BEM) have been, also, used in research works.

In summary, our main contribution in the present work consists of

- simulating the viscoelastic fluid flow with a PTT model,
- considering the non-confined cylinder geometry,
- and implementing the FVM in generalized orthogonal coordinates.

2. Outline of the thesis

Motivated by the objective of the viscoelastic flow simulation, the entire work in this thesis is divided into four chapters. A brief literature review is presented in the first chapter. This survey introduces the previous works concerning the viscoelastic fluid flow simulation past a cylinder. This chapter reviews the recent experimental and numerical studies in the field.

In the second chapter, the governing differential equations are stated. First, Cartesian conservation equations and the constitutive equation are written. Then, the transformation of coordinates is discussed and the equations are re-written in a generalized orthogonal coordinate system. The used stress splitting scheme is presented and the final form of the equations are stated.

The third chapter discusses the numerical methodology, first introducing the grid generation technique. Then, the spatial discretization is depicted emphasizing the descritized components of velocity, pressure and stress. Next, the time marching technique is described. Finally, mesh optimization is performed.

In the fourth chapter, the physical results are shown and discussed. The numerical code is first validated for the Newtonian fluid flow. Then, the viscoelastic results are presented and commented. A particular attention is paid to the effects of Reynolds and Deborah numbers on velocity, vorticity, pressure, extra-shear stress, normal stress difference and the drag and lift forces.

Finally, the conclusions of this work are drawn and perspectives for future work are proposed.

Chapter 1: LITERATURE REVIEW

1.1. Introduction

In this chapter, a literature survey is presented for the recent work concerning the flow of viscoelastic fluid past a cylinder. To help out in the implementation of the results, the flow regimes of flow around a cylinder for Newtonian fluid are first defined. Then, the different viscoelastic models are reviewed to show the advances of theoretical work in the domain. After that, an overlook of the different numerical methods applied in the field of viscoelastic fluid flow past a cylinder are presented. Next, the main experimental work is summarized. Finally, a summary of this review justifies the choice of flow regime, viscoelastic constitutive equation, and the applied numerical method.

1.2. Flow past a cylinder in Newtonian fluids

Over decades, bluff body wake flows have had a great deal of interest because of their direct engineering significance. As we are interested here in the flow of viscoelastic fluids, it seems to us adequate to recall the different regimes of flow past a cylinder in the simpler case of Newtonian fluid. This will help to understand the effects of viscoelasticity on the flow.

The Newtonian flow around a cylinder depends on the macroscopic Reynolds number:

$$\mathrm{Re} = \frac{DU}{\nu}, \qquad 1.1$$

where D is the cylinder diameter, U is the magnitude of the free stream flow velocity, and ν is the fluid kinematic viscosity.

In the book of Sumer and Fredsøe [2], nine flow regimes are specified for the flow around a smooth, circular cylinder in a steady current. These regimes are:

- The creeping flow with no separation from the cylinder surface ($\mathrm{Re} < 5$).
- The flow with stable wake ($5 \le \mathrm{Re} < 40$). In this regime, a fixed pair of symmetric vortices are formed downstream the cylinder.
- The laminar vortex shedding flow which is called in many references the von Karman street ($40 \le \mathrm{Re} < 200$). In this regime the flow is essentially two-dimensional with no variation in spanwise direction.
- The transition to turbulence regime ($200 \le \mathrm{Re} < 300$). The region of transition to turbulence moves towards the cylinder with the increase of Reynolds number. The vortices become three-dimensional (Williamson [3]).
- The subcritical regime ($300 \le \mathrm{Re} < 3\times10^5$) with completely turbulent wake.
- The critical regime ($3\times10^5 \le \mathrm{Re} < 3.5\times10^5$) having a turbulent boundary layer at the separation point on only one side of cylinder.
- The supercritical regime ($3.5\times10^5 \le \mathrm{Re} < 1.5\times10^6$). In this regime, the boundary layer becomes turbulent on both sides of the cylinder. However, the transition to turbulence in the boundary layer has not been completed yet.
- The upper transition regime ($1.5\times10^6 \le \mathrm{Re} < 4\times10^6$). Here, the boundary layer on one side of cylinder is completely turbulent.
- The final transcritical regime ($\mathrm{Re} > 4\times10^6$) with a completely turbulent flow everywhere.

The schematic drawings on Figure 1.1 summarize these flow regimes.

From this description, it is shown that the flow is laminar for Re < 200. As the nature of the viscoelastic fluids has not been yet completely understood, the vast majority of numerical simulations are still limited to laminar flow regime and most practical applications are in the laminar regime, with the noticeable exception of the turbulent drag reduction. The present work investigates a new problem, so the two-dimensional configuration will be considered. The three-dimensional analysis needs to employ the parallel computation techniques which are planned as a future step. Hence, we shall restrict this work to Re < 200 to perform laminar two-dimensional flow simulations.

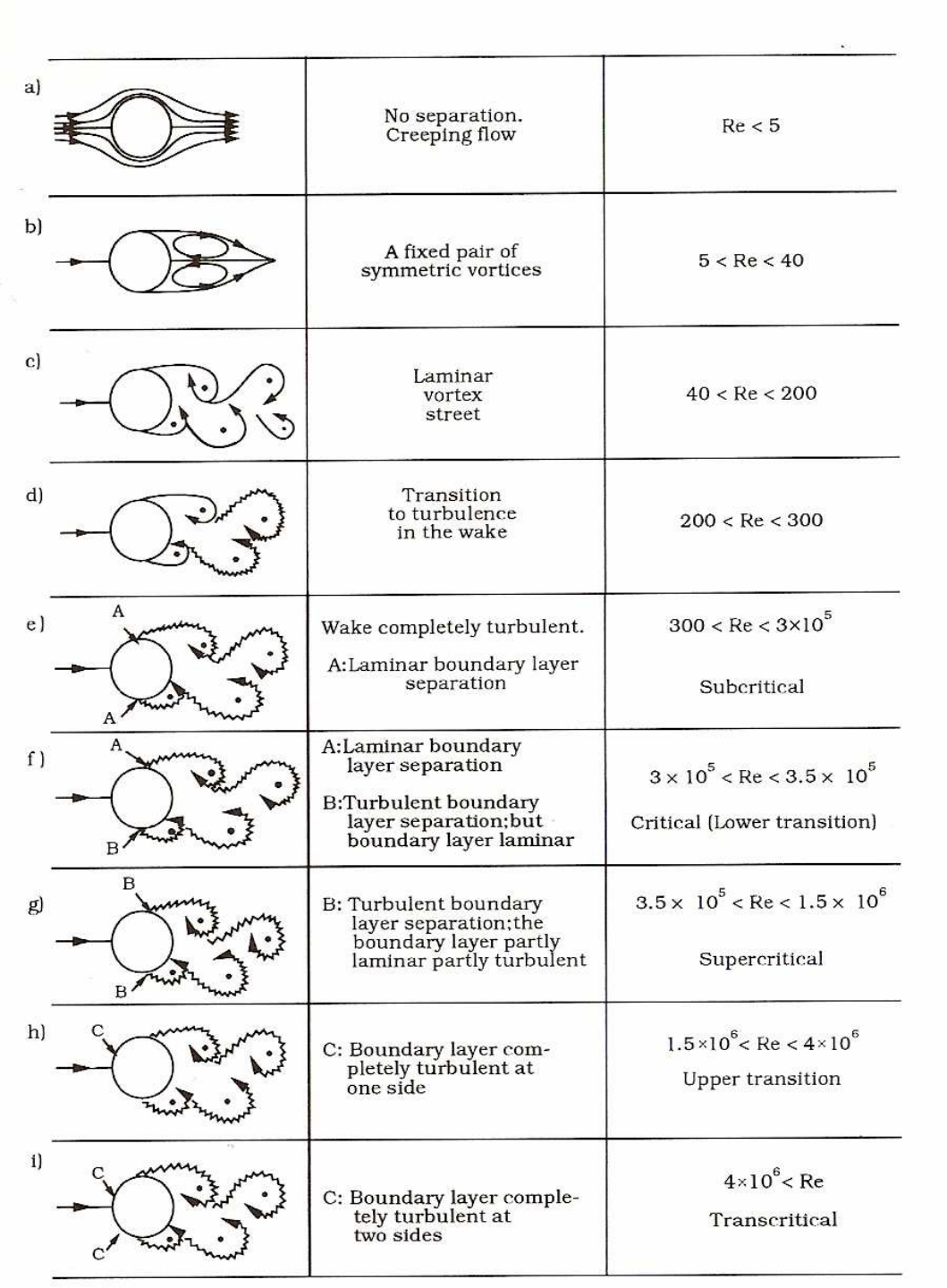


Figure 1.1 Regimes of flow around a smooth, circular cylinder in steady current (source: Sumer and Fredsøe [2])

1.3. Viscoelastic fluid models

In general, there are two main classes of viscoelastic fluid models: differential models describing the dilute solutions of polymer molecules, and integral models which are more appropriate for more concentrated polymer solutions or for melts. The present work applies a viscoelastic fluid model of differential type. So, we survey here the recent literature models of the flow past a cylinder using both types of models, but focusing more on the differential type. In this section, a brief historical note about viscoelastic fluid models is presented first. Then, the published works of different viscoelastic models are reviewed.

1.3.1 Brief history

For viscoelastic fluids, in particular polymeric liquids, there are many different constitutive equations proposed and employed. However, they all point out to the presence of at least one characteristic time constant λ in a differential or integral equation for the stress. The appearance of a time constant is related to the phenomenon of stress relaxation typical of viscoelastic fluids. The time constant λ gives rise to a new non-dimensional parameter, the Deborah number $\mathrm{De} = \lambda / t_0$ where the unit of time t_0 is a typical time scale of the flow. Another non-dimensional number is the Weissenberg number $Wi = \lambda \dot{\gamma}$ which relates the relaxation constant to a typical shear rate $\dot{\gamma}$ of the flow.

The simplest model designed to capture the slowest and the most important relaxation mode of a polymer chain in a dilute polymer solution is the elastic dumbbell model proposed by Kuhn in 1934. This model considers an elastic dumbbell immersed in a Newtonian solvent. This dumbbell consists of two beads of mass m_1 and m_2 interconnected by a spring having a stiffness constant of k, as shown in Figure 1.2. The position vectors of the two masses are represented by $\vec{r}_1$ and $\vec{r}_2$. The forces of spring on the two beads are $\vec{F}_1$ and $\vec{F}_2$.

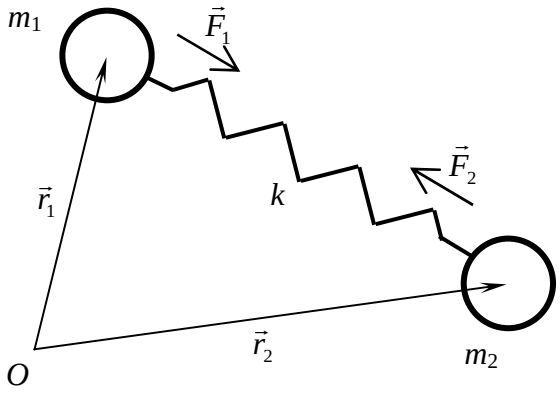


Figure 1.2 The dumbbell model

From that time, almost all the models are based on this concept to simulate the viscoelastic effects. First, the Langevin equation is used to relate the strength of the Brownian forces to the mobility of the polymer beads through the fluctuation dissipation theorem and this represents the micro-scale level. Then, the Fokker-Planck equation for the density distribution function of the end-to-end polymer chain vector is used to describe the flow-induced deformations and the restoring forces. By that, the models advanced to the macro-micro-scale level. In 1950, Oldroyd transferred the models to the macro-scale level as he introduced an important derivative of the polymer-contributed stress to guarantee the objectivity of the stress tensor. This derivative is the upper convected derivative and the first model of this type is called the Upper Convected Maxwell (UCM) model. After that, Oldroyd introduced his constitutive equation called Oldroyd-B model which combines the solvent and the polymer contributed stresses. This model describes many features of dilute solutions of polymers in highly viscous solvents (Boger fluids). These models fail to simulate complex flows as they have two main problems. The first problem is that they count only for a constant shear viscosity. The second one is that they predict an infinite stress at finite elongation rate which is not physically realistic. To fix these problems, new models were proposed like Phan-Thien/Tanner (PTT) model, Giesekus model and the Finitely Extensible Nonlinear Elastic (FENE) model of long-chained polymers.

1.3.2 Upper Convected Maxwell (UCM) and Oldroyd-B models

The UCM and Oldroyd-B models were introduced as a result of the definition of the upper convected derivative. The upper convected derivative of a tensor $\mathbf{A}$ is defined as:

$$\frac{\Delta}{\Delta t}\mathbf{A} \equiv \frac{\partial}{\partial t}\mathbf{A} + (\mathbf{v}\cdot\nabla)\mathbf{A} - (\nabla\mathbf{v})^{\mathrm{T}}\cdot\mathbf{A} - \mathbf{A}\cdot(\nabla\mathbf{v}), \qquad 1.2$$

where $\mathbf{v}$ is the velocity vector and ∇ is the vector differential operator.

These abovementioned constitutive equations simulate the viscoelastic effect as an upper derivative of the stress tensor. The constitutive equation of the UCM model is

$$\lambda\frac{\Delta\boldsymbol{\tau}}{\Delta t} + \boldsymbol{\tau} = 2\eta_p\mathbf{D}\,, \qquad 1.3$$

where λ is fluid time of relaxation, $\boldsymbol{\tau}$ is the viscoelastic stress tensor, η_p is the polymer-contributed viscosity and $\mathbf{D}$ is the rate of deformation tensor.

The Oldroyd-B model states that

$$\lambda\frac{\Delta\boldsymbol{\tau}}{\Delta t} + \boldsymbol{\tau} = 2\eta_0\mathbf{D} + 2\lambda\eta_N\frac{\Delta\mathbf{D}}{\Delta t}\,, \qquad 1.4$$

where η_0 is the total viscosity and η_N is the Newtonian solvent viscosity.

While the UCM constitutive equation remains an illustrative model and does not represent a real fluid behaviour, the Oldroyd-B model can represent some real Boger fluids. Since the introduction of these two models, many works have implemented them in many disciplines. We show here some examples of the use of theses models in the last decade for the flow past a cylinder.

Oliveira et al. [4] introduced a new finite-volume collocated method. To validate this new method, calculations have been carried out for two problems: the entry flow and the bounded and unbounded flows around a circular cylinder. Phan-Thien & Dou [5] simulated the flow past a confined cylinder using parallel distributed computations. They tested the UCM model and applied the PTT model to count for shear-thinning. Dou & Phan-Thien [6] continued to focus on the parallelisation but they used only the

Oldroyd -B model and added discrete elastic viscous split stress (DEVSS) formulation together with an independent interpolation of the vorticity. To evaluate a new stabilized three-field velocity-pressure-stress Galerkin/Least-Squares (GLS3), Behr et al. [7] tested this formulation on the case of flow past a cylinder placed in a channel. Sahin and Wilson [8] extended a dilation-free semi-staggered finite volume method which was proposed by Sahin [9] for viscoelastic fluid flows. This method is based on solving the incompressible Navier-Stokes equations on all-quadrilateral (2D)/ hexahedral (3D) unstructured meshes. They applied it to the problem of confined cylinder with blockage ratio of 0.5. Recently, Dou and Phan-Thien [10] proposed a parallelized unstructured FVM using pressure correction with triangular meshes with a co-located mesh arrangement. They simulated the flow of the Oldroyd-B fluid past a circular cylinder in a channel to validate the proposed method. They used a fine grid to reach a Deborah number of De = 1.6 at low Reynolds Re < 3.

Concerning integral models, Rasmussen [11] presented a new technique based on a Lagrangian kinematic description of the fluid flow and represents a further development of the 2D Lagrangian integral method (LIM) of UCM fluid. He attained a maximum Deborah number of De=0.8. The convergence of the method is demonstrated for the problem of a sphere moving in a cylinder filled with an UCM fluid. A highly parallel time integration method is presented by Caola et al. [12] to demonstrate the calculation of two-dimensional (2D) flow of an Oldroyd-B fluid around an isolated cylinder confined between two parallel plates.

From this survey, it is shown that UCM and Oldroyd-B models are still considered in many works. However, they are mainly employed to validate new methods and techniques or to establish theoretical hypotheses like the work of Doering *et al.* [13] and Renardy [14].

1.3.3 Phan-Thien/Tanner (PTT) model

The Phan-Thien-Tanner (PTT) model was firstly introduced [1] to overcome the problem of infinite stress at finite elongation rate. This model constrains the dumbbell length to a maximum allowable length. After that, Phan-Thien [15] has modified the PTT model to consider the shear-thinning effects. The PTT constitutive equation is written as

$$\lambda \frac{\Delta \boldsymbol{\tau}}{\Delta t} + Y\boldsymbol{\tau} = 2\eta_p \mathbf{D}\,. \qquad 1.5$$

In this equation, the parameter Y is a function of material properties which has either linear or exponential form.

The PTT model represents some real dilute polymer solutions. In the work of Baaijens et al. [16], the authors investigated the flow of a low density polyethylene (LDPE) melts past a confined cylinder. They tested the performance of two constitutive models: the exponential version of the PTT model and the Giesekus model. They performed the work in two parts; numerical and experimental. The contribution of their work is that they fitted the experimental data to find the real values of the viscoelastic numerical model constants. Dou and Phan-Thien [17] studied the flow past a confined cylinder but focused on the parallelisation. They applied the simplified form of the PTT model. The main objective of their work is the implementation of distributed computations. Phan-Thien and Dou [5] studied the drag coefficient of confined cylinder using parallel computation and concluded that the distribution of pressure along the cylinder will be changed by the normal stress for viscoelastic fluid. Also, they found that the normal stress reduces drag due to the non-symmetry about x-axis. They concluded that, for the PTT model, the drag reduction is mainly due to shear thinning. Chauviere and Owens [18] developed a new spectral element method for the accurate integration of the mixed elliptic hyperbolic system of partial differential equations. The method is illustrated by solving the benchmark problem of the flow of an Oldroyd-B and a PTT fluid past a cylinder in a channel. As stated in the previous section, Dou and Phan-Thien [10] simulated the PTT fluid flow past a confined cylinder to test the distributed computations for fine meshes. They found that the instability is due to an inflectional velocity profile, near the cylinder, generated by normal stress on the cylinder surface at high Deborah number. This can only be captured with fine meshes. Afonso et al. [19] studied the uniform steady flow of viscoelastic fluids past a cylinder placed between two moving parallel plates for five constitutive models (UCM, Oldroyd-B, FENE-CR, PTT and Giesekus). The aim of using five models is to assess the effect of rheological properties on the flow kinematics and wake patterns. Simulations were carried out under creeping flow conditions. Accurate solutions were obtained for PTT and FENE-CR models.

The PTT fluid has, also, many applications like rectangular pipe flow (Xue et al. [20], Yamamoto et al. [21]), circular pipe and channel flows (Cruz et al. [22]), flow through a contraction (Alves et al. [23]), lubrication (Akyildiz and Bellout [24]) …etc.

The PTT model is actively used in simulating the flow around a cylinder till recently. Also, it is noted that all these simulations concern the benchmark problem of a confined cylinder. Hence, simulating PTT fluid flow past a non-confined cylinder is a novelty, bearing in mind that the PTT model represents real fluids.

1.3.4 Giesekus model

The Giesekus model was introduced as a remedy for the problems of UCM and Oldroyd-B models. Its constitutive is equation states that

$$\lambda \frac{\Delta \boldsymbol{\tau}}{\Delta t} + \boldsymbol{\tau} + \frac{\alpha \lambda}{\eta_p} (\boldsymbol{\tau})^2 = 2\eta_p \mathbf{D}, \qquad 1.6$$

where α is a parameter representing the dimensionless “mobility factor”.

For the flow around a cylinder, the Giesekus model was used by Sun et al. [25] to simulate the case of confined cylinder using the FEM. The results showed a continuous decline of drag with Weissenberg number. Baaijens et al. [16] fitted a Giesekus 4-mode fluid to the low density polyethylene data. Hulsen et al. [26] implemented the FEM to investigate the flow of an Oldroyd-B and Giesekus fluids around a cylinder in a channel. They found that the Giesekus model gives convergent results for the stress in the wake beyond some rather small Weissenberg number.

Despite that the Giesekus model represents some real viscoelastic fluids; the non-linear term in its constitutive equation poses computational problems. This limits the the use of this model in numerical simulations.

1.3.5 Finitely Extensible Nonlinear Elastic (FENE) family of models

This type of models was introduced as an alternative to the Hookean spring force law. It uses the same dumbbell model but considers the connector force law proposed by Warner in 1972 stating that the force $\mathbf{F}$ is

$$\mathbf{F} = \frac{k\mathbf{Q}}{1-\left(Q^2/Q_0^{\,2}\right)}. \qquad 1.7$$

where $\mathbf{Q}$ is the end-to-end vector of the polymer chain, $Q^2 = \mathrm{Tr}\langle\mathbf{QQ}\rangle$ and Q_0 is some finite constant representing the fully stretched length of the molecules.

With this formulation, it is not possible to form the constitutive equation from the diffusion equation (Fokker-Planck equation) for the probability distribution function (PDF) directly as in the case of simple Hookean spring. Approximations are needed to form the constitutive equation. Each approximation approach leads to a different form of the constitutive equation. So, the FENE model is considered as a family of models according to the used approximation (FENE-P, FENE-L, FENE-CR).

The FENE family of models is employed in many studies. In the domain of flow past a cylinder, Oliveira [27] implemented the molecular-based FENE family of models to simulate the flow around unbounded cylinder. Results are obtained for Re=50-120 and De up to 80. His results showed that the formation length behind the cylinder is greatly increased for the elastic fluid, the vortex shedding frequency is attenuated by elasticity and time-averaged rms fluctuations of the spanwise velocity component are also much reduced. Lozinski and Chauvière [28] introduced a new method for solving efficiently the Fokker-Planck equation for FENE model. They studied the two-dimensional FENE fluid past a confined cylinder using the spectral element method. They proved the advantages of the proposed scheme over traditional stochastic simulations. Dou and Phan-Thien [29] investigated the criteria for the negative wake generation for various viscoelastic fluids. They simulated the flow of the PTT, FENE-CR, FENE-P, and Giesekus fluids past a cylinder in a channel, with the channel moving at a uniform speed. They showed that the critical condition for the negative wake generation and the amplitude of the velocity overshoot strongly depend on the value of gradient of the viscosity with respect to the shear rate. Ogata et al. [30] investigated the effect of surfactant solutions on the flow past a circular cylinder measuring the drag and by flow visualization. The used surfactant is a viscoelastic fluid equivalent to 200 ppm Ethoquad O/12 solutions. They fitted the results to the FENE-P fluid. They showed that the viscoelasticity, which related to the increased apparent shear viscosity, is one of the factors of the expansion of the stagnation zone upstream of the cylinder.

From this rapid survey, it is clear that the FENE family of models is more suitable to the micro-scale simulations and to study complex phenomena like turbulence. The impact of these models on the real fluids is still very limited.

1.3.6 Other models

In order to decrease the computational cost of the simulation process, Mompean et al. [31] presented a new methodology for the formulation of an algebraic extra-stress model (AESM) derivable from the Oldroyd-B constitutive equation for a viscoelastic fluid. An explicit algebraic tensor relation is derived directly from the differential constitutive relation by involving a slow variation condition on the evolution of the deviatoric part of the extra-stress tensor. Mompean [32] re-adapted this methodology for the PTT model. The application of this approach to viscoelastic fluids is very promising. The explicit AESM gives exactly the same results as the differential constitutive equations in the pure shear and pure elongational flows. In his thesis, Helin [33] applied two proposed algebraic models to simulate contraction flow 4:1 and curved circular channel. This family of models is promising because of their light computational cost. On the other hand, the determination of model coefficients is difficult and limited to benchmark problems which have well-established solutions.

There are many other constitutive equations describing the viscoelastic fluid behaviour. However, these models are less used in the case of flow around a cylinder. One can refer to Tanner [34], Phan-Thien [35], and Owens and Phillips [36] who reviewed these models.

1.4. Numerical work

In this section, recent advances of numerical work for the viscoelastic fluid flow past a cylinder are considered. We review the Finite Difference Method (FDM), the Finite Element Method (FEM), the Finite Volume Method (FVM), and the Spectral Methods (SM).

The FDM is based on the properties of Taylor expansions and on the straightforward application of the definition of derivatives. It is only applicable to structured grids and it remains the reference for all studies of numerical discretization.

Up to our knowledge, no FDM work is found in the last decade concerning viscoelastic flow around a cylinder.

Hulsen et al. [37] used the FEM to simulate the flow past a confined cylinder by determining the polymer stress from a microscopic model. They replaced the collection of individual polymer molecules by an ensemble of configuration fields, representing the internal degrees of freedom of the polymers. Matallah et al. [38] simulated the creeping flow of an Oldroyd-B fluid past a confined cylinder using a Taylor-Galerkin pressure correction method with consistent streamline upwind scheme. They focused on the evaluation of the features of Elastic Viscous Splitting Scheme (EVSS) and the recovery of velocity gradients. They concluded that at low Deborah number (De), the use of the conventional scheme is more efficient, while at high De number the recovery scheme is the superior choice. Sun et al. [25] compared between three stress-splitting schemes. The first scheme is the discrete adaptive splitting method for preserving the ellipticity of the momentum/continuity pair (the DAVSS formulation). The second scheme is the independent interpolation of the components of the velocity gradient tensor (DAVSS-G). The third one applies the discontinuous Galerkin (DG) method for solving the constitutive equation (DAVSS-G/DG). The studied problem was the flow past a cylinder in a channel with the Oldroyd-B and Giesekus constitutive models. Results showed that the DAVSS-G/DG is a robust and accurate numerical algorithm and that for an Oldroyd-B fluid model the steep stress gradients develop adjacent to the cylinder and in the downstream wake for increasing De. Fan et al. [39] introduced a new stabilized splitting formulation named MIX1 based on the incompressibility residual of the finite element discretizations and used the problem of flow past a cylinder in a channel to compare between the three formulations (EVSS, DEVSS, MIX1). While, their results proved the stability and robustness of MIX1 in a narrow range, accuracy and stability need further investigations and the role played by the perturbation term of the MIX1 method in flows that have a substantial Newtonian solvent contribution is not yet fully understood.

The high Weissenberg number problem (HWNP) arose to be a principal obstacle to the viscoelastic computations. This problem represents the critical value at which computations break down. Fattal & Kupferman [40] proposed that the cause of HWNP is a numerical instability caused by the failure to balance the exponential growth of the

stress (due to deformation) with convection. They introduced a remedy consisting in a change of variables into new variables that scale logarithmically with the stress tensor. This technique is adopted by Hulsen et al. [26] to the case of flow of an Oldroyd-B and a Giesekus fluids past a confined cylinder at high *Wi*. This problem is still under investigation as Coronado et al. [41] & [42] presented a new Galerkin/Least-Squares (GLS) stabilized finite element method for computing viscoelastic flows of Oldroyd-B and Larson-type fluids past a cylinder in a channel.

With the introduction of FVM, the simulation of viscoelastic fluid flow has entered a new era. Dou and Phan-Thien [17] reported a Parallel Virtual Machine (PVM) implementation of an unstructured FVM for the simplified PTT constitutive model. They tested the performance of the distributed computations on the flow past a cylinder between two parallel plates. Following the same way of parallel computations, Dou and Phan-Thien [6] combined the idea of the discrete adaptive elastic viscous split stress (DAVSS) formulation with the independent interpolation of the vorticity to get a new splitting scheme called DAVSS-ω. To validate the new formulation, they simulated the flow of an Oldroyd-B fluid around a cylinder in a channel and reached De=1.8 using unstructured FVM. The obtained results lead to important findings about the influence of viscoelasticity on drag. They found that the drag coefficient decreases with mesh refinement for the Oldroyd-B model. The objective of the work of Oliviera et al. [4] was to present a finite-volume based numerical method for non-orthogonal collocated grids, and to include second-order accurate interpolation schemes, for the prediction of Non-Newtonian flows. They tested this technique on an UCM fluid flowing past a cylinder in a channel for Re=20 and De=0.1-1.0. Continuing on the same road of collocated grids, Alves et al. [43] implemented two high-resolution schemes (MINMOD and SMART) to represent the convective terms. They computed the flow of UCM and Oldroyd-B fluids around a confined cylinder (blockage ratio 0.5). The results lead to predictions of the drag coefficient on the cylinder for the range of De = 0 – 0.9. The linear stability analysis for inertial flows of a viscoelastic fluid around a bluff body is studied by Sahin and Owens [44]. Their work consists of two folds; direct numerical simulation (DNS) and numerical simulation using a constant viscosity modified FENE-CR model. They investigated the problem of linear stability of two-dimensional viscous flow past a confined cylinder. With the same fluid model FENE-CR, Oliveira and Miranda [45] considered two-dimensional inertia-free (Re=0) flow of a constant-viscosity viscoelastic

fluid past a cylinder placed symmetrically in a channel with a blockage ratio of 0.5. Steady state results are obtained for De=0-10. Simulation showed that a small recirculation pulsating bubble was attached to the cylinder downstream stagnation point leading to an increase of drag coefficient with elasticity. Such a phenomenon for the inertia flow of viscoelastic fluids has not been previously reported.

In order to gain the advantages of the two methods, some hybrid Finite Element / Finite Volume (FE/FV) schemes were proposed. In the work of Wapperom and Webster [46] FEs are used to discretize the balance of mass and momentum and a FV method is used for the stress equation. This combination gives some improvements over the FE scheme. They tested the flow of an Oldroyd-B fluid past a confined cylinder. The benefit of the FE/FV hybrid scheme for complex flows appears in the improvement of efficiency.

At the beginning of the eighties, Spectral Methods (SM) was introduced to the field of CFD. Since then, considerable number of articles have been elaborated concerning the viscoelastic flow around a cylinder. Chauvière and Owens [47] developed a stabilised SEM by solving the flow of an Oldroyd-B and a PTT fluid past a cylinder in a channel. The method proved its efficiency and a De = 1.85 was achieved. An a-posteriori error indicator for viscoelastic flow calculations is proposed by Chauvière [48] for a previously proposed method. He verified this error indicator by solving the problem of the flow of an Oldroyd-B fluid past a cylinder in a channel. Owens et al. [49] developed a new spectral element scheme suitable for computations of viscoelastic flows at high Deborah numbers. They validated this scheme by simulating the flow past a single confined cylinder. They demonstrated the stability and accuracy properties of the new scheme.

1.5. Experimental Work

Like the numerical simulation, the experimental work on viscoelastic fluids faces many challenges because of the complexity of these fluids. In this section, a brief survey of the experimental work concerning the viscoelastic flow past a cylinder is presented.

Shiang et al. [50] used Particle Image Velocimetry (PIV) to measure the full-field instantaneous velocity in an inertia-less, viscoelastic flow past a confined circular cylinder. The investigated range of the Deborah number is De= 0.6-2.4. The flow is a creeping one with Re<5. They found that at relatively low De (0.6 - 1.2) the flow reached steady-state conditions rapidly (< 10 s) and for De = 1.8 - 2.4 the viscoelastic flow may require as long as 90 s to reach steady flow. Cadot and Lebey [51] visualized the wake behind a circular cylinder and concluded that a drastic change of the shape of the wake of viscoelastic solutions is observed compared to that observed for water injections. Also, they remarked that the aspect ratio of the wake is decreased, the wavelength of the vortices is increased, and a large region of slow fluid motion is developed behind the cylinder. This indicates a delay of the shear roll-up and thus an inhibition of the shear instability. Cadot & Kumar [52] found that viscoelasticity delayed the development of the two-dimensional instability and shifted it to longer wavelengths. They noted that the stabilizing effect of viscoelasticity inhibits the formation of vorticity filaments and reduce drag in turbulent flows. The paper of Cadot [53] continued the work aiming at giving a quantitative idea of the basic viscoelastic wake. He investigated the consequences of this modification on the pressure field. Cressman et al. [54] studied the velocity fluctuations behind a rod in a quasi-two-dimensional flowing soap film. They found that at a low concentration the velocity fluctuations are suppressed. This implies that the polymer strongly reduces the magnitude of the velocity fluctuations. Coelho and Pinho ([55], [56] and [57]) measured the vortex shedding frequency and formation length for flow around a cylinder with Newtonian and shear-thinning aqueous solutions of methyl hydroxyethyl cellulose (tylose) and carboxymethyl cellulose (CMC). They arrived at some important findings concerning the critical Reynolds numbers marking the onset and end of the various flow regimes. They commented the boundary-layer thickness and the diffusion length in the laminar shedding regime versus the shear-thinning and the fluid elasticity. This enormous sophisticated study clearly emphasized the effect of shear-thinning on the flow properties. Pipe and Monkewtiz [58] have characterized the influence of small amounts of fluid elasticity on the two-dimensional laminar vortex shedding instability and the effects on the fluctuating and time-average velocity fields. They mainly focused on the evaluation of critical Reynolds number and the frequency of bluff body fluctuations. It is remarked that only the last mentioned work investigated the flow past a non-confined cylinder.

1.6. Summary of the literature survey

From the aforementioned survey, this work aims at the simulation of the flow of a viscoelastic PTT fluid past a cylinder placed in an unbounded media using FVM for the following reasons:

1- The flow around a non-confined cylinder is almost unexplored area.

2- The PTT model represents real viscoelastic fluids. Besides its simplicity and accuracy, it is generally more stable than the Oldroyd-B and UCM models.

3- The FVM is very effective in CFD owing to its simplicity and low computational cost.

Chapter 2: THEORETICAL STUDY

In this chapter, the theoretical bases of the study are introduced. First, the governing equations are stated. Then, the general characteristics of extra-stress constitutive equation are discussed and the employed equation is reported. After that, the transformation of coordinates is investigated and the equations are re-written in generalized orthogonal coordinates.

2.1. Conservation equations

The motion of a fluid is completely described by the conservation laws for the three basic properties: mass, momentum, and energy. Since the isothermal flow is considered here, the governing equations are reduced to the conservation of mass (continuity equation) and the conservation of momentum. For the case of incompressible, unsteady flow, and neglecting the body forces, the equation of conservation of mass is written in Cartesian coordinate system as:

$$\nabla.\mathbf{v} = 0\,, \qquad 2.1$$

and the equation of conservation of momentum is

$$\rho \frac{\mathrm{D}}{\mathrm{D}t}\mathbf{v} = \nabla\left(-p\mathbf{I} + \mathbf{T}\right), \qquad 2.2$$

where $\mathrm{D}/\mathrm{D}t$ is the material (total) time derivative, ∇ is the gradient operator, $\mathbf{v}$ is the velocity field, p is the pressure field, $\mathbf{I}$ is the identity tensor, and $\mathbf{T}$ is the total stress tensor.

To close the system, it is necessary to establish some connection between the (kinematic) stress tensor and the velocity field which is the constitutive equation. For Newtonian fluids the constitutive equation is the Newton's law of viscosity:

$$\mathbf{T} = 2\eta_N \mathbf{D}\,, \qquad 2.3$$

where η_N is the Newtonian fluid viscosity (solvent viscosity in case of polymeric solutions). The rate-of-strain tensor $\mathbf{D}$ is defined as

$$\mathbf{D} = \frac{1}{2}\left[\nabla\mathbf{v} + (\nabla\mathbf{v})^{\mathrm{T}}\right], \qquad 2.4$$

where $(\nabla\mathbf{v})_{ij} = \partial v_i / \partial x_j$ is the macroscopic velocity gradient in the fluid and $(\nabla\mathbf{v})^{\mathrm{T}}$ is its transpose.

The behaviour of polymer solutions is defined as a "mixture" of viscoelastic properties of the polymer fraction and the properties of the Newtonian solvent (which is assumed to be of low molecular weight). A natural way to model this is to split the stress tensor into a Newtonian stress and a polymer extra-stress tensor τ :

$$\mathbf{T} = 2\eta_N\mathbf{D} + \boldsymbol{\tau}\,, \qquad 2.5$$

where $\boldsymbol{\tau}$ is the viscoelastic extra-stress tensor. The constitutive equation defines this extra-stress as a function of velocity field and viscoelastic material quantities like the relaxation time.

2.2. The constitutive equation

In order to find a constitutive equation that can represent the behaviour of the fluid, there are basically two approaches:

1. In the continuum approach, Newton's law of viscosity is modified or new equations are set up to include certain features such as shear-dependent viscosity and stress relaxation. Concepts of continuum mechanics can be used to determine relevant variables and operations. An example of this approach is the Maxwell model.

2. In the microstructure approach, the concepts of statistical mechanics are applied. Starting from a specific model for the individual polymer chains, microscopic expressions for the stress tensor and equations of motion can be derived. An example of this approach is the Oldroyd model.

The constitutive equation is expected to satisfy the following general requirements

- *Coordinate system independence*: This is a logical requirement of merely all physical laws that their validity does not depend upon expression in a unique coordinate system. This requirement establishes the application of tensor notation in the expression of the constitutive equation.
- *Determinism and local action*: Determinism concerns the time marching process. It ensures that the viscoelastic fluid has only memory and does not possess foresights. In other words, the stress is related to *only* the present and past time step values. Local action means the same property but for spatial discretization. This property guarantees that *only* the neighbouring particles are involved in determining the stress at a point.
- *Material objectivity:* The physical interpretation of material objectivity means that the material behaviour must be indifferent to the motion of an observer. Mathematically, it states that the constitutive equation must be "frame-indifferent" or indifferent to rigid body translations and rotations of the material.
- Equations for polymer solutions should also reduce to the Newtonian behaviour of the solvent at vanishing concentration.

In the general case of stress, the normal stress components $\tau_{11}, \tau_{22}, \tau_{33}$ are even functions of the shear rate. The shearing stress components $\tau_{12}, \tau_{13}, \tau_{23}$ are odd functions of the shear rate by a symmetry argument. The differences between the normal components must be zero for any fluid whose viscosity depends linearly on shear rate. However, this fact does not hold for the viscoelastic fluids. In viscoelastic fluids, two independent normal stress differences (N_1, N_2) can be defined as functions of shear rate:

$$\begin{aligned} N_1(\dot{\gamma}) &= \tau_{11} - \tau_{22}, \\ N_2(\dot{\gamma}) &= \tau_{22} - \tau_{33}. \end{aligned} \qquad 2.6$$

These differences are vanishing for $\dot{\gamma} = 0$.

In the present work, the viscoelastic extra-stress tensor is related to the velocity field through the constitutive equation proposed by Phan-Thien and Tanner [59]:

$$\lambda\left[\frac{\mathrm{D}}{\mathrm{D}t}\boldsymbol{\tau}-\mathbf{L}\boldsymbol{\tau}-\boldsymbol{\tau}\mathbf{L}^{\mathrm{T}}\right]+Y\boldsymbol{\tau}=2\eta_m\mathbf{D}\,. \qquad 2.7$$

where η_m is the molecular-contributed viscosity.

The effective velocity gradient tensor is defined as:

$$\mathbf{L}=\nabla\mathbf{v}-\xi\mathbf{D}\,, \qquad 2.8$$

where ξ is the Phan-Thien slip parameter which is estimated from linear-viscoelastic and viscometric data.

The variable Y has two forms:

- The linear form

$$Y=1+\frac{\varepsilon\lambda}{\eta_{m0}}Tr\langle\boldsymbol{\tau}\rangle\,. \qquad 2.9$$

- The exponential form

$$Y=\exp\left(\frac{\varepsilon\lambda}{\eta_{m0}}Tr\langle\boldsymbol{\tau}\rangle\right). \qquad 2.10$$

The variable ε is a material constant related to its elongation behaviour. The *zero-shear* rate molecular-contributed viscosity η_{m0} is related to the molecular-contributed viscosity η_m through the relation [60]:

$$\eta_m=\eta_{m0}\mu \quad , \quad \mu=\left(\frac{1+\zeta(2-\zeta)\lambda^2\dot{\gamma}^2}{\left(1+\Gamma^2\dot{\gamma}^2\right)^{(1-n)/2}}\right) \qquad 2.11$$

where $\dot{\gamma}=\sqrt{2\ \mathrm{Tr}\langle\mathbf{D}\rangle}$ is the shear rate, and Γ is a time parameter assumed here to be $\Gamma=\lambda$.

The constitutive equation can now be rewritten as a transport equation of $\boldsymbol{\tau}$:

$$\lambda \frac{\mathrm{D}}{\mathrm{D}t}\boldsymbol{\tau} = 2\mu\beta\eta_0 \mathbf{D} + \lambda\left(\mathbf{L}\boldsymbol{\tau} + \boldsymbol{\tau}\mathbf{L}^{\mathrm{T}}\right) - Y\boldsymbol{\tau}, \qquad 2.12$$

where $\eta_0 = \eta_N + \eta_{m0}$ is the zero-shear rate viscosity of the fluid and $\beta = \eta_{m0}/\eta_0$ is the retardation ratio.

According to the values of β, ε, and ξ, six models can be defined as shown on Table 2.1.

Table 2.1 Different fluid models obtained by changing the constitutive equation parameters β, ε, and ξ

ε	ξ	β	Viscosity	Model
0	0	0	$\eta_N = \eta_0$	Newtonian
0	0	1	$\eta_m = \eta_{m0} = \eta_0$	UCM
0	0	0< <1	$\eta_m = \eta_{m0}$	Oldroyd-B
-	-	1	$\eta_m = \eta_{m0} = \eta_0$	PTT
-	0	1	$\eta_m = \eta_{m0} = \eta_0$	SPTT (simplified PTT)
-	-	-		MPTT (modified PTT)

This form of the constitutive equation offers the following advantages:

- Linear viscoelastic behaviour at small strains.
- Good fit to viscosity and first normal stress difference for low density polyethylene for both steady and transient shearing.
- A non-zero second normal stress difference.
- Reasonable elongational behaviour at all elongation rates.

Now, equations 2.1, 2.2 and 2.12 represent a closed system of equations written in the Cartesian coordinate system. As the cylinder is considered as a curved obstacle immersed in the solution domain, the governing equations will be rewritten in the generalized coordinates.

2.3. Transformation to general orthogonal coordinates

Orthogonal curvilinear coordinate systems (or the general orthogonal coordinate) of various types turn out to be extremely useful in mechanics. For the complex geometries, the use of generalized coordinates is crucial. This type of coordinates stands to be an effective alternative to the unstructured grids. Working with these coordinate systems implies heavy mathematical work to transform the governing equations. Also, some terms are added to the governing equations due to the curvature of coordinates. This requires great attention to the physical significance of lengths and angles.

In the present work, the transformation technique proposed by Pope [61] is adopted. In his work, he stated the Navier-Stokes equations in general orthogonal coordinates to calculate the turbulent recirculating flows in a diffuser. Magnaudet et al. [62] applied this methodology to simulate the laminar Newtonian flow around a sphere. Also, Thais et al. [63] adapted this technique to solve the flow around a cylinder.

In this section, we introduce and discuss the transformation relations between the Cartesian and generalized orthogonal coordinate systems. Then, the governing equations are re-written in generalized orthogonal coordinates.

2.3.1 Coordinate transformation

Consider the physical Cartesian coordinate system $\vec{x}(x, y, z) \equiv (x_i)_{i=1,2,3}$ and the generalized orthogonal coordinate system $\vec{\psi}(\psi_1, \psi_2, \psi_3)$ as shown in Figure 2.1.

The generalized coordinates are expressed as functions of the Cartesian coordinates:

$$\begin{aligned} \psi_1 &= \psi_1(x_1, x_2, x_3) \\ \psi_2 &= \psi_2(x_1, x_2, x_3). \\ \psi_3 &= \psi_3(x_1, x_2, x_3) \end{aligned} \qquad 2.13$$

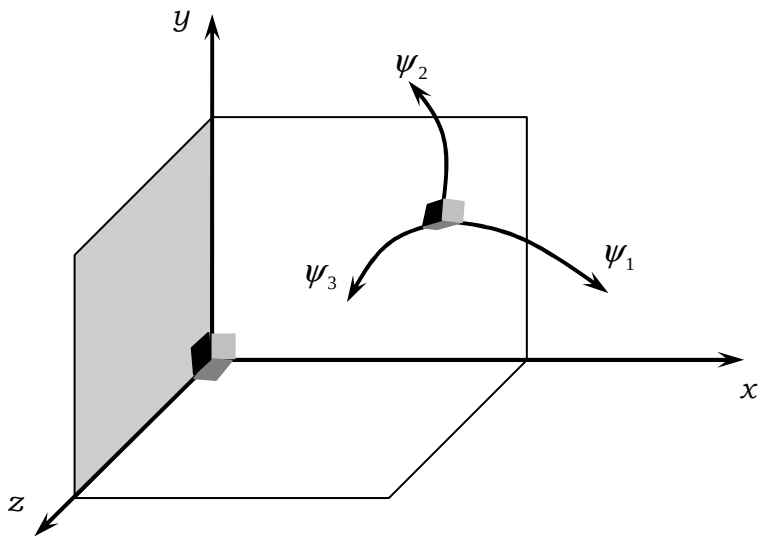


Figure 2.1 Cartesian and generalized orthogonal coordinate systems

The admissible transformation between two coordinate systems is carried out through the Jacobian:

$$\mathbf{J} = \frac{\partial x_i}{\partial \psi_j} = \begin{bmatrix} \frac{\partial x_1}{\partial \psi_1} & \frac{\partial x_1}{\partial \psi_2} & \frac{\partial x_1}{\partial \psi_3} \\ \frac{\partial x_2}{\partial \psi_1} & \frac{\partial x_2}{\partial \psi_2} & \frac{\partial x_2}{\partial \psi_3} \\ \frac{\partial x_3}{\partial \psi_1} & \frac{\partial x_3}{\partial \psi_2} & \frac{\partial x_3}{\partial \psi_3} \end{bmatrix}. \qquad 2.14$$

The columns of the Jacobian matrix define the base vectors $\mathbf{b}_i$ of the curvilinear coordinates:

$$\begin{aligned} \mathbf{b}_1 &= \begin{bmatrix} \frac{\partial x_1}{\partial \psi_1} & \frac{\partial x_2}{\partial \psi_1} & \frac{\partial x_3}{\partial \psi_1} \end{bmatrix}, \\ \mathbf{b}_2 &= \begin{bmatrix} \frac{\partial x_1}{\partial \psi_2} & \frac{\partial x_2}{\partial \psi_2} & \frac{\partial x_3}{\partial \psi_2} \end{bmatrix}, \\ \mathbf{b}_3 &= \begin{bmatrix} \frac{\partial x_1}{\partial \psi_3} & \frac{\partial x_2}{\partial \psi_3} & \frac{\partial x_3}{\partial \psi_3} \end{bmatrix}. \end{aligned} \qquad 2.15$$

The metric tensor $\mathbf{g}$ is defined as:

$$g_{ij} = \mathbf{b}_i \cdot \mathbf{b}_j . \qquad 2.16$$

The orthogonality condition implies that *only* the diagonal terms of the metric tensor are non zero. The scale factors h_i are defined as the square root of the diagonal elements of the metric tensor. Hence, the scale factors are written:

$$h_j = \sqrt{g_{jj}} \,. \qquad 2.17$$

Cartesian coordinates have the physical dimensions of length but, in general, this cannot be expected for curvilinear coordinates. The infinitesimal physical distances $\mathrm{d}\zeta_i$, in curvilinear coordinates, are evaluated using the scale factors:

$$\mathrm{d}\zeta_j = h_j \mathrm{d}\psi_j = \sqrt{g_{jj}}\,\mathrm{d}\psi_j \,. \qquad 2.18$$

It should be noted here that the normalisation of these physical distances is crucial. In order to express the quantities in physical length, the spatial derivatives are stated as functions of the infinitesimal physical distances. The usage of the physical coordinates keeps the physical magnitude of length and angles. In this work, the physical components in the curvilinear coordinates are noted by the symbol "$\breve{}$". For example, the physical components of a vector $\mathbf{A}$ are noted $\breve{A}_i$ and they are given by:

$$\breve{A}_i \equiv h_i A_i \qquad 2.19$$

where A_i is the transformed component in curvilinear system.

The advantage of expressing the variables in terms of their physical components, rather than their covariant or contravariant components, is that the vectors retain the same dimensions in all directions and in all locations. Besides, there are no additional terms for the stretching of the coordinate system. Accordingly, the physical velocity field $\breve{\mathbf{v}}(\breve{v}_i)_{i=1,2,3}$ is expressed as:

$$\breve{v}_i = h_i v_i \,. \qquad 2.20$$

These velocity components are derived by the normalisation of the curvilinear velocity contravariant components $v_i = \mathrm{d}\psi_i / \mathrm{d}t$. It should be noted here that there is no summation on indices in equations from 2.17 to 2.20.

In orthogonal coordinate system, the curvilinear form for the divergence operator $\nabla_{(i)}$ can be expressed in terms of stretching factors $H_i^{\ j}$. The stretching factors are defined as

$$H_i^{\ j} \equiv \frac{1}{h_i h_j}\frac{\partial h_i}{\partial \psi_j} = \frac{1}{h_i}\frac{\partial h_i}{\partial \zeta_j}, \qquad 2.21$$

and they represent the inverse of the radius of curvature of the j^{th} coordinate.

The curvilinear form for divergence operator is given by:

$$\nabla_{(i)}(\ ) \equiv \frac{\partial(\ )}{\partial \zeta_i} + \sum_{k \neq i} H_i^{\ k}(\ ). \qquad 2.22$$

The transformation of governing equations to the generalized orthogonal coordinates can be carried out using the following rules (Pope [61]):

- Scalars

$$A \to A,$$
$$\frac{\partial A}{\partial x_i} \to \frac{\partial A}{\partial \zeta_i}. \qquad 2.23$$

- Vectors

$$A_i \to \breve{A}_i,$$
$$\frac{\partial A_i}{\partial x_j} \to \frac{\partial \breve{A}_i}{\partial \zeta_j} - \breve{A}_j H_j^{\ i} + \breve{A}_k H_i^{\ k}\delta_{ij}, \qquad 2.24$$
$$\frac{\partial A_i}{\partial x_i} \to \nabla_{(i)}\breve{A}_i.$$

- Second-order tensors

$$A_{ij} \to \breve{A}_{ij},$$
$$\frac{\partial A_{ij}}{\partial x_i} \to \nabla_{(i)}\breve{A}_{ij} - \breve{A}_{ii}H_i^{\ j} + H_j^{\ k}\breve{A}_{jk}, \qquad 2.25$$

- Third-order tensors

$$A_{ijk} \to \breve{A}_{ijk},$$
$$\frac{\partial A_{ijk}}{\partial x_i} \to \nabla_{(i)}\breve{A}_{ij} - \breve{A}_{iij}H_i^{\ j} + \breve{A}_{jik}H_j^{\ i} - \breve{A}_{iji}H_i^{\ k} + \breve{A}_{kij}H_k^{\ i}, \qquad 2.26$$

where δ_{ij} is the Kronecker delta.

2.3.2 Governing equations in generalized orthogonal coordinate

Using the transformation relations mentioned in the previous subsection, the velocity gradient is expressed as:

$$\nabla_{(i)}\left(\breve{v}_j\right)=\frac{\partial \breve{v}_j}{\partial \zeta_i}-H_i^{\ j}\breve{v}_i+\sum_k H_j^{\ k}\breve{v}_k\delta_{ij}\ . \qquad 2.27$$

Consequently, the form of the rate of deformation tensor in curvilinear coordinates is given by:

$$\breve{D}_{ij}=\frac{1}{2}\left(\frac{\partial \breve{v}_i}{\partial \zeta_j}+\frac{\partial \breve{v}_j}{\partial \zeta_i}-H_j^{\ i}\breve{v}_j-H_i^{\ j}\breve{v}_i+2\sum_k H_i^{\ k}\breve{v}_k\delta_{ij}\right). \qquad 2.28$$

The generalized representation of the effective velocity gradient tensor is given by:

$$\begin{aligned}\breve{L}_{ij}&=\frac{\partial \breve{v}_j}{\partial \zeta_i}-H_i^{\ j}\breve{v}_i+\sum_k H_j^{\ k}\breve{v}_k\delta_{ij}\\&-\frac{\xi}{2}\left(\frac{\partial \breve{v}_i}{\partial \zeta_j}+\frac{\partial \breve{v}_j}{\partial \zeta_i}-H_j^{\ i}\breve{v}_j-H_i^{\ j}\breve{v}_i+2\sum_k H_i^{\ k}\breve{v}_k\delta_{ij}\right).\end{aligned} \qquad 2.29$$

The governing equations can now be rewritten in generalized orthogonal coordinate system as follows:

The continuity equation is transformed as:

$$\sum_i \nabla_{(i)}\left(\breve{v}_i\right)=0\ . \qquad 2.30$$

The conservation of momentum equation is re-formulated to be:

$$\begin{aligned}&\frac{\partial}{\partial t}\rho\breve{v}_j+\sum_i \nabla_{(i)}\left(\rho\breve{v}_i\breve{v}_j-2\eta_N\breve{D}_{ij}-\breve{\tau}_{ij}\right)=-\frac{\partial p}{\partial \zeta_j}\\&-\sum_i H_j^{\ i}\left(\rho\breve{v}_i\breve{v}_j-2\eta_N\breve{D}_{ij}-\breve{\tau}_{ij}\right)+\sum_i H_i^{\ j}\left(\rho\breve{v}_i\breve{v}_i-2\eta_N\breve{D}_{ii}-\breve{\tau}_{ii}\right).\end{aligned} \qquad 2.31$$

The viscoelastic constitutive equation (equation 2.12) is re-written as:

$$\lambda\left(\frac{\partial \breve{\tau}_{ij}}{\partial t}+\nabla_{(i)}\left(\breve{v}_j \breve{\tau}_{ij}\right)-\sum_k \breve{v}_k \breve{\tau}_{kj} H_k{}^i+\sum_k \breve{v}_i \breve{\tau}_{kj} H_i{}^k-\sum_k \breve{v}_k \breve{\tau}_{ik} H_k{}^j+\sum_k \breve{v}_j \breve{\tau}_{ik} H_j{}^k\right) \qquad 2.32$$
$$=2\mu\beta\eta_0\ \breve{D}_{ij}+\lambda\left(\breve{L}_{ik}\breve{\tau}_{kj}+\breve{\tau}_{jk}\breve{L}_{ki}\right)-Y\breve{\tau}_{ij}.$$

Now, the closed system of the three equations 2.30, 2.31, and 2.32 has to be solved to simulate the flow of a viscoelastic fluid.

2.4. Stress splitting scheme

Several methods have been proposed in the literature to retain an elliptic contribution of the momentum equation which is particularly important if a purely viscous contribution is absent or small compared to the viscoelastic contribution. One way to achieve this is the application of a change of variables, known as the Elastic-Viscous Stress Splitting (EVSS) formulation. This scheme was introduced by Perera and Walters [64]. Later, Mendelson et al. [65] extended it for the flow of a second-order fluid. Beris et al. [66] adapted this scheme to viscoelastic fluid flows. The key point of the EVSS is to split the stress tensor into elastic and viscous components by separating explicitly the elastic and viscous stresses:

$$\boldsymbol{\tau}=\boldsymbol{\Sigma}+2\eta_m\mathbf{D}. \qquad 2.33$$

The tensor $\boldsymbol{\Sigma}$ represents the purely elastic stress, while the other term stands for the .viscous, or Newtonian-like, stress. By substitution, the constitutive equation 2.12 is written as follows:

$$\lambda\frac{\Delta}{\Delta t}\boldsymbol{\Sigma}+Y\boldsymbol{\Sigma}=2\eta_m\left(1-Y\right)\mathbf{D}-2\lambda\eta_m\frac{\Delta}{\Delta t}\mathbf{D} \qquad 2.34$$

In the curvilinear coordinates, equation 2.32 is stated as:

$$\lambda\left[\frac{\partial \breve{\Sigma}_{ij}}{\partial t}+\nabla_{(i)}v_j\breve{\Sigma}_{ij}-\sum_k \breve{v}_k\breve{\Sigma}_{kj}H_k{}^i+\sum_k \breve{v}_i\breve{\Sigma}_{kj}H_i{}^k-\sum_k \breve{v}_k\breve{\Sigma}_{ik}H_k{}^j+\sum_k \breve{v}_j\breve{\Sigma}_{ik}H_j{}^k\right]$$
$$-\lambda\left(\breve{L}_{ik}\breve{\Sigma}_{kj}+\breve{\Sigma}_{jk}\breve{L}_{ki}\right)+Y\breve{\Sigma}_{ij}=2\eta_m(1-Y)\breve{D}_{ij}+2\lambda\eta_m\left(\breve{L}_{ik}\breve{D}_{kj}+\breve{D}_{jk}\breve{L}_{ki}\right)$$
$$-2\lambda\eta_m\left[\frac{\partial \breve{D}_{ij}}{\partial t}+\nabla_{(i)}v_j\breve{D}_{ij}\right] \qquad 2.35$$
$$-2\lambda\eta_m\left[\sum_k \breve{v}_k\breve{D}_{kj}H_k{}^i-\sum_k \breve{v}_i\breve{D}_{kj}H_i{}^k+\sum_k \breve{v}_k\breve{D}_{ik}H_k{}^j-\sum_k \breve{v}_j\breve{D}_{ik}H_j{}^k\right]$$

2.5. Summary of the theoretical study

- The governing equations of the problem under consideration are the conservation equations of mass and momentum and the viscoelastic constitutive equation.
- The closed system of governing equations is presented in Cartesian coordinate system: equations 2.1, 2.2, and 2.7.
- The equations are transformed to the generalized orthogonal coordinate system: equations 2.29, 2.30, and 2.31.
- The stress splitting scheme (EVSS) is introduced.
- The final system of equations to be resolved is:

$$\sum_i \nabla_{(i)}\left(\breve{v}_i\right)=0 \qquad 2.30$$

.

$$\frac{\partial}{\partial t}\rho\breve{v}_j+\sum_i \nabla_{(i)}\left(\rho\breve{v}_i\breve{v}_j-2\eta_N\breve{D}_{ij}-\breve{\tau}_{ij}\right)=-\frac{\partial p}{\partial \zeta_j}$$
$$-\sum_i H_j{}^i\left(\rho\breve{v}_i\breve{v}_j-2\eta_N\breve{D}_{ij}-\breve{\tau}_{ij}\right)+\sum_i H_i{}^j\left(\rho\breve{v}_i\breve{v}_i-2\eta_N\breve{D}_{ii}-\breve{\tau}_{ii}\right). \qquad 2.31$$

$$\lambda\left[\frac{\partial \breve{\Sigma}_{ij}}{\partial t}+\nabla_{(i)}v_j\breve{\Sigma}_{ij}-\sum_k \breve{v}_k\breve{\Sigma}_{kj}H_k{}^i+\sum_k \breve{v}_i\breve{\Sigma}_{kj}H_i{}^k-\sum_k \breve{v}_k\breve{\Sigma}_{ik}H_k{}^j+\sum_k \breve{v}_j\breve{\Sigma}_{ik}H_j{}^k\right]$$
$$-\lambda\left(\breve{L}_{ik}\breve{\Sigma}_{kj}+\breve{\Sigma}_{jk}\breve{L}_{ki}\right)+Y\breve{\Sigma}_{ij}=2\eta_m(1-Y)\breve{D}_{ij}+2\lambda\eta_m\left(\breve{L}_{ik}\breve{D}_{kj}+\breve{D}_{jk}\breve{L}_{ki}\right)$$
$$-2\lambda\eta_m\left[\frac{\partial \breve{D}_{ij}}{\partial t}+\nabla_{(i)}v_j\breve{D}_{ij}\right] \qquad 2.35$$
$$-2\lambda\eta_m\left[\sum_k \breve{v}_k\breve{D}_{kj}H_k{}^i-\sum_k \breve{v}_i\breve{D}_{kj}H_i{}^k+\sum_k \breve{v}_k\breve{D}_{ik}H_k{}^j-\sum_k \breve{v}_j\breve{D}_{ik}H_j{}^k\right]$$

Chapter 3: NUMERICAL METHODOLOGY

In this chapter, the numerical solution of the governing equations defined in the previous chapter is presented. Spatial and temporal stepping schemes are introduced. After that, the boundary conditions are established. Finally, the optimization of mesh is presented.

3.1. The Finite Volume Method (FVM)

The Finite Volume Method (FVM) is one of the most widely applied numerical methods today in Computational Fluid Dynamics (CFD). The appeal of this widespread method lies on its generality, its conceptual simplicity and it easiness of implementation for arbitrary grids, structured as well as unstructured [67]. The FVM is based on *cell-averaged values* which distinguish it from the finite difference and finite element methods where the main numerical quantities are the *local function* values at the mesh points.

The general form of the transport equation can be used to describe all the governing equations:

$$\frac{\partial}{\partial t}(\Lambda\Phi)+\frac{\partial}{\partial x_j}(\Lambda u_j\Phi)=\frac{\partial}{\partial x_j}\left(\Theta\frac{\partial\Phi}{\partial x_j}\right)+S_\Phi, \qquad 3.1$$

where Φ is the transported quantity which can be a scalar, a vector component, or a tensor. The coefficients Θ and Λ have different meanings depending on the transported variable. The first left-hand side term is the temporal rate of change term, the second one is the convective term, the first right-hand side term is the diffusion term, and the last term S_Φ is the source term which includes all terms that cannot be accommodated in the convective or diffusive terms. Table 3.1 shows the different corresponding quantity for each governing equation.

Table 3.1 Variables of the generalized transport equation and their corresponding quantities in the governing equations.

Equation	Φ	Θ	Λ	S_Φ
Continuity	1	0	ρ	0
Momentum	u_i	η_{m0}	ρ	$-\frac{\partial p}{\partial \zeta_j}-\sum_i H_j^i\left(\rho\breve{v}_i\breve{v}_j-2\eta_N\breve{D}_{ij}-\breve{\tau}_{ij}\right)$ $+\sum_i H_i^j\left(\rho\breve{v}_i\breve{v}_i-2\eta_N\breve{D}_{ii}-\breve{\tau}_{ii}\right)$
Constitutive	τ_{ij}	0	λ	$2\mu\beta\eta_0\,\breve{D}_{ij}+\lambda\left(\breve{L}_{ik}\breve{\tau}_{kj}+\breve{\tau}_{jk}\breve{L}_{ki}\right)-Y\breve{\tau}_{ij}$ $+\sum_k\breve{v}_k\breve{\tau}_{kj}H_k{}^i-\sum_k\breve{v}_i\breve{\tau}_{kj}H_i{}^k$ $+\sum_k\breve{v}_k\breve{\tau}_{ik}H_k{}^j-\sum_k\breve{v}_j\breve{\tau}_{ik}H_j{}^k$

The solution domain is discretized into mesh points. Once a grid has been generated, the FVM consists in associating a control volume (CV) to each mesh (nodal) point. The essential step in the FVM is the integration of the transport equation 3.1 over the CV, then applying Gauss' divergence theorem yielding:

$$\frac{\partial}{\partial t}\int_{CV}(\Lambda\Phi)\mathrm{d}V+\int_{CS}\hat{n}.\left(\Lambda u_j\Phi\right)\mathrm{d}A=\int_{CS}\hat{n}.\left(\Theta\frac{\partial\Phi}{\partial x_j}\right)\mathrm{d}A+\int_{CV}S_\Phi\mathrm{d}V\,, \qquad 3.2$$

where *CS* stands for control surface with $\hat{n}$ defined as its outward unit vector and d*A* as the infinitesimal area and d*V* is the infinitesimal volume.

In time dependent problems, the integration is carried out in two steps; integration with respect to position (spatial discretization) and then integration with respect to time (time marching). The general integrated form of the transport equation is:

$$\int_{\Delta t}\left(\frac{\partial}{\partial t}\int_{CV}(\Lambda\Phi)\,\mathrm{d}V\right)\mathrm{d}t+\int_{\Delta t}\left(\int_{CS}\hat{n}.\left(\Lambda u_j\Phi\right)\mathrm{d}A\right)\mathrm{d}t = \int_{\Delta t}\left(\int_{CS}\hat{n}.\left(\Theta\frac{\partial\Phi}{\partial x_j}\right)\mathrm{d}A\right)\mathrm{d}t+\int_{\Delta t}\left(\int_{CV}S_\Phi\,\mathrm{d}V\right)\mathrm{d}t. \qquad 3.3$$

3.2. Spatial discretization

For space discretization, the steady transport equation is derived from the general unsteady equation 3.3, as:

$$\int_{CS} \hat{n}.\left(\Lambda u_j \Phi\right) \mathrm{d}A = \int_{CS} \hat{n}.\left(\Theta \frac{\partial \Phi}{\partial x_j} \right) \mathrm{d}A + \int_{CV} S_\Phi \mathrm{d}V \qquad 3.4$$

The net diffusive flux (first right-hand term) affects the transported property along its gradients in all directions. On the other hand, the net convective flux (left-hand term) spreads influence only in the flow direction. The second right-hand term represents the generation or destruction of the property within the CV. The relative strength of convection and diffusion must be kept in mind while generating the mesh to get a stable computation process.

Now, the differential equations are expanded to algebraic difference equations. The order of expansion influences the accuracy of computation. As the problem under consideration is a two-dimensional problem, the computations are carried out by sweeping the solution domain from west to east ant sweeping domain from south to north. Figure 3.1 illustrates the notation for points and distances of scalar-variables node (pressure nodes), x-direction vector-components (velocity node) and y-direction vector-components. In this notation, V^i designates the physical volume of the control volume with the index $i = p,u,v$ standing for pressure, vector x-component, or vector y-component volumes respectively.

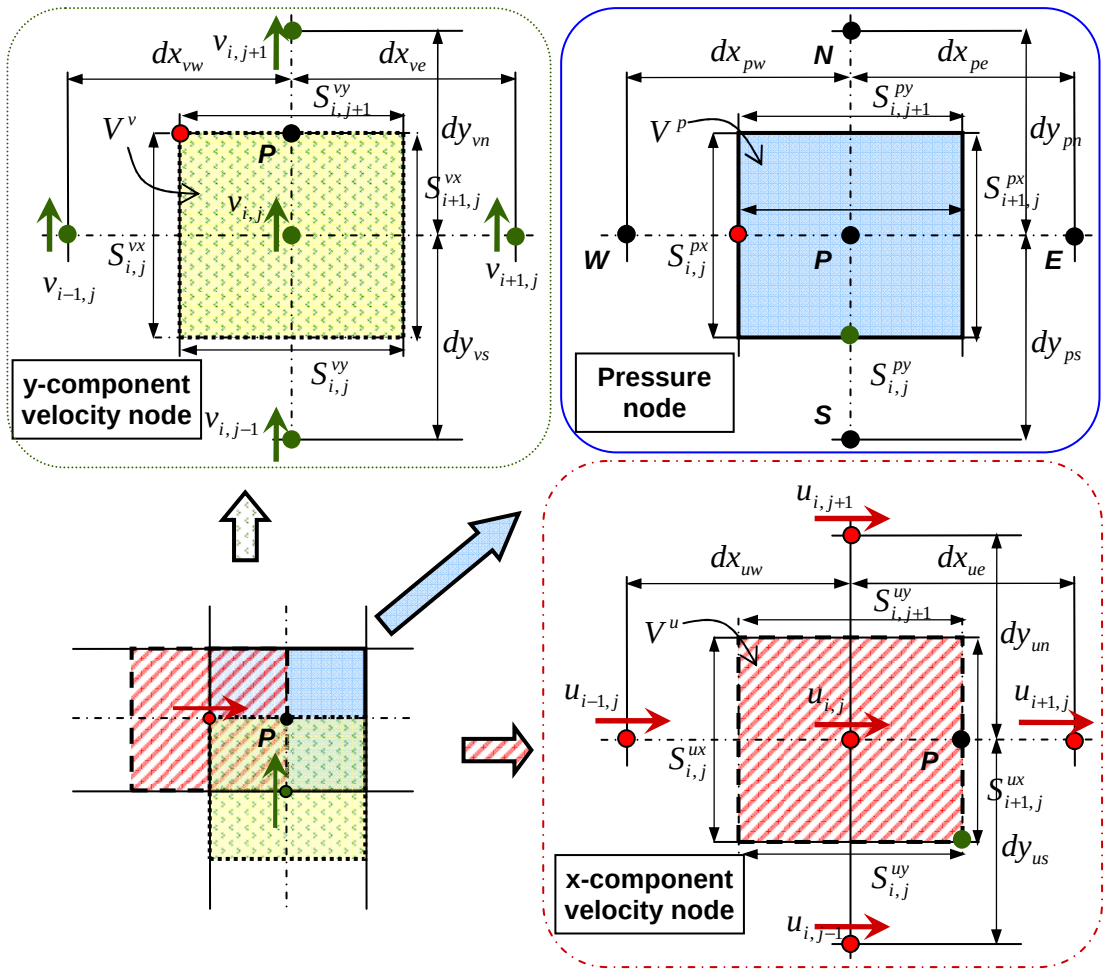


Figure 3.1 Notation for points and distances for pressure velocity control volumes

The physical surface area of the control volume face is denoted by $S_{i,j}^{nm}$ where the upper first index letter $n = p,u,v$ means the pressure, vector x-component, or vector y-component volumes respectively and the second letter $m = xy$ indicates the CV face either in x-direction or in y-direction, while the lower index letters give the order of the CV. Physical distances between successive nodes are noted by dx_{rq} for x-direction and dy_{rq} in y-direction where the first index letter $r = p,u,v$ means the pressure, vector x-component, or vector y-component volumes respectively and the second letter $q = n,s,e,w$ indicates the attitude either north, south, east, or west. It is obvious that in the present 2D case, all areas are reduced to lengths and all volumes are reduced to areas.

It should be reminded that the physical components in the curvilinear coordinates are noted by the symbol "$\breve{}$". For example, the physical components of a vector **A** are noted $\breve{A}_i$. In the two-dimensional case, the physical velocity field is $\breve{\mathbf{v}}(\breve{u},\breve{v})$.

Accordingly, the continuity equation is discretized as:

$$\left(\breve{u}_{i,j+1}S^{px}_{i,j+1}-\breve{u}_{i,j}S^{px}_{i,j}\right)+\left(\breve{v}_{i+1,j}S^{py}_{i+1,j}-\breve{v}_{i,j}S^{py}_{i,j}\right)=0 \qquad 3.5$$

The momentum equation in x-direction is developed as:

$$\begin{aligned}&\left(\frac{\partial\rho\breve{u}}{\partial t}\right)V^u+\underbrace{\left(\breve{u}\breve{u}-\left(2\eta_0\breve{D}_{11}+\breve{\Sigma}_{11}\right)\right)}_{1}S^{ux}_{i+1,j}-\underbrace{\left(\breve{u}\breve{u}-\left(2\eta_0\breve{D}_{11}+\breve{\Sigma}_{11}\right)\right)}_{2}S^{ux}_{i,j}\\&+\underbrace{\left(\breve{u}\breve{v}-\left(2\eta_0\breve{D}_{12}+\breve{\Sigma}_{12}\right)\right)}_{3}S^{uy}_{i,j+1}-\underbrace{\left(\breve{u}\breve{v}-\left(2\eta_0\breve{D}_{12}+\breve{\Sigma}_{12}\right)\right)}_{4}S^{uy}_{i,j}\\&=\left(\frac{2\left(p_{(i,k)}-p_{(i-1,k)}\right)}{S^{uy}_{i,j}+S^{uy}_{i,j+1}}\right)V^u\underbrace{\left[H^1_2\left(\breve{v}\breve{v}-\left(2\eta_0\breve{D}_{22}+\breve{\Sigma}_{22}\right)\right)-H^2_1\left(\breve{v}\breve{u}-\left(2\eta_0\breve{D}_{21}+\breve{\Sigma}_{21}\right)\right)\right]}_{5}V^u\end{aligned} \qquad 3.6$$

In this equation, the terms are evaluated using the *u*-CV.

In order to carry out the computations in the highest possible accuracy, two second-order interpolating schemes are used. The diffusion terms are calculated with the second order accurate Centered Difference Scheme. The convective terms are evaluated using the second-order accurate "Quadratic Upstream Interpolation Scheme for Convective Kinematics" (QUICK) scheme [68]. With that, the convective and diffusive terms are written at the four faces of the control volume as follows:

At the 'East' face – term (1):

The convective term is:

$$\breve{u}\breve{u}=\frac{1}{2}\left(\breve{u}_{i,j}+\breve{u}_{i,j+1}\right)\left[\frac{1}{2}\breve{u}_{i,j}+\breve{u}_{i+1,j}+\frac{1}{8}\left(2\breve{u}_{n,j}-\breve{u}_{n-1,j}-\breve{u}_{n+1,j}\right)\right], \qquad 3.7$$

$$\text{where } n=\begin{cases}i+1 & \ldots \quad \frac{1}{2}\left[\breve{u}_{i,j}+\breve{u}_{i+1,j}\right]<0,\\ i & \ldots \quad \frac{1}{2}\left[\breve{u}_{i,j}+\breve{u}_{i+1,j}\right]\geq 0.\end{cases}$$

The stress is expressed as:

$$2\eta_0 \breve{D}_{11} + \breve{\Sigma}_{11} = 2\eta_0 \left(\frac{\breve{u}_{i+1,j} - \breve{u}_{i,j}}{S^{vy}_{i,j+1}} + H_1^2\Big|_{p(i,j)} \frac{\breve{v}_{i,j+1} + \breve{v}_{i,j}}{2} \right) + \breve{\Sigma}_{11}. \qquad 3.8$$

where $H_1^2\Big|_{p(i,j)}$ is the stretching factor calculated for the $\left(i^{th}, j^{th}\right)$ pressure control volume which belongs to the pressure node at the face "east".

At the 'West' face – term (2):

The convective term is:

$$\breve{u}\breve{u} = \frac{1}{2}\left(\breve{u}_{i,j} + \breve{u}_{i-1,j}\right)\left[\frac{1}{2}\breve{u}_{i,j} + \breve{u}_{i-1,j} + \frac{1}{8}\left(2\breve{u}_{n-1,j} - \breve{u}_{n-2,j} - \breve{u}_{n,j}\right)\right], \qquad 3.9$$

$$\text{where } n = \begin{cases} i & \ldots \quad \frac{1}{2}\left[\breve{u}_{i,j} + \breve{u}_{i-1,j}\right] < 0, \\ i-1 & \ldots \quad \frac{1}{2}\left[\breve{u}_{i,j} + \breve{u}_{i-1,j}\right] \geq 0. \end{cases}$$

The stress is expressed as:

$$2\eta_0 \breve{D}_{11} + \breve{\Sigma}_{11} = 2\eta_0 \left(\frac{\breve{u}_{i,j} - \breve{u}_{i-1,j}}{S^{vy}_{i-1,j+1}} + H_1^2\Big|_{p(i-1,j)} \frac{\breve{v}_{i-1,j+1} + \breve{v}_{i-1,j}}{2} \right) + \breve{\Sigma}_{11}. \qquad 3.10$$

At the 'North' face – term (3):

The convective term is:

$$\breve{u}\breve{v} = \frac{1}{2}\left(\breve{v}_{i,j+1} + \breve{v}_{i-1,j+1}\right)\left[\frac{1}{2}\breve{u}_{i,j} + \breve{u}_{i,j-1} + \frac{1}{8}\left(2\breve{u}_{i,n-1} - \breve{u}_{i,n-2} - \breve{u}_{i,n}\right)\right], \qquad 3.11$$

$$\text{where } n = \begin{cases} j+1 & \ldots \quad \frac{1}{2}\left[\breve{v}_{i,j+1} + \breve{v}_{i,j}\right] < 0, \\ j & \ldots \quad \frac{1}{2}\left[\breve{v}_{i,j+1} + \breve{v}_{i,j}\right] \geq 0. \end{cases}$$

The stress is expressed as:

$$2\eta_0\breve{D}_{12}+\breve{\Sigma}_{12}=2\eta_0\left(\frac{\breve{v}_{i,j+1}-\breve{v}_{i-1,j+1}}{S^{uy}_{i,j+1}}-H^1_2\Big|_{u(i,j+1)}\frac{\breve{v}_{i,j+1}+\breve{v}_{i-1,j+1}}{2}\right)$$
$$+2\eta_0\left(\frac{\breve{u}_{i,j+1}-\breve{u}_{i,j}}{S^{vy}_{i,j+1}}-H^2_1\Big|_{u(i,j+1)}\frac{\breve{u}_{i,j+1}+\breve{v}_{i,j}}{2}\right)+\breve{\Sigma}_{12}. \qquad 3.12$$

where $H^2_1\Big|_{u(i,j+1)}$ is the stretching factor calculated for the $\left(i^{th},\, j+1^{th}\right)$ control volume of x-direction vector component which belongs to the *u*-node at the "south" face.

At the 'South' face – term (4):

The convective term is:

$$\breve{u}\breve{v}=\frac{1}{2}\left(\breve{v}_{i,j}+\breve{v}_{i-1,j}\right)\left[\frac{1}{2}\breve{u}_{i,j-1}+\breve{u}_{i,j-2}+\frac{1}{8}\left(2\breve{u}_{i,n-2}-\breve{u}_{i,n-3}-\breve{u}_{i,n-1}\right)\right], \qquad 3.13$$

where $n=\begin{cases} j & \ldots \quad \frac{1}{2}\left[\breve{v}_{i,j}+\breve{v}_{i,j-1}\right]<0, \\ j-1 & \ldots \quad \frac{1}{2}\left[\breve{v}_{i,j}+\breve{v}_{i,j-1}\right]\geq 0. \end{cases}$

The stress is expressed as:

$$2\eta_0\breve{D}_{12}+\breve{\Sigma}_{12}=2\eta_0\left(\frac{\breve{v}_{i,j}-\breve{v}_{i-1,j}}{S^{uy}_{i,j}}-H^1_2\Big|_{u(i,j)}\frac{\breve{v}_{i,j}+\breve{v}_{i-1,j}}{2}\right)$$
$$+2\eta_0\left(\frac{\breve{u}_{i,j}-\breve{u}_{i,j-1}}{S^{vy}_{i,j}}-H^2_1\Big|_{u(i,j)}\frac{\breve{u}_{i,j}+\breve{v}_{i,j-1}}{2}\right)+\breve{\Sigma}_{12}. \qquad 3.14$$

The source term – term (5):

The convective term is:

$$\breve{v}\breve{v}=\left[\frac{1}{4}\left(\breve{v}_{i,j}+\breve{v}_{i,j+1}+\breve{v}_{i-1,j+1}+\breve{v}_{i-1,j}\right)\right]^2, \qquad 3.15$$

and

$$\breve{v}\breve{u}=\frac{1}{4}\left(\breve{v}_{i,j}+\breve{v}_{i,j+1}+\breve{v}_{i-1,j+1}+\breve{v}_{i-1,j}\right)\breve{u}_{i,j} \qquad 3.16$$

The stress is expressed as:

$$2\eta_0 \breve{D}_{22} + \breve{\Sigma}_{22} = 2\eta_0 \left(\frac{\breve{v}_{i,j+1} - \breve{v}_{i-1,j+1} + \breve{v}_{i,j} - \breve{v}_{i-1,j}}{S^{uy}_{i,j+1} + S^{uy}_{i,j}} - H^1_2\Big|_{u(i,j)} \breve{u}_{i,j} \right) + \breve{\Sigma}_{22}, \qquad 3.17$$

where $H^2_1\Big|_{u(i,j)}$ is the stretching factor calculated for the $\left(i^{th}, j^{th}\right)$ control volume of x-direction vector component.

In a similar way,

$$\begin{aligned} 2\eta_0 \breve{D}_{21} + \breve{\Sigma}_{21} &= 2\eta_0 \left(\frac{\breve{u}_{i,j+1} - \breve{u}_{i,j}}{S^{vy}_{i,j} + S^{vy}_{i,j+1}} - H^2_1\Big|_{u(i,j)} \breve{u}_{i,j} \right) \\ &+ 2\eta_0 \left(\frac{\breve{v}_{i,j+1} - \breve{v}_{i-1,j+1} + \breve{v}_{i,j} - \breve{v}_{i-1,j}}{S^{uy}_{i,j} + S^{uy}_{i,j+1}} - H^1_2\Big|_{u(i,j)} \frac{\breve{v}_{i,j} + \breve{v}_{i,j+1} + \breve{v}_{i-1,j+1} + \breve{v}_{i-1,j}}{4} \right) + \breve{\Sigma}_{21}. \end{aligned} \qquad 3.18$$

All terms are evaluated in a similar way like convective and diffusive terms in momentum conservation equation.

3.3. Time discretization

For the time marching algorithm, the first-order accurate Euler forward explicit scheme is applied obeying the adaptation of Marker and Cell algorithm developed by Mompean and Deville [69]. In this method, the mass conservation equation, the pressure gradient term in the conservation of momentum equation and the boundary conditions are evaluated at the new time level (n+1). The other advection, diffusion, and source terms in the momentum conservation equation are evaluated at the old time level (n). This decoupling procedure is based on a semi-implicit projection method in pressure developed by Harlow and Welch [72].

The mass conservation equation is enforced in the new time level as:

$$\nabla_{\zeta_1}\left(\breve{u}^{n+1}\right) + \nabla_{\zeta_2}\left(\breve{v}^{n+1}\right) = 0. \qquad 3.19$$

The momentum conservation equation in x-direction is:

$$\begin{aligned}&\frac{\breve{u}^{n+1}-\breve{u}^{n}}{\Delta t}+\left\{\left(\breve{u}\breve{u}-\left(2\eta_0\breve{D}_{11}+\breve{\Sigma}_{11}\right)\right)S^{ux}_{i+1,j}-\left(\breve{u}\breve{u}-\left(2\eta_0\breve{D}_{11}+\breve{\Sigma}_{11}\right)\right)S^{ux}_{i,j}\right.\\&+\left(\breve{u}\breve{v}-\left(2\eta_0\breve{D}_{12}+\breve{\Sigma}_{12}\right)\right)S^{uy}_{i,j+1}-\left(\breve{u}\breve{v}-\left(2\eta_0\breve{D}_{12}+\breve{\Sigma}_{12}\right)\right)S^{uy}_{i,j}\\&\left.-\left[H^1_2\left(\breve{v}\breve{v}-\left(2\eta_0\breve{D}_{22}+\breve{\Sigma}_{22}\right)\right)-H^2_1\left(\breve{v}\breve{u}-\left(2\eta_0\breve{D}_{21}+\breve{\Sigma}_{21}\right)\right)\right]V^u\right\}^n\\&=-\frac{1}{\rho}\left(\frac{2V^u\left(p_{(i,k)}-p_{(i-1,k)}\right)}{S^{uy}_{i,j}+S^{uy}_{i,j+1}}\right)^{n+1}.\end{aligned}\qquad 3.20$$

It can be rearranged in the form:

$$\breve{u}^{n+1}=\Delta t\left\{B^n_{u\,i,k}-\frac{1}{\rho}\left(\frac{2V^u\left(p_{(i,k)}-p_{(i-1,k)}\right)}{S^{uy}_{i,j}+S^{uy}_{i,j+1}}\right)^{n+1}\right\},\qquad 3.21$$

with

$$\begin{aligned}B^n_{u\,i,k}=&-\left\{\left(\breve{u}\breve{u}-\left(2\eta_0\breve{D}_{11}+\breve{\Sigma}_{11}\right)\right)S^{ux}_{i+1,j}-\left(\breve{u}\breve{u}-\left(2\eta_0\breve{D}_{11}+\breve{\Sigma}_{11}\right)\right)S^{ux}_{i,j}\right.\\&+\left(\breve{u}\breve{v}-\left(2\eta_0\breve{D}_{12}+\breve{\Sigma}_{12}\right)\right)S^{uy}_{i,j+1}-\left(\breve{u}\breve{v}-\left(2\eta_0\breve{D}_{12}+\breve{\Sigma}_{12}\right)\right)S^{uy}_{i,j}\\&\left.-\left[H^1_2\left(\breve{v}\breve{v}-\left(2\eta_0\breve{D}_{22}+\breve{\Sigma}_{22}\right)\right)-H^2_1\left(\breve{v}\breve{u}-\left(2\eta_0\breve{D}_{21}+\breve{\Sigma}_{21}\right)\right)\right]V^u\right\}^n+\frac{\breve{u}^n}{\Delta t}.\end{aligned}\qquad 3.22$$

The solution algorithm consists of substituting the value of $\breve{u}^{n+1}_{i,j}$ at the mass conservation equation. Hence, a Poisson equation is obtained for the pressure:

$$C_1p^{n+1}_{i-1,j}+C_2p^{n+1}_{i+1,j}+C_3p^{n+1}_{i,j+1}+C_4p^{n+1}_{i,j}-C_5p^{n+1}_{i,j}=Q_p{}^n,\qquad 3.23$$

where

$$\begin{aligned}C_1&=\frac{2S^{px}_{i,j}}{S^{ux}_{i,j}+S^{ux}_{i,j+1}},\\C_2&=\frac{2S^{px}_{i+1,j}}{S^{ux}_{i+1,j}+S^{ux}_{i+1,j}},\\C_3&=\frac{2S^{px}_{i,j+1}}{S^{vx}_{i+1,j+1}+S^{vx}_{i+1,j}},\\C_4&=\frac{2S^{px}_{i,j}}{S^{vx}_{i+1,j}+S^{vx}_{i+1,j-1}},\\C_5&=C_1+C_2+C_3+C_4,\quad\text{and}\\Q_p{}^n&=S^{px}_{i+1,j}B^n_u\big|_{i+1,j}-S^{px}_{i,j}B^n_u\big|_{i,j}+S^{py}_{i,j+1}B^n_v\big|_{i,j+1}-S^{py}_{i,j}B^n_v\big|_{i,j}.\end{aligned}\qquad 3.24$$

Then, solving the linear system of equations $\sum_m C_m p^{n+1} = Q_p{}^n$ at each time step gives the pressure filed at $t = n+1$. Finally, by re-substituting in equation 3.21 the new pressure field a new velocity field, obeying the incompressibility constraint, is obtained.

As the matrix of coefficients of the pressure matrix depend only on the geometry, the matrix is formed once and for all after constructing the grid. In order to solve this linear system of equations, the Cholesky method is applied. Appendix A shows the flowchart of the developed code.

3.4. Solution domain, boundary and initial conditions

A schematic drawing of the solution domain is shown in Figure 3.2. The origin of coordinate system coincides with the cylinder centre. In order to reach a non-confined (unbounded) case, the boundaries of the domain are taken 30 times the cylinder radius upstream, 60 times downstream, and 30 times apart on each cylinder side. According to Persillon and Braza [70], extension of the solution domain 15 cylinder diameter upstream, 30 diameters downstream, and 10 diameters on each side is fair enough to avoid boundary effects.

At the entry (*west*) side, the only imposed condition is the entry uniform velocity U_0 in x-direction and since the entrance is sufficiently far from the cylinder, any curvature effect is negligible. At the outlet (*east*) side, a zero-pressure boundary condition is imposed. For the *north* and *south* sides, symmetry boundary conditions are imposed: zero-gradient across the boundary for x-direction component, and zero-velocity for the y-direction component. At the beginning of computations, all velocities in internal CVs, pressures, viscoelastic stresses are zero-initialized. Also Figure 3.2 illustrates the boundary conditions.

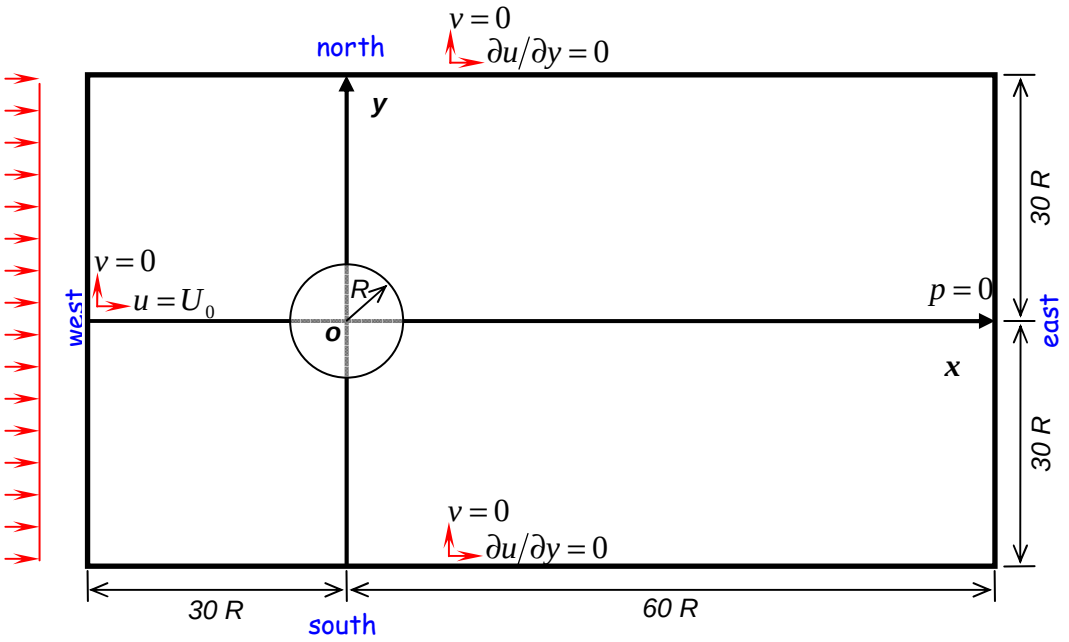


Figure 3.2 Schematic drawing showing the domain solution limits and boundary conditions

3.5. Grid generation and optimisation

3.5.1 Grid generation

In 3D case the CVs are parallelogram with nodal point *P* and 6 faces noted by the capital letters *N*,*S*,*E*,*W*,*T*, and *B* which stand for north, south, east, west, top, and bottom respectively. In our 2D case the CVs are reduced to rectangles. Figure 3.3 shows the 3D and 2D control volumes.

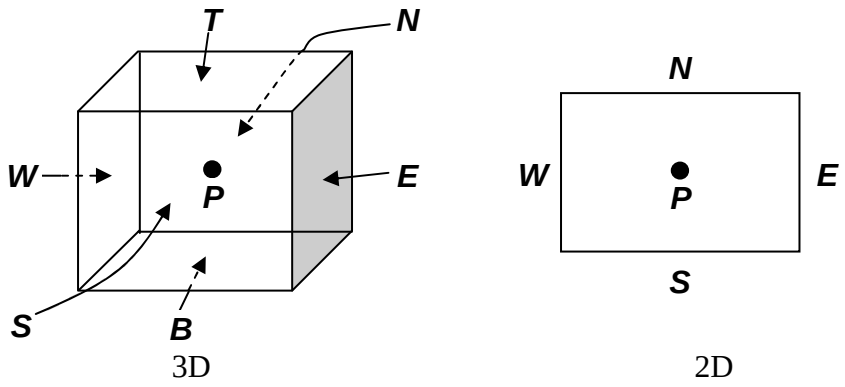


Figure 3.3 Control volume notation for 3D and 2D cases

However, if the velocities and pressures are both evaluated at the nodes of an ordinary CV a highly non-uniform pressure field can act like a uniform field in the discretized momentum equations [71]. To overcome this problem the technique of *staggered grid* is used [72]. The principle of this method is to evaluate the scalar quantities, like pressure and temperature, at nodal points and calculate the other vector components, like velocities, at the staggered grid centered on cell faces. Figure 3.4 emphasizes the staggered grid with capital letters noting the pressure CV and small letters designating the velocity CV.

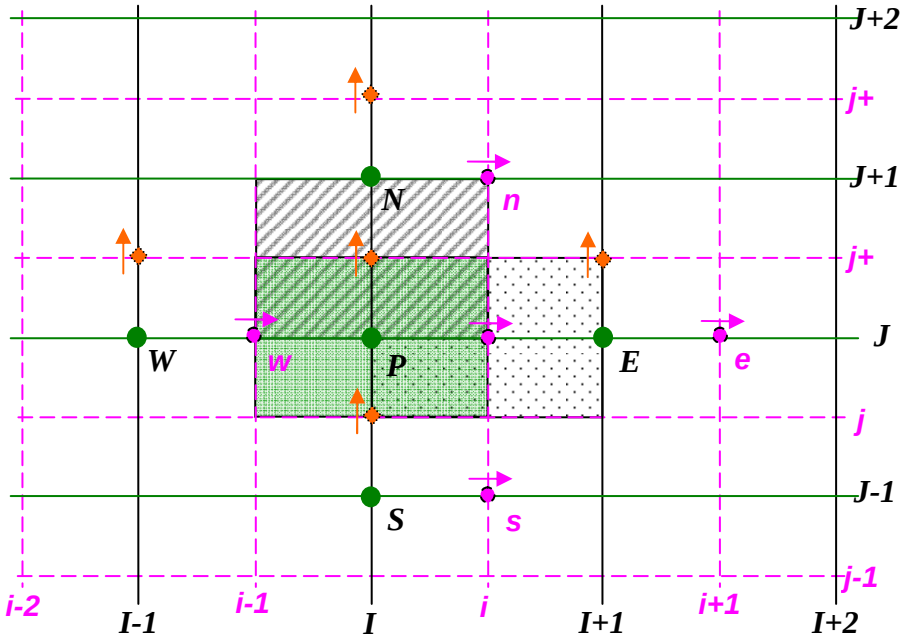


Figure 3.4 Control volume for calculating scalar quantities (solid colour and capital letters) and control volume for evaluating vector components (hatched and dotted colours with small letters)

In this work, the presentation of governing equations in generalized orthogonal coordinates is adopted. Hence, an *admissible transformation* of coordinates must be found. Aris [73] stated that the coordinate transformation is admissible (or proper) if it is invertible and if the ratio of volume elements in the two coordinate systems, which is called the Jacobian *J*, always exists and does not vanish.

In order to generate an orthogonal grid, we use the velocity potential ϕ and the stream function ψ of the potential flow past a cylinder:

$$\phi = U_0 x\left(1+\frac{R^2}{x^2+y^2}\right), \qquad 3.25$$

$$\psi = U_0 y\left(1-\frac{R^2}{x^2+y^2}\right), \qquad 3.26$$

$$z)_{generalized} = z)_{Cartesian.} \text{ for the 3D case,} \qquad 3.27$$

where U_0 is the free-upstream velocity, R is the cylinder radius and x, y are the horizontal and vertical position measured at the Cartesian grid whose origin is located at the cylinder centre..

It is obvious that these relations are valid only for $\sqrt{x^2+y^2} \geq R$. The Jacobian of transformation from the Cartesian coordinate system (x, y, z) to the generalized coordinate system (ϕ, ψ, z) is defined as:

$$|J| = \begin{vmatrix} \frac{\partial x}{\partial \phi} & \frac{\partial y}{\partial \phi} & \frac{\partial z}{\partial \phi} \\ \frac{\partial x}{\partial \psi} & \frac{\partial y}{\partial \psi} & \frac{\partial z}{\partial \psi} \\ \frac{\partial x}{\partial z} & \frac{\partial y}{\partial z} & \frac{\partial z}{\partial z} \end{vmatrix} \qquad 3.28$$

In the present work, the case of the long cylinder is considered; i.e. two-dimensional simulations. Hence, we shall continue with the two-dimensional analysis.

The Jacobian of Cartesian to generalized coordinates $|J|$ can be found by solving the equations 3.25 and 3.226 for the variables (x, y). To achieve this it is better to divide the transformation into two steps; taking the standard polar coordinates (r, θ) as intermediate coordinates. By that, we write:

$$\phi = U_0 \cos\theta\left(r+\frac{R^2}{r}\right), \qquad 3.29$$

$$\psi = U_0 \sin\theta\left(r - \frac{R^2}{r}\right). \qquad 3.30$$

The values of (r,θ) are calculated for each stream line; i.e. for fixed $\psi > 0$. For given (ϕ,ψ), the value of $\alpha = r^2$ is the root of the quadratic equation:

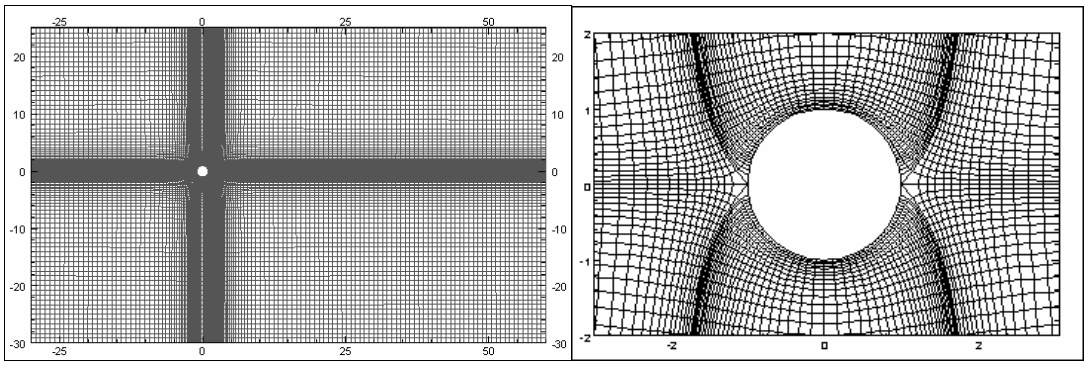
$$U_0^2\alpha^4 - (\phi^2 + \psi^2)\alpha^3 + 2R^2(\phi^2 - \psi^2 - U_0^2R^2)\alpha^2 - R^4 = 0, \qquad 3.31$$

The value of θ is calculated from:

$$\theta = \arccos\left(\frac{r\varphi}{U_0(r^2 + R^2)}\right). \qquad 3.32$$

If (x,y) are obtained from $x = r\cos\theta$ and $y = r\sin\theta$.

By applying these transformations, an orthogonal grid of the type shown in Figure 3.5 is obtained.



(a) (b)

Figure 3.5 Generated orthogonal grid:
(a) the whole grid, (b) zoomed view around the cylinder

After manipulating the equations, the Jacobian has the following form:

$$J = \frac{1}{U_0|\mathrm{K}|}\mathrm{K}; \qquad \mathrm{K} = \begin{bmatrix} 1-\frac{R^2}{r^2}\cos 2\theta & \frac{R^2}{r^2}\sin 2\theta \\ -\frac{R^2}{r^2}\sin 2\theta & 1-\frac{R^2}{r^2}\cos 2\theta \end{bmatrix}. \tag{3.33}$$

The columns of the Jacobian represent the *base vectors* (b_j) of the generalized coordinate system.

$$\begin{aligned} \mathbf{b}_1 &= \frac{1}{U_0|\mathrm{K}|}\left[1-\frac{R^2}{r^2}\cos 2\theta; \quad -\frac{R^2}{r^2}\sin 2\theta\right], \\ \mathbf{b}_2 &= \frac{1}{U_0|\mathrm{K}|}\left[;\frac{R^2}{r^2}\sin 2\theta \quad 1-\frac{R^2}{r^2}\cos 2\theta\right]. \end{aligned} \tag{3.34}$$

The multiplication of the base vectors results in the *metric tensor* $\mathbf{g}$:

$$\mathbf{g} = \begin{bmatrix} \frac{1}{U_0{}^2|\mathrm{K}|} & 0 \\ 0 & \frac{1}{U_0{}^2|\mathrm{K}|} \end{bmatrix} \tag{3.35}$$

It is noted here that the off-diagonal terms are nil which proves the orthogonality of the considered curvilinear coordinate.

3.5.2 Mesh optimization

In order to get well converged results, five mesh grids are tested: M1 ($N_1 x N_2 = 320$x160), M2 (300x150), M3 (250x130), M4 (200x100), and M5 (160x80).

The used machine is an office PC having an "Intel® Core™ 2 Quad" processor, Q6600- 2.40GHz, , 4 cores, and 4 logical processors and total physical memory of 3325.14 MB.

Table 3.2 shows the characteristics of the computational meshes and the corresponding computation time for each mesh. The total number of nodes is N_c, the number of nodes on the cylinder is N_{cyl}. The symbols $\delta s^i_{\min/\max}$, $(i = p,u,v)$ stand for minimum and maximum side lengths of pressure, x-component, or y-component control

volumes. The symbols $V^{i}_{\min/\max}$, $(i = p,u,v)$ represent the minimum and maximum areas of pressure, x-component, or y-component control volumes.

Table 3.2 characteristics of the computational meshes.

Mesh	$N_1 \times N_2$	N_c	$\delta s^{p}_{\min}$	$\delta s^{p}_{\max}$	$\delta s^{u}_{\min}$	$\delta s^{u}_{\max}$	$\delta s^{v}_{\min}$	$\delta s^{v}_{\max}$
M1	320x160	51681	1.8419E-2	2.0184	1.9485E-2	2.0183	1.8427E-2	2.0176
M2	300x150	45451	8.5977E-3	2.0149	8.5972E-3	2.0149	9.0946E-3	2.0120
M3	250x130	32881	8.5980E-3	2.0160	8.5972E-3	2.0160	9.0951E-3	2.0131
M4	200x100	20301	9.6126E-3	2.0224	9.6120E-3	2.0222	1.0234E-2	2.0188
M5	160x80	13041	1.0435E-2	2.0272	1.0432E-2	2.0270	1.1167E-2	2.0231

Mesh	N_{cyl}	$V^{p}_{\min}$	$V^{p}_{\max}$	$V^{u}_{\min}$	$V^{u}_{\max}$	$V^{v}_{\min}$	$V^{v}_{\max}$
M1	71	8.6414E-4	0.4169	8.6388E-4	0.4169	8.6387E-4	0.3987
M2	65	8.0418E-4	0.4943	8.4744E-4	0.4943	8.4743E-4	0.4766
M3	61	8.6227E-4	0.6961	9.0893E-4	0.6961	9.0887E-4	0.6959
M4	55	1.3195E-3	1.3386	1.3987E-3	1.3386	1.3978E-3	1.2967
M5	51	1.7186E-3	2.2308	1.8306E-3	2.2309	1.8312E-3	2.2303

Table 3.3 illustrates the computational characteristics of the used grids. The symbol *mem* shows the quantity of total used memory by the code. the term t_{comp} is the total computation time for a total physical time of 600 with a time step $\Delta t = 1.0\times10^{-3}$. These figures concerns a viscoelastic flow at Reynolds number Re = 100 and Deborah number De = 0.05.

Table 3.3 computational characteristics of meshes.

Mesh	t_{comp} [sec.]	*mem* [MB]
M1	425863.8	203.14
M2	334510.6	171.97
M3	292026.0	112.53
M4	196527.6	62.59
M5	110925.7	37.04

In the anticipation of the results needed in chapter 4, four non-dimensional quantities are considered to evaluate the mesh senstivity:

- The non-dimensional frequency represented by the Strouhal number $Str = 2Rf/U_0$ where f is the frequency of vortex shedding.
- The drag force represented by the average drag coefficient C_d.

- The lift force represented by the root mean square lift coefficient C_{l-rms}.
- The base pressure evaluated through the average base pressure coefficient C_{bp}.

Table 3.4 illustrates the values of non-dimensional quantities for different mesh grids.

Table 3.4 Comparison of non-dimensional quantities for different mesh grids.

	M1	*M2*	$\frac{M2-M1}{M1}\%$	*M3*	$\frac{M3-M1}{M1}\%$	*M4*	$\frac{M4-M1}{M1}\%$	*M5*	$\frac{M5-M1}{M1}\%$
Str	0,1693	0,1694	0,02%	0,1697	0,21%	0,1690	-0,18%	0,1676	-1,03%
C_d	1,3739	1,3732	-0,05%	1,3750	0,08%	1,3697	-0,31%	1,3688	-0,37%
C_{l-rms}	0,1714	0,1732	1,03%	0,1766	3,01%	0,1900	10,84%	0,1989	16,05%
C_{bp}	-0,7766	-0,7767	0,01%	-0,7807	0,52%	-0,7820	0,69%	-0,7824	0,74%

From Table 3.4, it is clear that only the lift coefficient is sensitive to the mesh used. Mesh M_3 represents an optimum grid as it offers moderate computational cost without loss of accuracy. However, upon implementation of the code for higher Deborah number, it is found that this grid is too fine that it limits the results to De = 0.1. Using the coarser grid M_4 allows us to reach De = 0.25. From Table 3.4, it is observed that using grid M_4 is still in acceptable limits for the different non-dimensional numbers. Bearing in mind that the uncertainty on the lift coefficient reaches 10%. Hence, grid M_4 is employed in the rest of the work.

For this selected grid, the effect of the time step is studied. Four time steps are tested; $\Delta t_1 = 0.5\times10^{-3}$, $\Delta t_2 = 1.0\times10^{-3}$, $\Delta t_3 = 1.5\times10^{-3}$, and finally $\Delta t_4 = 2.0\times10^{-3}$ which is the largest time step that gives convergent results.

Figure 3.6 shows the effect of changing the time step on the instantaneous values of the vertical velocity, drag coefficient and lift coefficient. It is seen that the increase of the time step leads to a phase shift of the three quantities. For the drag force, the change of the time step increases the mean drag coefficient. The running time for different time steps is shown in Table 3.5. Values of the four non-dimensional quantities are also calculated and the relative change with respect to the smallest time step is computed for each non-dimensional quantity are given in Table 3.6.

From Table 3.6 and Table 3.5, it is seen that $\Delta t = 1\times10^{-3}$ offers good accuracy with a reasonable running time.

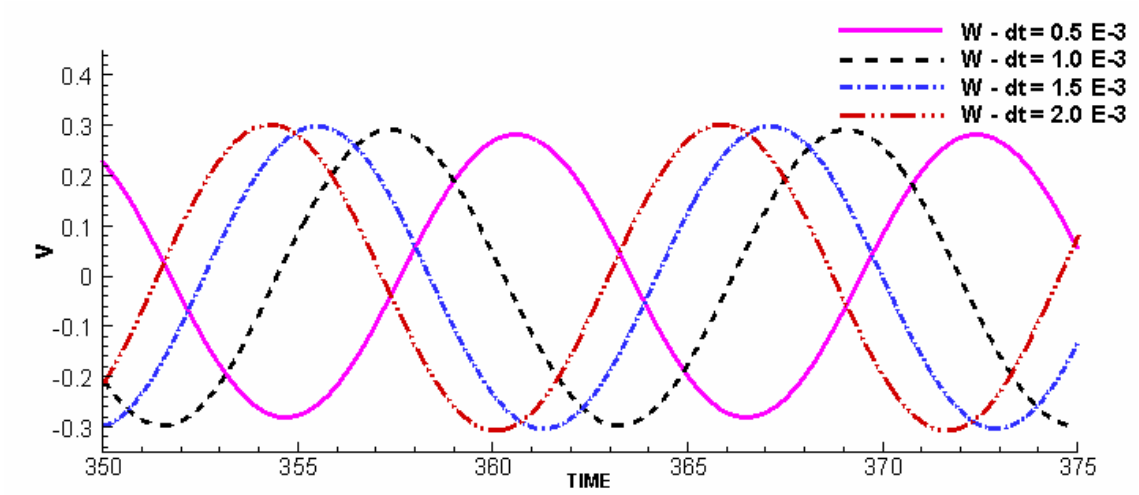
Table 3.5 Running time for different time steps.

Time step	Running time [sec.]
$\Delta t_1 = 0.5\times10^{-3}$	257526.9
$\Delta t_2 = 1.0\times10^{-3}$	196527.6
$\Delta t_3 = 1.5\times10^{-3}$	139780.0
$\Delta t_4 = 2.0\times10^{-3}$	105790.1

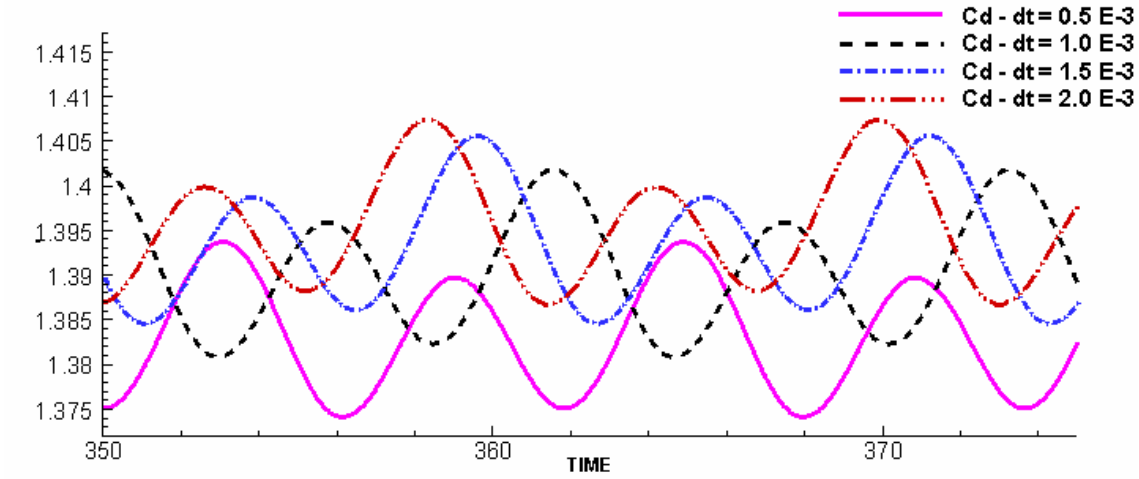
Table 3.6 Relative change of values of non-dimensional quantities for different time steps.

	$\frac{dt2-dt1}{dt1}\%$	$\frac{dt3-dt1}{dt1}\%$	$\frac{dt4-dt1}{dt1}\%$
Str	0,02%	0,21%	-0,18%
C_d	-0,05%	0,08%	-0,31%
C_{l-rms}	1,03%	3,01%	10,84%
C_{bp}	0,01%	0,52%	0,69%

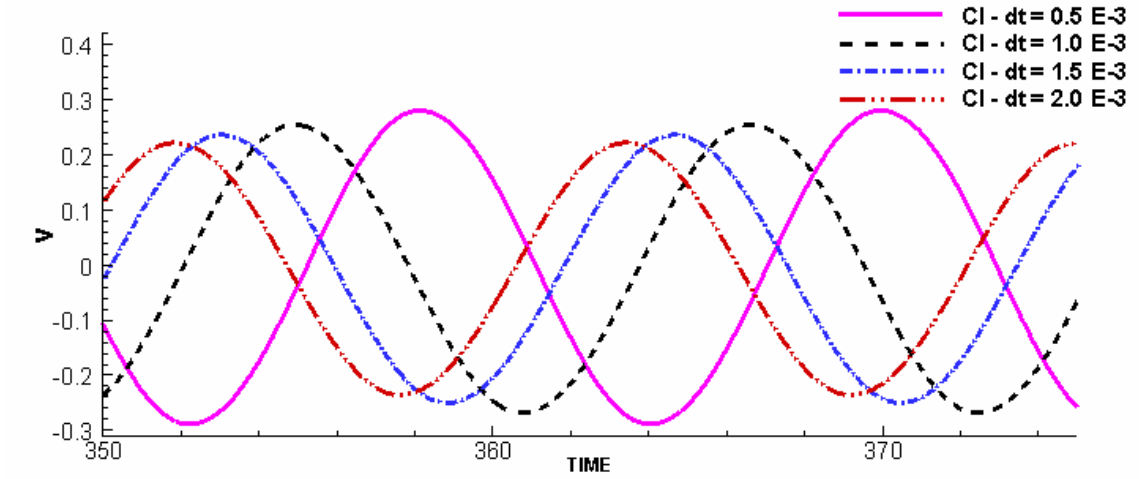
Finally, the influence of the number of points on the cylinder surface on the obtained results is checked. For the selected grid M_4 and with the optimized time step $\Delta t = 1\times10^{-3}$, four values of N_{cyl} are checked; $N_{cyl-1} = 61$, $N_{cyl-2} = 51$, $N_{cyl-3} = 41$, and $N_{cyl-4} = 31$. Greater values did not give convergent results and smaller values dramatically deteriorate the results. Figure 3.7 shows the results of the non-dimensional quantities for different numbers of points on the cylinder. Figure 3.7 proves that $N_{cyl} = 41$ is the most convenient. In summary, the selected grid is M_4 (200x100) with $N_{cyl} = 41$ and $\Delta t = 1.0\times10^{-3}\,\text{sec}$.



(a)



(b)



(c)

Figure 3.6 Effect of changing the time step on (a) vertical velocity, (b) drag coefficient and (c) lift coefficient

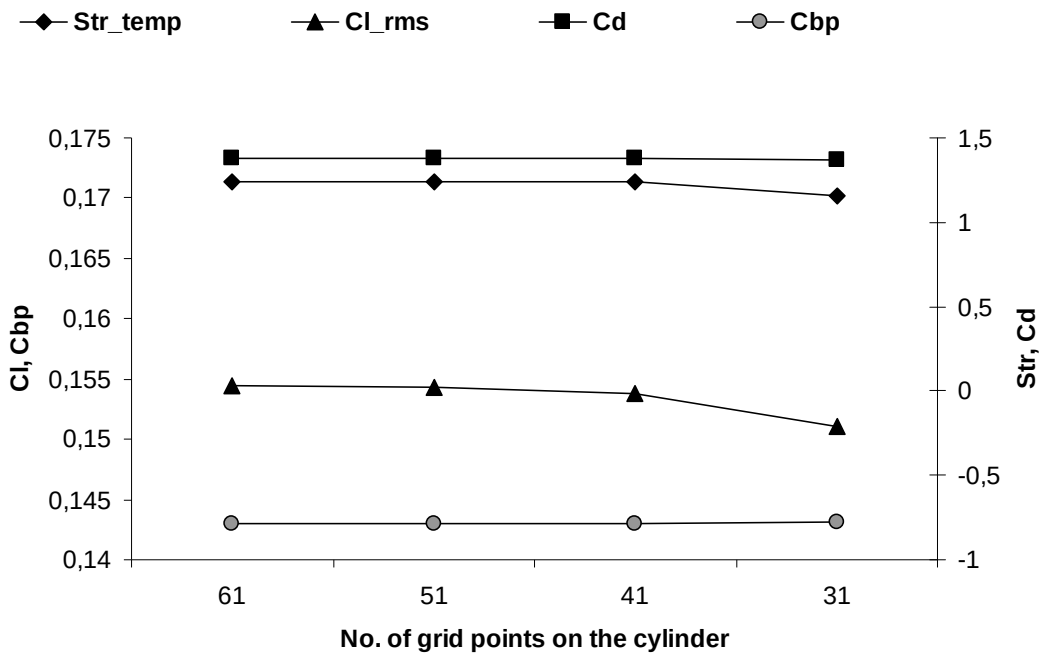


Figure 3.7 Values of non-dimensional quantities for different number of points on cylinder

3.6. Summary of numerical methodology

- The Finite Volume Method (FVM) with a staggered grid is applied to solve the governing equations.
- The convective terms are evaluated using the second-order accurate QUICK scheme. The diffusion terms are calculated with the second order accurate centred difference scheme.
- For the time marching algorithm, the first-order accurate Euler forward explicit scheme is applied obeying the adaptation of Marker and Cell algorithm
- The velocity potential and the stream function of the potential flow are used to generate the mesh.
- A grid dependence study was carried out. The grid is has 200x100 nodes with 41 grid points on the cylinder and a time step $\Delta t = 1.0 \times 10^{-3}$

Chapter 4: RESULTS AND DISCUSSION

4.1. Overview

After stating the governing equations and discussing the numerical method, this chapter introduces the physical results for the problem under consideration. The case of viscoelastic PTT fluid past a non-confined cylinder is almost unexplored. As mentioned in the literature review, almost all the published works concern the confined cylinder because it is considered as one of the benchmark problems used to validate numerical codes. Up to our knowledge, only two works can be found treating the non-confined cylinder; the article of Oliveira [27] who simulates the FENE-CR fluid and that of Pipe & Monkewitz [58] who investigated experimentally the Ginzburg-Landau fluid flow. On the other hand, many results are available for the Newtonian fluid flow past a non-confined cylinder; e.g. Willamson [74], Persillon & Braza [70], Thais et al. [75], Ramšak et al. [76]. Consequently, the simulation of Newtonian fluid flow is first carried out to validate the present code. For the viscoelastic fluid case, the results are validated by comparing the behaviour of the different quantities against the corresponding results for the confined cylinder case and against those of other viscoelastic fluids flowing past a non-confined cylinder.

The outline of this chapter is arranged to show the Newtonian fluid results at first. Then, the viscoelastic fluid results are presented. For the viscoelastic results, we show the results of the particular quantities directly related to the viscoelastic fluids which are the extra-shear stress and the normal stress difference. Then, the results for the main physical quantities influenced by the elasticity of the fluid are presented. These quantities are the pressure, the velocity field and the vorticity. For each quantity, an overall view of the flow domain is drawn for Reynolds and Deborah numbers. To quantify the results, curves are plotted versus Reynolds and Deborah numbers. The final part of this section discusses the viscoelastic effects on Strouhal number, lift and drag coefficients. In each step, the trend of the present findings is commented and compared to the previous literature.

4.2. Results for Newtonian fluid

The developed code is tested for the Newtonian case by setting the polymer relaxation time to zero. The results of this work are compared with the works of:

- Liu et al. [77] who studied the transition to turbulence using a numerical approach based on multigrid and preconditioning methods.
- Thais et al. [63] who carried out their work for a Newtonian laminar flow using a staggered FVM.
- Oliveira [27] who simulated the viscoelastic flow with a collocated FVM.
- Ramšak et al. [76] who applied the Boundary Element Method (BEM) to simulate the unsteady laminar flow.

Table 4.1 shows the number of points N_c and the non-dimensional quantities: the Strouhal number Str, the average drag coefficient C_d, the root mean square of the lift coefficient C_{l-rms}, and the average base pressure coefficient C_{bp} for the present work and the literature at Re = 100.

Table 4.1 Verification of Newtonian results versus literature (Re = 100)

	Present work	Liu et al.	Thais *et al.*	Oliveira	Ramšak et al.
N_c	20000	12228	12800	19860	50000
Str	0.173	0.164	0.171	0.167	0.172
C_d	1.356	1.350	1.348	1.370	1.299
C_{l_rms}	0.173	0.339	0.261	-	0.173
C_{bp}	-0.788	-0.848	-0.808	-	-

Values in Table 4.1 show a good agreement with the present work. The present value of Strouhal number is close to the previous works (0.0% - 4.2%) although our result is systematically larger. This is possibly due to the finer mesh and the used discretization method of the present work. For the average drag coefficient, the range of difference with other works is 0.36% - 5.9% and the present result seems to be larger. Regarding the root mean square lift coefficient, there is a noticeable dispersion of the values. For the average base pressure, the values are also very close (2.0% - 6.6%).

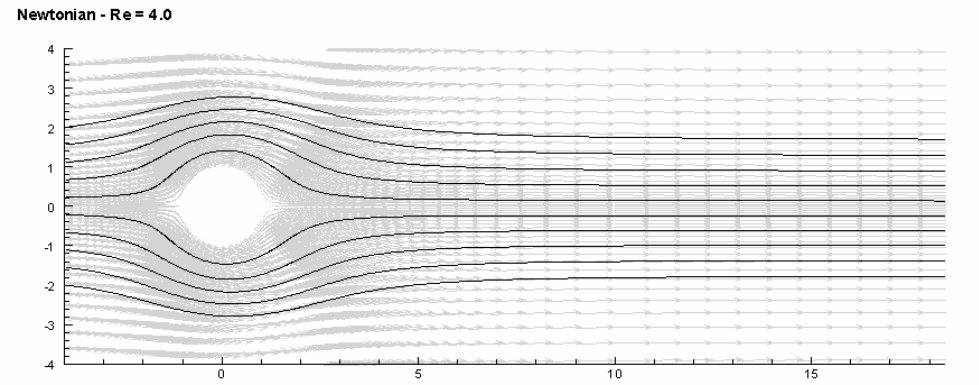
Another way to asses the present results is the phenomenon of vortex shedding which is called in many references the "von Kàrmàn street". Present simulations show up that the flow past a cylinder exhibits three successive regimes:

- Creeping regime (Re < 5) with no separation from the cylinder.
- Laminar steady regime ($5 \leq \mathrm{Re} < 47$) in which two steady vortices are created behind the cylinder. The vortices are symmetric about the x-axis. As the Reynolds number increases the inertia force dominates over the viscous force and the instability region becomes bigger and elongated.
- Laminar vortex shedding regime ($\mathrm{Re} \geq 47$) where the two vortices are no longer symmetric or steady announcing the onset of the von Kàrmàn street.

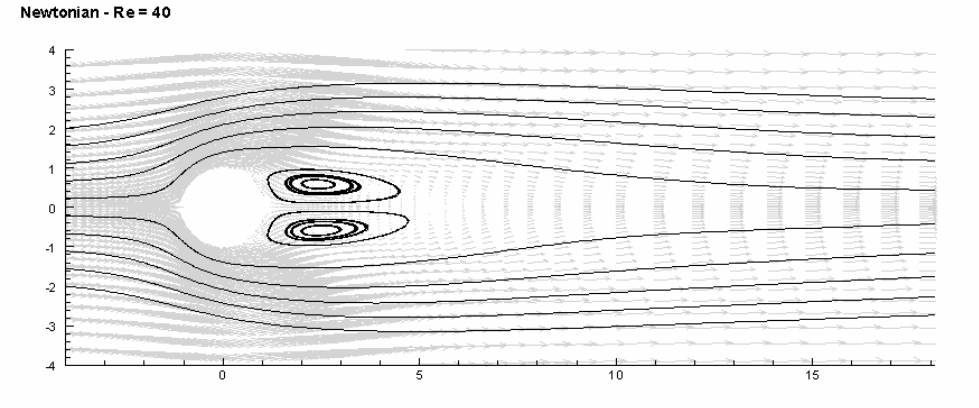
Our present results agree very well with the previous literature like the experimental work of Williamson [74] who found $\mathrm{Re}_{cr} = 49$, Pipe & Monkewitz [58] who arrived at $\mathrm{Re}_{cr} = 50$, and Coutanceau & Defaye [78] with $\mathrm{Re}_{cr} = 47$. Figure 4.1 depicts the velocity profile around the cylinder for Re=4, 40, and 47 respectively clarifying the different pre-mentioned flow regimes. Results for the Newtonian case are summarized in Table 4.2.

Table 4.2 Results for Newtonian case.

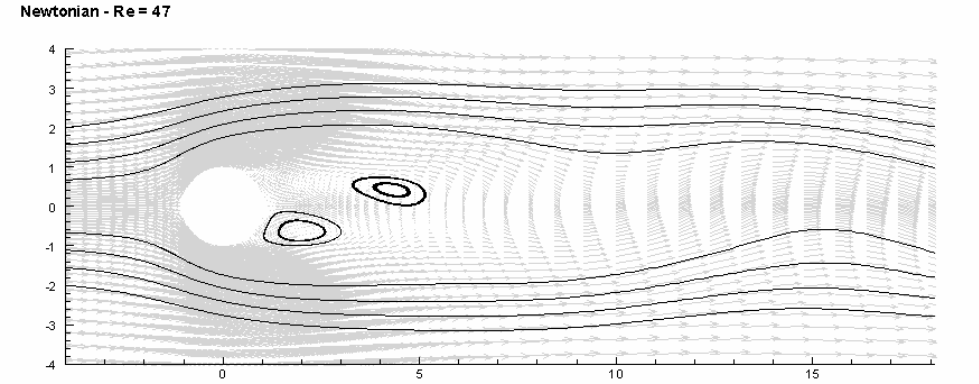
Re	*Str*	C_d	C_{l_rms}	C_{bp}
40	0.1177	1.5400	0.0005	-0.5788
45	0.1200	1.4700	0.0017	-0.5662
47	0.1210	1.4477	0.0063	-0.5643
50	0.1252	1.4332	0.0225	-0.5783
60	0.1388	1.4030	0.0630	-0.6289
80	0.1584	1.3691	0.1238	-0.7142
100	0.1726	1.3558	0.1729	-0.7883
125	0.1862	1.3538	0.2251	-0.8706
150	0.1957	1.3593	0.2622	-0.9357
175	0.2052	1.3647	0.2994	-1.0007
200	0.2120	1.3693	0.3231	-1.0472



(a)



(b)



(c)

Figure 4.1 Velocity field for a Newtonian fluid flow at: (a) Re = 4, (b) Re = 40, and (c) Re = 47

4.3. Viscoelastic Results

The experimental literature ([51], [54], [56]) indicates that a very small amount of polymer additives strongly affects the flow properties compared to the purely Newtonian flow. The viscoelastic effects manifest themselves mainly in the reduction of the drag force, the reduction of the frequency of vortex shedding, and the increase in the length of formation of the downstream instability region. The higher elongational viscosity of viscoelastic fluids is quoted as responsible for these observations. It is expected from the numerical simulation to corroborate these experimental results.

The applied viscoelastic fluid model is the simplified Phan-Thien-Tanner (SPTT) model in its exponential form. The used model parameters are $\eta_N = 0$, $\xi = 0$, $\varepsilon = 0.1$, $\beta = 1$ and $n = 1$ (equations 2.10, 2.11, and 2.12)

Results are obtained by fixing the overall fluid density at unity and assuming a unit velocity at the far upstream entry and changing the polymer viscosity to get different Reynolds number for the same Deborah number. Then, the polymer relaxation time is increased to vary the Deborah number.

Two longitudinal sections (S1 and S2), two cross sections (S3 and S4), two streamlines (SLu and SLd) and a downstream point on the x-axis (*h*) are selected (cf. Figure 4.2) to study the evolution of the main flow properties.

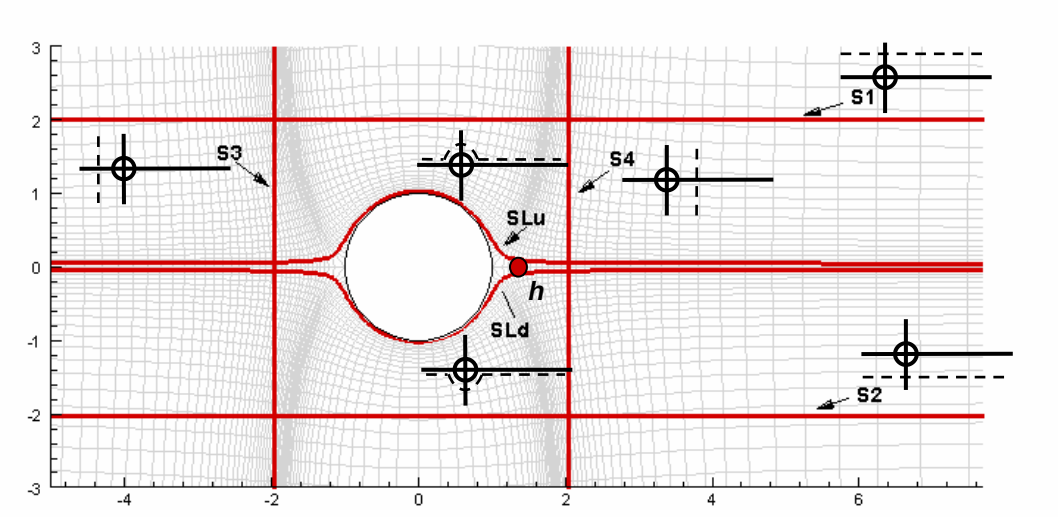


Figure 4.2 Longitudinal and cross sections, and streamlines used to quantify the results.

4.3.1 Extra-Shear Stress

Viscoelastic fluids are characterized by introducing extra-stresses to the flow. These stresses change all fluid fields and bring up the well-known properties of rod climbing, die swell…etc. Till now, the full comprehension of these extra-stresses and the accompanied phenomena is not complete and several researches are still exploring these areas.

In this section and in the next one, these extra-stresses are introduced and commented. This section concerns the off-diagonal component of the stress tensor which represents the shear stress. In the next section, the diagonal components (normal stresses) will be presented.

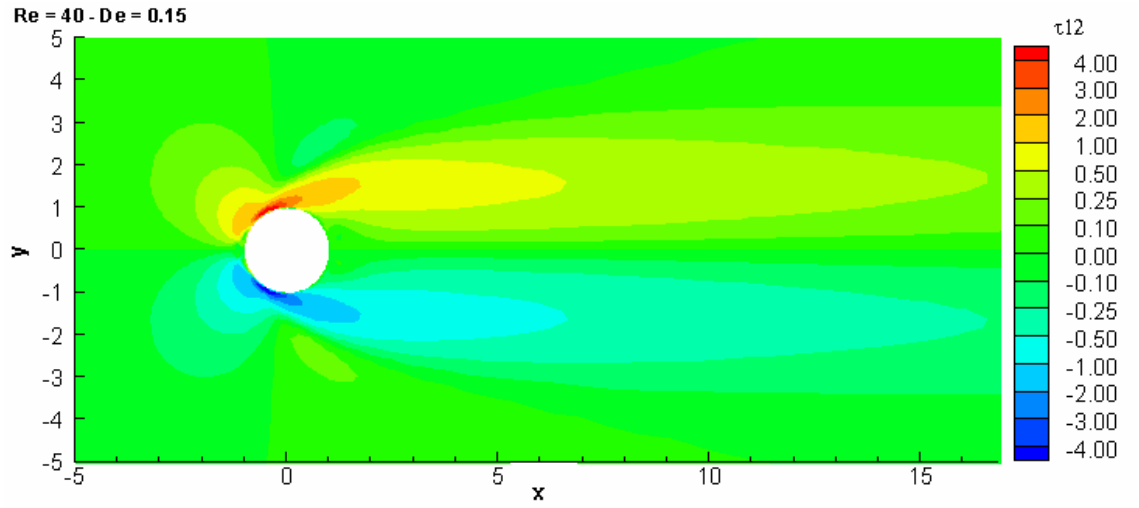
4.3.1.a Influence of Reynolds number on the extra-shear stress

It is well known that the shear stresses are directly related to the fluid viscosity. The main objective of this section is to explore and quantify this relation. As usual, the Reynolds number is used as an indicator of the fluid viscosity as they are in inverse proportionality.

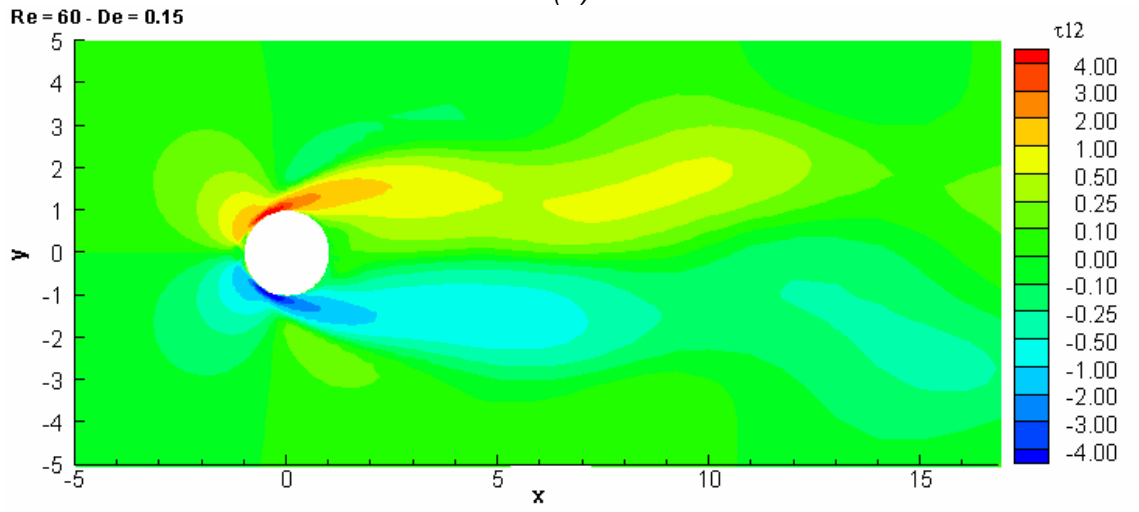
In order to represent the distributions and values of the extra-shear stress, the following expression of the normalized extra-shear stress is used:

$$\tau_{12} = \bar{\tau}_{12} \frac{\eta_0 U_0}{R} \qquad 4.1$$

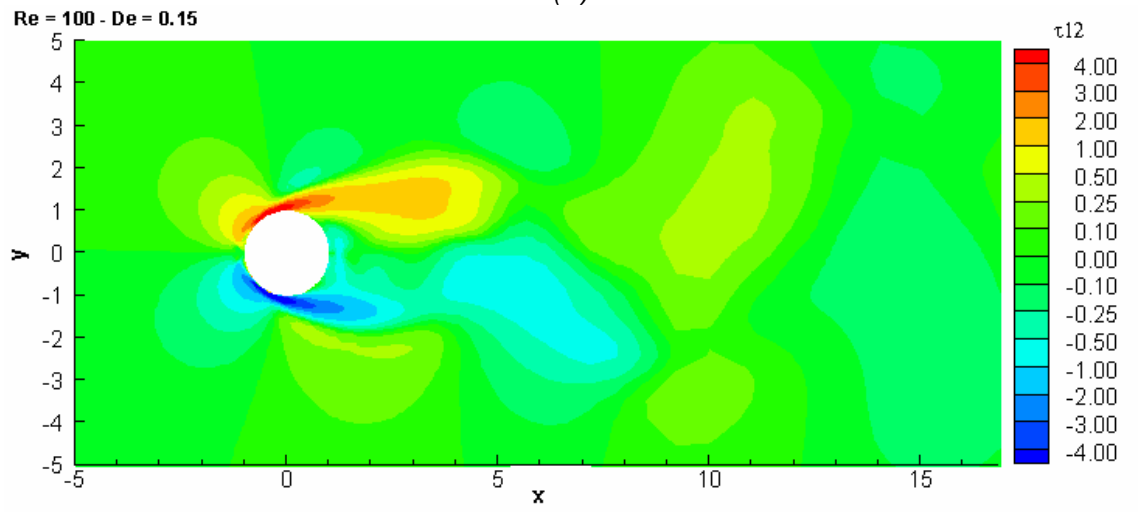
where $\bar{\tau}_{12}$ is the calculated value of extra-shear stress, η_0 is the total fluid viscosity, U_0 is the far upstream entry velocity, and R is the cylinder radius.



(a)



(b)



(c)

Figure 4.3 Extra-shear stress distribution for De = 0.15 at (a) Re = 40, (b) Re = 60, and (c) Re = 100

Figure 4.3 depicts the extra-shear stress distributions for De = 0.15 with Re= 40, 60, and 100 respectively. From these shear distributions, it is clear that extra-shear stress is strongly influenced by the increase of the Reynolds number. The maximum extra-shear stress zone is located at the cylinder surface on the upstream side and this location does not change with the Reynolds number. Before the onset of the laminar vortex shedding instability, the extra-shear stress is symmetrically distributed about the x-axis. With the onset of the von Karman vortex street, the extra-shear stress contours are extended and deformed. With further increase of the Reynolds number, a periodic alternance of positive and negative shear zone are found along the x-axis which indicates strong flow instabilities.

For the flows having $\mathrm{Re} < \mathrm{Re}_{cr}$, the zero-extra-shear stress contour is plotted on Figure 4.4 for a viscoelastic fluid (De=0.15) flowing with Re = 40 and 45. This figure illustrates that the change of the shear stress is very slight for this flow regime.

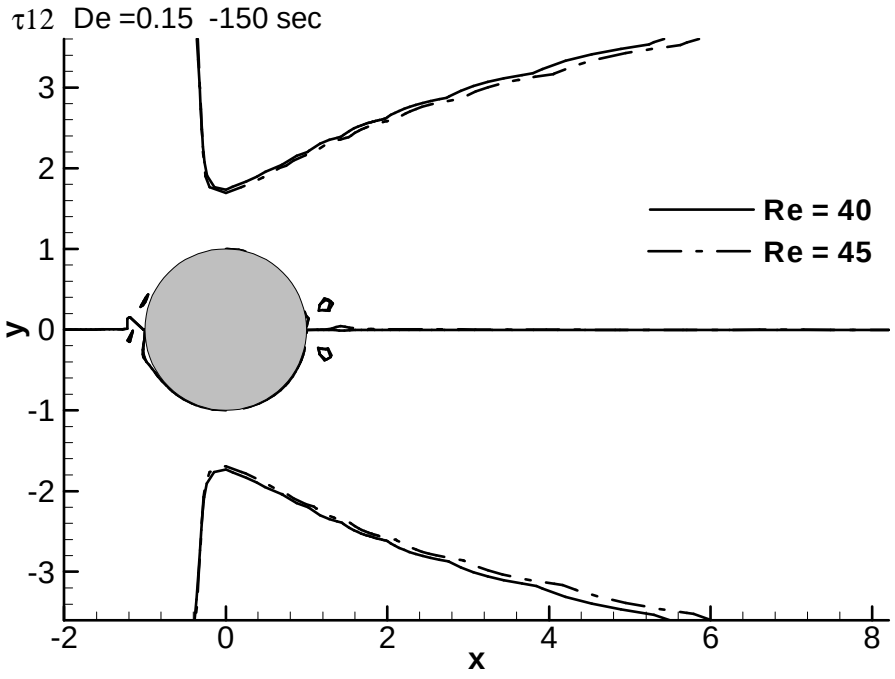


Figure 4.4 Zero-extra-shear stress contour at De = 0.15 for Re=40 and 45.

With the onset of vortex shedding, the extra-shear stress becomes extremely complicated as shown on Figure 4.5. This figure shows the zero-extra-shear stress for De=0.15 at Re = 80, 100 and 125.

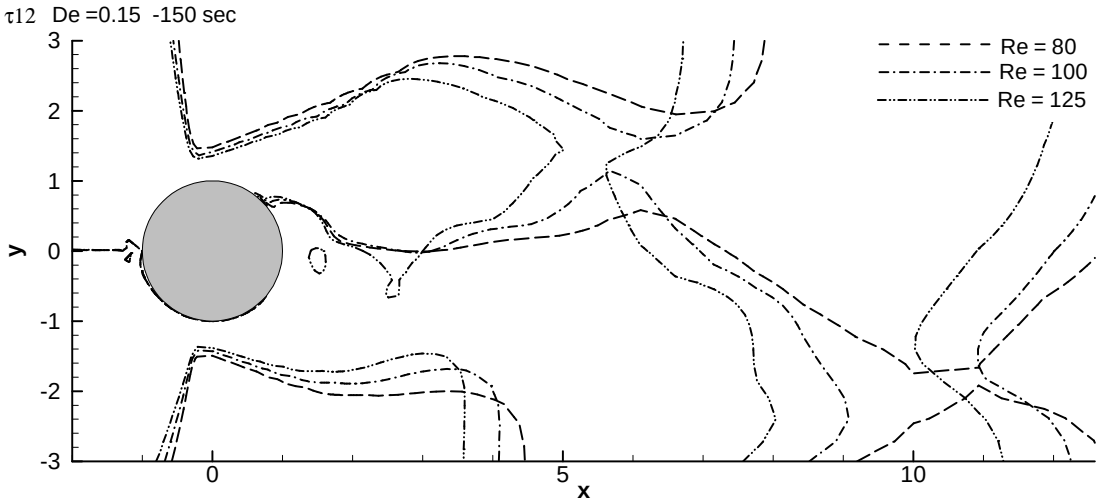
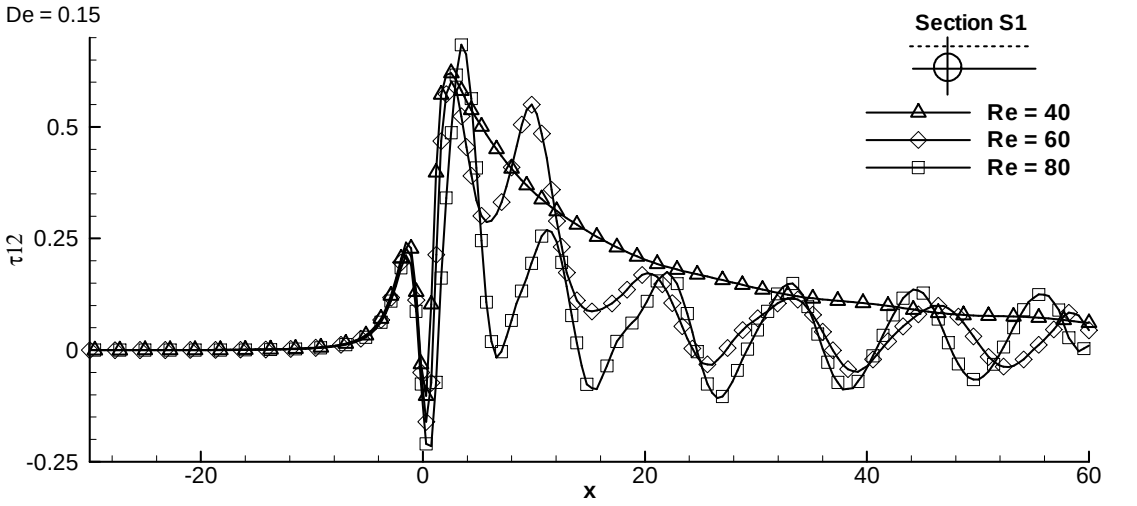


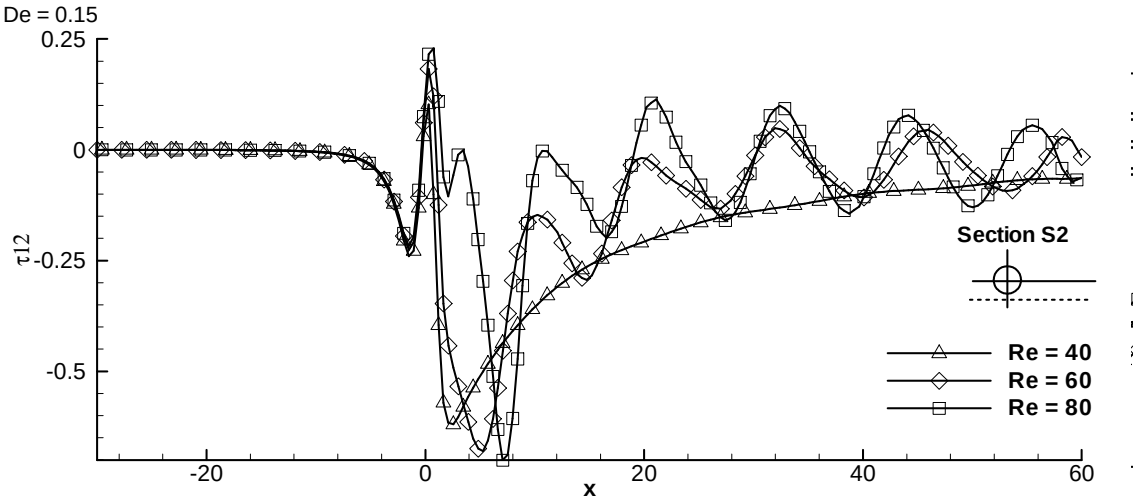
Figure 4.5 Zero-extra-shear stress contour at De = 0.15 for Re=80, 100 and 125.

Figure 4.5 shows the non-homogeneity of the extra-shear stress which is linked to the increase of Reynolds number. Simultaneously, the contours tend to be vertical downstream the cylinder for elevated Reynolds number. This is possibly due to the decrease of fluid viscosity and the normal stress differences. This shows the complexity of viscoelastic flows with instabilities.

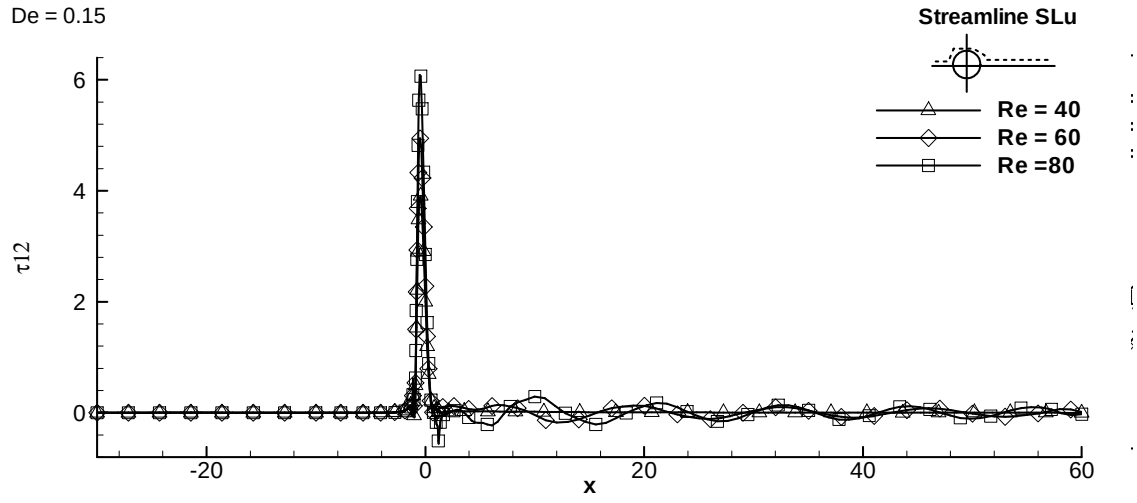
Some sample values of the extra-shear stress are given in Figure 4.6 which plots these values for Deborah number of De = 0.15 at different Reynolds number at section S1, section S2, and streamline SLu. These curves are plotted for the time instant.



(a)



(b)



(c)

Figure 4.6 Extra-shear stress magnitudes at De = 0.15 for Re = 40, 60, and 80 along :
(a) section S1, (b) section S2, and (c) streamline SLd.

Curves on Figure 4.6 show that the normalized magnitude of the extra-shear stress reaches a maximum of order 6 on the streamline adjacent to the cylinder on the upstream side. This maximum value increases by 19% when the Reynolds number increases from 40 to 60. For a Reynolds number increase from 60 to 80, the maximum normalized value of the shear stress increases by 22%. The increase of Reynolds number leads to strong changes downstream till a distance about 4~8*R*, then the fluctuations of the extra-shear stress become longitudinal waves with decaying amplitude. Note that the changes of the upstream flow are almost negligible.

4.3.1.b Influence of Deborah number on the extra-shear stress

In this subsection, we consider the influence of the Deborah number. To explore this effect, flows with a fixed Reynolds number are examined at different Deborah numbers. For this, we consider two of flow kinds: the first one is the stable flow with the steady vortices and the other is the flow with laminar vortex shedding instability.

For a steady flow, Figure 4.7 shows the contour lines of opposite signed shear stress (0.5 and -0.5) for Re = 40 at different Deborah numbers. This figure demonstrates that the fluid elasticity causes the shear stress contour to shrink and shift in the flow direction. This effect is noticeable on the upstream side of the cylinder, while it is negligable downstream the cylinder.

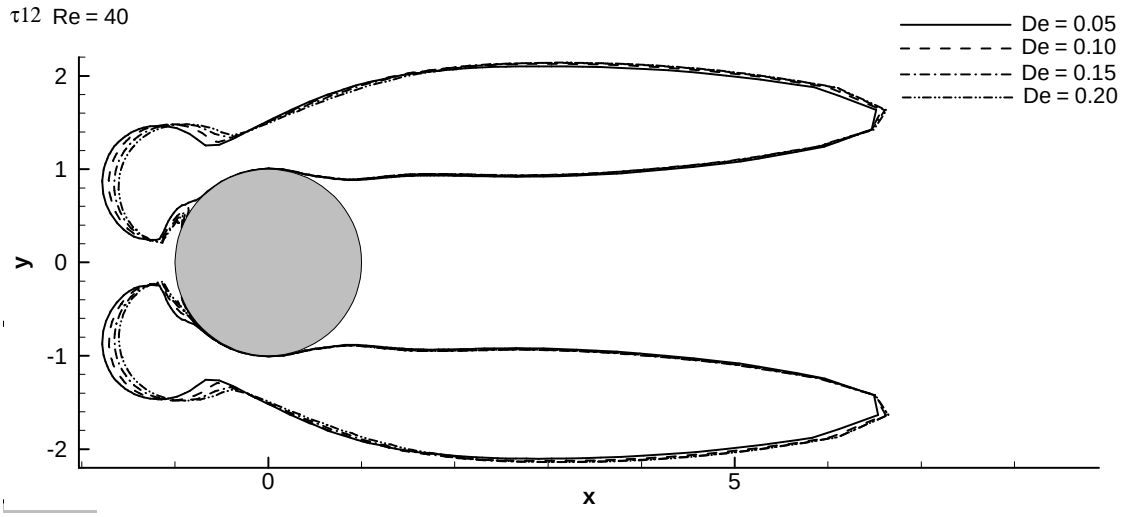


Figure 4.7 Extra-shear stress contours for Re = 40 and different Deborah numbers

Magnitudes of the extra-shear stress are plotted for a flow with Re = 40 at different Deborah numbers along section S1 and along streamline SLu (Figure 4.8). This figure shows that the difference in magnitudes of shear with Deborah number is very small and almost unnoticeable for this flow regime.

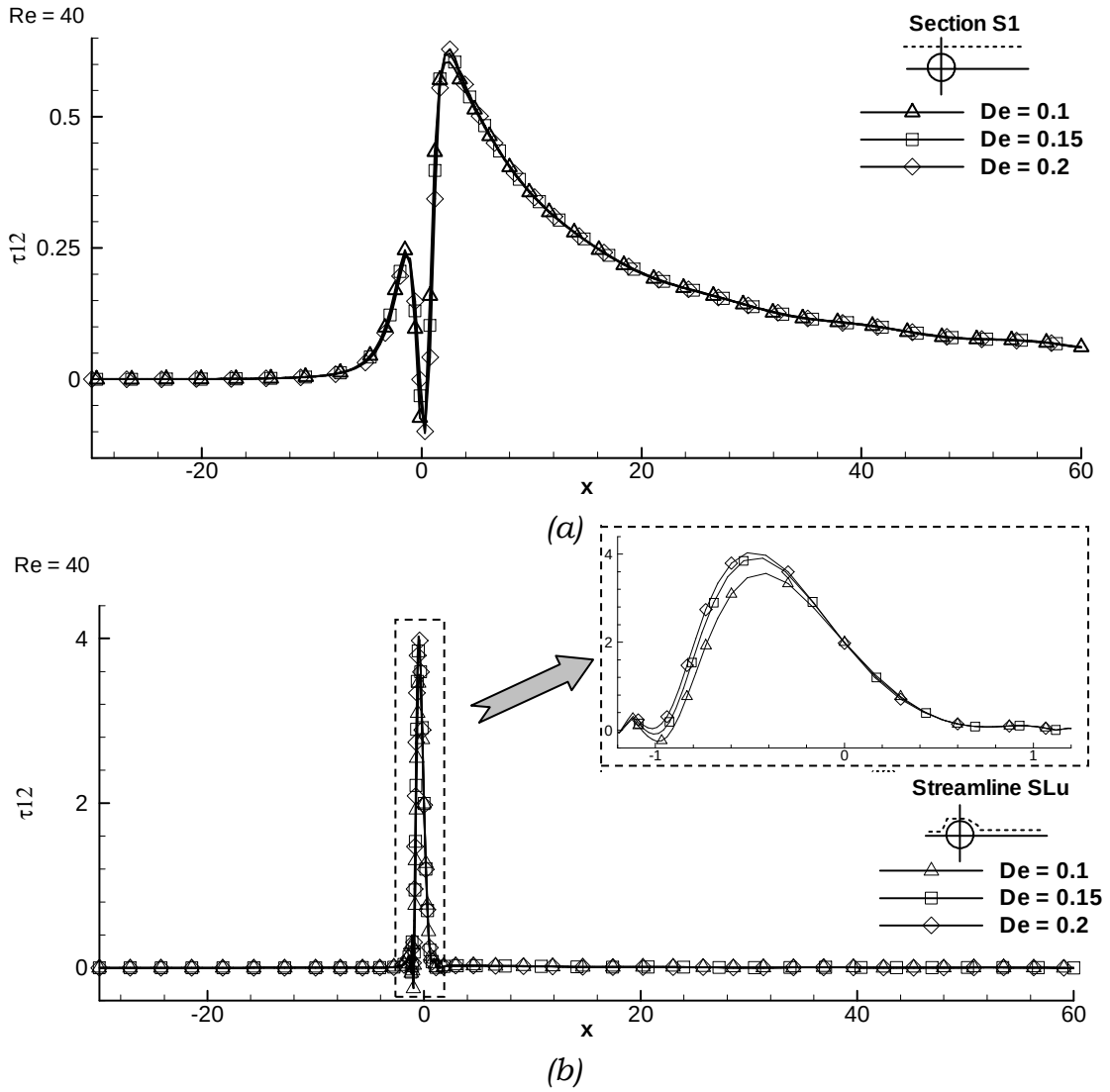
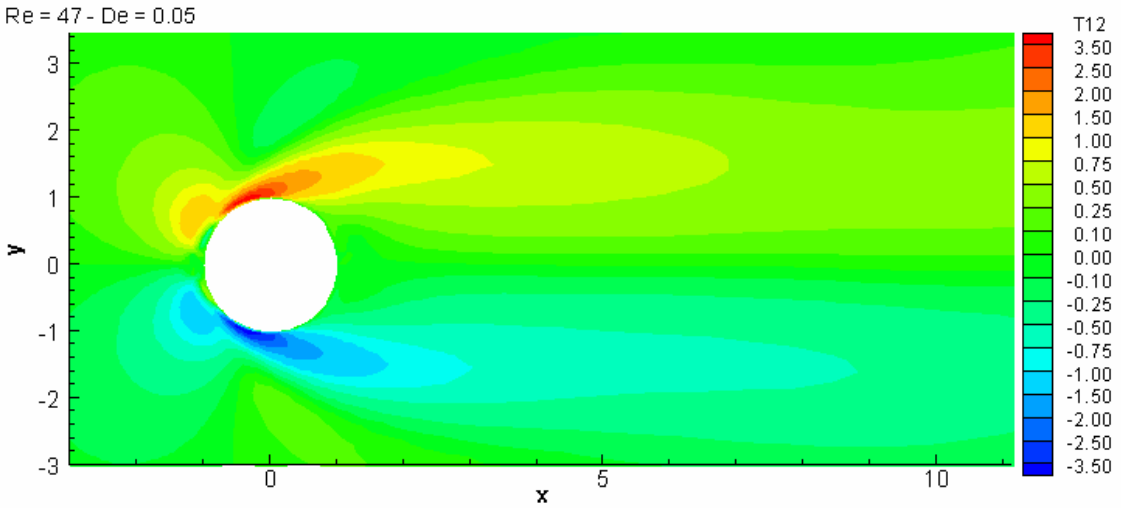
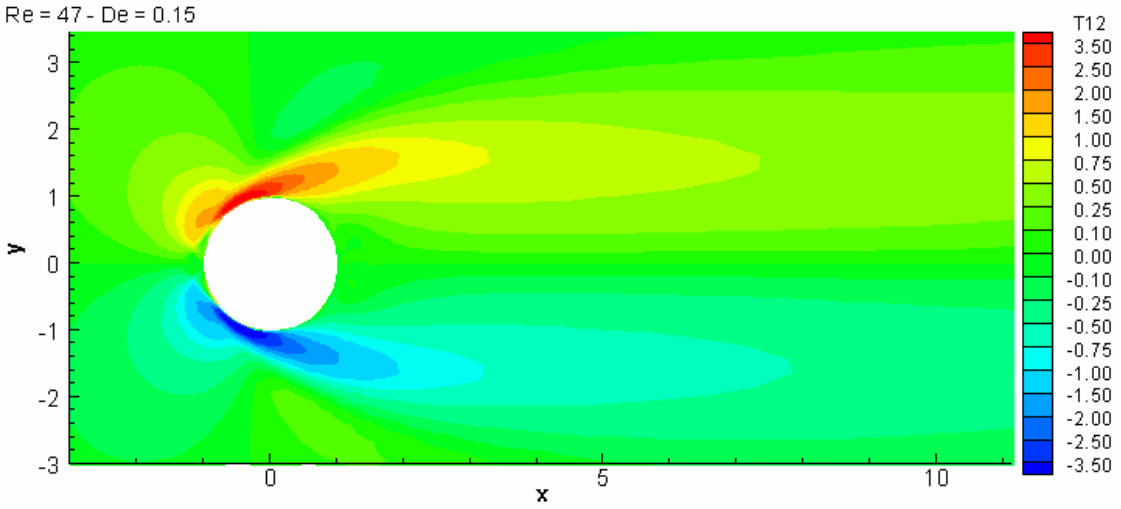


Figure 4.8 Extra-shear stress magnitude for Re = 40 at different Deborah number along (a) section S1 and (b) streamline SLu

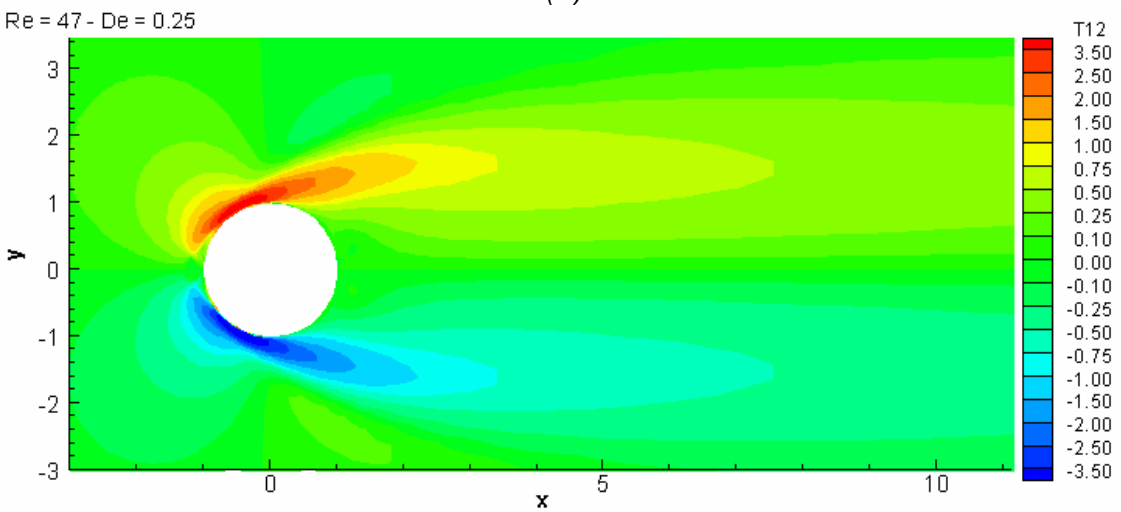
Figure 4.9 shows the extra-shear stress distribution for the critical Reynolds number Re = 47 at De=0.05, 0.15, and 0.25, respectively. We can see the asymmetry of the extra-shear stress at De = 0.05. Also, it is remarked that the increase of Deborah number restores the symmetry of the extra-shear stress distribution which indicates a restoring of the flow stability and the suppression of the vortex shedding instability.



(a)



(b)



(c)

Figure 4.9 Extra-shear stress at Re = 47 with: (a) De = 0.05, (b) De = 0.15, and (c) De = 0.25

The reduction of the shear stress contour asymmetry is shown on Figure 4.10 as contour lines of normalized shear stress of 0.5 and -0.5 are drawn for De = 0.05, 0.15, and 0.25 at Re = 47. The difference between negative and positive shear stress contours are indicated for different Deborah numbers. While this difference is 1.9 unit length in the case of De = 0.05, it reduces to zero for De = 0.25.

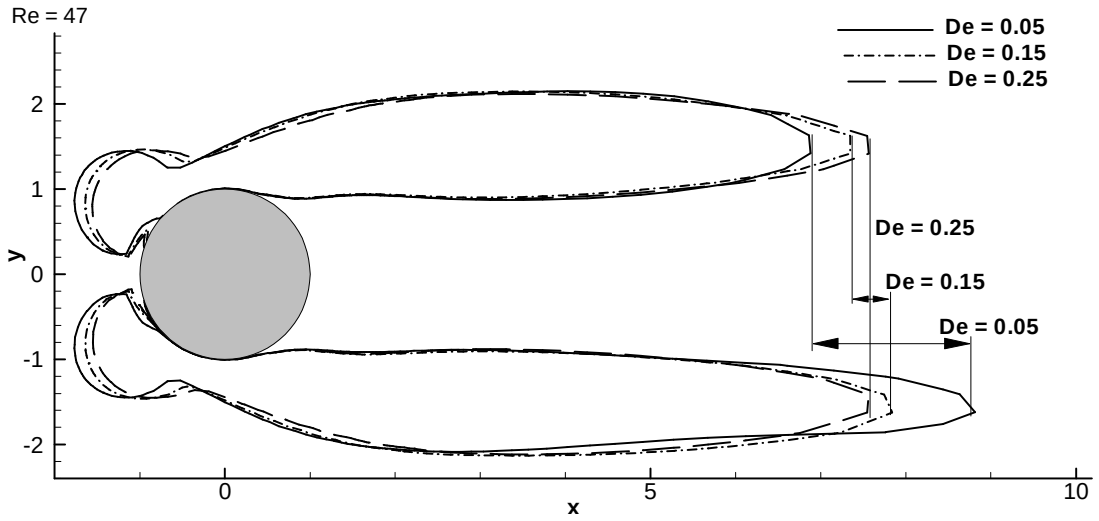


Figure 4.10 Extra-shear stress contour at Re = 47 for De = 0.05, 0.15, and 0.25 with indication of asymmetry reduction

To review the magnitudes of the extra-shear stress, Figure 4.11 and Figure 4.12 provide these magnitudes for all sections defined in Figure 4.2 for a flow having Re = 47 with various Deborah numbers. From these curves, it is noticed that the effect of the increased Deborah number manifests itself in relaxing the fluctuations on section S2. On Figure 4.11 b, the magnitude of the negative shear stress peak is augmented by 8% for a Deborah number increase from 0.05 to 0.25. At the streamline SLu, the shear stress peak increases by 27% when the Deborah number increases from 0.05 to 0.25.

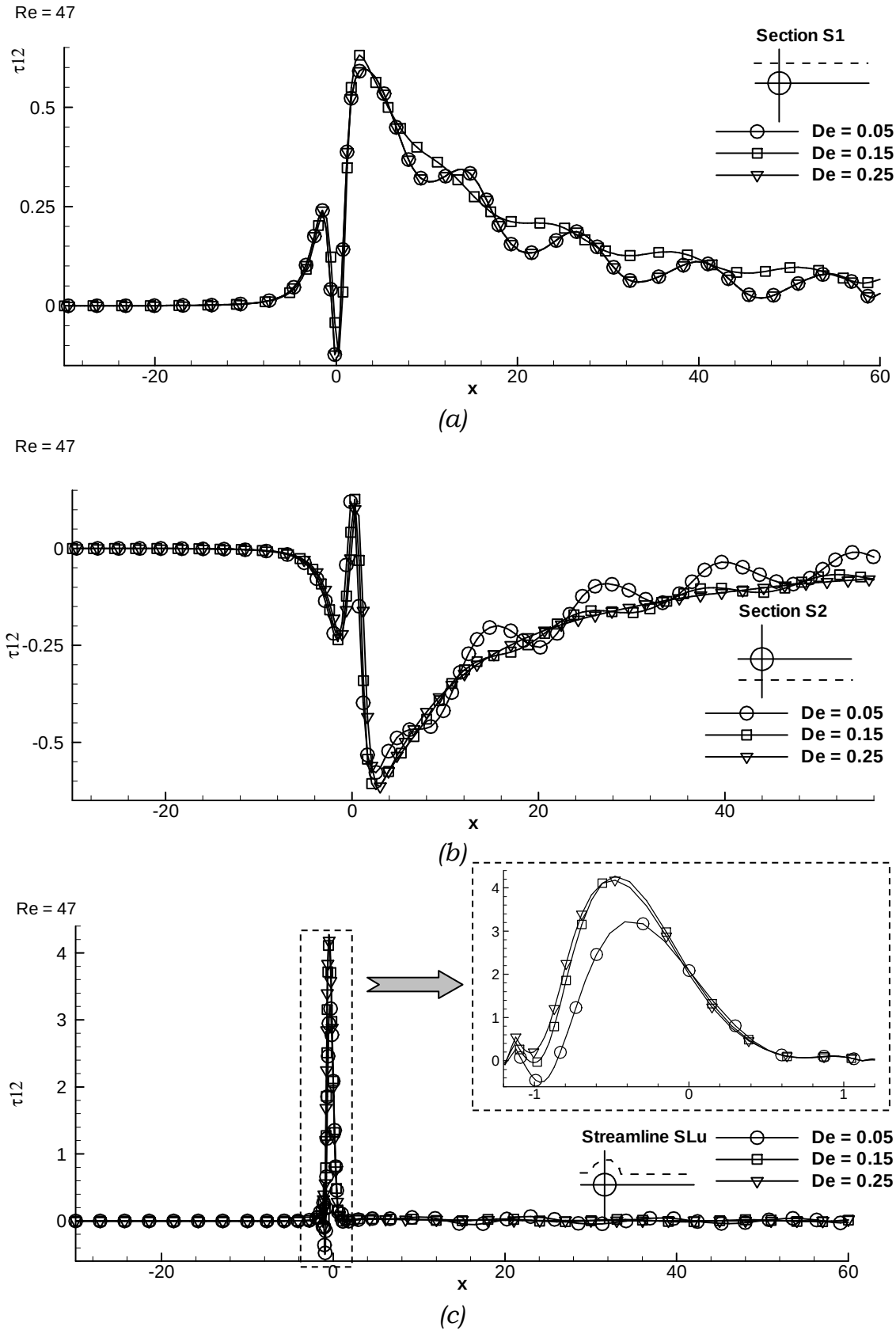
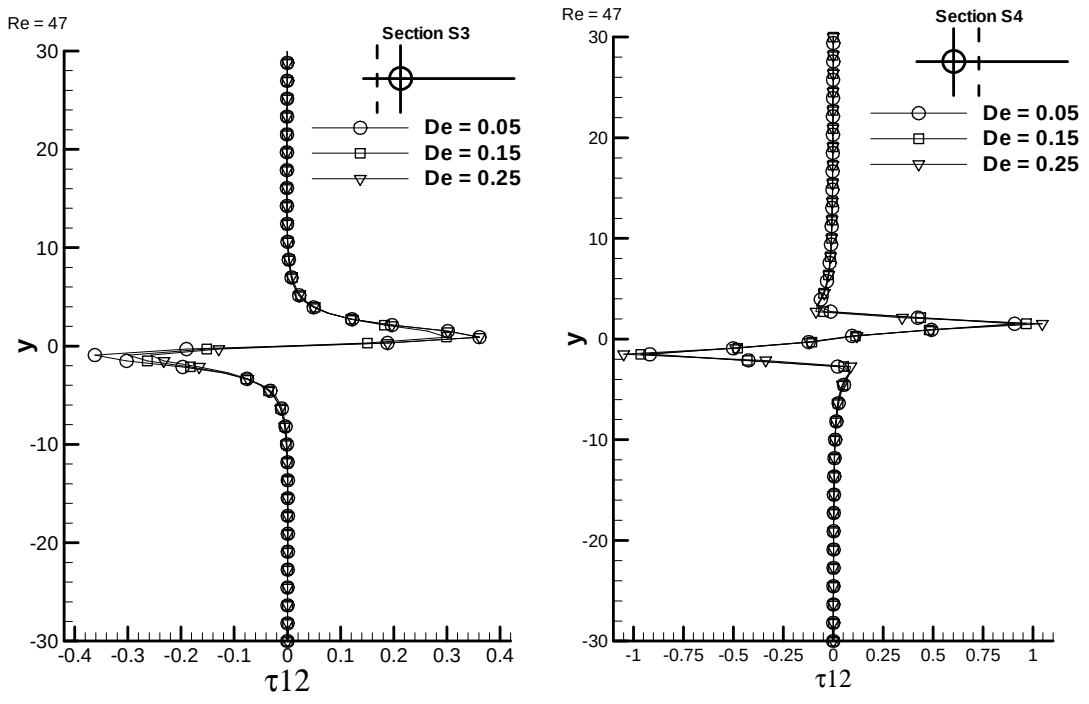


Figure 4.11 Extra-shear stress magnitudes for Re = 47 along: (a) section S1, (b) section S2 and (c) streamline SLu



(a) *(b)*

Figure 4.12 Extra-shear stress magnitudes for Re = 47 at: (a) section S3 and (b) section S4

It should be noted here that in the case of the bounded cylinder the boundary conditions impose zero-velocity at the boundaries located at 2*R*. From Figure 4.12, it is remarked that the largest magnitude of shear stress is found near the location 2*R* leading to differences between the confined and non-confined cylinder cases.

4.3.2 Normal stress difference

For a Newtonian fluid in a laminar shear flow, the normal stresses are always equal. Because of the viscoelastic properties, the normal stresses are different and two normal stress differences are established to express the change of normal stresses. For two-dimensional flows, only the first normal stress difference ($N_1 = \sigma_{11} - \sigma_{22}$) is relevant. Both the normal stress differences and the shear viscosity are called the viscometric functions characterizing the material viscometric properties of the fluid.

In this section, the effects of Reynolds and Deborah numbers on the normal stress difference are presented. The calculated values of normal stress difference are scaled as:

$$N_1 = \overline{N}_1 \frac{\eta_0 U_0}{R} \qquad 4.2$$

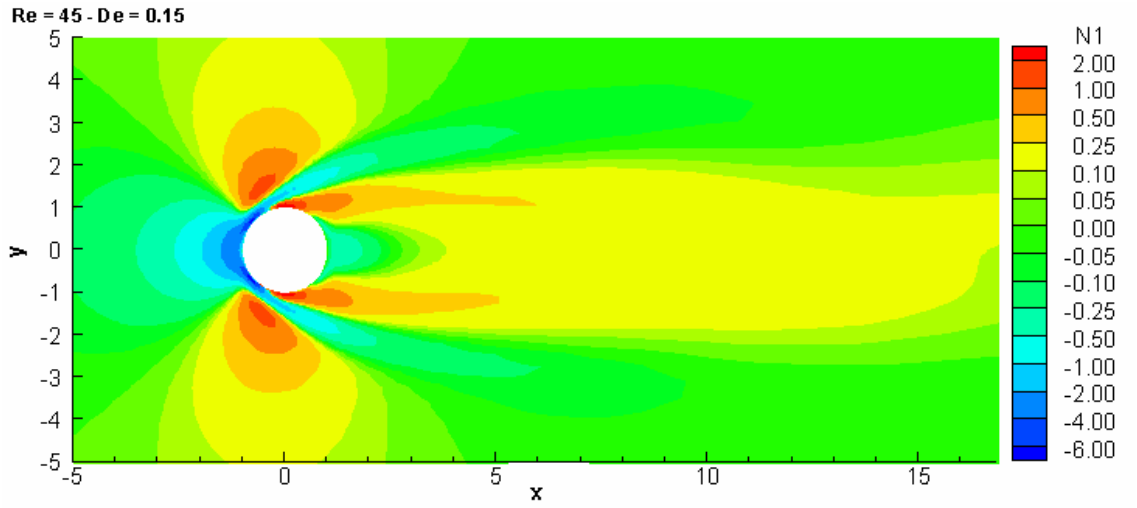
where $\overline{N}_1$ is the dimensional value of the first normal stress difference, η_0 is the total fluid viscosity, and U_0 is the far entry free stream velocity.

4.3.2.a Influence of Reynolds number on the normal stress difference

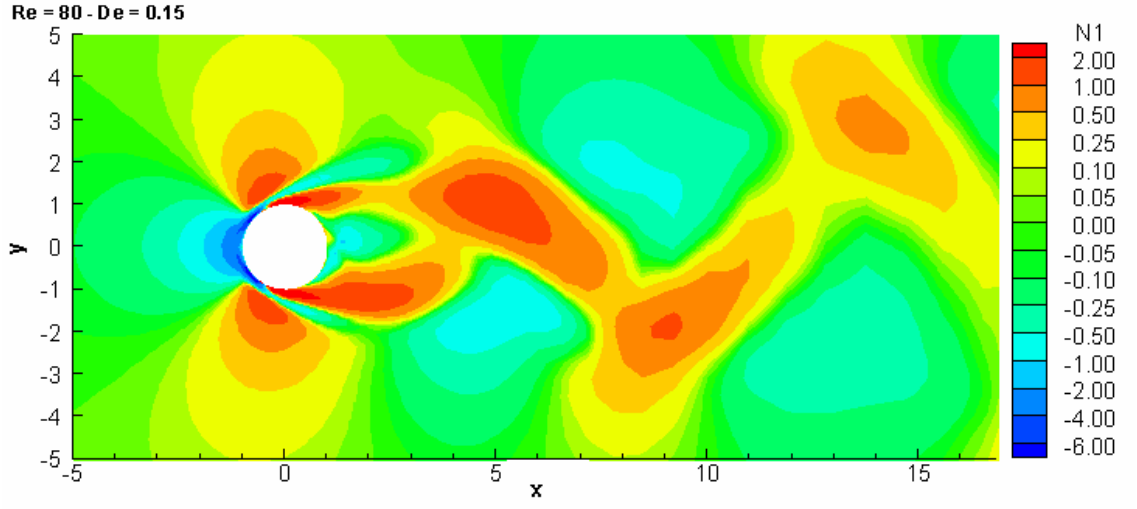
The increase of the Reynolds number leads to the onset of the von Karman street instability. Normally, the initiation of flow instabilities brings up strong perturbations in the flow properties. The normal stress difference is not expected to deviate from this rule. As the Reynolds number increases, the viscous forces decrease and the effect of the normal stresses becomes more obvious.

Figure 4.13 illustrates the change of the normal stress difference distribution around the cylinder for fluids at De = 0.15 and for Re = 45, 80, and 150, respectively. All these distributions show that the increase of the Reynolds number leads to increase of the positive normal stress difference. This indicates that the normal stresses in the flow direction are growing faster than the stresses in the lateral direction. This shows the extensional effects of the viscoelasticity.

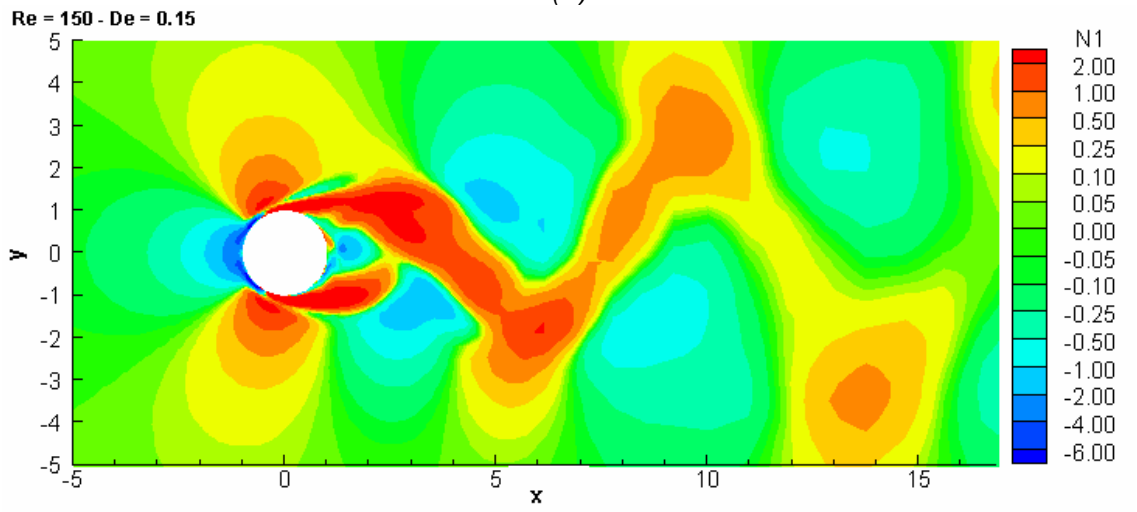
Concerning the steady vortex regime, Figure 4.14 shows the zero-normal stress difference for Re = 40 and 45 and fixed Deborah number De =0.15. This figure illustrates that the contours appear to be regular and symmetric. With the increase of Reynolds number, the contour is simply extended with no deformation.



(a)



(b)



(c)

Figure 4.13 First normal stress difference distribution for De = 0.15 at: (a) Re = 45, (b) Re = 80 and (c) Re = 150

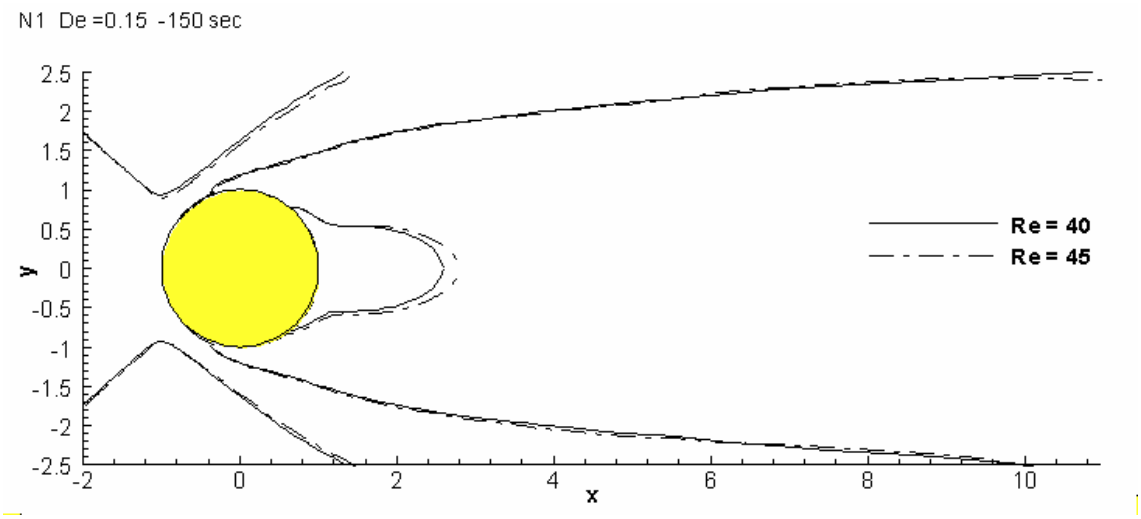


Figure 4.14 Zero-normal stress difference contour for De = 0.15 at Re = 40 and 45

For the regime of laminar vortex shedding, the changes in the normal stresses caused by the increase of Reynolds number are complex. In order to demonstrate this, Figure 4.15 shows the zero-normal stress difference contour for De = 0.15 at Re = 80, 100, and 125. This figure depicts the strong changes with fluid viscosity. Oppositely to the steady regime, the increase of the Reynolds number leads to shrinkage of the contours. Also, it is noted that the contours are deformed especially around the cylinder. This illustrates the complexity of the interaction of flow instability with viscoelasticity.

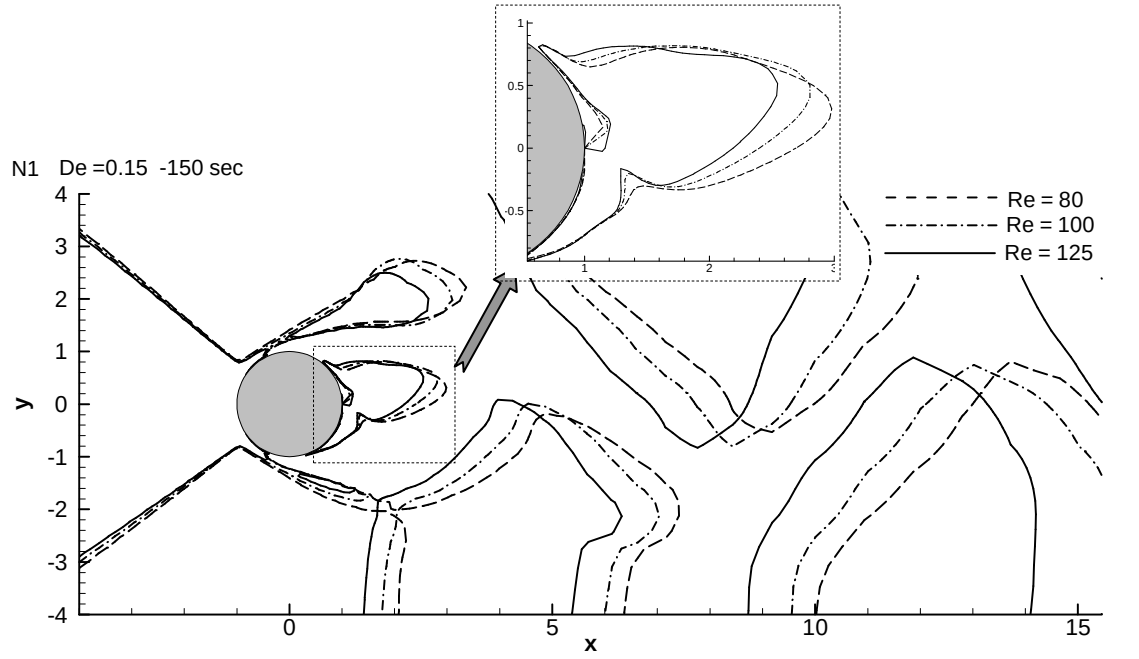
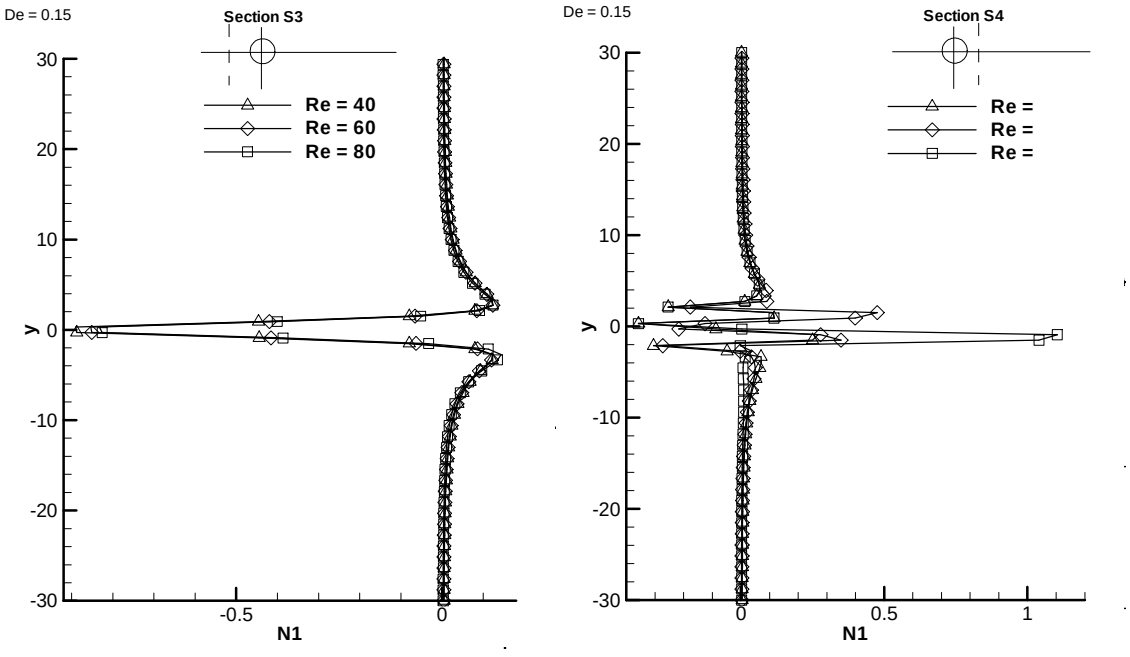


Figure 4.15 Zero-normal stress difference contour for De = 0.15 at Re = 80, 100 and 125

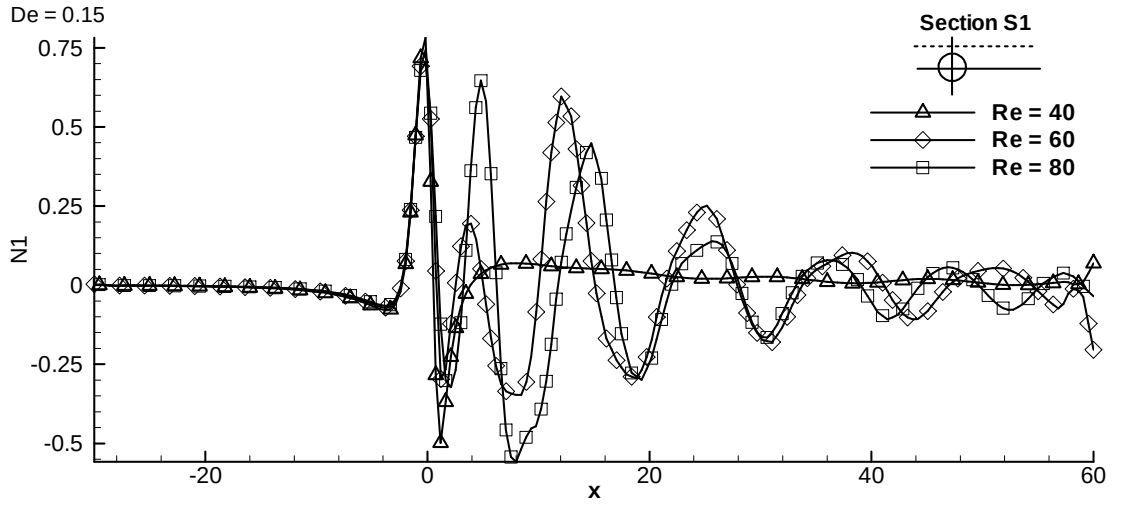
The magnitudes of the first normal stress difference at De = 0.15 are plotted on Figure 4.16 and Figure 4.17 for the sections S3, S4, S1, and S2, and streamline SLu, respectively. From these figures, on can observe that:

- Along the x-axis, the maximum magnitudes are found with on the cylinder surface. The maximum is increased by about 23% when the Reynolds number increases from 40 to 80.
- The values and fluctuations on the lower section S2 are stronger than their corresponding on section S1. The maximum value occurs on the lower section at a distance of about 10*R*. This maximum increases by about 80% when the Reynolds number increases from 60 to 80.
- On the two cross-sections, the upstream side does not largely affected by the Reynolds number as the maximum value decreases by about 2% keeping the symmetry around the x-axis. For the downstream side, the changes are very remarkable in behaviour and magnitudes as the maximum magnitude increases about 135% for the increase of the Reynolds number from 40 to 60. One should bear in mind the onset of the flow instability at Re = 47.

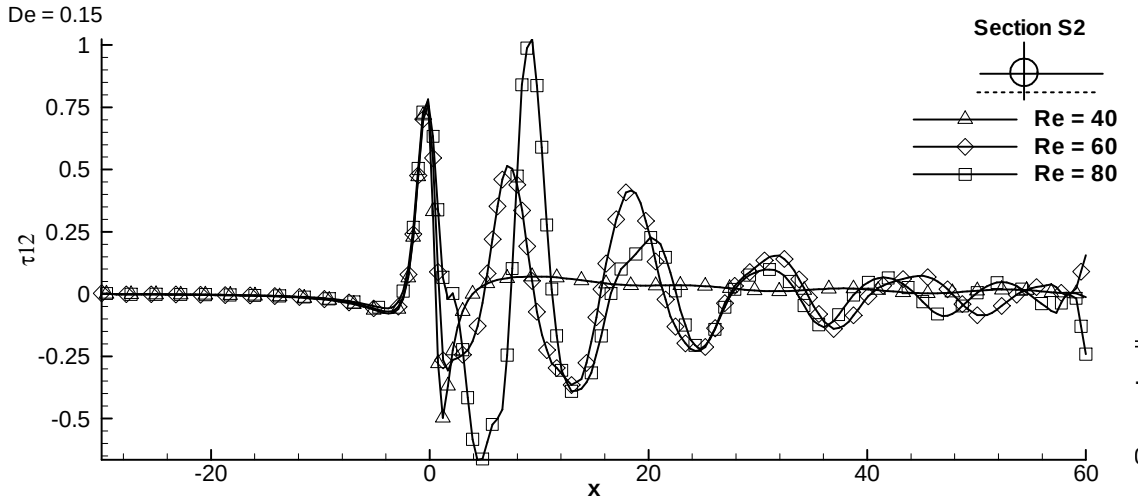


(a) *(b)*

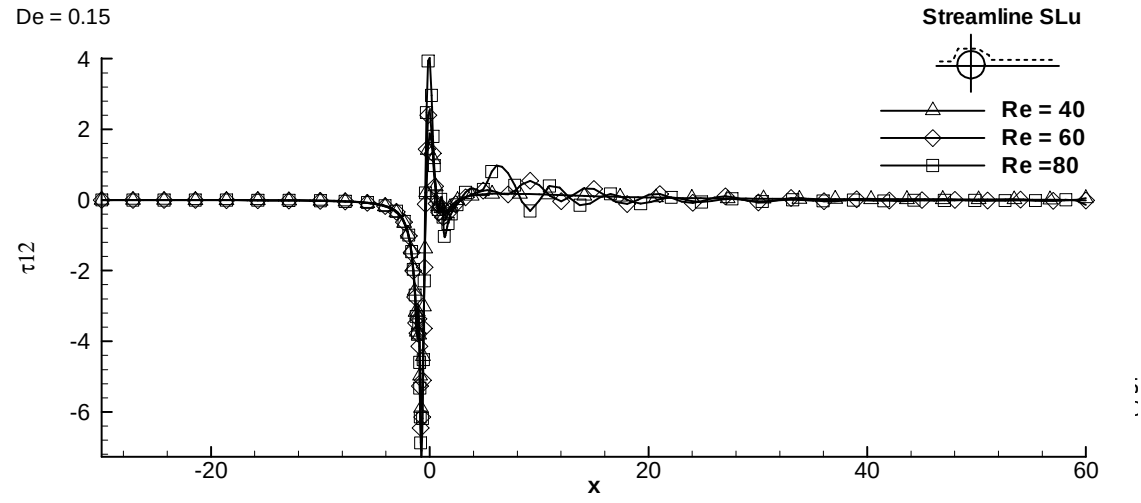
Figure 4.16 Normal stress difference magnitudes for De = 0.15 at: (a) section S3 and (b) section S4.



(a)



(b)



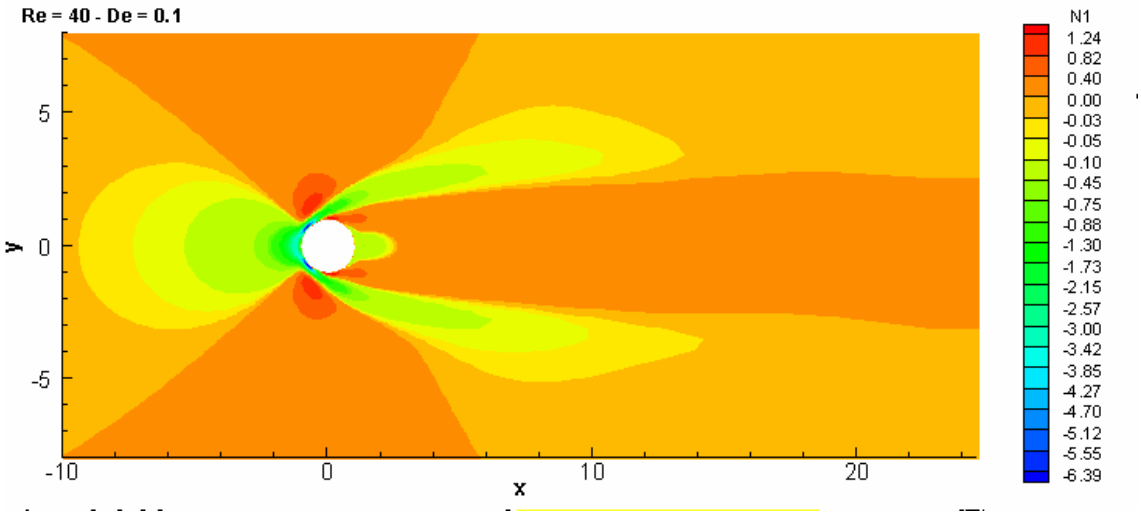
(c)

Figure 4.17 Normal stress difference magnitudes for De = 0.15 at: (a) section S1, (b) section S2, and (c) streamline SLu.

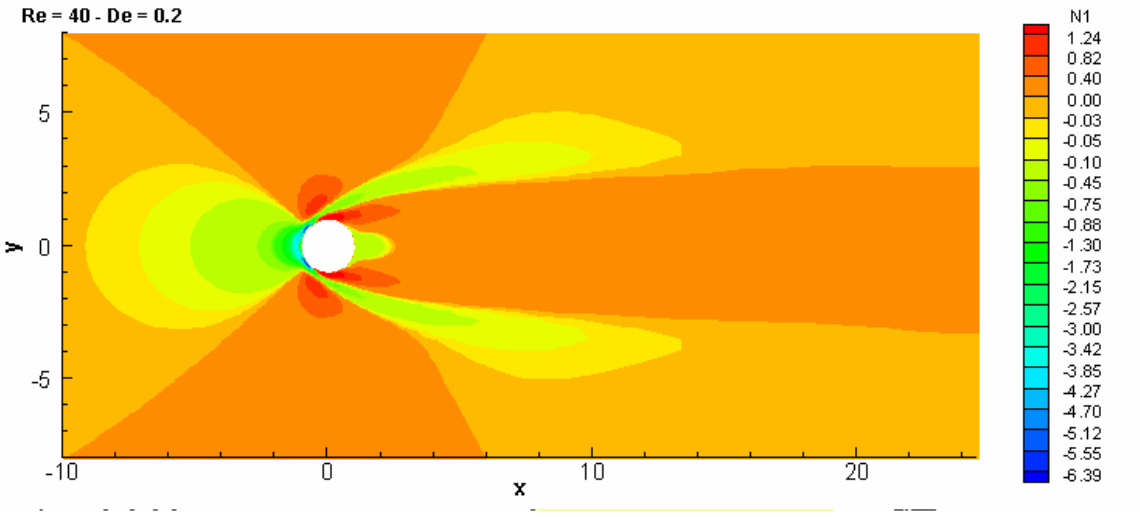
4.3.2.b Influence of Deborah number on the normal stress difference

As shown for the shear stress, the increased Deborah number suppresses the flow fluctuations while restoring the flow stability. In order to demonstrate this effect on the normal stress difference, we consider the case of Re = 40 ($Re < Re_{cr}$) and the flow at Re = 47 ($Re = Re_{cr}$).

For the steady vortex regime, Figure 4.18 shows the normal stress difference for Re= 40 at De = 0.1 and 0.2, respectively. On this figure, we notice a small reduction of normal stress difference on both sides of the cylinder with increasing Deborah number.



(a)



(b)

Figure 4.18 Normal stress difference distribution for Re = 40 at: (a) De = 0.1 and (b) De = 0.2

The zero-normal stress difference contour line is plotted on Figure 4.19 for Re = 40 at De = 0.05, 0.1, 0.15, and 0.2. Downstream of the cylinder, these contours show a tendency to shrink the negative zones of the normal stress difference which means the increase of the first normal stress. The downstream zero-contour length decreases by about 8% when Deborah number increases from 0.1 to 0.2. On both sides of the cylinder, the contours extend and their width increases.

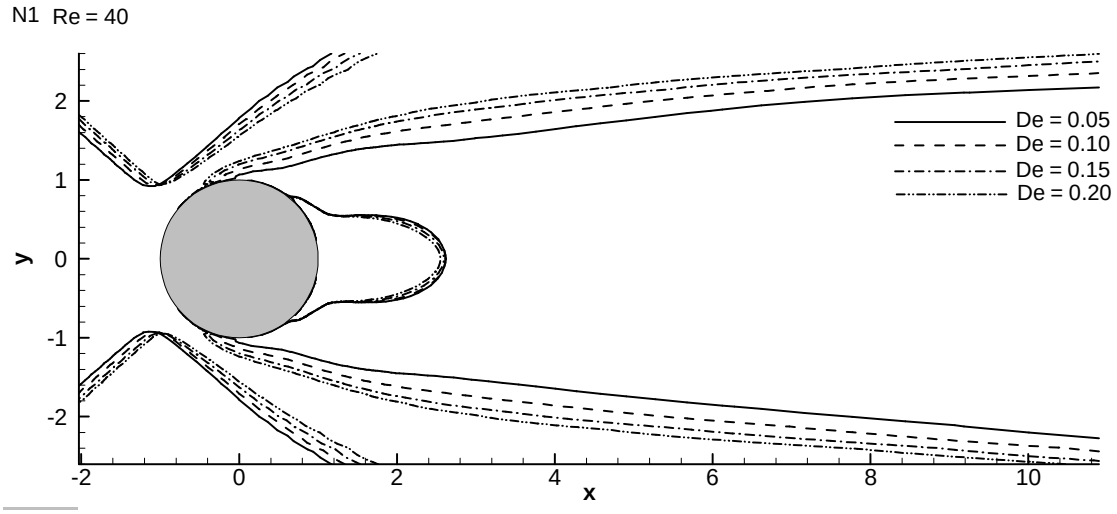
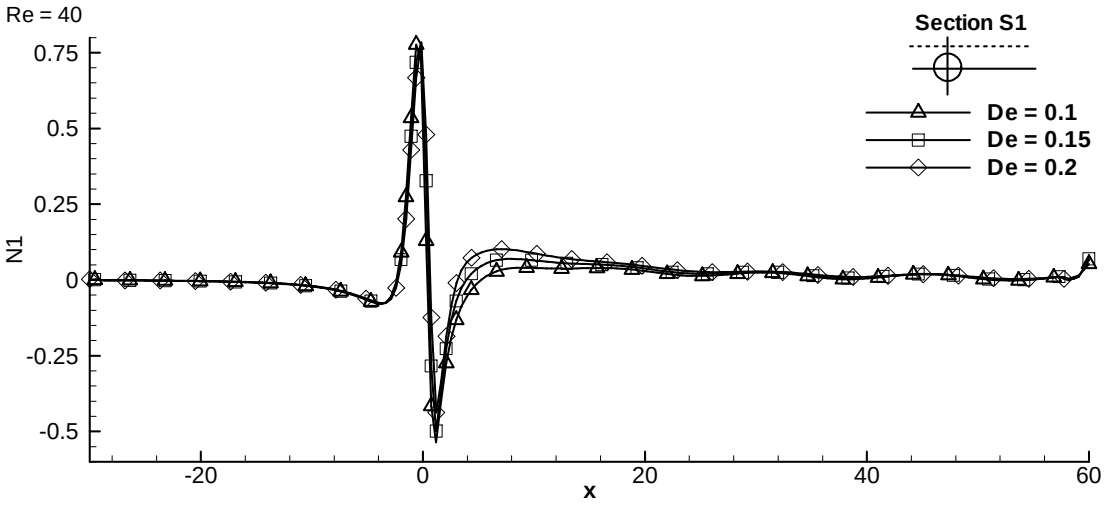
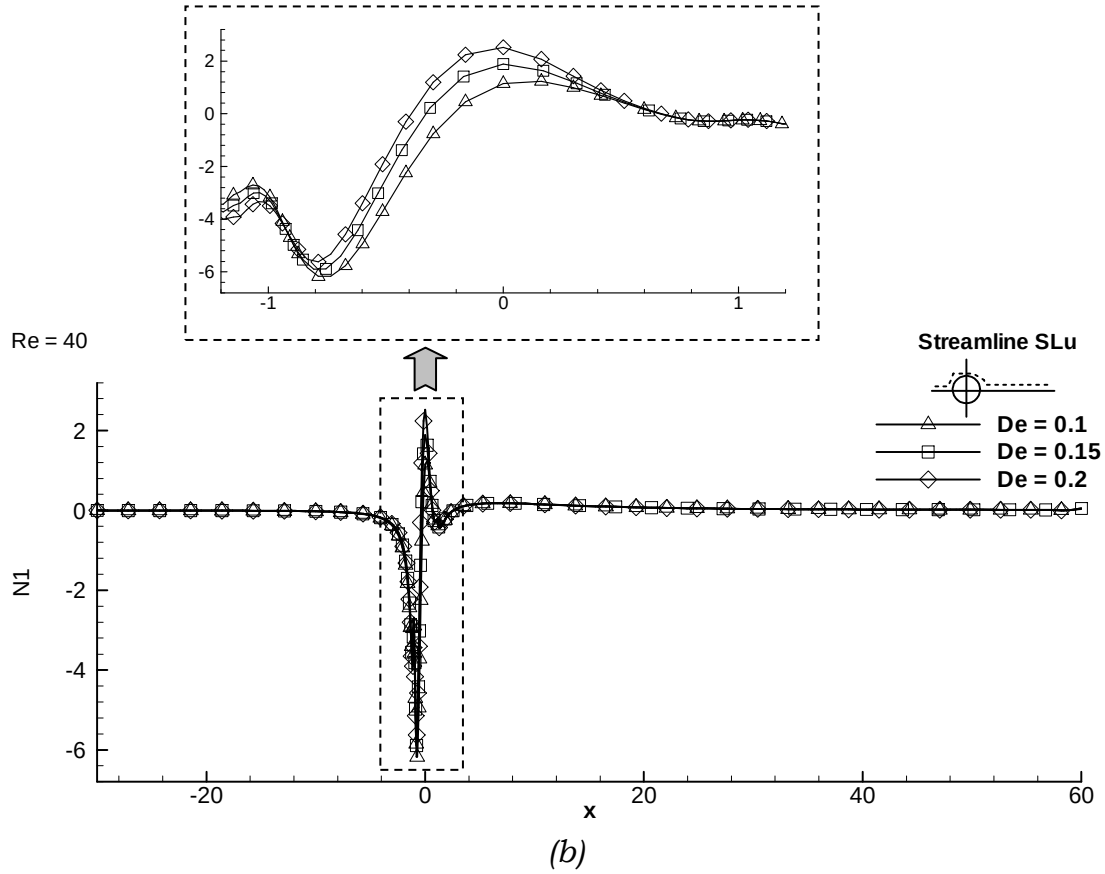


Figure 4.19 Zero-normal stress difference contour for Re = 40

The magnitudes of the normal stress difference are drawn on Figure 4.20 for Re =40 at De = 0.1, 0.15, and 0.2 along section S1 and along streamline SLu. Through these curves, we can see that the influence of the fluid elasticity manifest itself in a zone which is extended almost to 25 *R* downstream of the cylinder. Also, this influence changes the magnitudes of normal stress difference within a narrow range of about 5% for Deborah number increase of 0.1. On the x-axis and in the neighbourhood of the cylinder, the fluid elasticity shifts the range of normal stress difference by about 3% towards the positive values.



(a)



(b)

Figure 4.20 Normal stress difference values for Re = 40 along: (a) section S1 and (b) streamline SLu

For the regime of $\mathrm{Re} \geq \mathrm{Re}_{cr}$, Figure 4.21 represents the first normal stress difference for the critical Reynolds number (Re = 47) at De = 0.05, 0.15, and 0.25, respectively.

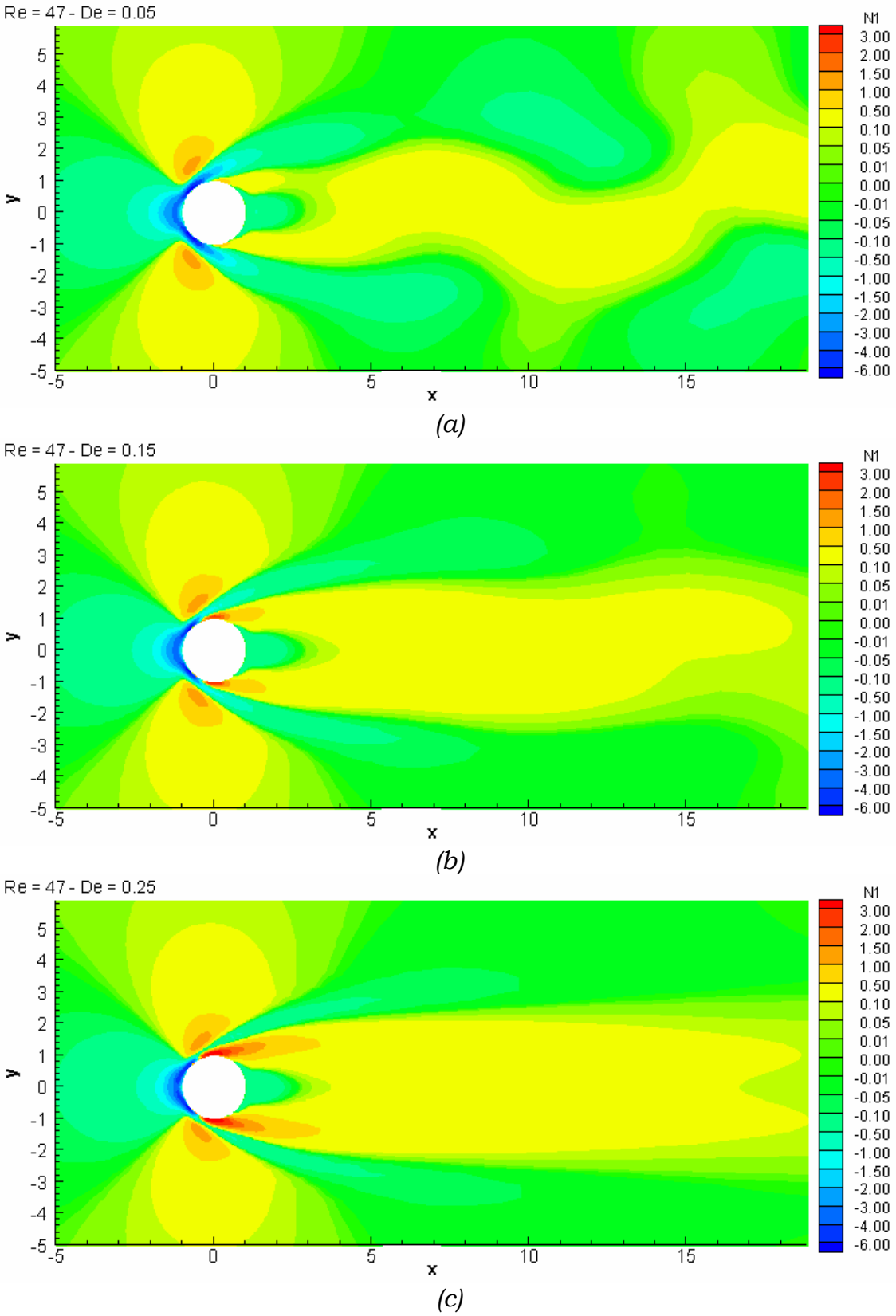


Figure 4.21 Normal stress difference distribution for Re = 47 at: (a) De = 0.05, (b) De = 0.15 and (c) De = 0.25

Figure 4.22 demonstrates the zero-normal stress contour line for Re = 47 and De=0.05, 0.15, and 0.25. This figure illustrates the reduction of the instability with increased Deborah number. Also, one can notice the increase of the stresses in the flow direction (extensional stresses) over the lateral stresses causing the extension of the instability zones and the reduction of their width.

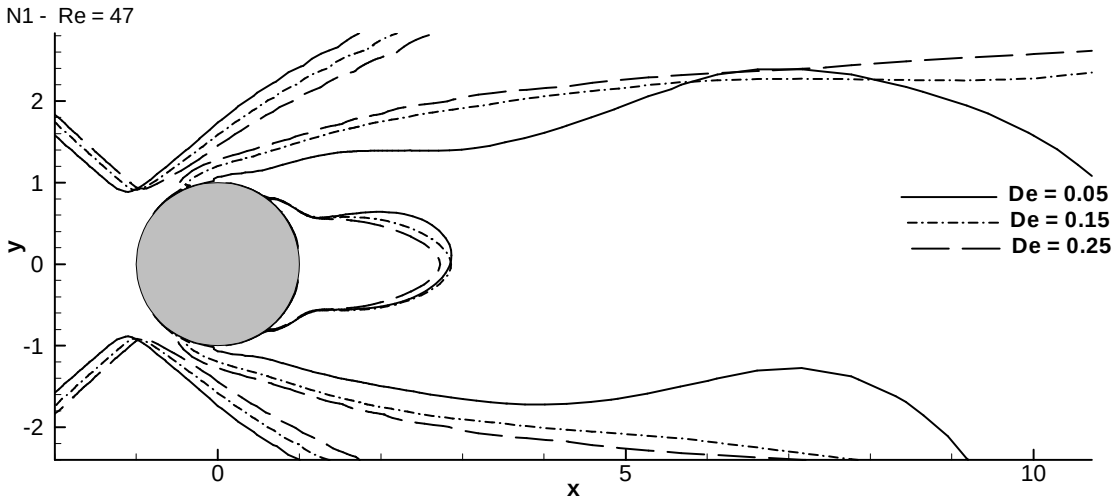
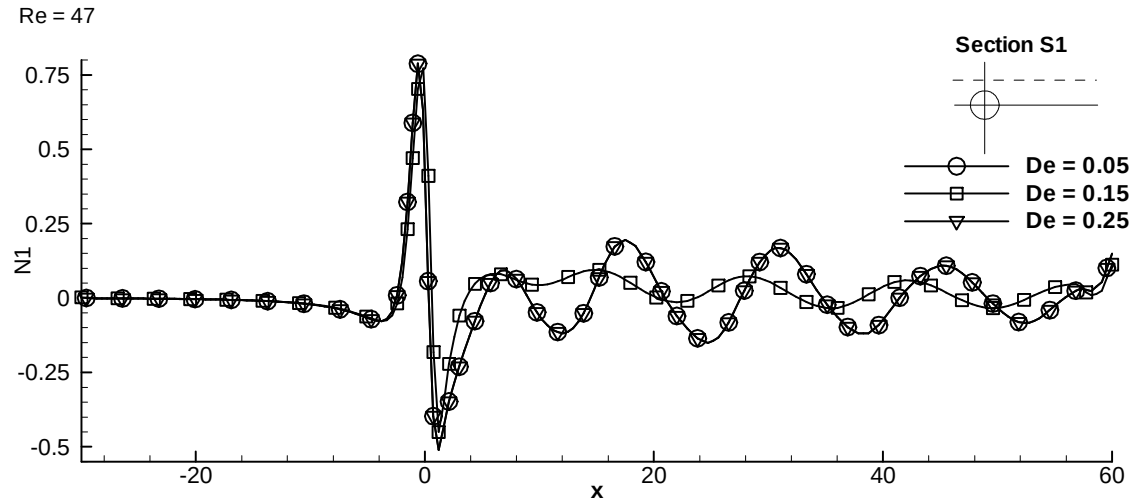
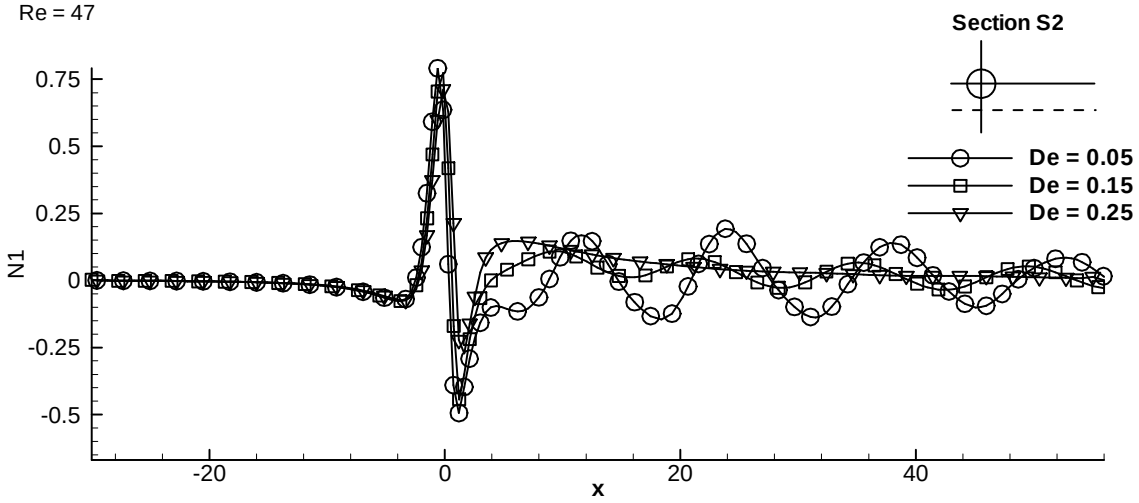


Figure 4.22 Zero-normal stress difference contour for Re = 47 at De = 0.05, 0.15 and 0.25

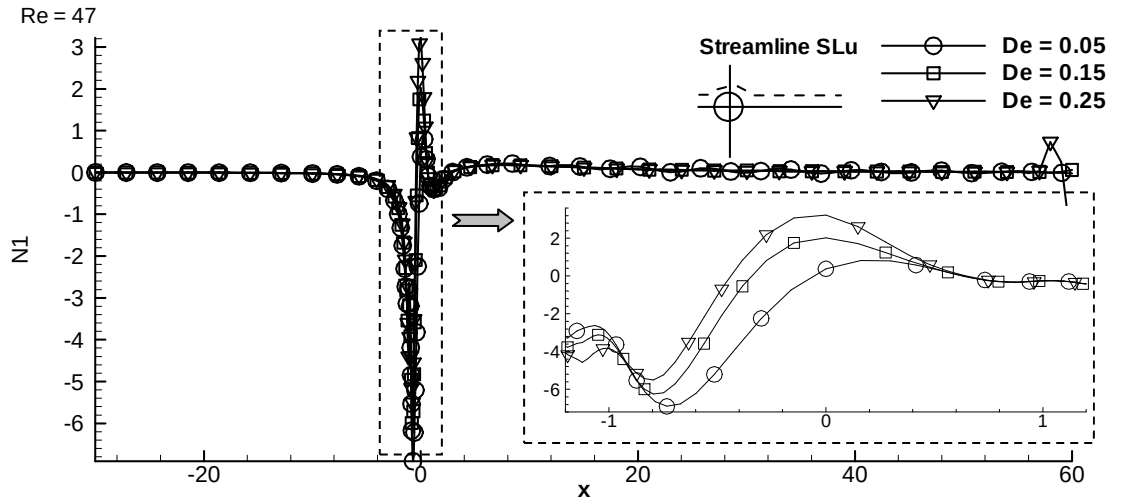
The magnitudes of the normal stress difference, shown on Figure 4.23, are drawn for Re = 47 with different Deborah number along sections S1 and S2, and along streamline SLu, respectively. The trend of these values resembles the same trend as the values of extra-shear stress. The effect of fluid elasticity is more obvious on the lower section S2. Fluid elasticity suppresses the fluctuations on the x-axis by about 7% but shifts the range to higher values. Along upper section S1, the values for De = 0.05 coincide with those for De = 0.25 while for section S2, there is a pronounced difference between the two Deborah numbers.



(a)



(b)



(c)

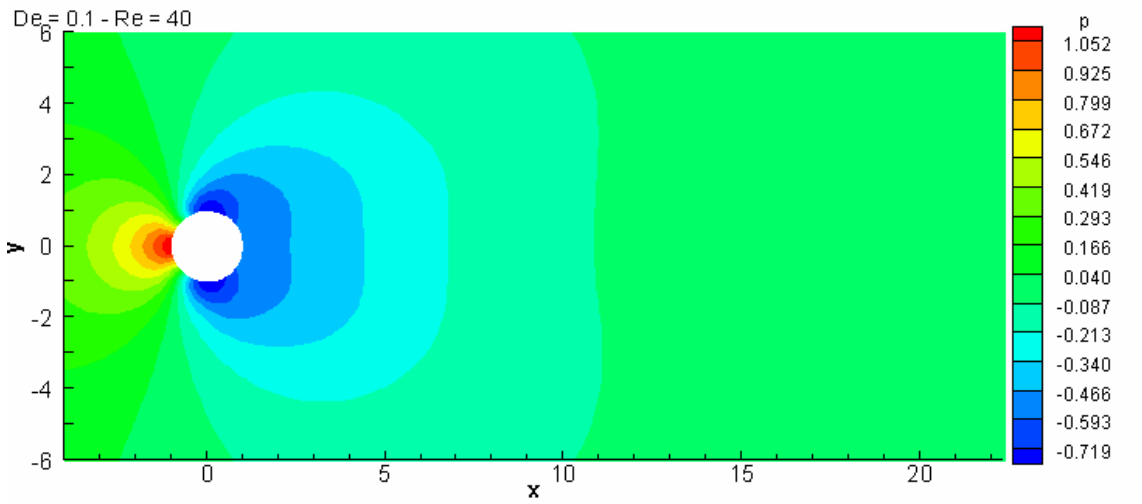
Figure 4.23 Normal stress difference magnitudes for Re = 47 along: (a) section S1, (b) section S2, and (c) streamline SLu

4.3.3 Pressure distribution

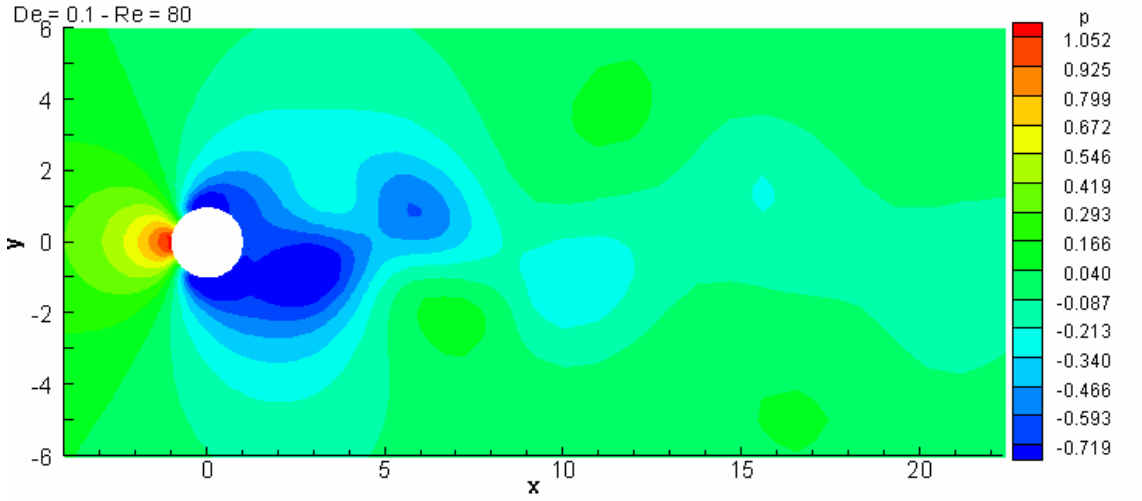
In the literature, the reduction of the drag force in the presence of viscoelasticity is strongly related to the change of the pressure distribution around the cylinder. The proposed mechanism linking the pressure distribution and the drag reduction assumes that the interaction between the shear layer and the recirculating flow decreases with the elasticity. As a result, the entrainment of fluid from the formation region is reduced. Consequently the base pressure has to increase to compensate for the reduced shear stresses in order to maintain the force equilibrium. The increase of pressure behind the cylinder decreases the pressure drop across the cylinder. In this section, the pressure distribution is introduced revealing its change with viscoelasticity.

4.3.3.a Influence of Reynolds number on the pressure

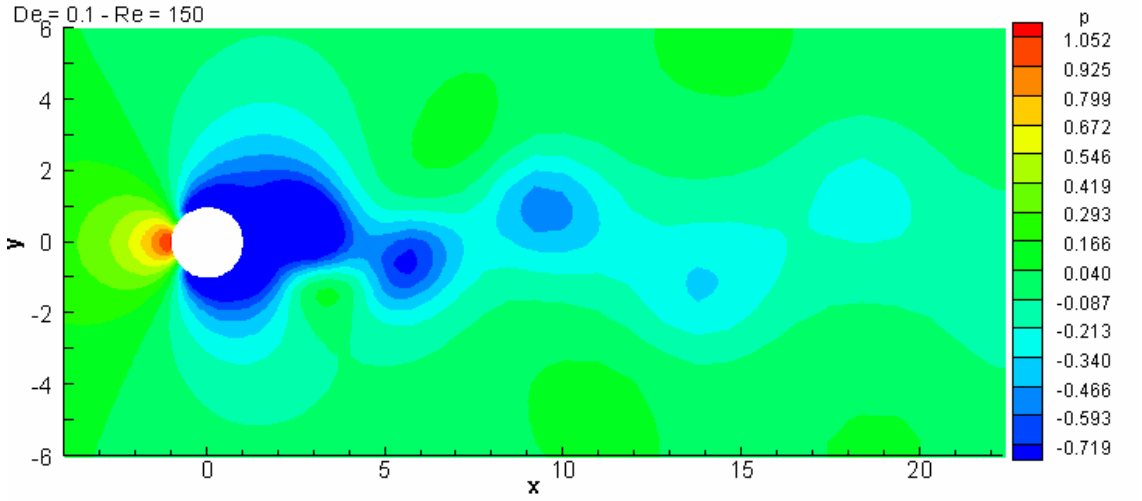
We consider here the change of the pressure distribution with the increase of the Reynolds number. The normalized values of pressure $P_n = 2P/U_0^2$ are used to evaluate the viscoelastic effects on flow pressure. Figure 4.24 illustrates the pressure distribution of the flow with Re = 40, Re = 80, and Re = 150 at De=0.1. In this figure, it can be observed that while the positive pressure area (upstream) is very lightly influenced, the negative pressure area (downstream) is strongly influenced with the growing Reynolds number. This relative difference leads to greater pressure drop across the cylinder. Also, it is remarked the obvious effect of the flow instability on the pressure distribution as we pass from Re = 40 (Figure 4.24 a) to Re = 80 (Figure 4.24 b). Further increase of the Reynolds number increases the negative pressure magnitudes downstream the cylinder.



(a)



(b)



(c)

Figure 4.24 Pressure distribution for viscoelastic fluid at De=0.1 for: (a) Re = 40, (b) Re = 60, and (c) Re = 100

To better understand this effect, three pressure contour lines are drawn in Figure 4.25 and Figure 4.26. These contour levels are the zero-pressure level, a positive pressure level, and the corresponding negative pressure level. In Figure 4.25, the pressure contours are drawn for Re = 35, 40, and 45 ($\mathrm{Re} < \mathrm{Re}_{cr}$), while Figure 4.26 represents the same contours for Re = 80, 100, and 125 ($\mathrm{Re} > \mathrm{Re}_{cr}$). An examination of these figures allows extracting the following remarks:

- For both regimes, the positive-pressure contour keeps its uniformity and it shrinks with increasing the Reynolds number.
- For $\mathrm{Re} < \mathrm{Re}_{cr}$, the negative-pressure contour shrinks while keeping its uniformity.
- For $\mathrm{Re} > \mathrm{Re}_{cr}$, the negative-pressure contour loses its uniformity and approaches the cylinder.
- In general, while the positive pressure area shrinks with increasing Reynolds number, the negative-pressure area extends which means increased pressure drop.
- For $\mathrm{Re} > \mathrm{Re}_{cr}$, there is an asymmetry about the x-axis which is clear from the zero-pressure line. This is a consequence of the developed normal stresses due to the fluid elasticity (see section 4.3.1).

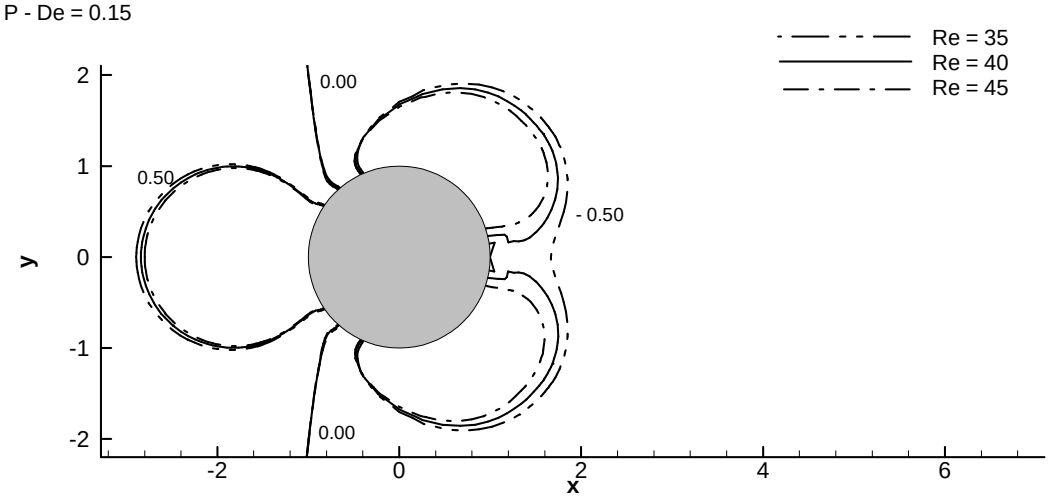


Figure 4.25 Pressure contours for viscoelastic fluid at De = 0.1 for Re = 35, 40, and 45.

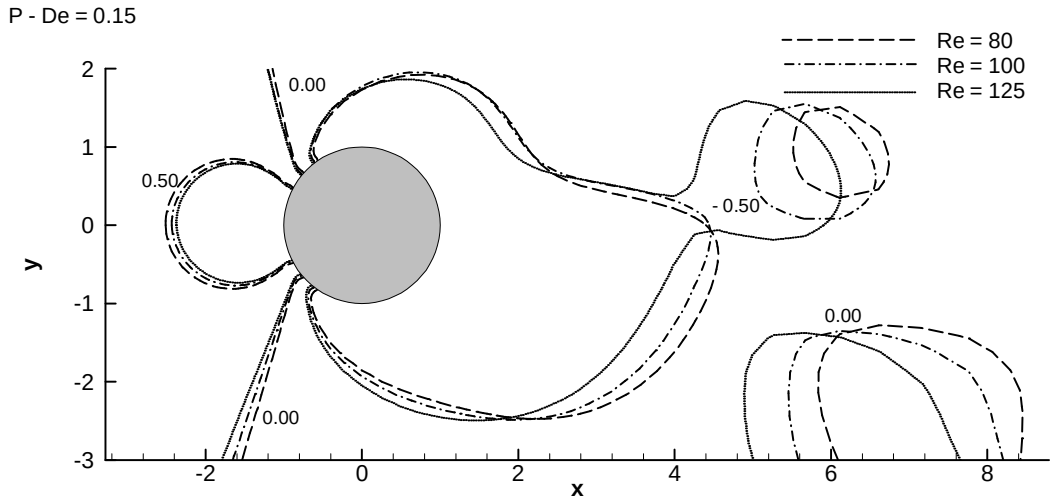


Figure 4.26 Pressure contours for viscoelastic fluid having De = 0.1 for Re = 80, 100, and 125

To quantify the present results, the normalized magnitudes of pressure are plotted along the sections S3, S4, S1, and S2 and the upper streamline SLu, respectively, for Reynolds numbers Re= 40, 60, and 80 for De = 0.1 as shown in Figure 4.28 and Figure 4.29.

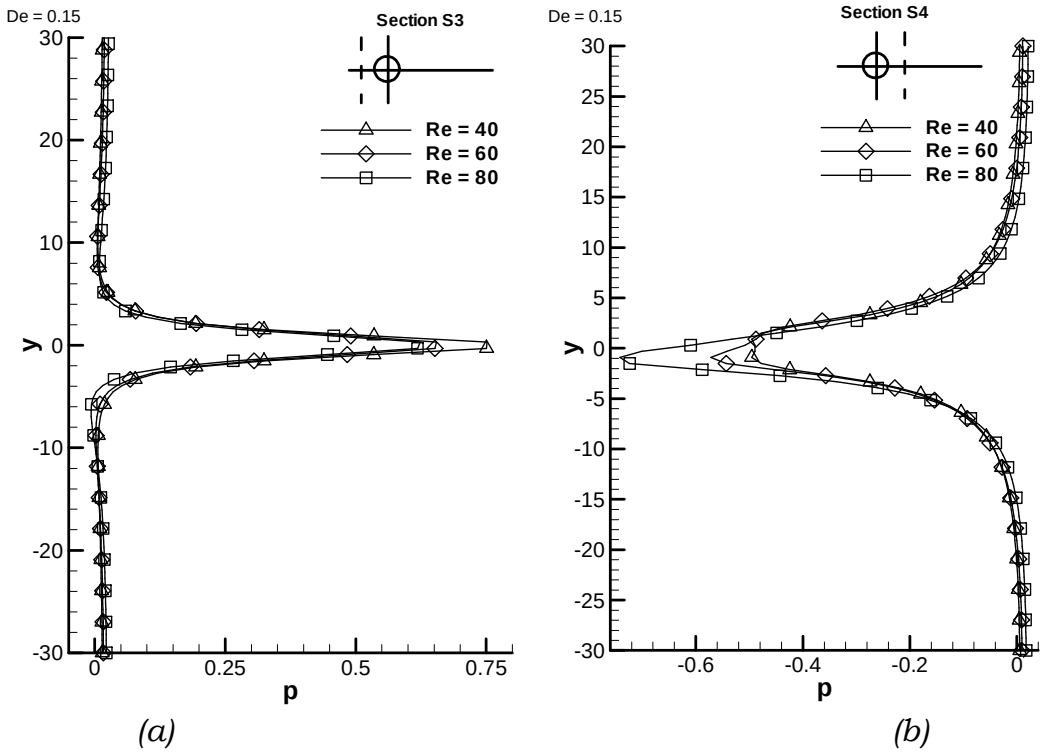
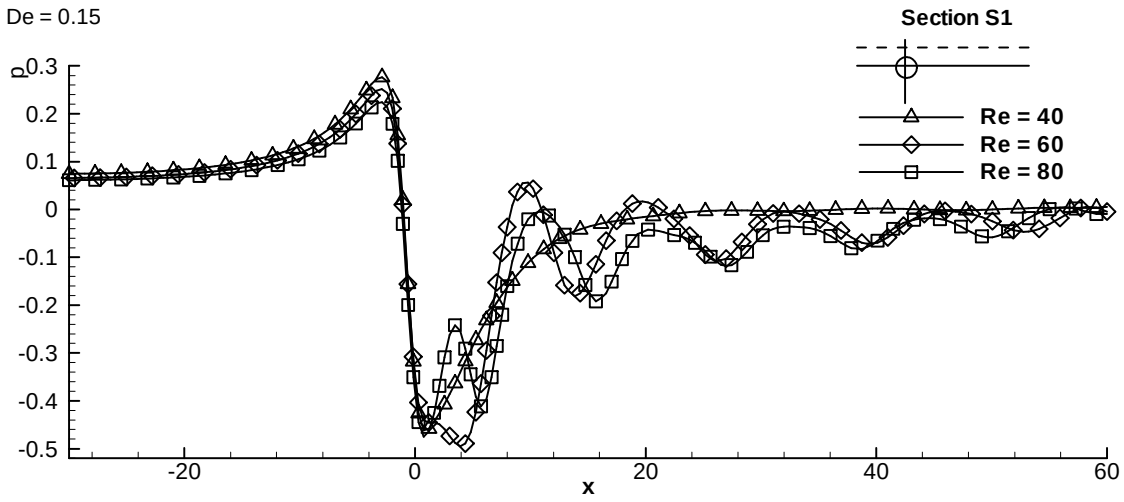
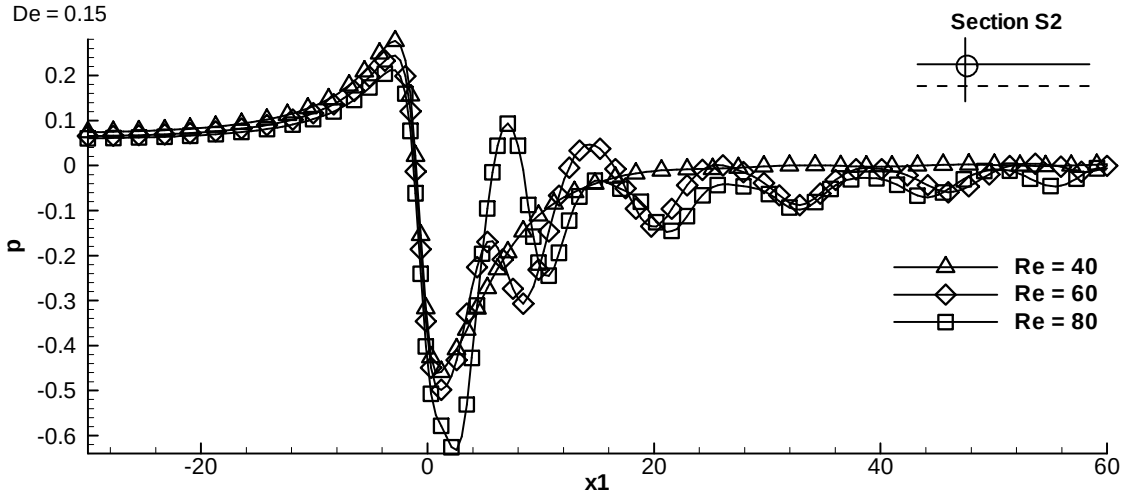


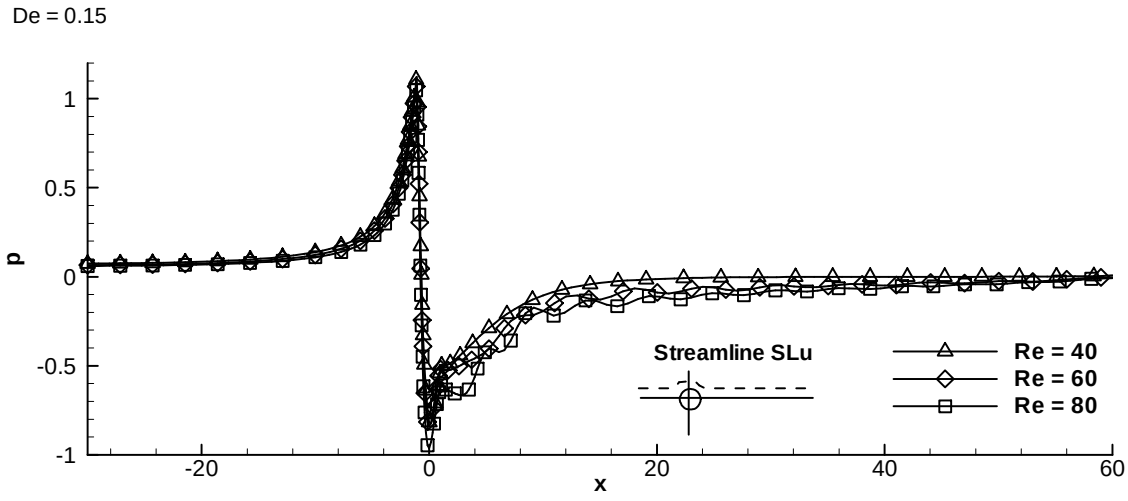
Figure 4.27 Magnitudes of pressure for De =0.1 and different Re at: (a) section S3 and (b) section S4



(a)



(b)



(c)

Figure 4.28 Pressure for De =0.1 and different Re along: (a) section S1, (b) section S2 and (c) streamline SLu

Based on Figure 4.28 and Figure 4.29, it seems clear that:

- Increasing the Reynolds number mainly affects the wake donstream the cylinder (negative pressure values).
- From section S3, the reduction of the fluid viscosity causes some negative pressure values at the lower upstream cylinder side which assists the change of lift force.
- From section S4, the maximum value of negative-pressure increases with the Reynolds number (22% for Reynolds number increase from 40 to 60 and 100% for Reynolds number increase from 40 to 100).
- For sections S1 and S2, the increasing Reynolds number causes pressure fluctuations which may reach positive-pressure values downstream the cylinder.
- The reduction of the positive-pressure range on the upstream side is (15~32%), while the change on the down stream side may reach 100% at $x \approx 8R$.
- Along the x-axis, the pressure drop is always maintained as the positive pressure upstream the cylinder attains a value of order 1.25, while the negative pressure downstream the cylinder does not exceed -1.

To spot the pressure drop across the cylinder, Figure 4.29 provides a look on the values of pressure over the cylinder surface. From this figure, we observe negative pressure values upstream the cylinder. These values increase with increased Reynolds numbers which can contribute to the drag reduction.

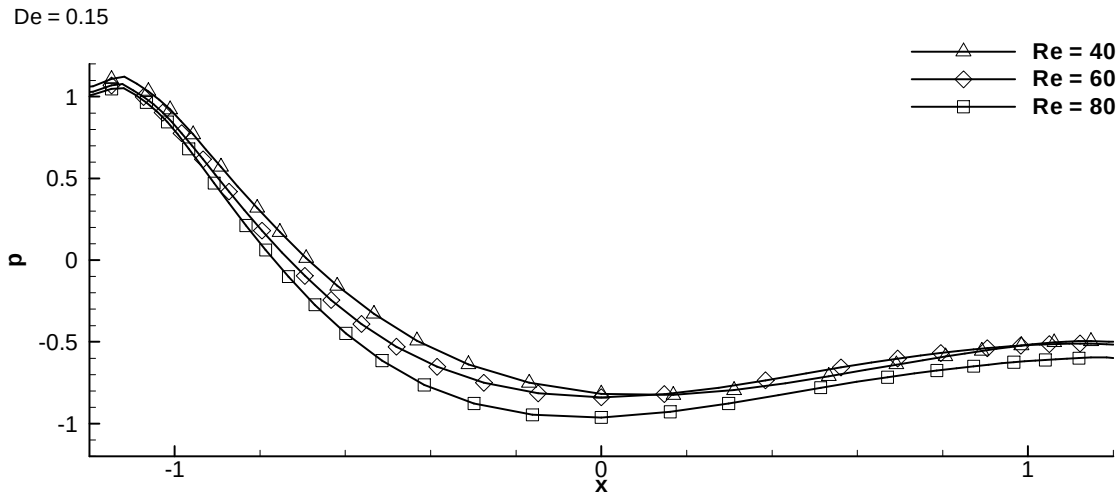


Figure 4.29 Normalized pressure over the cylinder surface for De=0.15 and different Reynolds numbers

A final remark can be drawn from the shift of the separation point towards the upstream with growing Reynolds number. This shift is demonstrated at Figure 4.30 by taking a zoomed view at the upper zero-pressure line. The separation point is defined by the wake angle θ_w measured from the upstream and increases in clockwise sense.

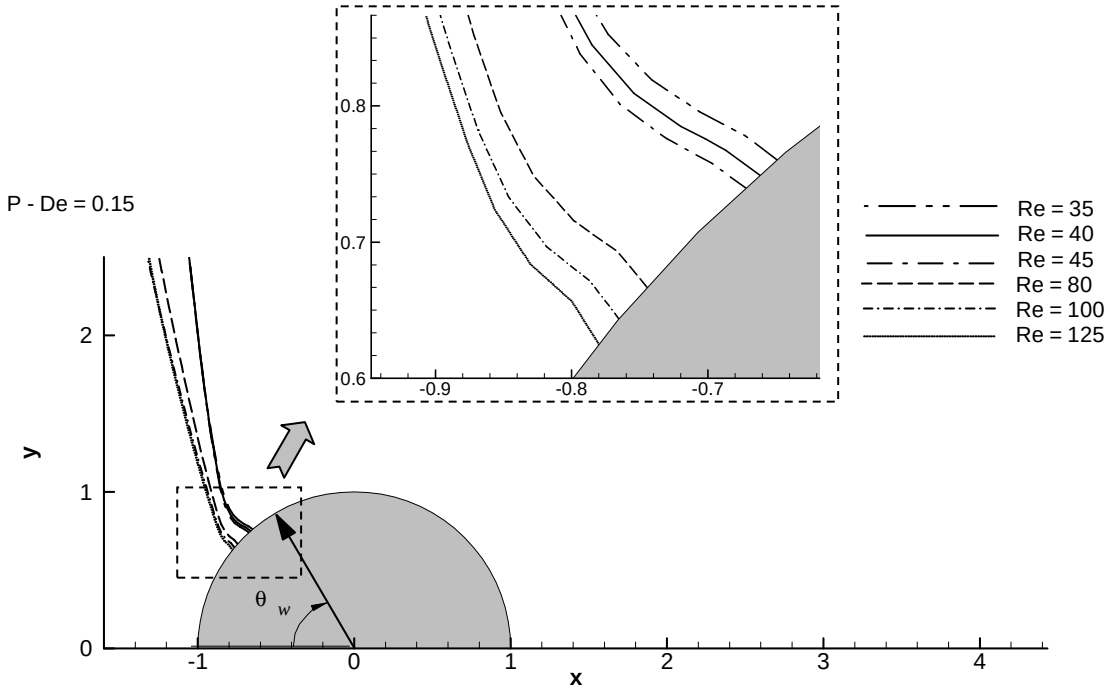


Figure 4.30 Shift of separation point with increased Reynolds number

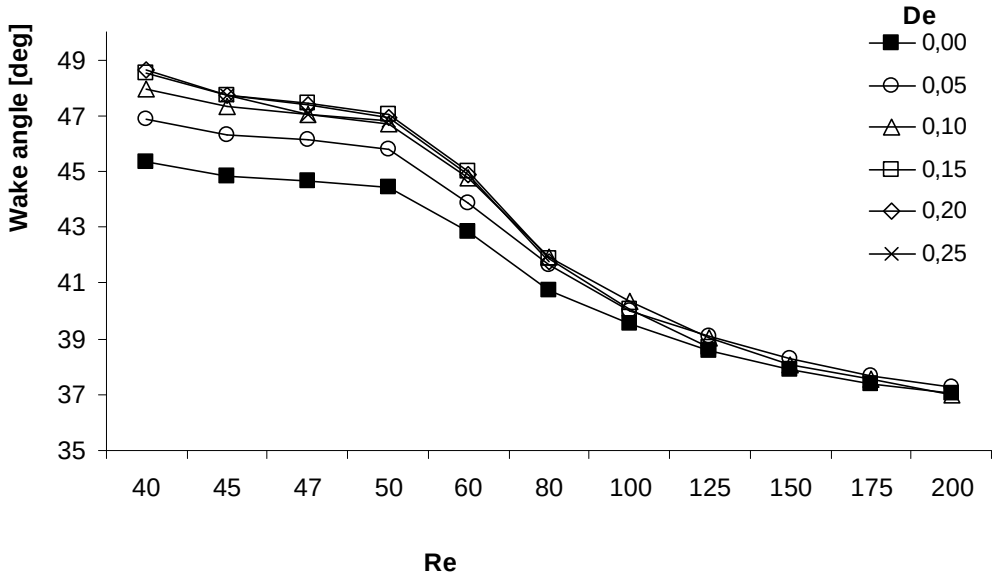


Figure 4.31 Wake angle versus Reynolds number for different Deborah numbers

Figure 4.31 gives the values of the wake angle versus Reynolds number expressed at different Deborah number. From Figure 4.30 and Figure 4.31, it is clear that the wake angle decreases with the reduction of the fluid viscosity but in a narrow range (40°-49°). These results are in good agreement with the experimental results of Coelho & Pinho [57] and numerical simulation of Sahin & Owens [44] which are both carried out for a confined cylinder. In the work of Coelho & Pinho [57], they found that the wake angle range is (70°-73°). We believe that the difference between the present results and their result is due to the difference of the studied range of Reynolds number adopted by these authors ($Re = 10^3 \sim 10^5$).

4.3.3.b Influence of Deborah number on the pressure

Experimental and numerical investigations show that, for a constant viscosity, the fluid elasticity has a stabilizing effect upon two-dimensional viscoelastic fluid flow past a confined cylinder. In this subsection, the effect of fluid elasticity is investigated for the non-confined cylinder. Generally speaking, the extensional properties of viscoelastic fluids reduce the flow kinetic energy contained in the downstream flow fluctuations. This leads to more stabilized flow and reduced pressure distributions.

For flows with $Re < Re_{cr}$, Figure 4.32 shows three pressure contour liness (zero-pressure, negative-pressure, and positive-pressure) at Re = 40 for De = 0.0, 0.1, and 0.2. From this figure, it is noted that, even in this stable regime, the effect of Deborah number is small. The effect of increasing Deborah number is very small on the positive (upstream) pressure. For the zero-pressure contour lines, the increase of Deborah number shifts the contour downstream leading to a smaller pressure drop. For the negative-pressure, the contours shrink especially near the stagnation point giving more relaxation to the pressure drop across the cylinder.

The magnitudes of pressure on the section S1 and the streamline SLu are plotted in Figure 4.33 for Re = 40 at De 0.0, 0.1, and 0.2. These curves show a very slight change of normalized pressure magnitudes with the increase of Deborah number.

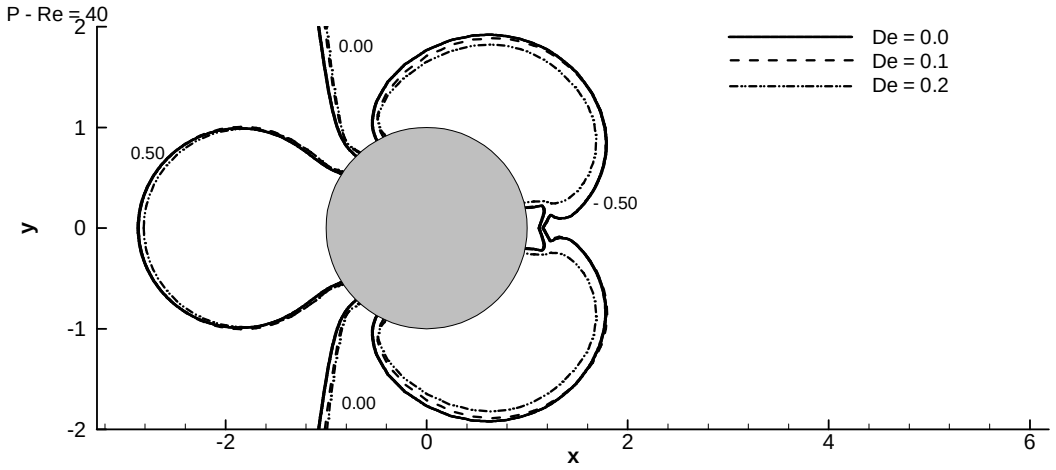


Figure 4.32 Effect of fluid elasticity on pressure contours at Re = 40 with De = 0.0, 0.1, and 0.15

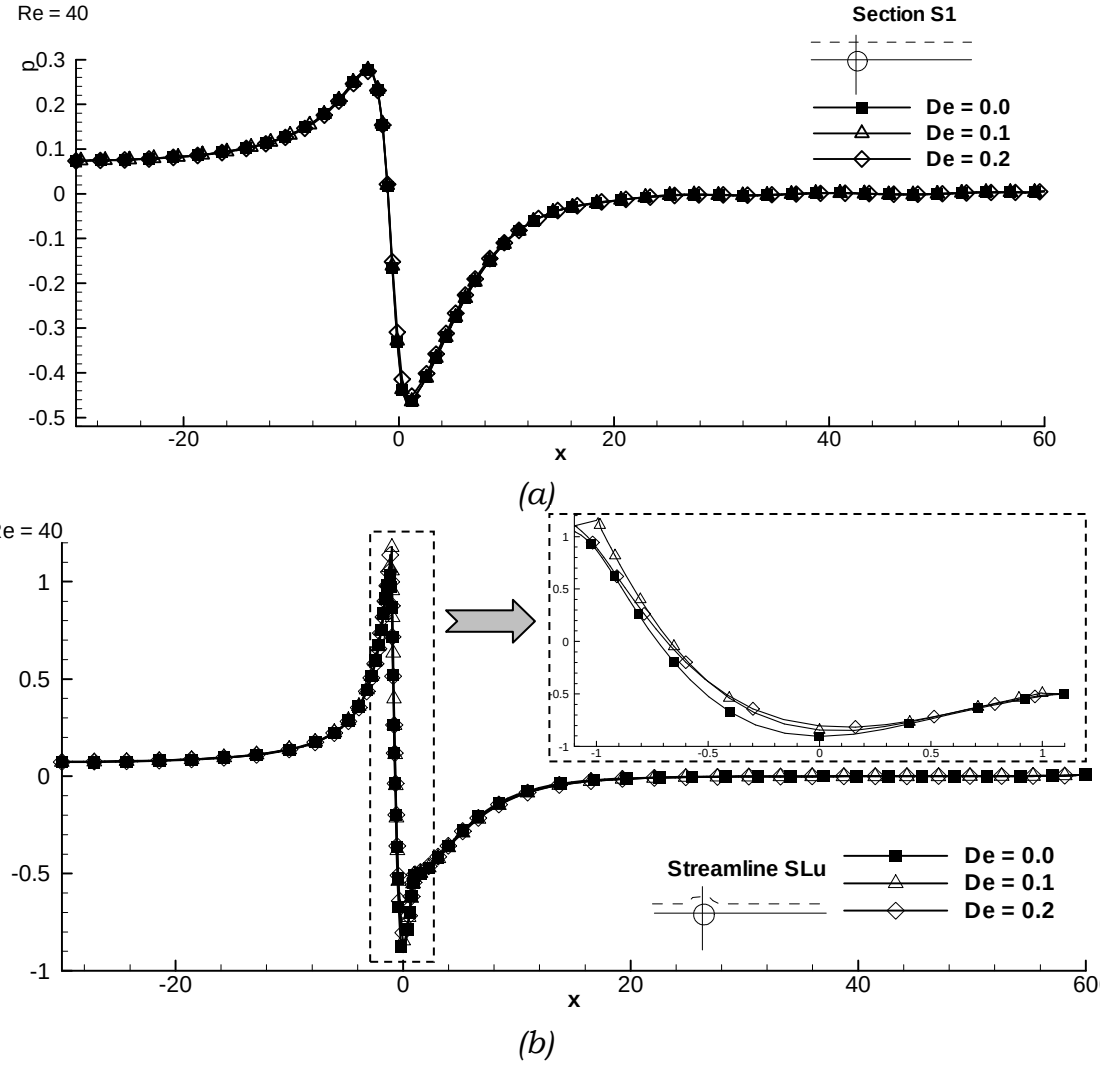
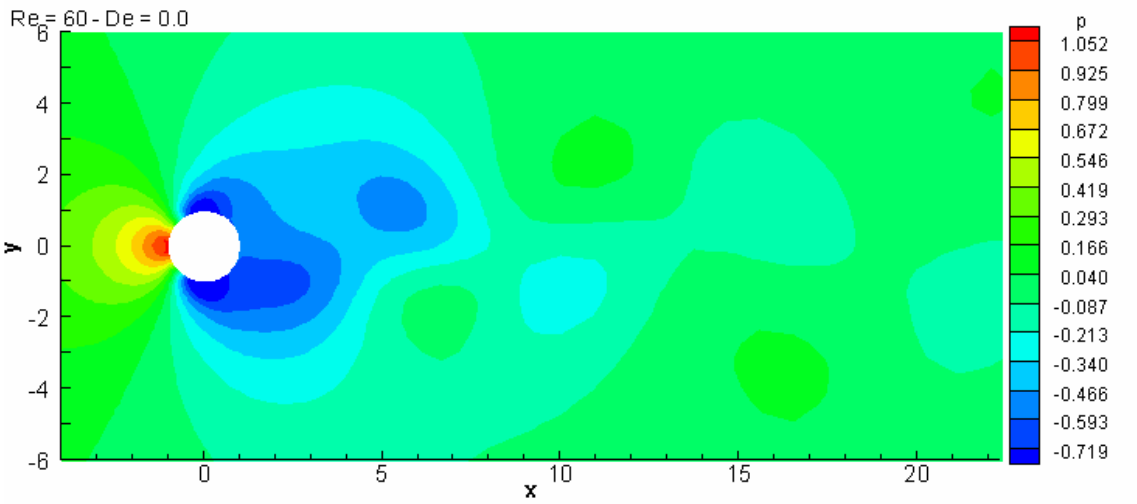


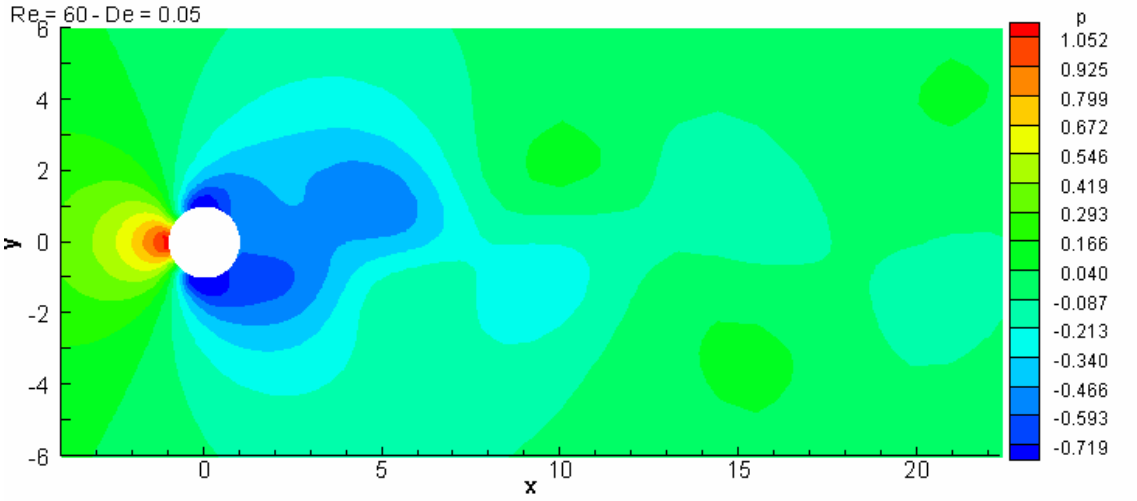
Figure 4.33 Magnitudes of the normalized pressure at Re = 40 on (a) section S1 and (b) streamline SLu.

For the flows in the laminar vortex shedding regime, Figure 4.34 demonstrates the pressure distribution at Re = 60 for a Newtonian flow with De = 0.0 and a viscoelastic fluid with De = 0.05 and De = 0.15, respectively. Despite the very slight increase of the fluid elasticity (De = 0.05), the negative pressure contours downstream the cylinder strongly decreases from Newtonian fluid (Figure 4.34 a) to viscoelastic fluid (Figure 4.34 b). With further increase of Deborah number, most of maximum negative pressure zone downstream the cylinder vanishes as shown in Figure 4.34 c. On the other hand, the effect of fluid elasticity on the positive pressure zone upstream the cylinder is unnoticeable on these plots. In order to a clear overview over this effect, Figure 4.35 shows three normalized pressure contours (zero-pressure, positive pressure, and negative pressure) for Newtonian fluid and viscoelastic fluids with De = 0.05 and De = 0.15 at Re = 60. On Figure 4.35, it is noticed that the fluid elasticity shifts the zero-pressure contour towards downstream which leads to a reduction of the pressure drop across the cylinder. On the upstream side, the change of positive-pressure contour is negligible. On the downstream side, the negative-pressure contours are strongly affected as the contours are obviously extended. It should be noticed that further increase of the Deborah number re-shifts the negative-pressure contour upstream.

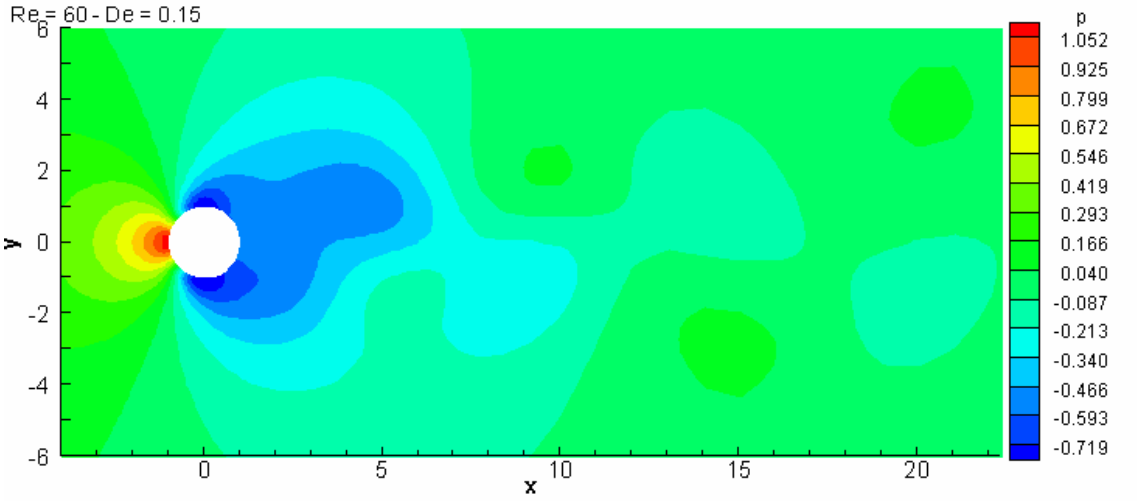
For the wake angle, the fluid elasticity shifts the separation point downstream but further increase of fluid elasticity does not remarkably affects the separation point which is clear from Figure 4.36.



(a)



(b)



(c)

Figure 4.34 Effect of fluid elasticity on pressure distribution at Re= 60 (a) De = 0.0, (b) De = 0.05, and (c) De = 0.15

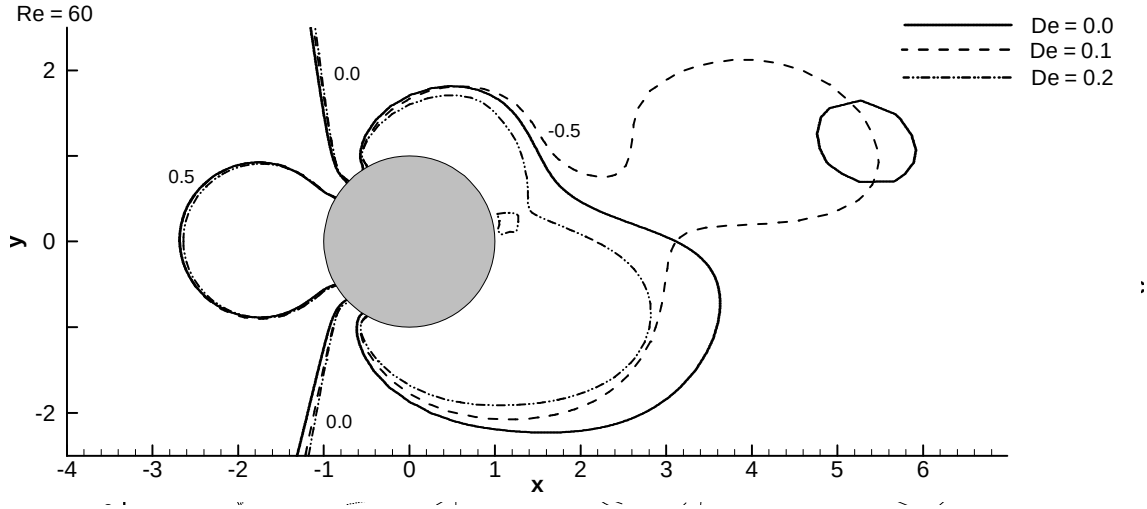


Figure 4.35 Effect of fluid elasticity on pressure contours at Re=60 and different Deborah numbers

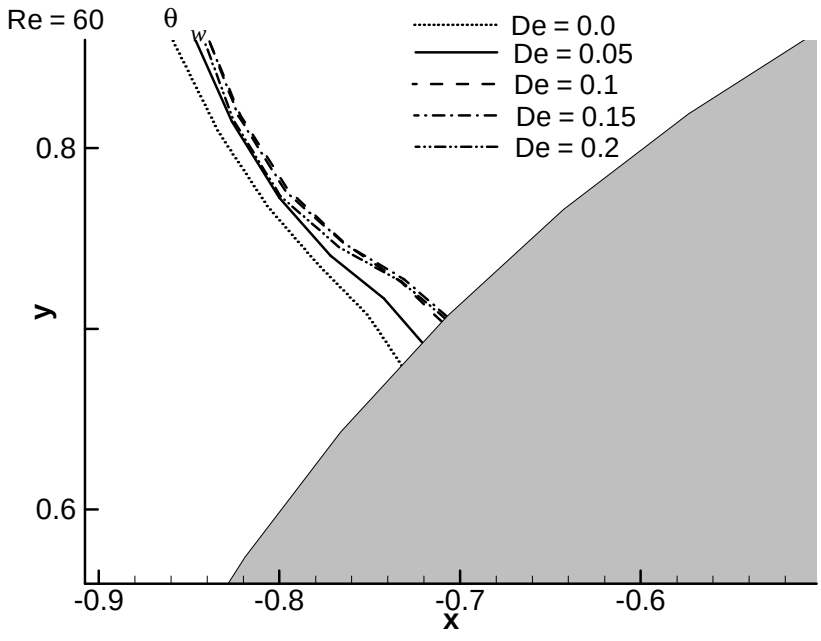


Figure 4.36 Effect of Deborah number on the separation point at Re= 60.

Figure 4.37 plots the values of the wake angle versus the Deborah number for various Reynolds numbers. From this figure, one can observe that the wake angle increases to a plateau with the fluid elasticity then decreases with a slower rate. For each Reynolds number, the range of change, is narrow (2° - 3°). It is noted that, the Newtonian fluid always has the smallest wake angles.

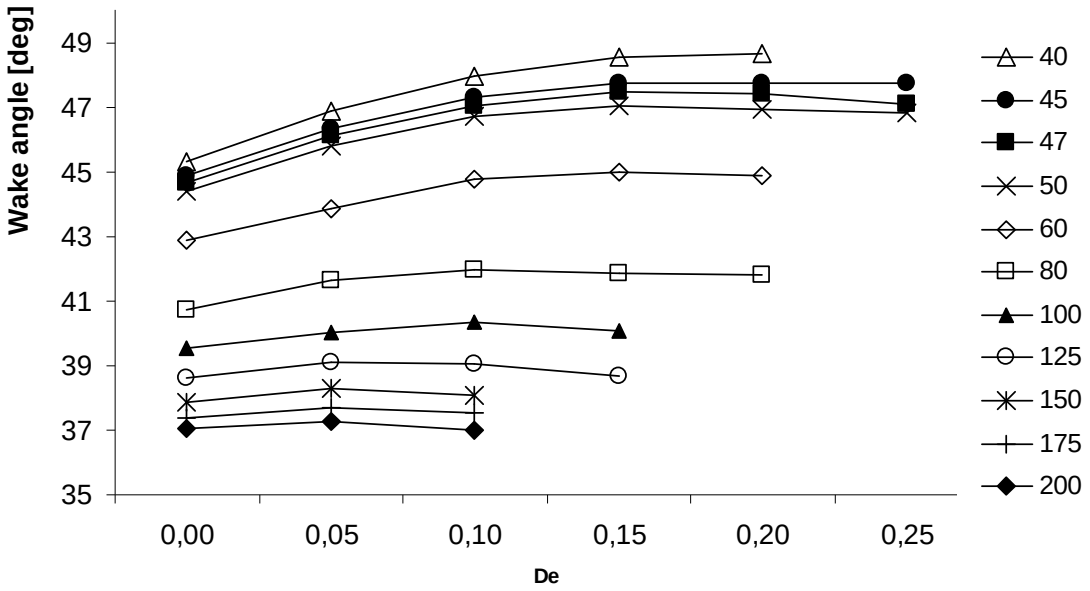


Figure 4.37 Wake angle versus the Deborah number for different Reynolds number.

Figure 4.38 shows the values of the normalized pressure along section S1, along the lower streamline SLd, and at the cross-sections S3 and S4 for Re = 60 at De = 0.0, 0.1, and 0.2. On this figure, we can see no remarkable change at the upstream values and a slight decrease of pressure value downstream the cylinder. The range of pressure value change on downstream side is about 7%.

It should be noted here, that the present findings are consistent with the results of Coehlo & Pinho [57], McKinley et al. [79] and Cadot & Leby [51].

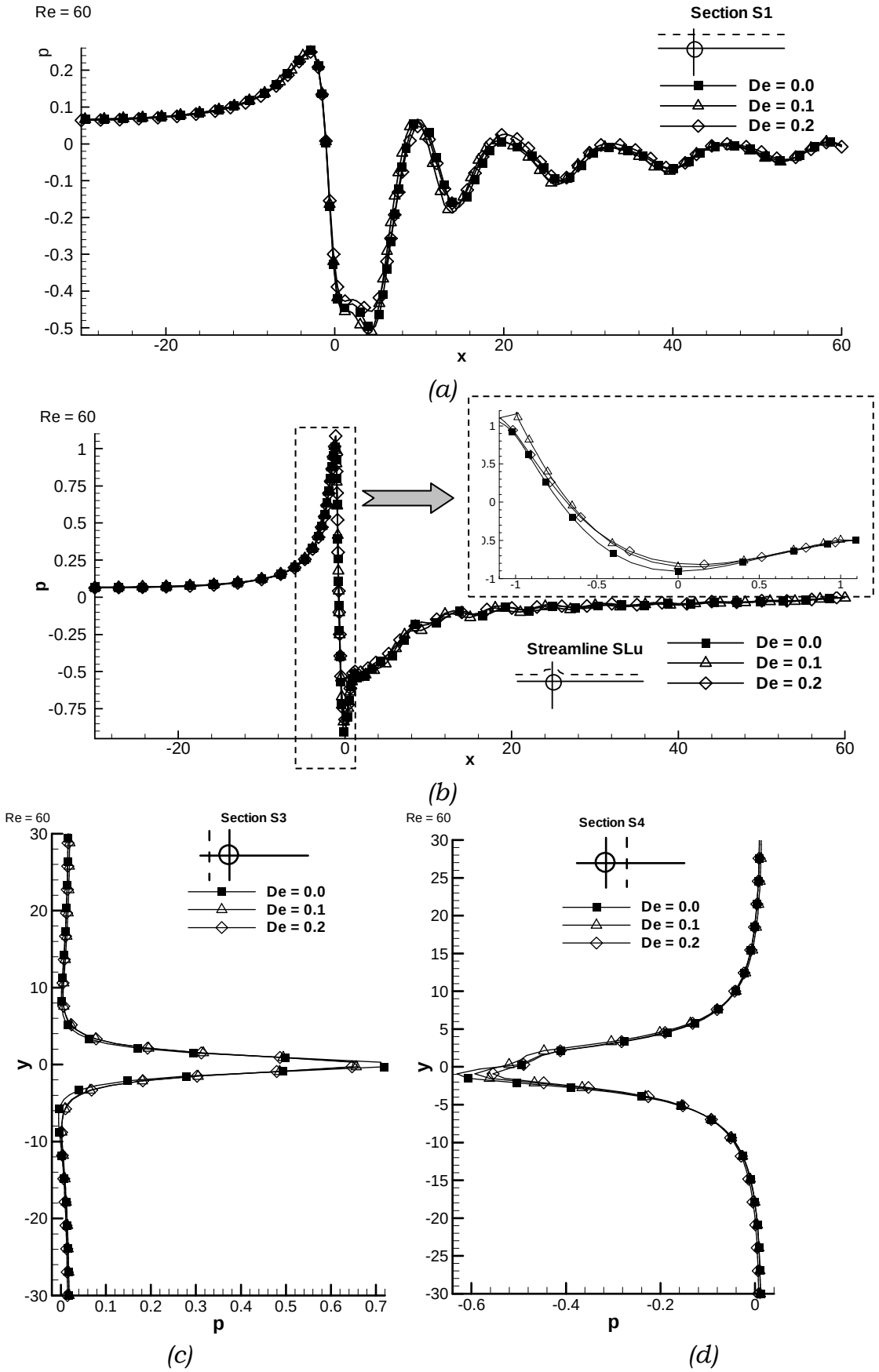


Figure 4.38 Normalized pressure at Re = 60 on (a) section S1, (b) Streamline SLd, (c) section S3, and (d) section S4.

4.3.4 Vorticity

In Newtonian fluid mechanics, Helmholtz decomposition proposes that, under certain conditions, the solution of Navier-Stokes equations can be decomposed into a rotational part and an irrotational part satisfying Laplace's equation [80]. Generally, the rotational and irrotational velocities are strongly coupled and they have to satisfy the boundary conditions. In viscoelastic fluids, the coupling of the rotational and irrotational flows is more complicated than in Newtonian fluids because in most models of viscoelastic fluids, the stress is expressed as a non-linear function of the velocity field. This is the main reason which restricts this work to the *laminar* vortex shedding regime. At higher Reynolds number, the vortices become three dimensional and the turbulent regime appears with all its complexity.

The main objective of this section is to introduce the effect of viscoelastic fluids on the vorticity (the rotational part of the velocity). The vorticity is expressed as

$$\vec{\omega} = \vec{\nabla} \times \vec{u}. \qquad 4.3$$

In the present work, the values of the vorticity are presented in the normalized form

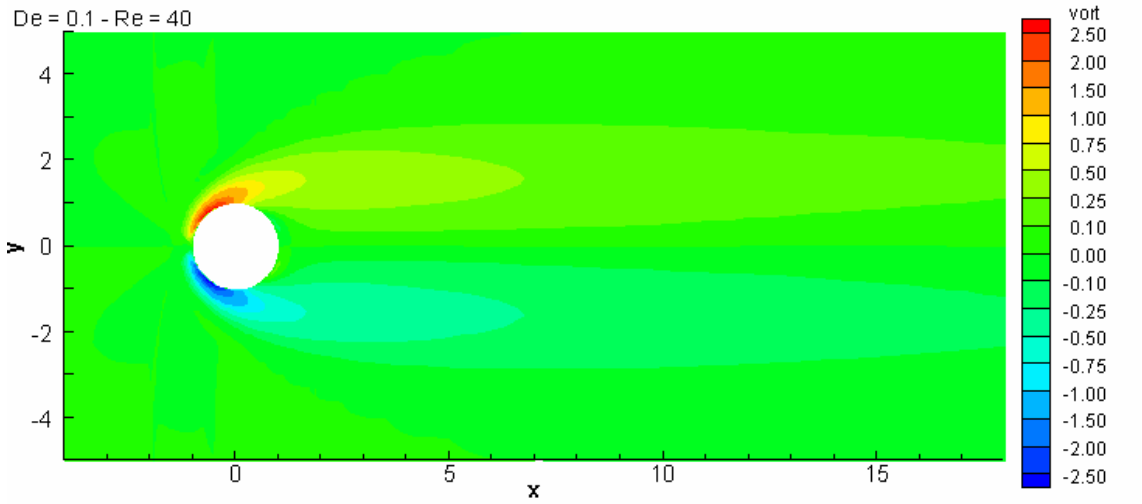
$$\omega = \overline{\omega} \frac{R}{U_0}, \qquad 4.4$$

where $\overline{\omega}$ is the dimensional value of vorticity.

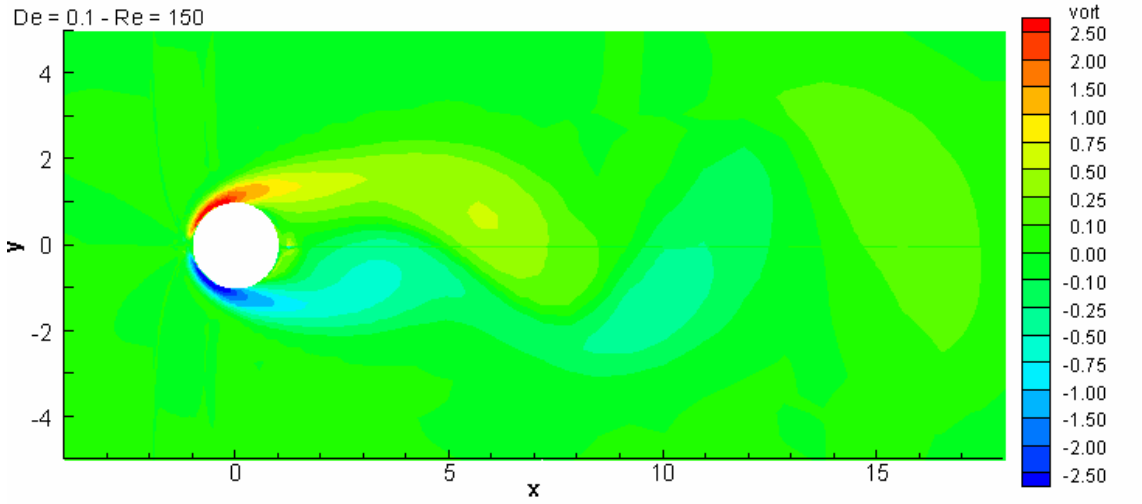
First, the influence of Reynolds number is discussed. Then, the effect of the fluid elasticity is introduced.

4.3.4.a Influence of Reynolds number on the vorticity

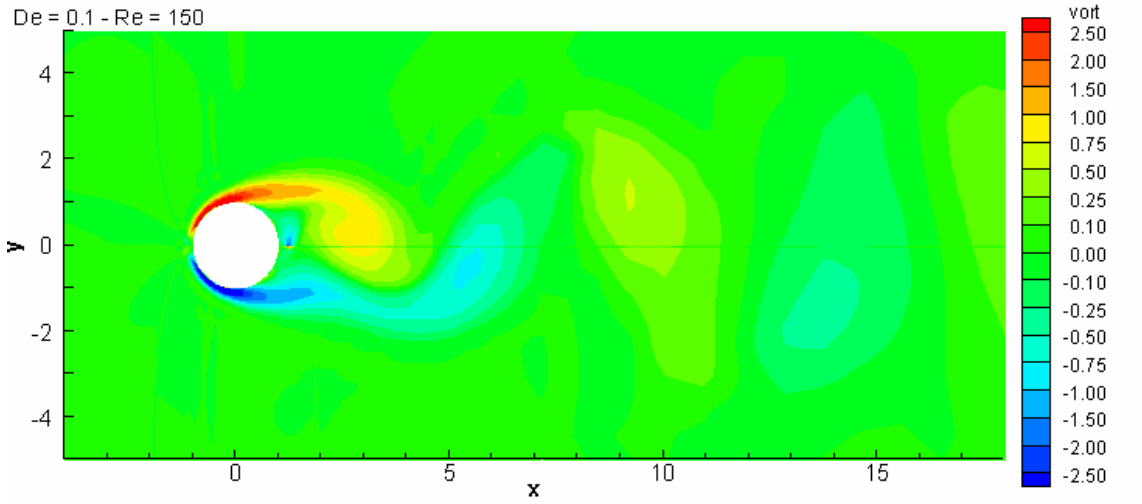
In order to show the effect of Reynolds number on the vorticity, the Deborah number is fixed and the Reynolds number is increasing. Figure 4.39 illustrates the vorticity of a viscoelastic fluid having De= 0.1 and Re = 40, 80, and 150 respectively. This figure shows that the vorticity is maximum close to both sides of the cylinder. There, two opposite-sign high vorticity zones are found.



(a)



(b)

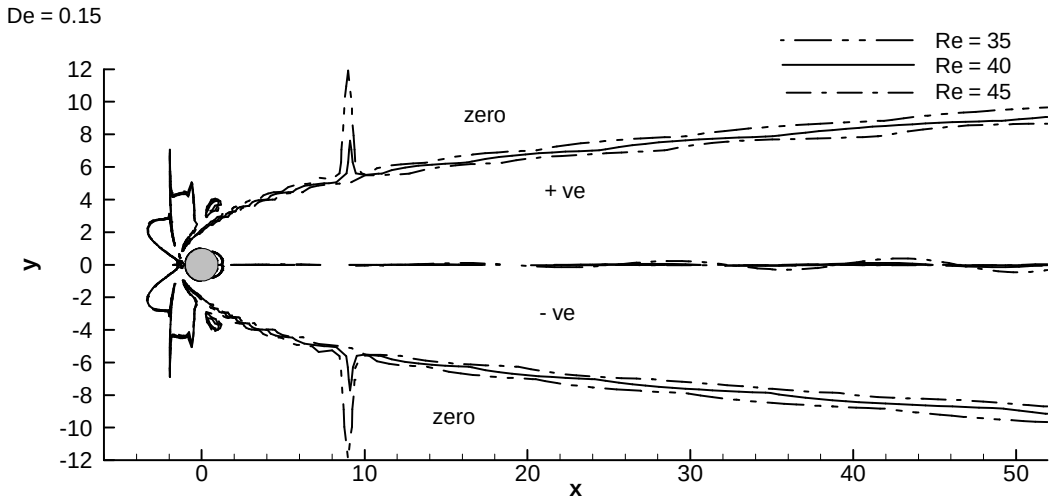


(c)

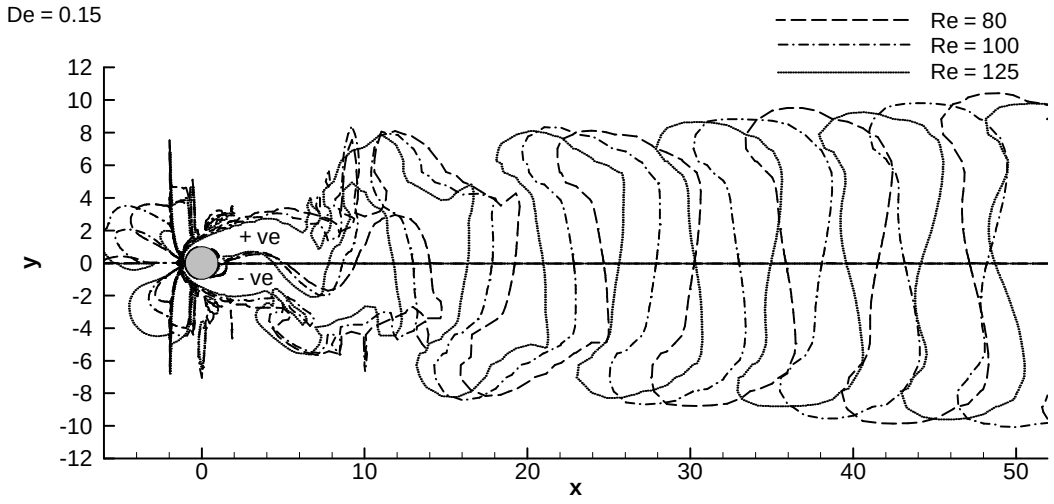
Figure 4.39 Normalized vorticity profile for De = 0.15 at: (a) Re = 40, (b) Re = 80 and (c) Re = 150

The two vorices start upstream the cylinder and extend down stream. Increasing the Reynolds number, the flow becomes less stable and the two vortices fluctuate and lose their symmetry about the x-axis. Hence, the flow passes to the unsteady regime.

Figure 4.40 gives an insight on the influence of Reynolds number on the vorticity as it shows the zero-vorticity contour for the two flow regimes. Figure 4.40 a represents the steady vortex regime with Re = 35, 40, and 45, while Figure 4.40 b represents the laminar vortex shedding regime with Re = 80, 100, and 125.



(a)

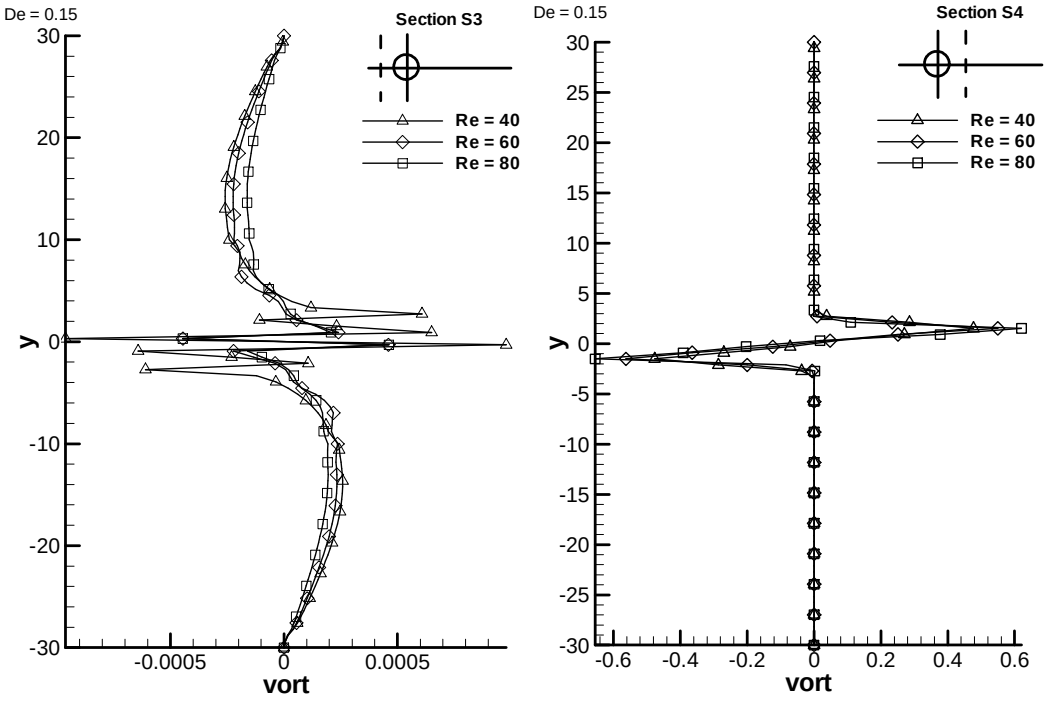


(b)

Figure 4.40 Zero-vorticity contour for De = 0.15 at (a) Re = 35, 40, and 45, and (b) Re = 80, 100, and 125.

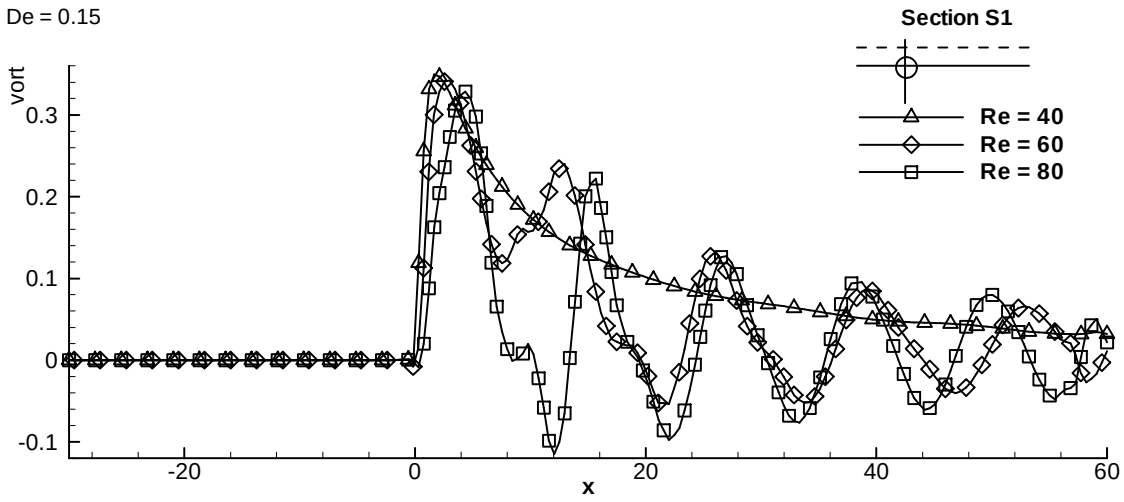
It can be seen from Figure 4.40 that the increase of Reynolds number tends to narrow the cylinder wake for both flow regimes. For $\mathrm{Re} < \mathrm{Re}_{cr}$, the vorticity contour is uniform and symmetric about the x-axis. With the onset of the von Karman street, the recirculation zone becomes very complicated on the upstream side. The increase of Reynolds number beyond Re_{cr} causes the recirculation zone to approach the cylinder announcing stronger flow instability. In both flow regimes, it should be noted that the width of the recirculation zone extends up to about 12*R*. This leads to obvious differences between the confined and non-confined cylinder cases.

The magnitudes of the vorticity for Re = 40, 60, and 80 at De = 0.15 are given on Figure 4.41 and Figure 4.42.

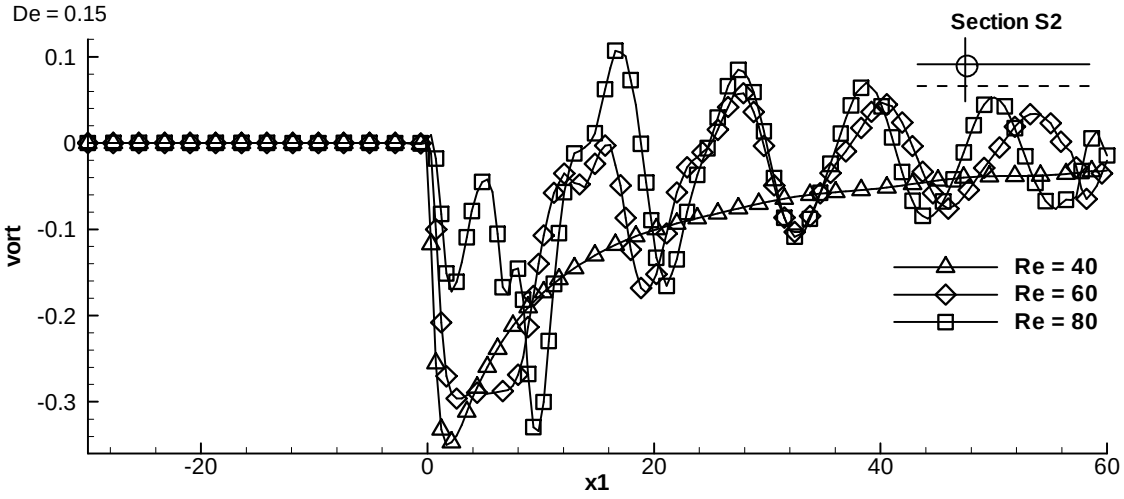


(a) *(b)*

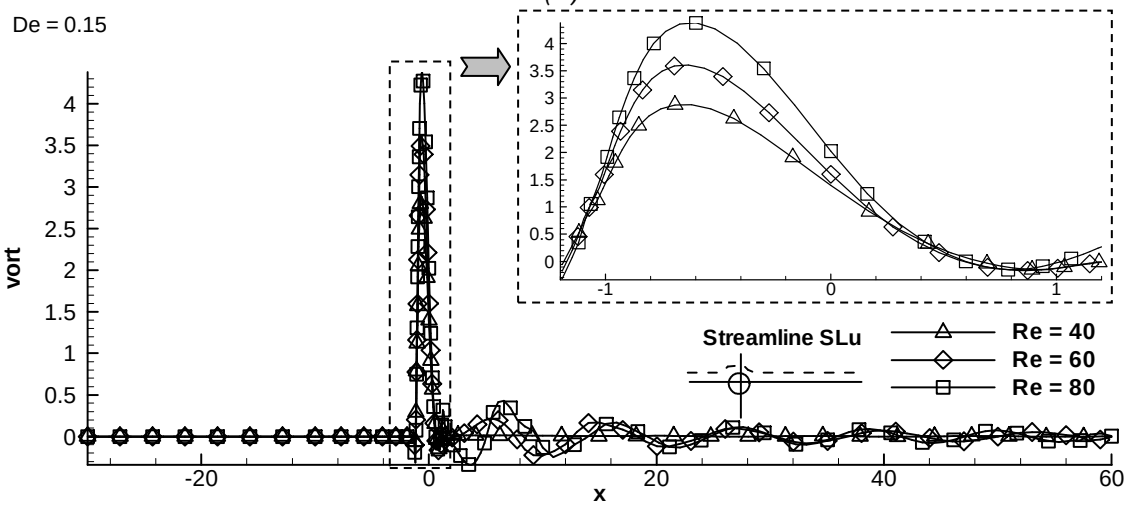
Figure 4.41 Normalized vorticity values for De = 0.15 at (a) Section S3 and (b) Section S4



(a)



(b)



(c)

Figure 4.42 Normalized vorticity values for De = 0.15 along (a) Section S1, (b) Section S2 (c) Upper streamline SLu

From Figure 4.41 and Figure 4.42, it can be concluded that:

- On the sections S1 and S2, the change of the maximum absolute magnitude of the vorticity is changed with the Reynolds number by about 3%.
- The maximum magnitude of the vorticity is (2~4.5) and it takes place close to the cylinder on the upstream side. Over the rest of the domain, the magnitude of the vorticity is in the range of (-0.5~0.5). The location of maximum magnitude is strongly related to the separation point (cf. Figure 4.30).
- The principal changes of vorticity take place downstream the cylinder at a distance of 5~10*R*. These changes compromise both values and signs and they are not systematic.
- For the cross sections, while the change in vorticity values upstream the cylinder range is (-0.001~0.001), the range of theses change downstream the cylinder is (-0.6~0.6).

4.3.4.b Influence of Deborah number on the vorticity

This subsection is devoted to the study of the effect of Deborah number on the vorticity. We introduce first the case of flow with $\mathrm{Re} < \mathrm{Re}_{cr}$. Next, this effect is introduced for $\mathrm{Re} \geq \mathrm{Re}_{cr}$.

In order to examine the flows with Reynolds number lower than the Newtonian critical Reynolds number, Figure 4.43 shows the vorticity of the case of Re = 45 with De = 0.0 and 0.2. We can see here that the flow is still uniform and stable. Only small difference can be seen between the profiles.

Figure 4.44 plots the zero-circulation contour for the Re = 40 at De = 0.0, 0.1, and 0.2. On this figure, it is noticed that the increase of Deborah number inhibits the fluctuations of the vorticity contour on both sides of the cylinder. Also, it decreases the width of the vorticity zone. On the upstream side, increase of Deborah number has a complicated effect that cannot be described by simple reduction or extension. Recalling that the maximum vorticity magnitudes occur upstream, this shows the complexity of the viscoelastic fluids.

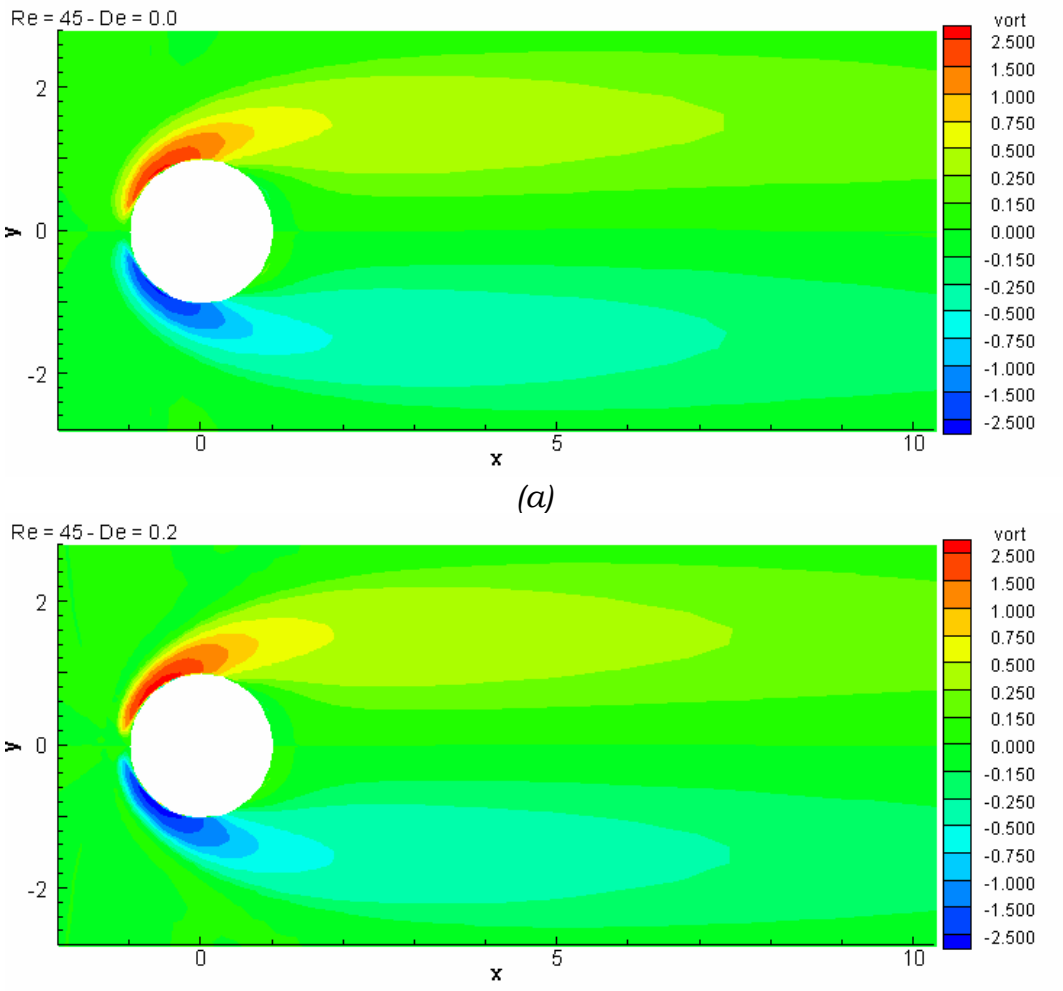


Figure 4.43 Vorticity profile for Re = 45 with (a) De = 0.0, (b) De = 0.1 and (c) De = 0.2

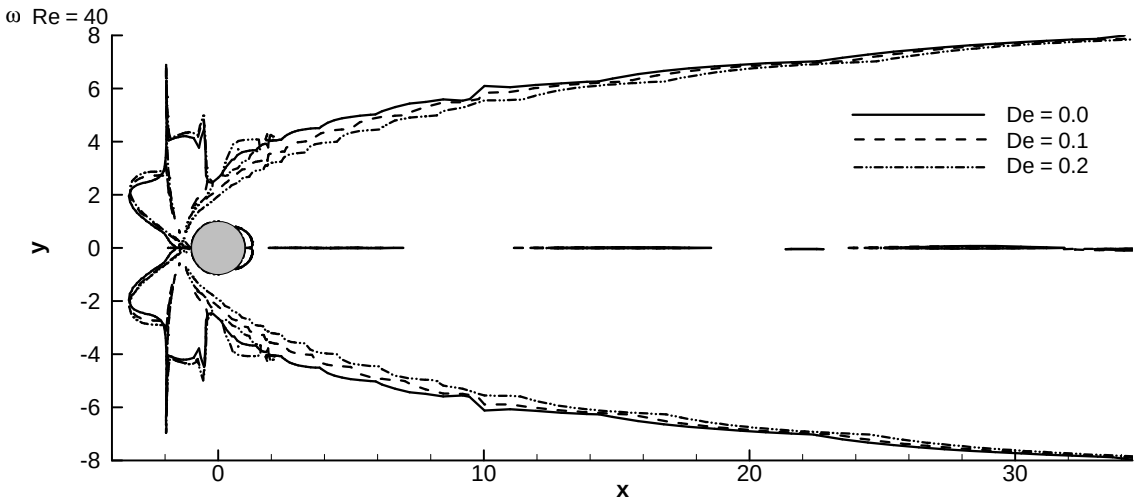
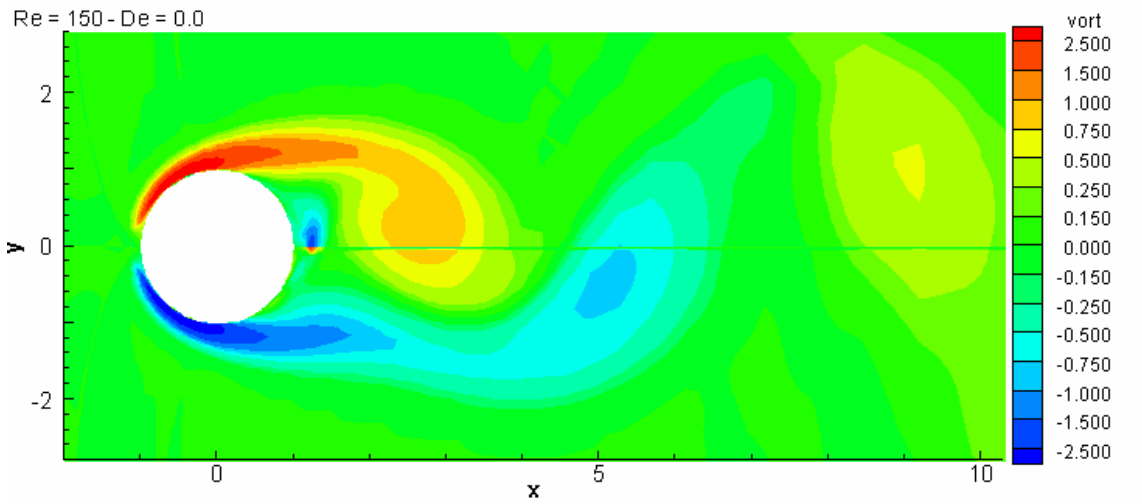
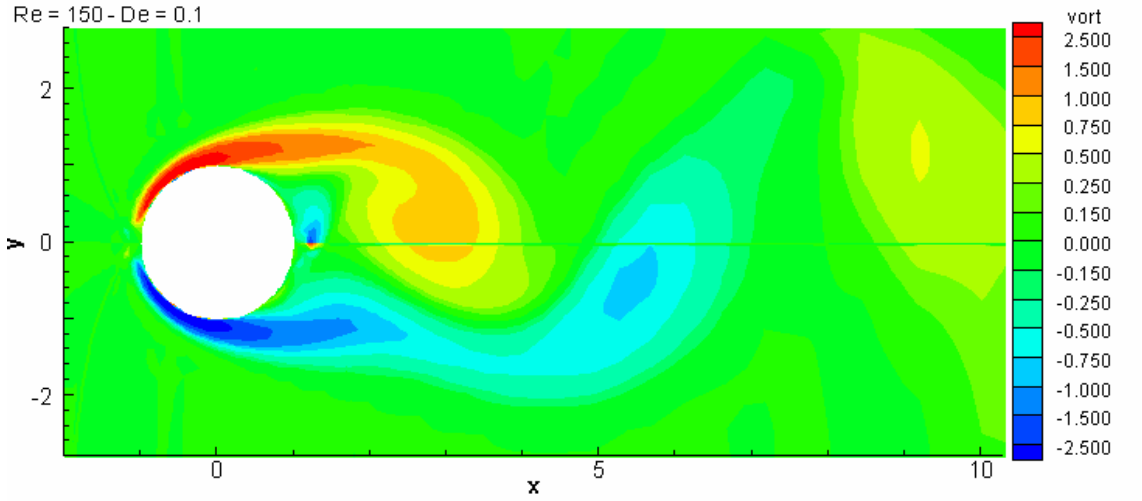


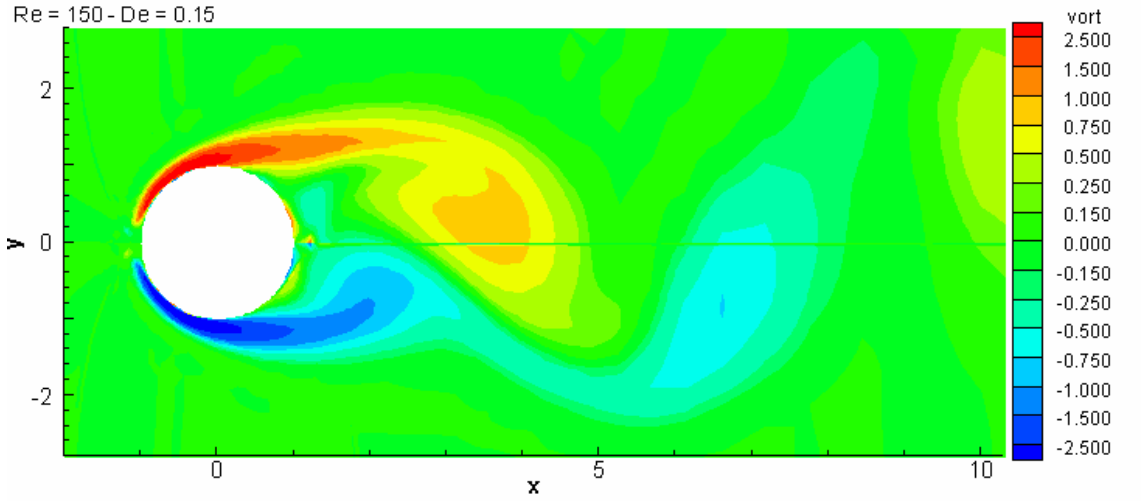
Figure 4.44 Zero-vorticity contours for Re = 40 with different Deborah number



(a)



(b)



(c)

Figure 4.45 Vorticity profile for Re = 100 with (a) De = 0.0, (b) De = 0.05 and (c) De = 0.15

For flows in the laminar vortex shedding regime, we selected the flow at Re=150 to draw the vorticity contours at De = 0.0, 0.1 and 0.15, respectively (cf. Figure 4.45). This figure shows that fluid elasticity extends the vorticity contours. Figure 4.46 shows the zero-viscosity contour for a viscoelastic flow having Re = 60 with De = 0.0, 0.10, and 0.2.

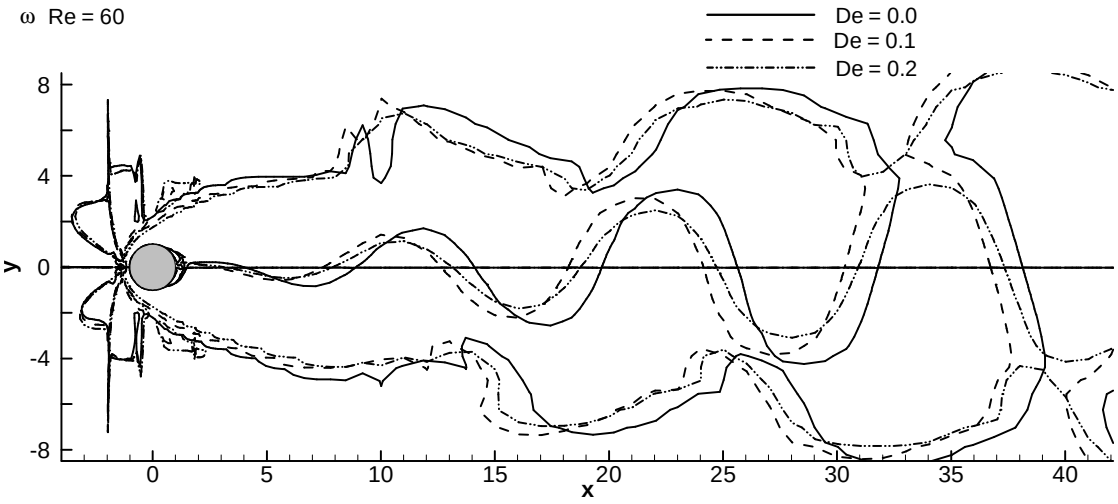


Figure 4.46 Vorticity profile for Re = 100 with (a) De = 0.0, (b) De = 0.05 and (c) De = 0.15

From Figure 4.46, we see that, in general, the vorticity contour extends with the fluid elasticity if we look on far downstream. However, on near downstream and on both sides of the cylinder, the situation is too complicated to be distinguished.

Figure 4.47 and Figure 4.48 show the magnitudes of the vorticity along the sections S1, S2, S3, and S4 and the streamline SLu. From these figures we see that for De = 0.2 the peaks are reduced of about 3~5%. Also, it is noticed that the magnitude range at the upstream section S3 is ± 0.0005, while at the downstream side the range is ± 0.6.

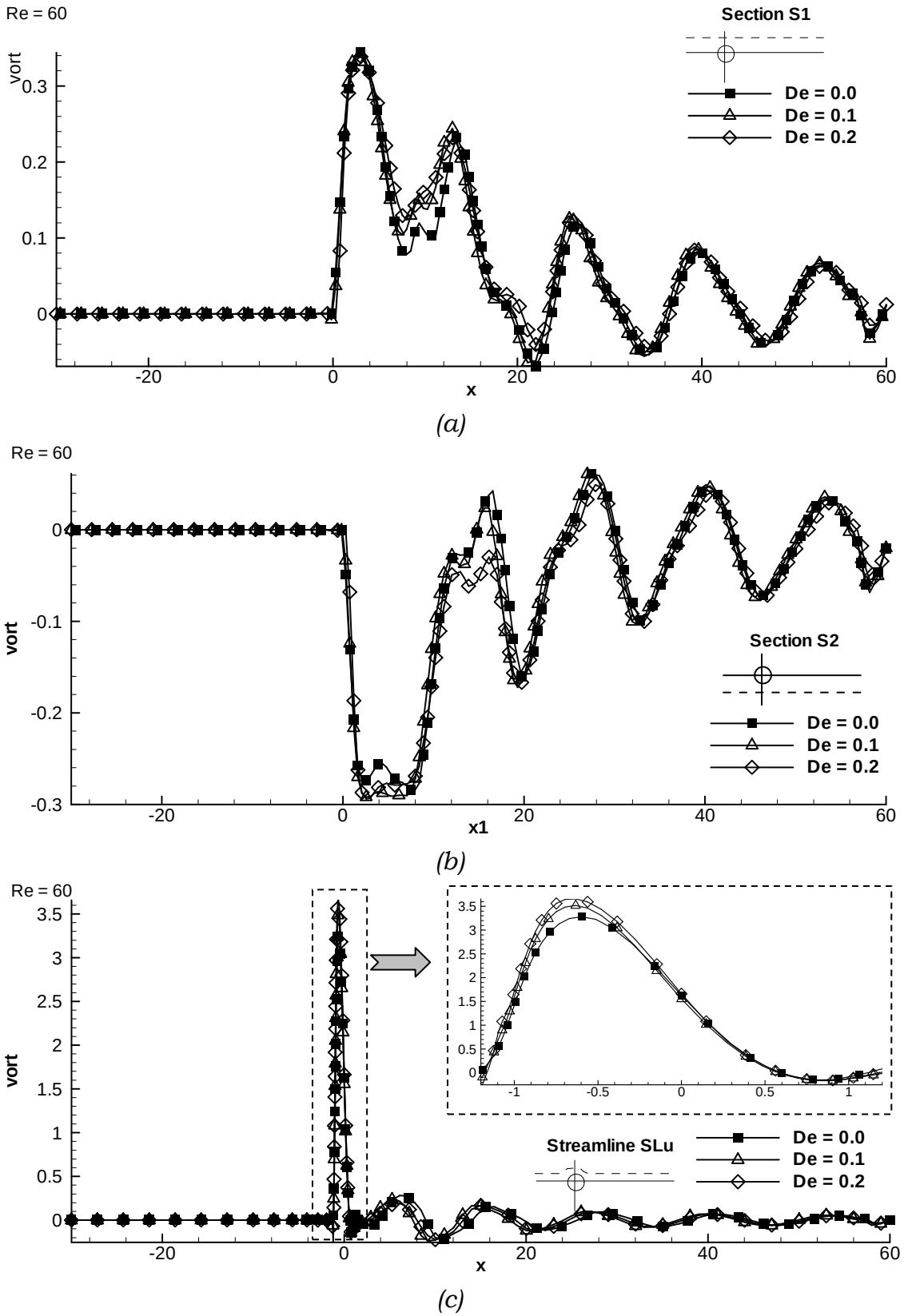


Figure 4.47 Magnitudes of vorticity for Re = 100 at (a) Section S1 and (b) Upper streamline SLu

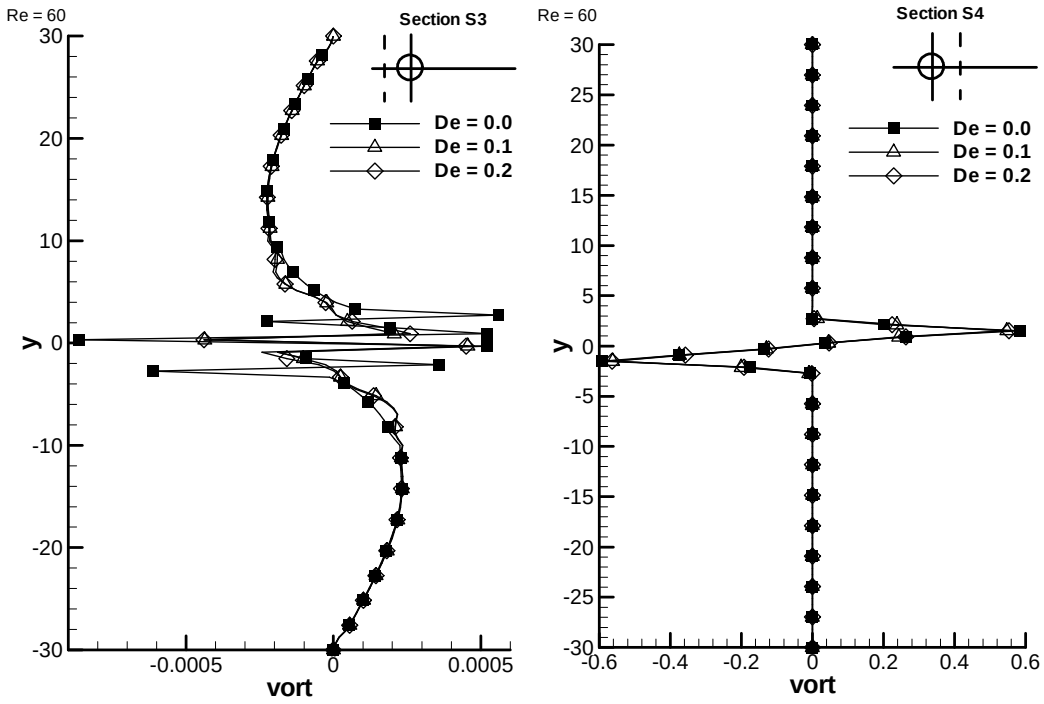


Figure 4.48 Magnitudes of vorticity for Re = 100 at (a) Section S1 and (b) Upper streamline SLu

These results agree with the experimental work of Cressman et al. [54] who found that the polymer lengthens the boundary layer behind the rod. They believed that this stretching effect arises from the elongational viscosity. They showed the vortex street in a polymer free film and in a film where the polymer concentration 30 wppm. Also, the present results are consistent with the measurement of Coehlo & Pinho [56]. These authors found that fluid elasticity was found to have the opposite effect to shear-thinning, reducing the vortex shedding frequency since it increased the formation length.

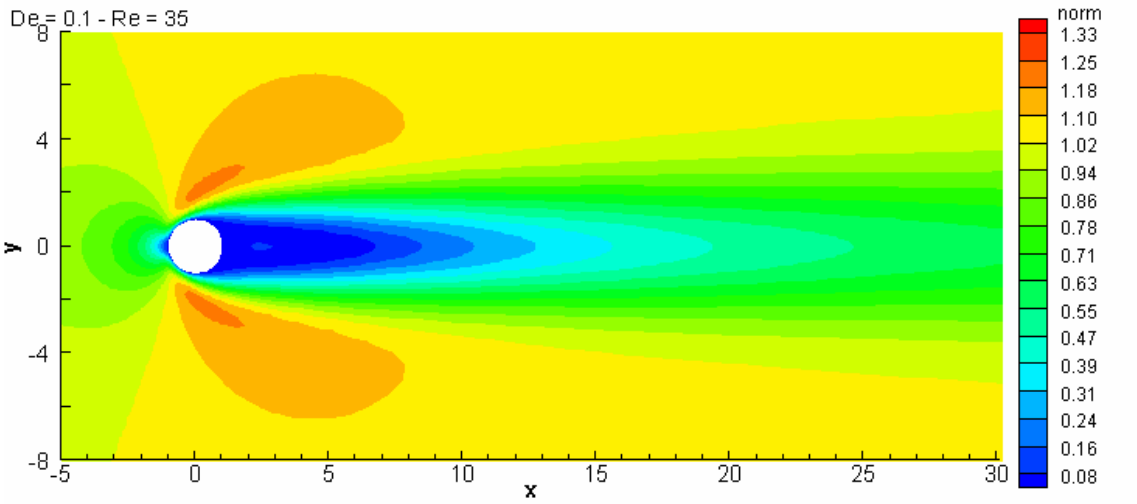
4.3.5 Velocity profile

The modifications of the flow velocity profile by the addition of long chain polymers are the issue of many studies either experimental or numerical. Up till now, the full understanding of these modifications is not complete. As mentioned in the literature survey, most of the elaborated work on the viscoelastic fluid flow past a cylinder concerns the bounded cylinder case.

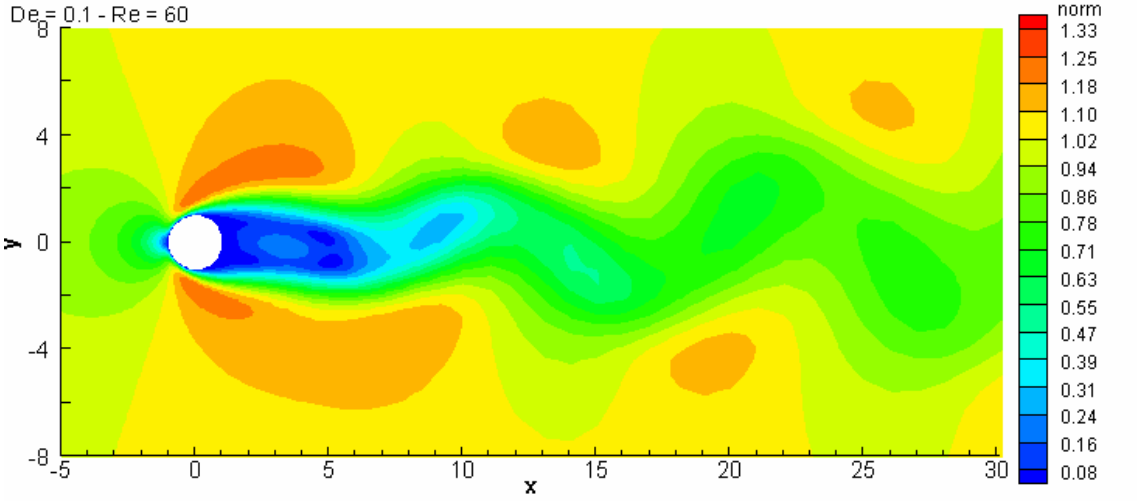
4.3.5.a Influence of Reynolds number on the flow velocity

In this subsection, a fixed Deborah number is considered and the Reynolds number is changed to plot the flow velocity profile past the cylinder. Figure 4.49 shows the normalized velocity magnitude for De = 0.1 at Re = 35, 60, and 125 respectively. These velocity profiles show the strong effect of the Reynolds number on the flow behaviour. Both the upstream and downstream zones are influenced. The upstream zone shrinks with the increase of the Reynolds number, while the downstream zone extends and fluctuates laterally with growing Reynolds number. As the Reynolds number increases beyond the critical Reynolds number, both the amplitude and frequency of the fluctuations increase progressively.

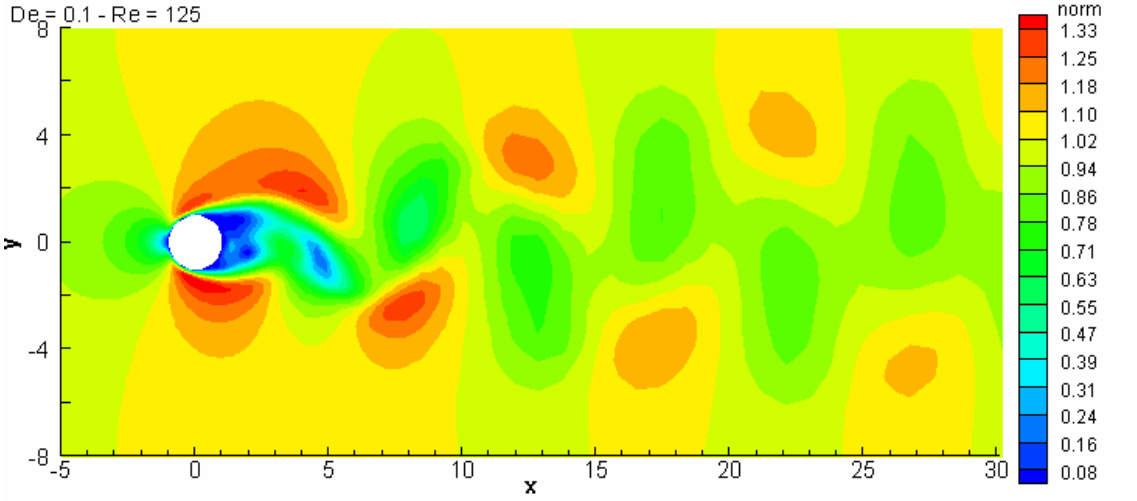
Figure 4.50 gives a more detailed view of this influence as the contour of unit normalized velocity is drawn for Re = 35, 40, and 45 (Figure 4.50 a) representing the steady vortex regime and at Re = 80, 100 and 125 representing the laminar vortex shedding regime (Figure 4.50 b). From this figure, it is noted that, in general, the upstream zone is less influenced then the downstream one. For the steady regime, increasing the Reynolds number widens the velocity contour. For the unsteady regime, the contours approach the cylinder when increasing the Reynolds number.



(a)



(b)



(c)

Figure 4.49 Normalized velocity for viscoelastic fluid with De=0.1 at: (a) Re = 35, (b) Re = 60, and (c) Re = 125

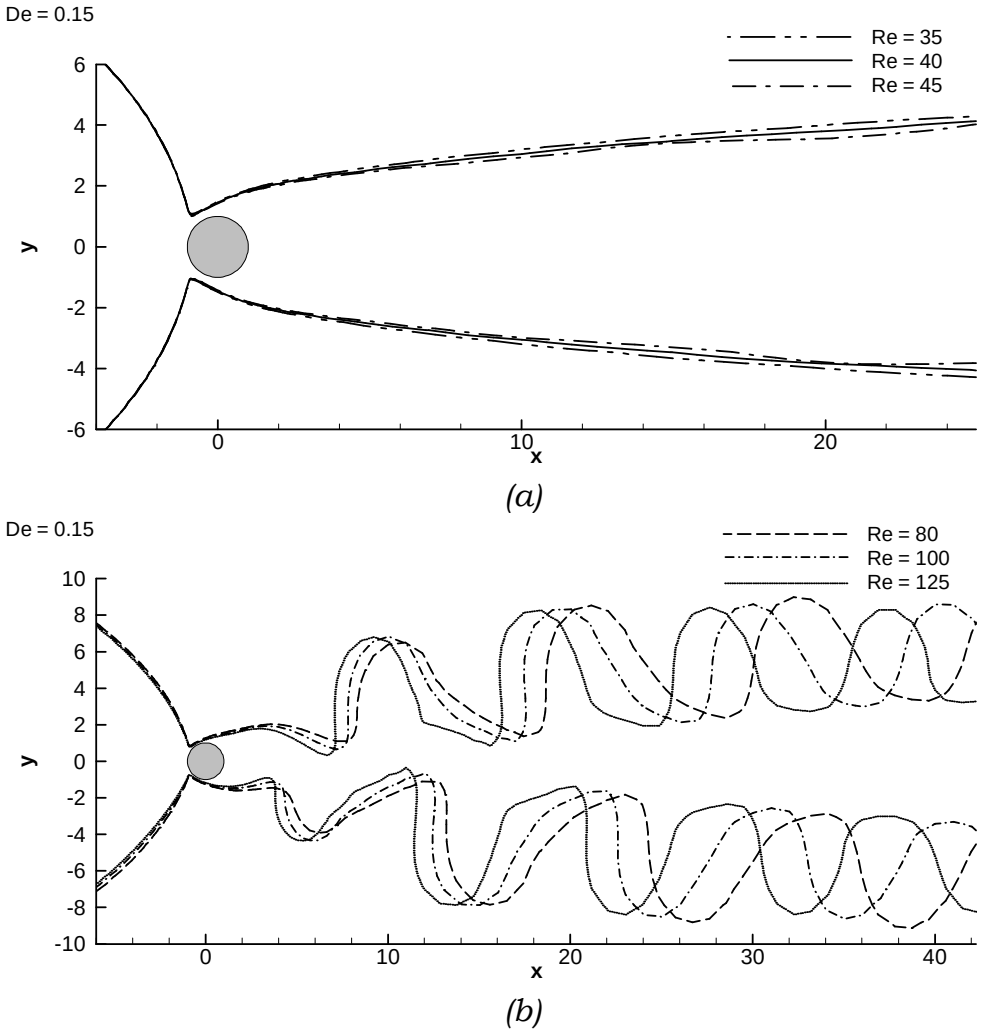


Figure 4.50 Contour of unit normalized velocity for De = 0.15 at: (a) Re = 35, 40 and 45 and (b) Re = 80, 100, and 125.

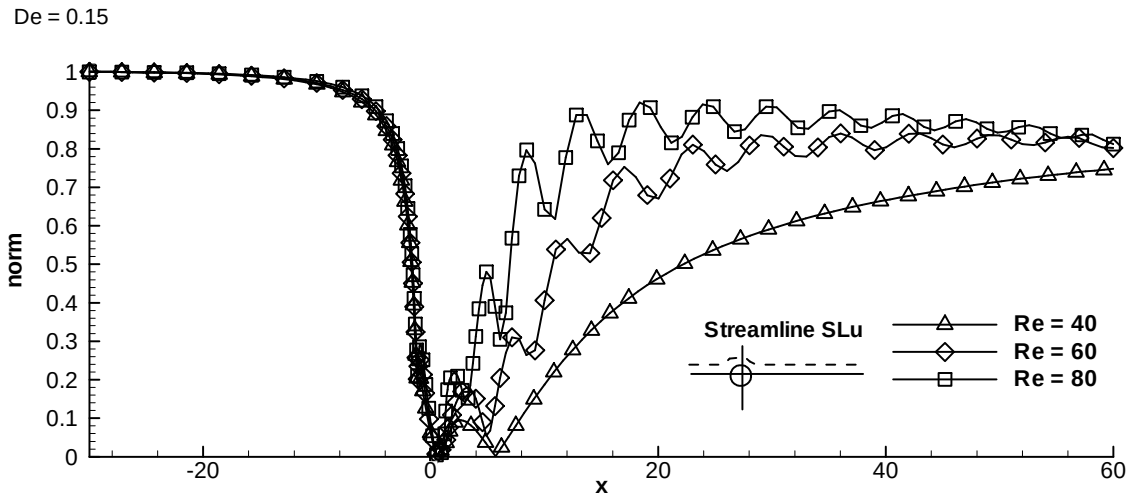
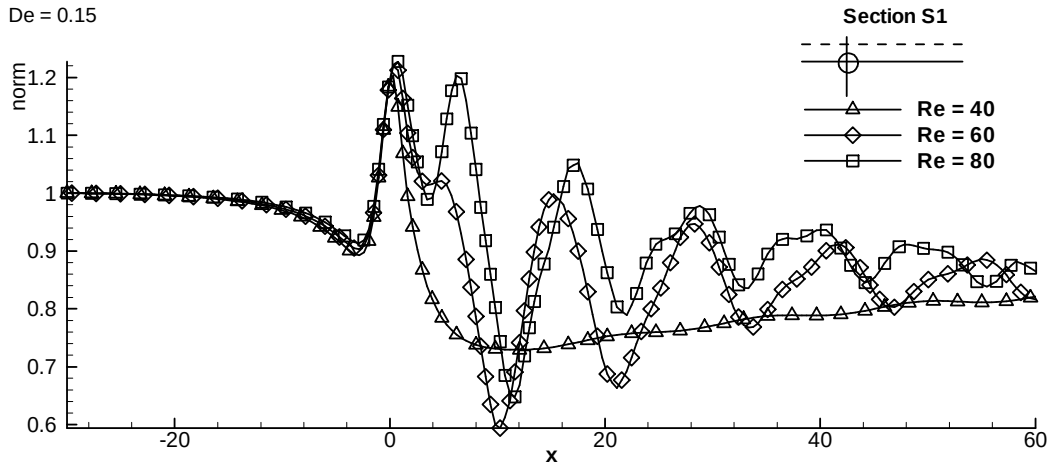
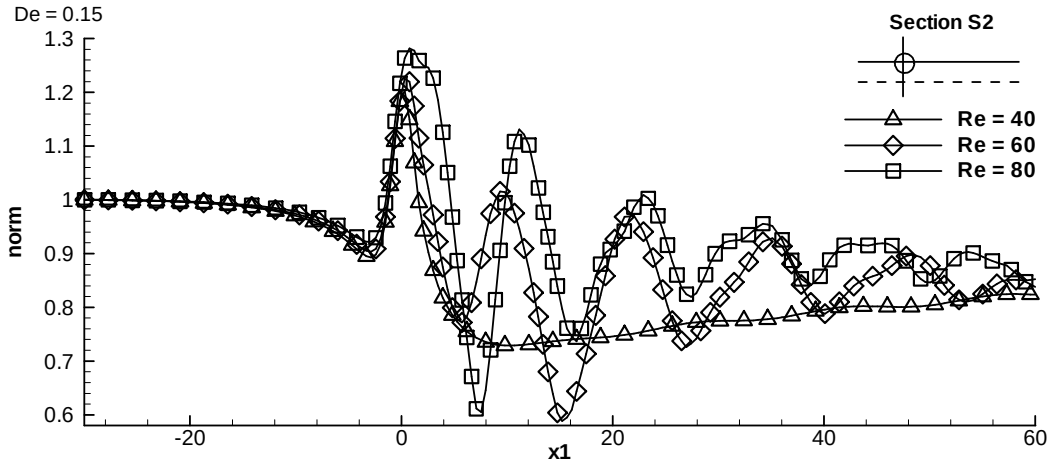


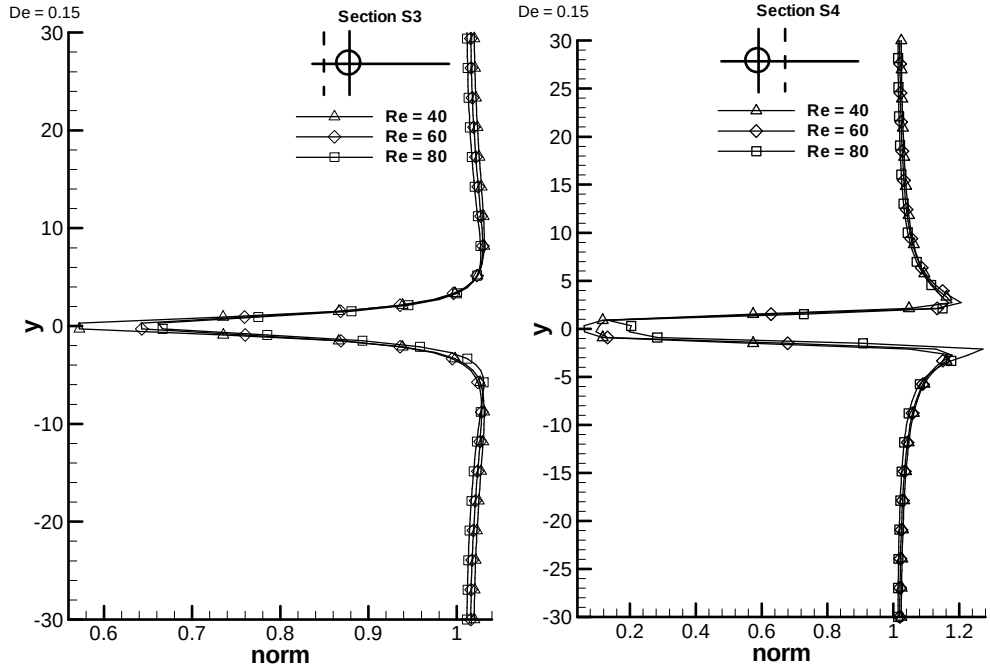
Figure 4.51 Velocity magnitudes for De = 0.15 at Re =40,60, and 100 along the streamline SLu



(a)



(b)



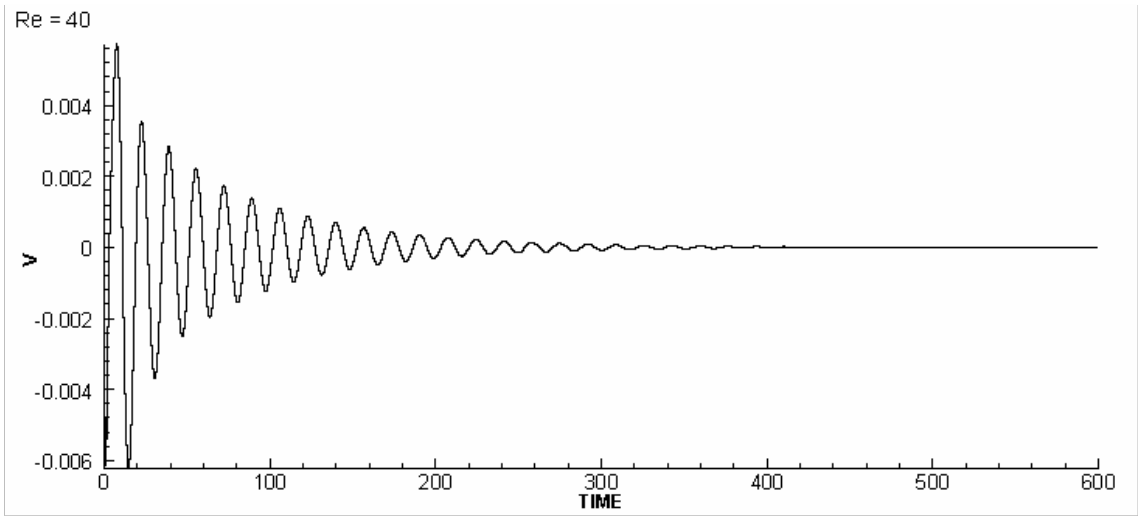
(c) *(d)*

Figure 4.52 Velocity magnitudes for De = 0.15 at:
(a) section S1, (b) section S2, (c) section S3, and (d) section S4

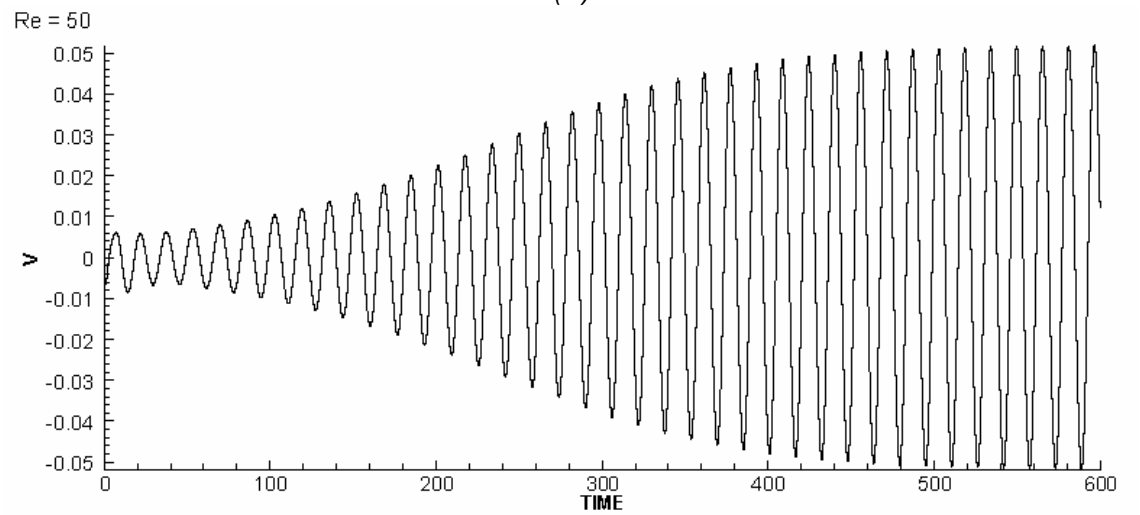
To quantify the effect of the Reynolds number on the flow velocity, Figure 4.51 and Figure 4.52 provide the magnitudes of the normalized velocity along sections S1, S2, S3, and S4 and the streamline SLu at De =0.15 for Re = 40, 60 and 80. From these two figures, it is noted that:

- There is no velocity fluctuation at Re = 40 which is expected from the steady regime. For higher Reynolds numbers in the unsteady regime, the fluctuations of the downstream velocity decay gradually till the exit of the domain.
- At sections S1 and S2, the differences in the upstream region are negligible compared to the differences in downstream region.
- For section S3, the velocities exhibit a symmetric profile, while for section S4, the symmetry breaks down at the unsteady Reynolds numbers.
- On the x-axis, the velocity values are of same order of magnitude as the far entry velocity, while at sections S1 and S2 the maximum velocity values increase about 30% above the entry velocity.

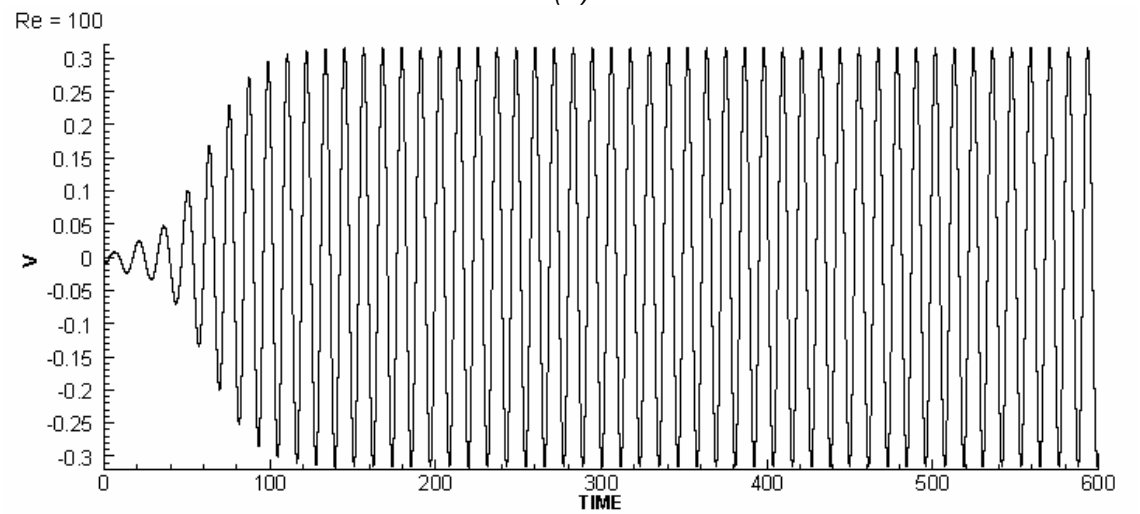
A downstream point *h* (cf. Figure 4.2) on the x-axis has been chosen to visualize the instantaneous fluctuations of the velocity field (Figure 4.53). These time histories prove that the velocity fluctuations are very small (±0.005) and decay for the Re = 40 which is expected behaviour as this value is still in the regime of laminar steady flow. The time histories in the two other cases ($\mathrm{Re} > \mathrm{Re}_{cr}$) do not decay but they arrive at an asymptotic fluctuating state (or maximum amplitude) for $\mathrm{Re} < \mathrm{Re}_{cr}$ after a certain time. This rise time t_r is decreasing with Reynolds number. It is also noted that the amplitude of the fluctuations is progressively increasing with the Reynolds number. Figure 4.54 shows the monotonic change in the vertical velocity amplitude as a function of Reynolds number for different Deborah numbers.



(a)



(b)



(c)

Figure 4.53 Time history of vertical velocity component for De=0.1 at (a) Re = 40, (b) Re = 50, and (c) Re = 100

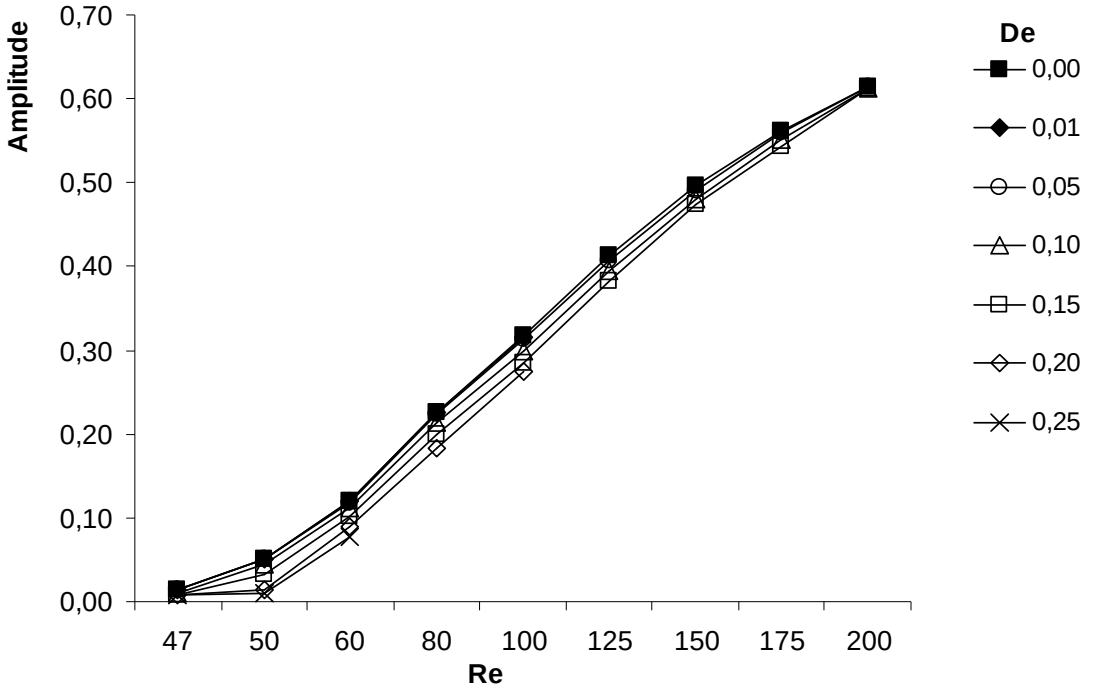


Figure 4.54 Amplitude of vertical velocity fluctuations versus Reynolds number for different Deborah numbers

It is evident from Figure 4.54 that the amplitude of the vertical velocity increases monotonically beyond the critical Reynolds number. Also, the amplitude for viscoelastic flow is always less than for the corresponding Newtonian flow.

The rise time of fluctuations is plotted on Figure 4.55 against the Reynolds number for various Deborah numbers. For steady flow (not shown on Figure 4.55), before the onset of laminar vortex shedding, the fluctuations attain the maximum amplitude after about 14 and then the fluctuations decay. Viscoelasticity seems to delay the critical Reynolds number since the amplitude for Re = 47 and 50 is nil for De = 0.01 and 0.05.

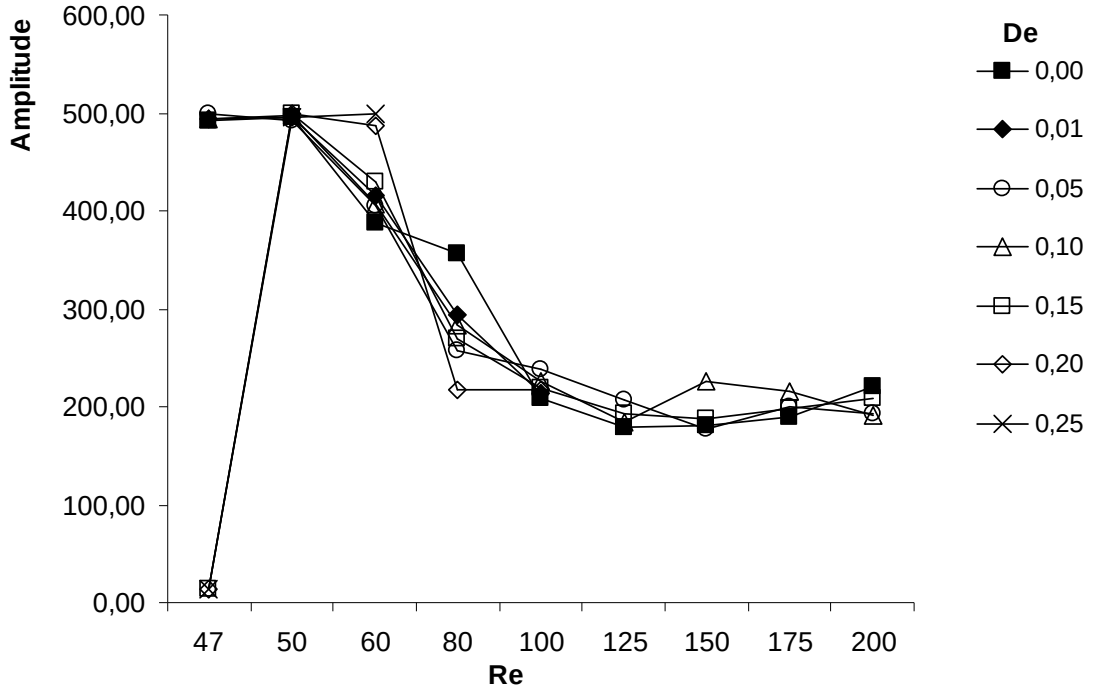


Figure 4.55 Rise time of velocity fluctuations versus Reynolds number for different Deborah numbers

With the onset of the von Karman street instability, the fluctuations do not decay and reach the maximum amplitude after longer times. For increasing Deborah number, the peak of the rise time shifts towards higher Reynolds number; which implies a higher critical Reynolds number for viscoelastic fluids.

An important quantity that expresses the flow fluctuations is the frequency of these fluctuations. This frequency is used to couple the flow to the structure in studies of fluid-structure interaction. In most of literature studies the fluctuation frequency presented as non-dimensional form represented by the Strouhal number $Str = df/U_0$. However, the only experimental work treating the flow of viscoelastic fluid past a *non*-confined cylinder, up to our knowledge, is the work of Pipe & Monkewtiz [58]. In this work, they expressed the non-dimensional frequency using the Roshko number which is defined as

$$R_{sk} = \frac{f\rho D^2}{\eta_0}, \qquad 4.5$$

where f is the frequency, ρ is the fluid density, D is the cylinder diameter, and η_0 is the fluid total viscosity.

Pipe & Monkewtiz [58] stated that the relation between Roshko number and Reynolds number is represented by the quadratic fit (for De = 0.01~0.03).

$$R_{sk} = -2.29 + 0.15\,\mathrm{Re} + 3.25\times10^{-4}\,\mathrm{Re}^2 \qquad 4.6$$

We compared our results to this relation and found excellent agreement. Figure 4.56 represents Roshko number (Rsk) versus the Reynolds number for different Deborah numbers together with Pipe & Monkewtiz [58] relation. In this figure, we can see the increase of the Roshko number with the increasing Reynolds number.

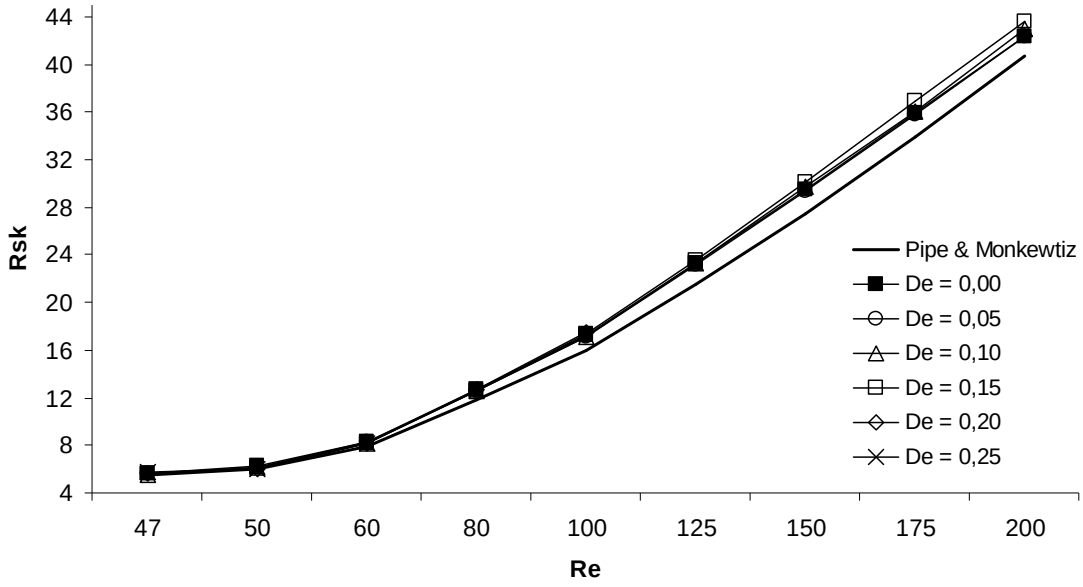
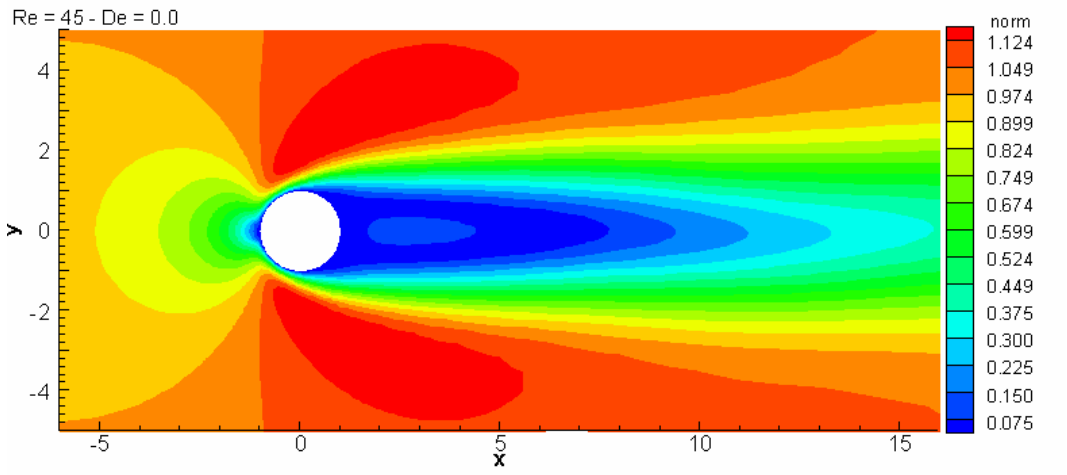


Figure 4.56 Roshko number versus Reynolds number for different Deborah numbers with comparison to the formula of Pipe & Monkewtiz [58]

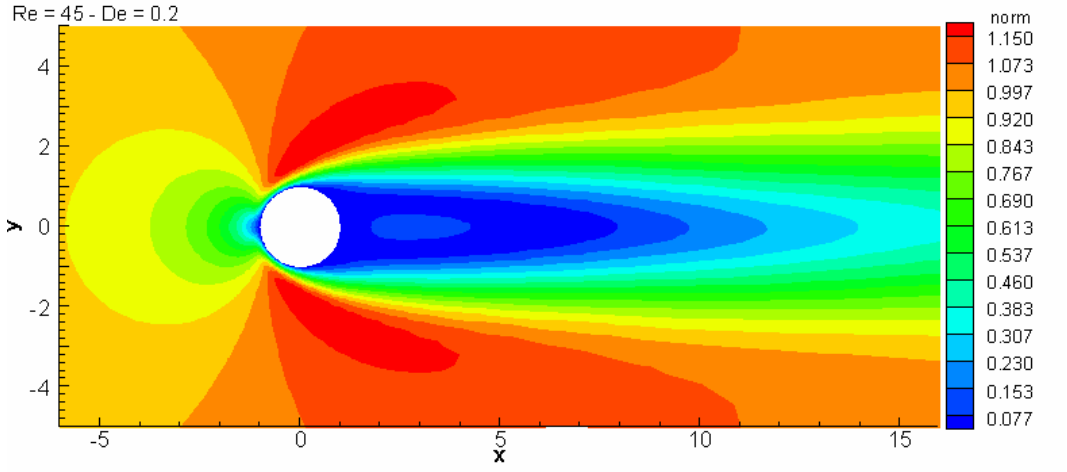
4.3.5.b Influence of Deborah number on the velocity field

In this subsection, the influence of the fluid elasticity on the velocity field is studied. The Reynolds number is fixed and the Deborah number is increased as an indicator of the fluid elasticity. It is known from the previous experimental and numerical studies that viscoelasticity has a stabilizing effect on the velocity field ([10] [16], and [56]). The study here distinguish between the steady regime ($\mathrm{Re} < \mathrm{Re}_{cr}$) and the unsteady regime ($\mathrm{Re} \geq \mathrm{Re}_{cr}$).

Looking at this effect for the steady regime ($\mathrm{Re} < \mathrm{Re}_{cr}$), Figure 4.57 shows the velocity field for Re = 45 at De = 0.0 and 0.2. This figure shows almost no difference despite the difference of Deborah number. The flow is still steady but the velocity contours are slightly extended. Figure 4.58 visualises this extension as it plots a single velocity contour for Re = 40 at different Deborah numbers. This figure illustrates the extension of the velocity contours with the increased fluid elasticity. However, it is noted that for De = 0.2 the velocity contour re-shrinks. Unfortunately, we cannot get higher values of Deborah to complete this investigation as many references mentioned the critical Deborah number at which the laminar vortex shedding is initiated. This will be one of our future work goals.



(a)



(b)

Figure 4.57 Normalized velocity profile for Re = 45 at (a) De = 0.0, (b) De = 0.2

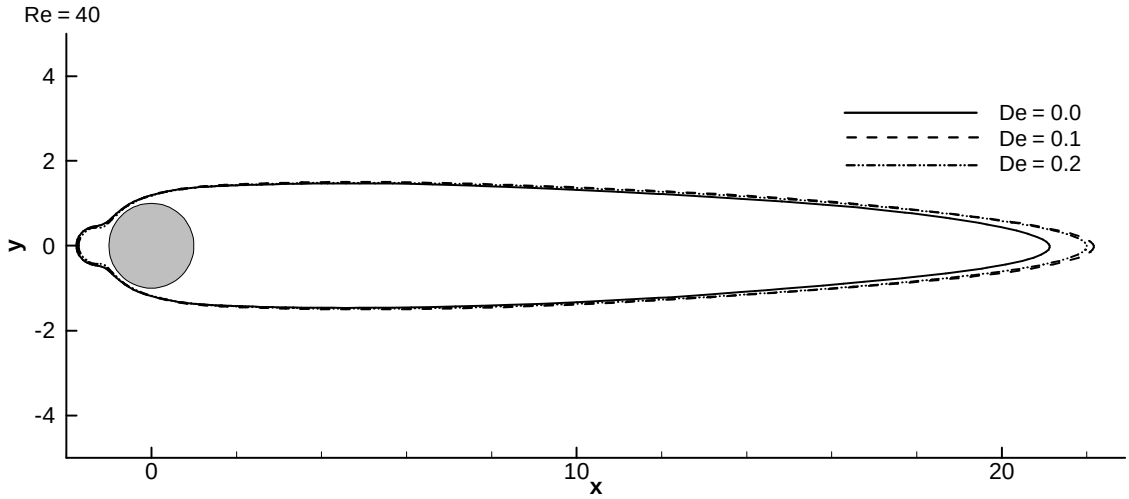


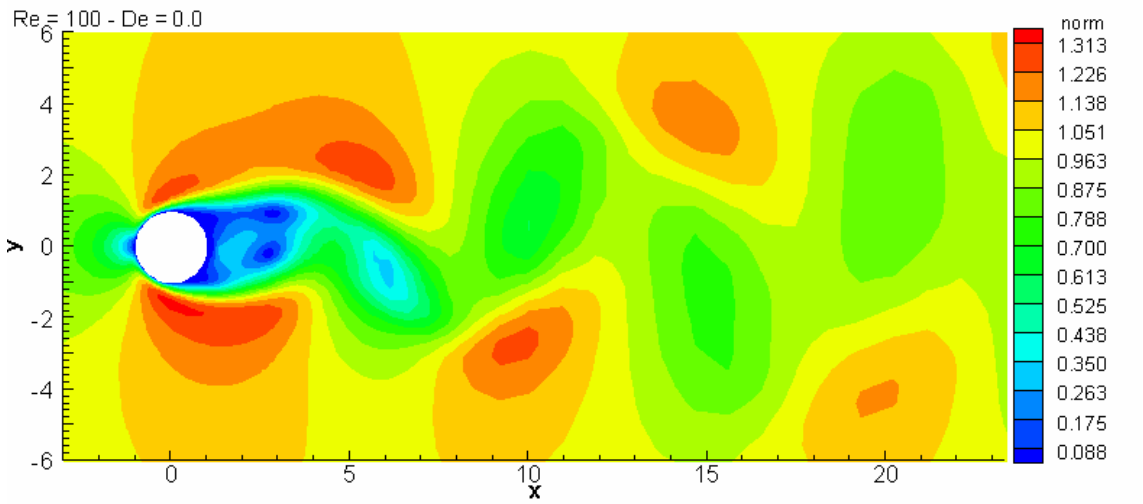
Figure 4.58 Effect of fluid elasticity on velocity contours for Re<Recr

Concerning the unsteady regime, Figure 4.59 shows the velocity profile for Re=100 and De = 0.0, 0.1, and 0.15 respectively. These profiles show the strong influence of the Deborah number on the downstream instability zone. When increasing the Deborah number, the velocity contours extend and the width of the downstream wake decreases.

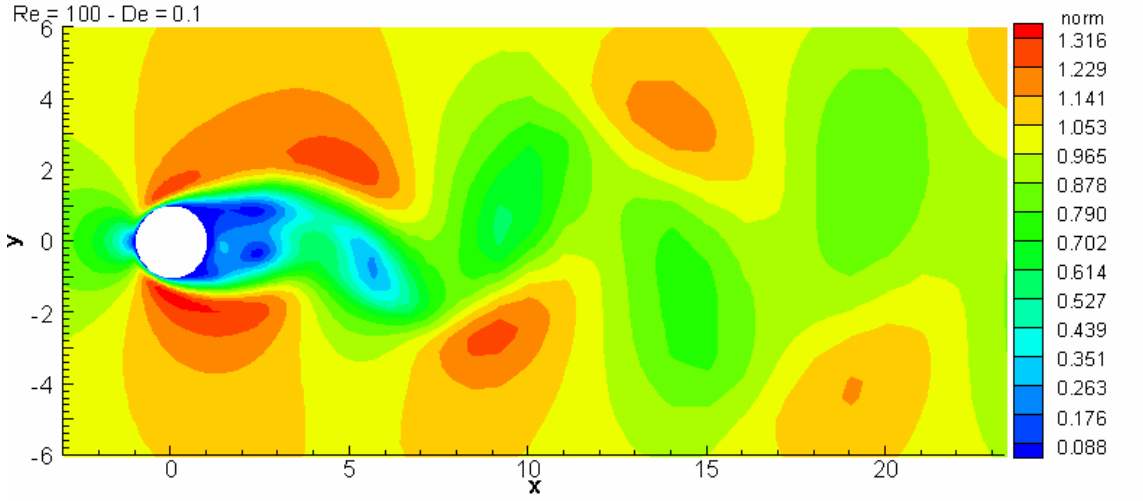
To get a more quantified view on the change of the velocity contours with the fluid elasticity, Figure 4.60 demonstrates only one velocity contour drawn for Re = 60 at De=0.0, 0.1, and 0.2. It can observed in this figure the decrease of the contour length with the Deborah number. Also, the elongation of the contours with the Deborah number is clear.

To get an idea about the fluid elasticity effect on the values of the flow velocities, Figure 4.62 and Figure 4.61 show the values of flow velocity along the section S1, the streamline SLu, the section S3, and the section S4, respectively for a flow having Re = 60 and different Deborah number. From these two figures, it is remarked that:

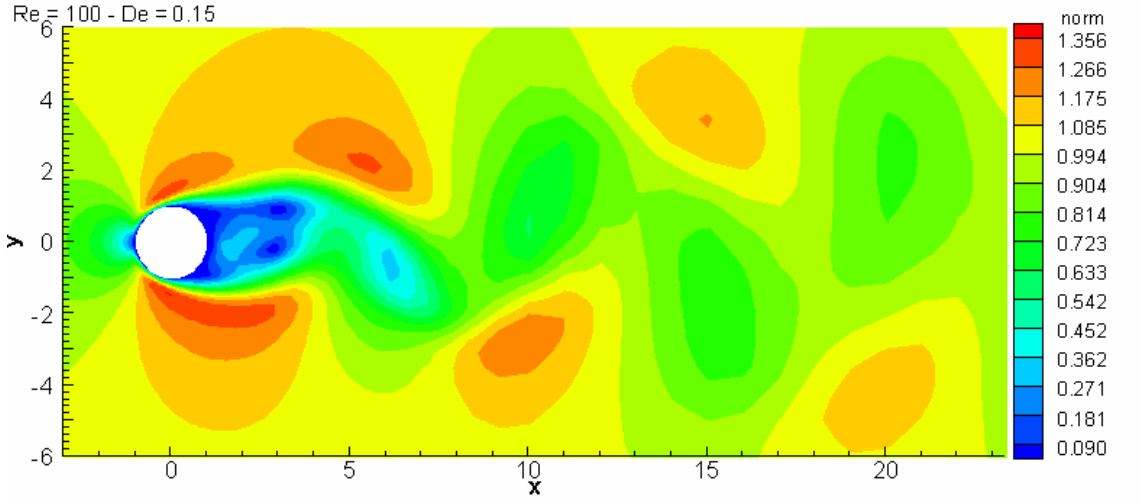
- The maximum reduction of velocity occurs at the second downstream velocity peak. This reduction is of the order 10% for De = 0.2.
- The suppression of the velocity is obvious along the x-axis, while the higher velocity values occur far from the x-axis.
- For the cross sections, the maximum change of velocity takes place on the x-axis on the upstream side. The velocity at this point increases 14% for Deborah number 0.2.



(a)



(b)



(c)

Figure 4.59 Normalized velocity field for Re = 100 at (a) De = 0.0, (b) De = 0.1, and (c) De = 0.15

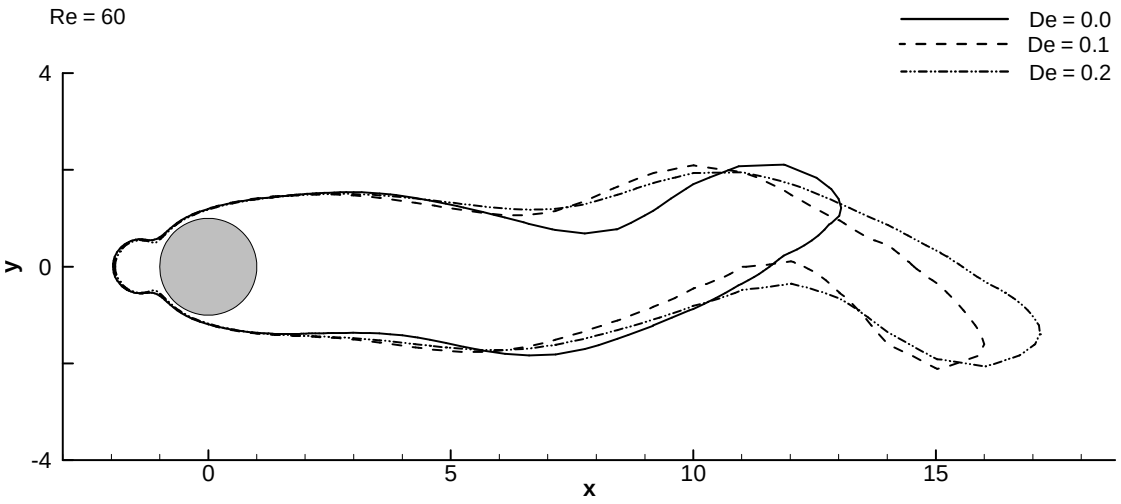
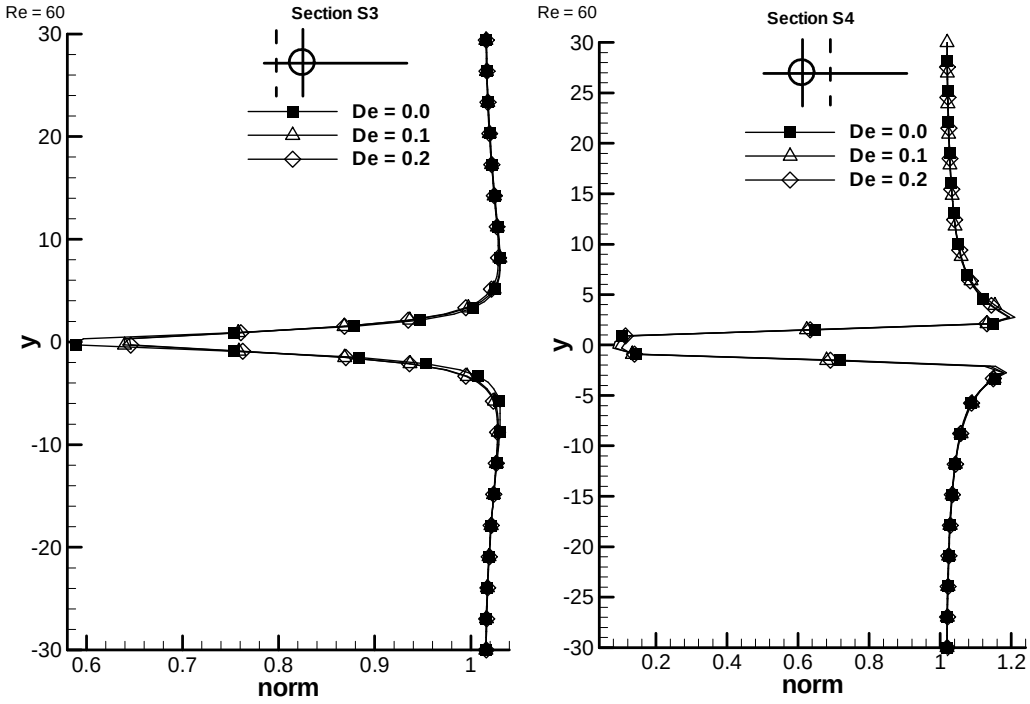
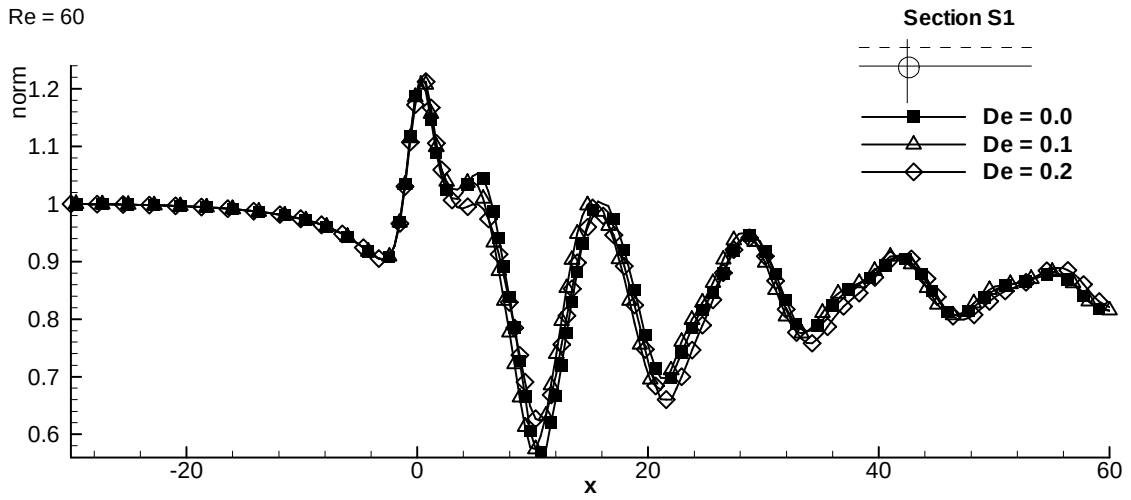


Figure 4.60 change of velocity contours with the Deborah number at Re = 60.

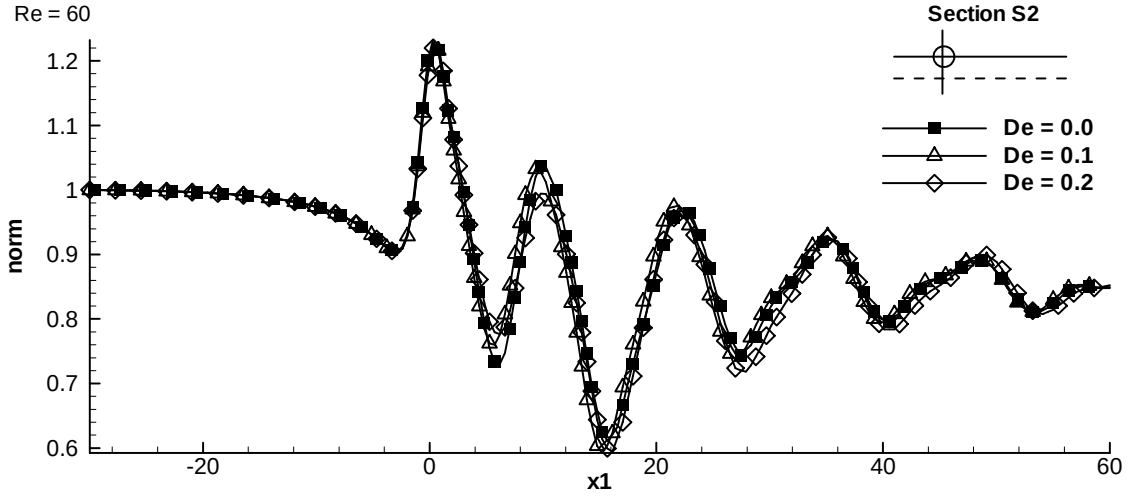


(a) *(b)*

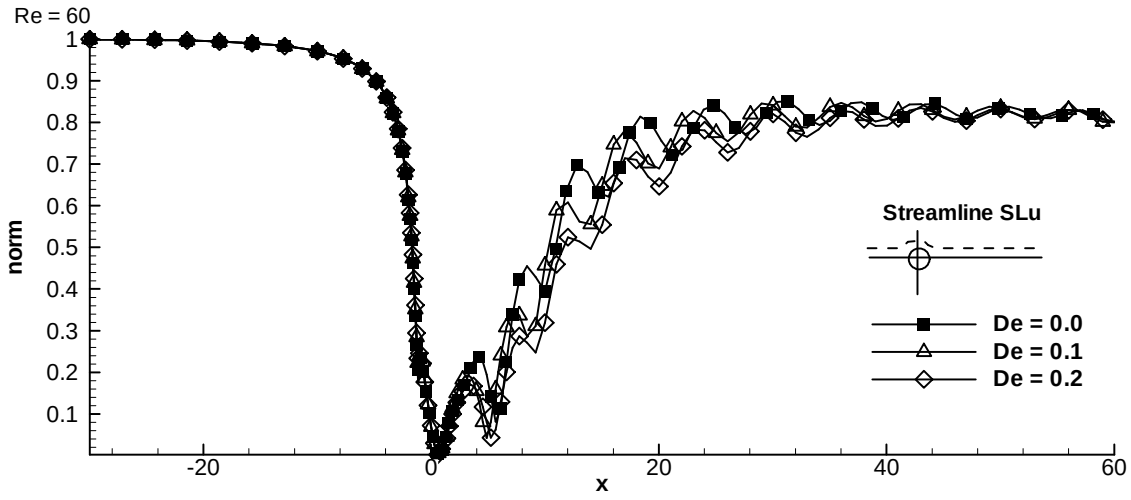
Figure 4.61 Normalized velocity magnitudes for Re = 60 at (a) Section S3 and (b) Section S4



(a)



(b)



(c)

Figure 4.62 Normalized velocity values for Re = 60 at (a) Section S1 and (b) Upper streamline SLu

The characteristics of the flow fluctuations are also influenced by the fluid elasticity. Normally, the extended velocity contours are accompanied with reduced fluctuations. Figure 4.63 presents the reduction of the amplitude of velocity fluctuations with the fluid elasticity for different Reynolds numbers $\mathrm{Re} > \mathrm{Re}_{cr}$.

Figure 4.64 shows the rise time of the flow fluctuations to the maximum amplitude versus the Reynolds number for various Deborah numbers. It is noticed from this figure, that the critical Reynolds number for the Newtonian fluid exhibits increasing rise time which attains its maximum at De = 0.1 then re-decreases. This explains the balance between the reduction of viscous forces, the cause of instability, and the increase of fluid elasticity which re-stabilizes the flow. Normally, the rise time for already stable flows does not affected by fluid elasticity (in studied range of Deborah number), while the flows with laminar vortex shedding are influenced by the fluid elasticity as the rise time decreases.

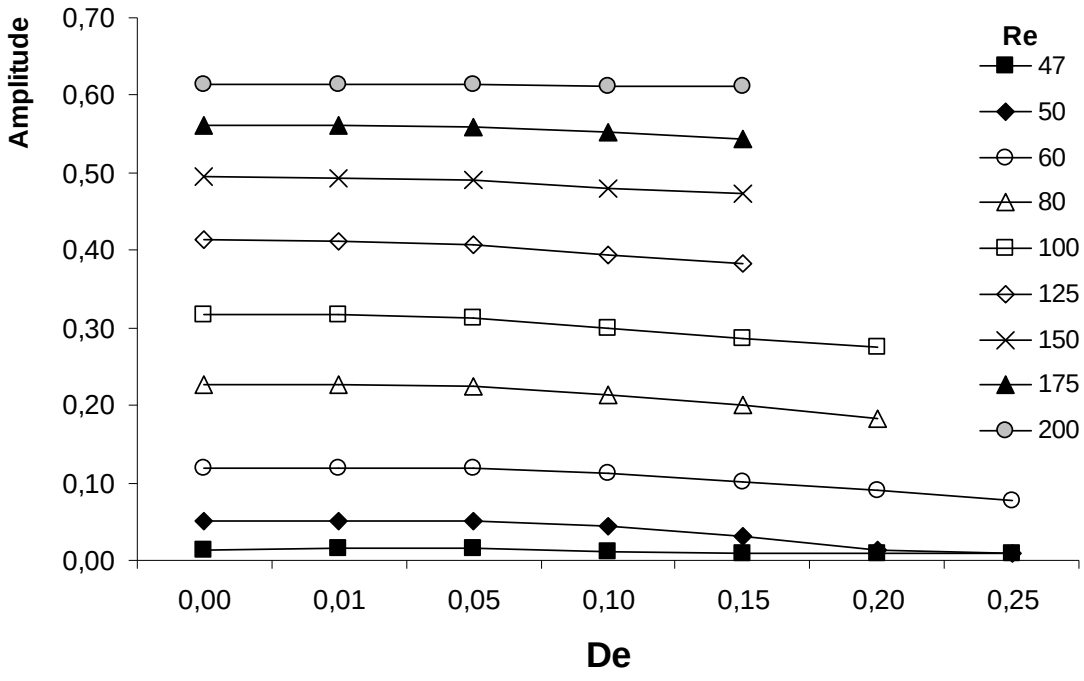


Figure 4.63 Amplitude of vertical velocity fluctuations versus Deborah number for different Reynolds numbers

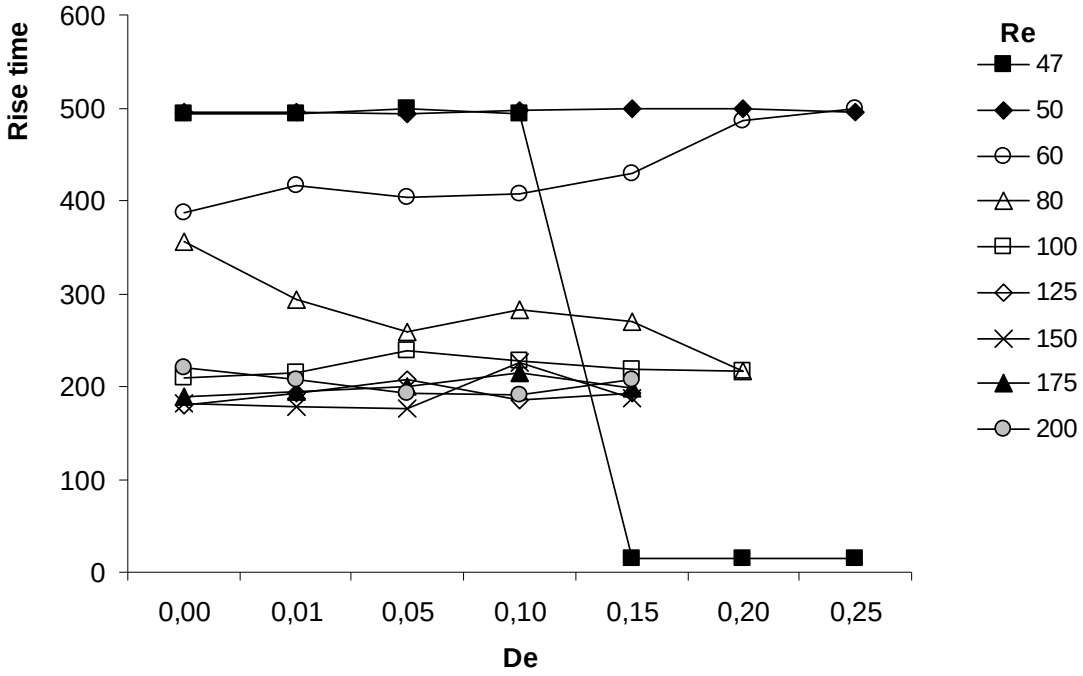


Figure 4.64 Rise time of velocity fluctuations versus Deborah number for different Reynolds numbers

For Re = 60, it is important to notice here that amplitude of the fluctuations decreases with the increasing Deborah number at Figure 4.63, while the rise time increases (see Figure 4.64). This indicates the complexity of the problem as not only the elastic properties of the fluid will stabilize the flow so simply. It is proposed that the effect of normal stresses play an important role in the force balance. This is supported by the concept of critical Deborah number which is discussed by Mckinely et al. [79] who studied the purely elastic flow instabilities. Since we use the PTT model which ignores the solvent (Newtonian) viscosity, the descritized equation of momentum conservation becomes less stable. Hence, higher Deborah numbers cannot be achieved. In our future work, it is intended to use some sophisticated splitting schemes to enhance the computational stability in order to reach higher Deborah numbers. However, in the present range of Deborah number, we cannot verify the concept of critical Deborah number at which the flow returns to the laminar vortex shedding instability.

4.3.6 Strouhal number

The frequency of the flow field fluctuations is an important quantity of the unsteady flow field. We preferred to devote a separate section for studying this frequency because of its importance. As most of the flow properties, the frequency is expressed in the literature in a non-dimensional form. One of the widely spread form of the nod-dimensional frequency is the Strouhal number

$$Str = \frac{fD}{U_0}, \qquad 4.7$$

where f is the frequency of the flow field, D is the cylinder diameter, and U_0 is the free stream velocity.

In the present work, the frequency is evaluated by taking the Fourier transform for the vertical component of velocity. In this section, the change of the Strouhal number versus the Reynolds number and the Deborah number is presented.

Figure 4.65 presents the Strouhal number plotted versus the Reynolds number for different Deborah numbers. It is noted that a progressive increase of the frequency of the flow fluctuations takes place at the critical Reynolds number. The augmentation of the fluctuation frequency is explained by the reduction of the fluid viscosity which decreases the flow stability. Also, the introduction of normal stresses in the flow as an important feature of the viscoelastic fluids enhances these fluctuations. On the molecular level, this can be explained by the elastic characteristics of the polymer particles considered in the dimple assumption.

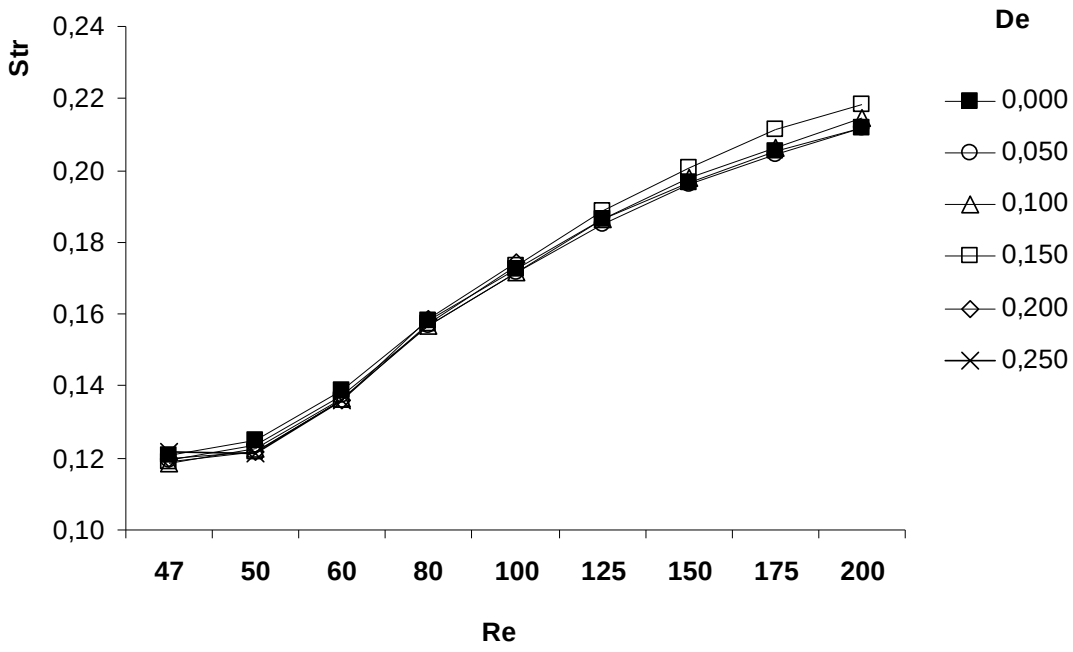


Figure 4.65 Strouhal number versus Reynolds number for different Deborah numbers.

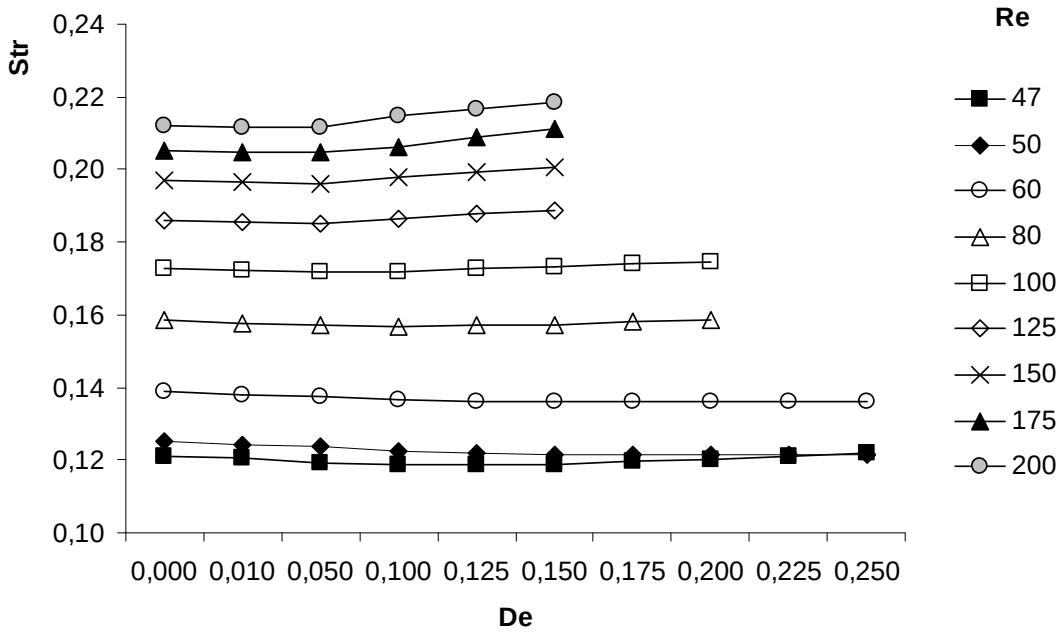


Figure 4.66 Strouhal number versus Deborah number for different Reynolds numbers.

Figure 4.66 illustrates the Strouhal number versus the Deborah number. These curves show that a very small change is noticed with the Deborah number. For moderate Reynolds numbers, the Strouhal number decreases with the Deborah number, while for larger Reynolds numbers, the Strouhal number increases with the Deborah number. As the fluctuation of the flow field is a result of flow instability and fluid viscoelasticity, it is difficult to owe this frequency augmentation to a single reason.

These results are in acceptable agreement with the results of Oliveira [27] , Afonso et al. [19], and Coelho and Pinho [56].

4.3.7 Drag Force

All the flow quantities discussed above can be resumed in the computation of the forces on the cylinder. Note that the force on the cylinder is a very important quantity to evaluate the effect of the fluid properties and to couple the present results with further analyses. In our two-dimensional analysis, drag and lift forces are used to evaluate the fluid property influences. Lift and drag forces are calculated from the resolution of the total force $\mathbf{F}$ exerted on the cylinder which defined as:

$$\mathbf{F} = \int_S \left(-p\mathbf{I} + \boldsymbol{\tau}\right).\mathbf{n}\mathrm{d}S \qquad 4.8$$

where S is an infinitesimal line segment on the stream line and $\mathbf{n}$ is the unit vector directed outward. Hence, in generalized orthogonal coordinates the lift F_L and the drag F_D forces are expressed as:

$$\begin{aligned} F_L &= \int_S \left(\tau_{12}.\frac{\partial x}{\partial \zeta_1} + \left(-p + \tau_{22}\right)\frac{\partial x}{\partial \zeta_2} \right) dS \\ F_D &= \int_S \left(\tau_{12}.\frac{\partial y}{\partial \zeta_1} + \left(-p + \tau_{22}\right)\frac{\partial y}{\partial \zeta_2} \right) dS \end{aligned} \qquad 4.9$$

The drag force is more important in our case for two reasons. Firstly, the laminar flow past a cylinder produces no lift before vortex shedding and very small lift $O(e-3)$ with the vortex shedding instability. Secondly, the most obvious effect of polymer addition is the drag reduction. In this section, the drag force is studied and the next section is devoted to the lift force.

In the following discussion, the effect of the fluid viscosity is introduced firstly, then the influence of fluid elasticity is presented.

The drag force per unit length of cylinder is expressed through the drag coefficient:

$$C_d = F_D\left(\frac{1}{\rho R U_0^{\,2}}\right) \qquad 4.10$$

Figure 4.67 plots the average drag coefficient versus the Deborah number for different Reynolds number. Figure 4.68 expresses root mean square of the drag coefficient against the Deborah number. These figures illustrate some increase of the drag force with the Deborah number till 0.05. Then, the well-known drag decrease starts for De > 0.05. It is thought that the introduction of normal stresses to the flow induces an increase of the drag in the beginning of the passage from Newtonian to viscoelastic fluid. After that, the extensional properties come over the effect of normal stresses and cause drag reduction. It should be noted that Oliveira [27] got similar results. In his his work, he showed that the drag coefficient increases for De = 0.5 and 1.0, then drag re-decreases.

Physically, the drag has two main origins; pressure and stresses. We can split drag into four parts [5]: the pressure drop across the cylinder, the pressure drop due to the shear stress distribution, the pressure drop owing to the normal stress, and the friction shear stress. The viscoelastic effects stabilize the flow and reduce both the pressure drop across the cylinder and the shear stress distribution. Although, normal stresses appear in viscoelastic fluids, the friction factor is reduced. As a result the drag force decreases because of viscoelastic effects.

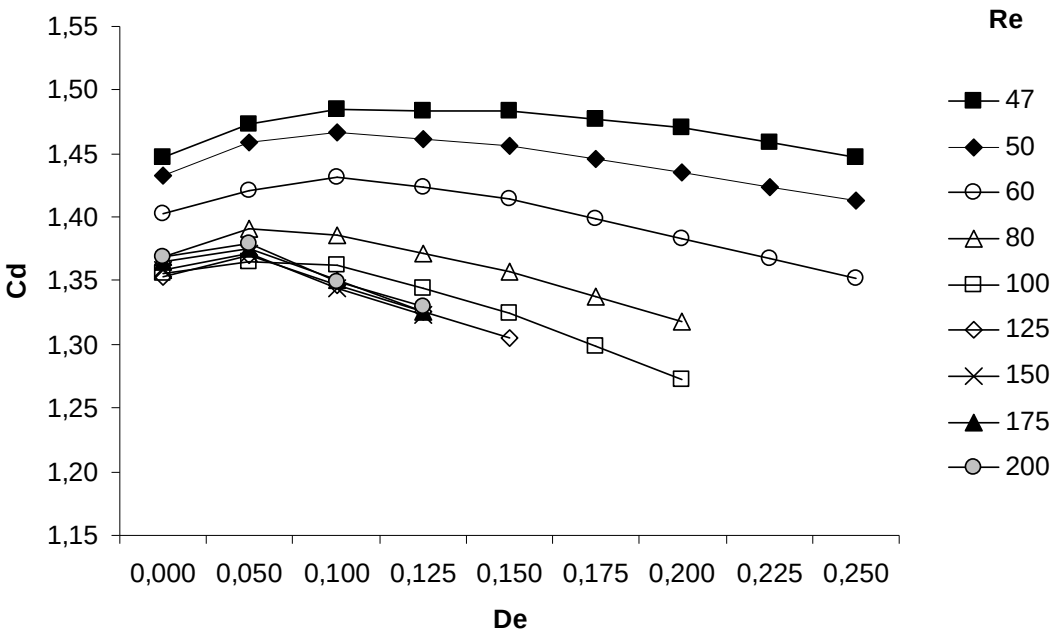


Figure 4.67 Average drag force coefficient versus Deborah number for different Reynolds numbers

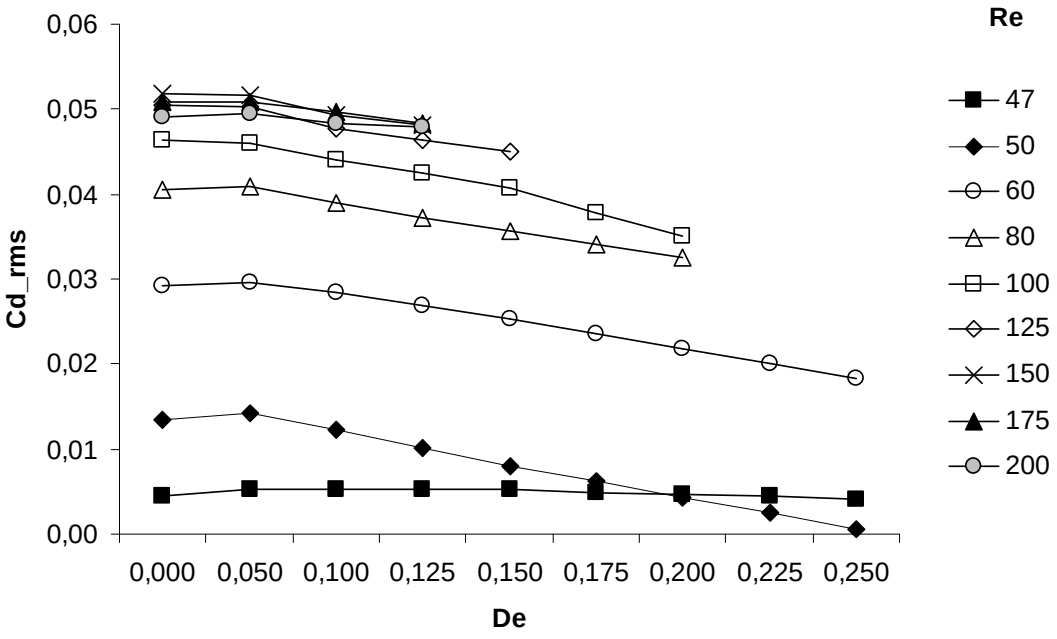


Figure 4.68 Root mean square drag force coefficient versus Deborah number for different Reynolds numbers

It should be noted that these results are only obtained for the non-confined cylinder, while for the literature treating the confined cylinder, the drag decreases with a minor amount of the fluid elasticity. This increase and re-decrease of the drag can be explained as a difference between confined and non-confined cylinder problems. This is proven by referring to Figure 4.11, Figure 4.23, Figure 4.38, Figure 4.47, and Figure 4.61 which show the magnitudes of the flow fields at sections S1 and S2. In all these figures, remarkable values of the stresses, pressure, and velocity are found at a side distance (-3R to 10 R). In the case of the confined cylinder, these values are forced to zero.

A downstream point on the x-axis is selected to plot the time history of the drag. Figure 4.69 shows the instantaneous drag coefficient at this point for Re = 100 and the different Deborah numbers. This figure illustrates that for De > 0.1, the drag force rapidly decreases. Also, even at this point the drag for De = 0.1 is greater than that for the Newtonian fluid.

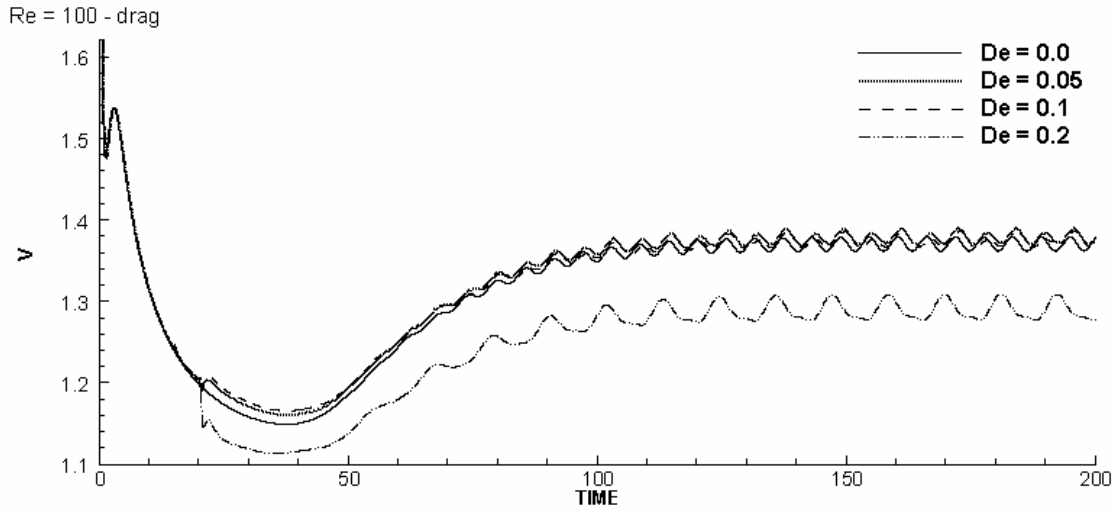


Figure 4.69 Time history of the drag at Re = 100 for different Deborah number

The increase of the Reynolds number reduces the viscous stresses and allows the normal stresses to play greater roles causing drag reduction. Figure 4.70 and Figure 4.71 illustrate the average drag coefficient and its root mean square versus the Reynolds number for different Deborah number. On this figure, it is that the drag force decreases with Reynolds number. The rate of decrease of drag increases with the Deborah number. It is also noted from these figures that with the onset of vortex shedding

instability, the Newtonian drag is always greater than the drag of viscoelastic fluid with De > 0.05.

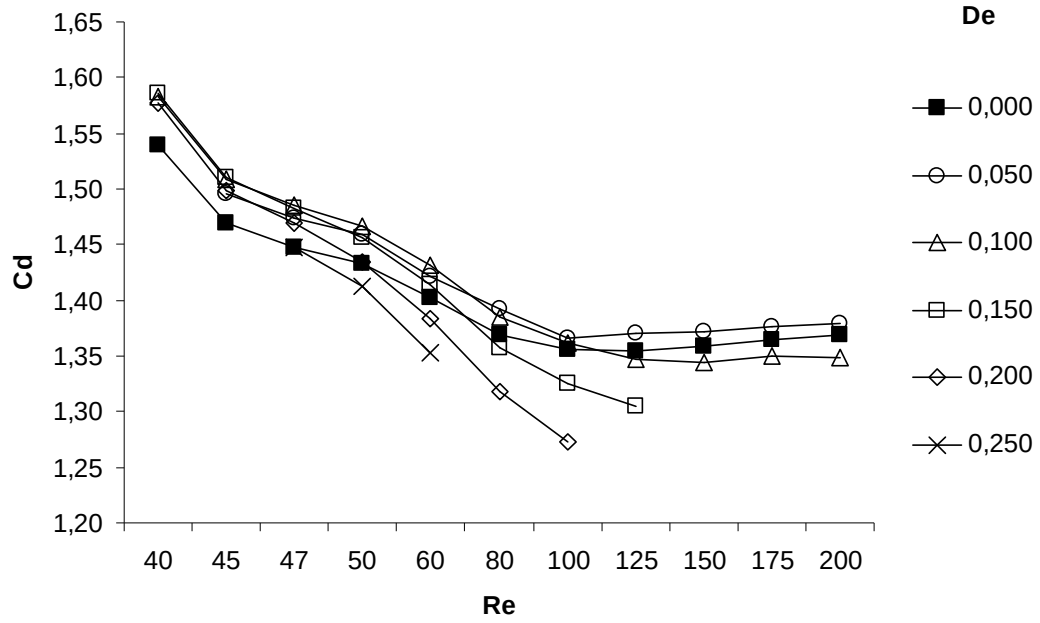


Figure 4.70 Average drag force coefficient versus the Reynolds number for different Deborah number

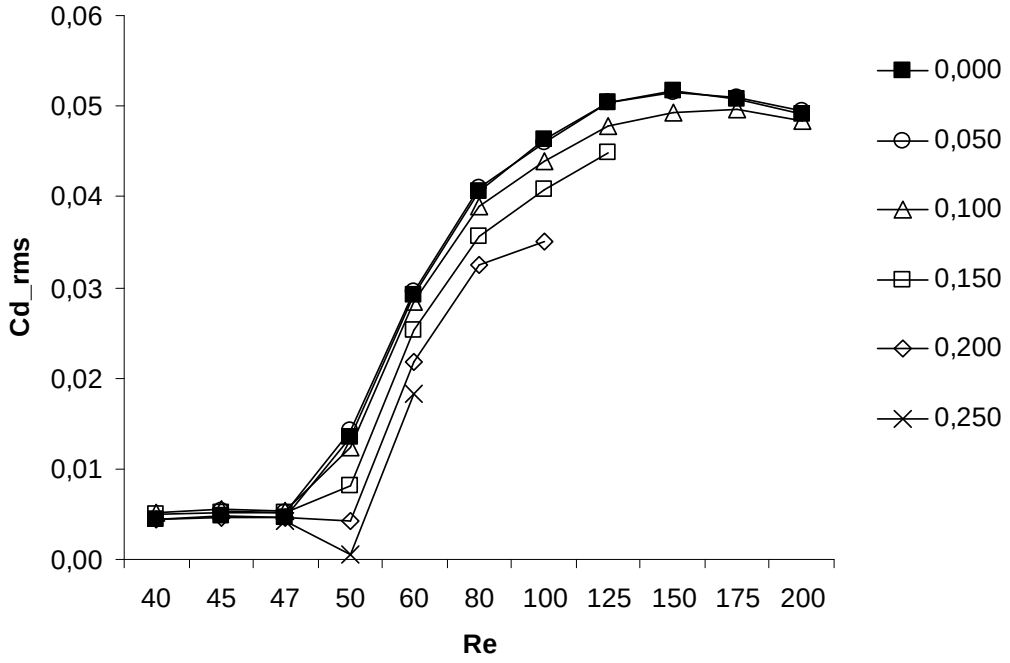


Figure 4.71 Average root mean square drag force coefficient versus the Reynolds number for different Deborah number

4.3.8 Lift Force

For the flow past a cylinder, the lift force represents 0~5% of the force on cylinder. This fact remains in the case of viscoelastic fluids. The principal effects of the fluid elasticity occur because of the extensional properties of fluid which means that the drag force is substantially affected by the fluid elasticity. The lift force per unit length of cylinder can be introduced via the lift coefficient

$$C_l = F_L\left(\frac{1}{\rho R U_0^{\ 2}}\right) \qquad 4.11$$

Figure 4.72 plots the root mean square of lift coefficient versus Deborah number for different Reynolds numbers. This figure shows the decrease of the lift coefficient with the increase of Deborah number

Looking to the influence fluid viscosity on lift force, Figure 4.73 represents the root mean square of the lift coefficient versus Reynolds number. Results show increasing root-mean-square value of lift coefficient with Reynolds number.

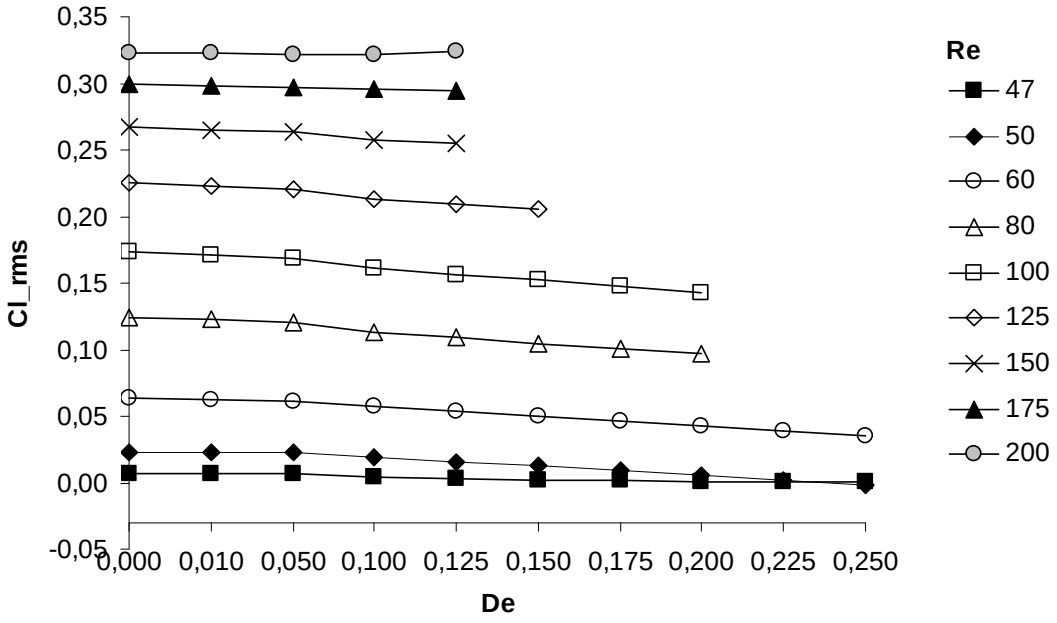


Figure 4.72 Root mean square of the lift coefficient versus the Deborah number for different Reynolds number

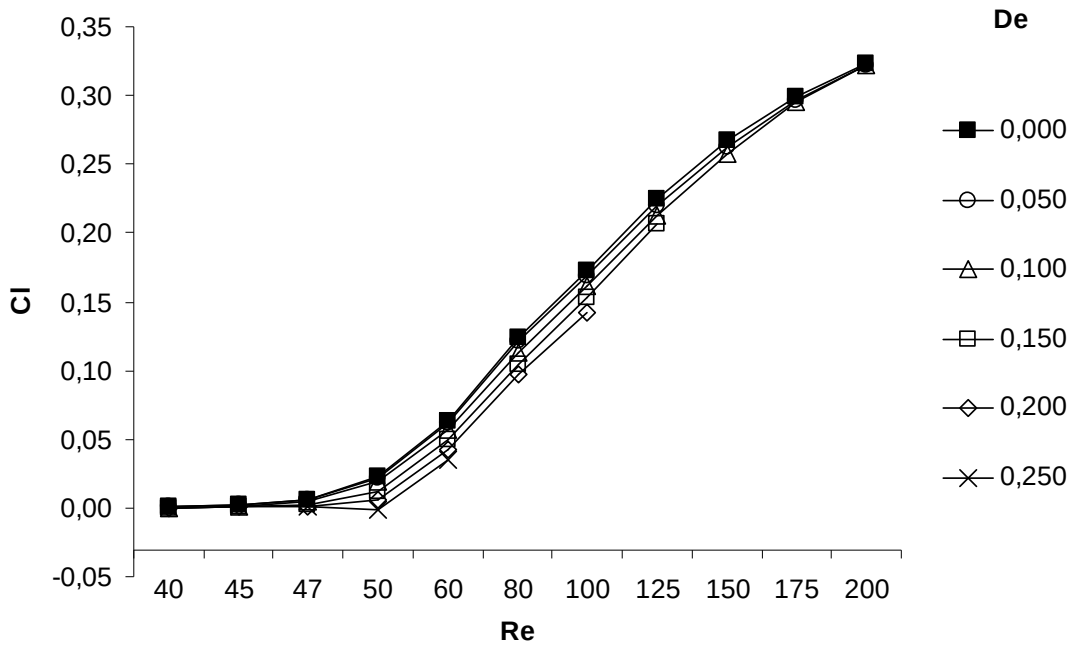


Figure 4.73 Root mean square of the lift coefficient versus the Reynolds number for different Deborah number

Chapter 5: CONCLUSIONS & PERSPECTIVES

5.1. Conclusions

The two-dimensional flow of a viscoelastic PTT fluid past a non-confined cylinder is simulated numerically. The Cartesian governing equations are transformed to the generalized orthogonal coordinates and solved with a finite volume method on staggered grid. An x-direction unit entry far upstream velocity is imposed at the west boundary limit, while symmetry boundary conditions are imposed at both north and south boundaries. At the outlet (east) side, a zero-pressure boundary condition is imposed. The domain is sufficiently extended to guarantee a non confined geometry. The studied range of Reynolds number is limited to the two-dimensional flow instabilities ($Re < 200$) and Deborah number varied in the range 0.0 to 0.25.

The convective terms are evaluated using the second-order accurate QUICK scheme [68]. The diffusion terms are calculated with the second order accurate centred difference scheme. For the time marching algorithm, the first-order accurate Euler forward explicit scheme is applied obeying the adaptation of Marker and Cell algorithm. The grid is optimized to be is 20000 nodal points.

The obtained results for Newtonian flow, indicate that the flow exhibits three regimes; creeping regime ($Re < 5$) with no separation from the cylinder, laminar steady regime ($5 \leq Re < 47$) in which two steady symmetric vortices are created, and the laminar vortex shedding regime ($Re \geq 47$) in which the two vortices are no longer symmetric and steady and the von Kàrmàn street is established. Results for the Newtonian case are compared to the literature. It is seen that the present values are in close agreement with previous studies: the difference is (0.0% - 4.2%) for the Strouhal number and (0.36% - 5.9%) for the drag coefficient. These results can be considered as a good validation.

The viscoelastic results are validated by comparing the non-dimensional fluctuations frequency (Roshko number) to the equation reported by Pipe & Monkewitz [58] which

relates the Reynolds number and the Roshko number. The present results show good agreement in trend and values with this equation. The present viscoelastic results provide the following conclusions:

- The extra-shear stress

  Extra-shear stress is strongly influenced by the Reynolds number. The maximum extra-shear stress zone is located at the cylinder surface on the upstream side and this location does not change with the Reynolds number. For the steady flow regime, the extra-shear stress is symmetrically distributed about the x-axis. With the onset of the von Karman vortex street, the extra-shear stress zones are extended and well deformed. With further increase of the Reynolds number, a periodic alternance of positive and negative shear zone are found along the x-axis. The increase of Reynolds number causes strong changes downstream till a distance of about 10 *R*, then the fluctuations of the extra-shear stress become longitudinal waves with decaying amplitude.

  For steady flow regime, the Deborah number affects the upstream shear stress and the downstream shear is almost unaffected.

- The first normal stress difference:

  The normal stress magnitudes increase with the Reynolds number. These effects show the increase of the stresses in the main flow direction (extensional stresses) over the lateral stresses causing the extension of instability zones and reduction of their width.

  Increasing the Deborah number suppresses the fluctuation of the stress field. The influence of the Deborah number manifests itself in a zone of about 25 *R* downstream the cylinder. The Deborah number changes the magnitude of the first normal stress difference within a narrow range.

- The pressure distribution:

  With the increase of the Reynolds number, the positive pressure area (upstream) is lightly influenced, while the negative pressure area (downstream) is strongly influenced. The positive-pressure contour keeps its uniformity with the increasing

Reynolds number. On the other side, the negative-pressure contour loses its uniformity. The increase of the Reynolds number causes some negative pressure values at the lower upstream cylinder side which assists the change of lift force. The wake angle decreases with the reduction of the fluid viscosity but in a narrow range (40°-49°).

Despite the very slight increase of the Deborah number, the negative pressure contours downstream the cylinder strongly decreases from Newtonian fluid to viscoelastic fluid. With further increase of Deborah number most of maximum negative pressure zone downstream the cylinder vanishes. On the other hand, the effect of Deborah number on the positive pressure zone upstream the cylinder is unnoticeable. The range of change of the wake angle, for each Reynolds number, is very narrow (2° - 3°). The Newtonian fluid has the largest wake angles.

- The vorticity:

With the increase of Reynolds number, the flow becomes less stable and the two recirculation zones extend and fluctuate. At higher Reynolds numbers, another two recirculation zones appear downstream on the x-axis. At a side distance of 2*R*, the change of the maximum vorticity magnitude is not largely changed with the fluid viscosity (3%). The maximum magnitude of vorticity occurs on the cylinder surface at the upstream side.

- The velocity field:

The upstream velocity field shrinks when increasing of the Reynolds number, while the downstream zone extends and fluctuates laterally with the Reynolds number. As the Reynolds number increases beyond the critical Reynolds number, both amplitude and frequency of fluctuations increase progressively. On the x-axis, the velocity values are in the same order of magnitude as the far entry velocity, while at a side distance of 2*R* the maximum velocity magnitude increases by about 30% higher than the entry velocity. When increasing the Deborah number, the velocity contours extend and the width of the instability zone decreases. The reduction of velocity is in the order of 10% for De = 0.2.

- The Strouhal number

  The Strouhal number increases with the Reynolds number. The results show that a very small change of the Strouhal number is noticed with the Deborah number. For moderate Reynolds numbers, the Strouhal number decreases with the Deborah number, while for larger Reynolds numbers, the Strouhal number increases with the Deborah number. The frequency of fluctuations for viscoelastic fluids is always smaller than the corresponding Newtonian fluid.

- The drag force:

  The drag force decreases with the Reynolds number. The rate of decrease of drag increases the Deborah number. Results illustrate some increase of the drag force with the increased Deborah number till De = 0.05. Then, the well-known drag decrease starts for De > 0.05. Oliveira [27] got similar results.

- The lift force:

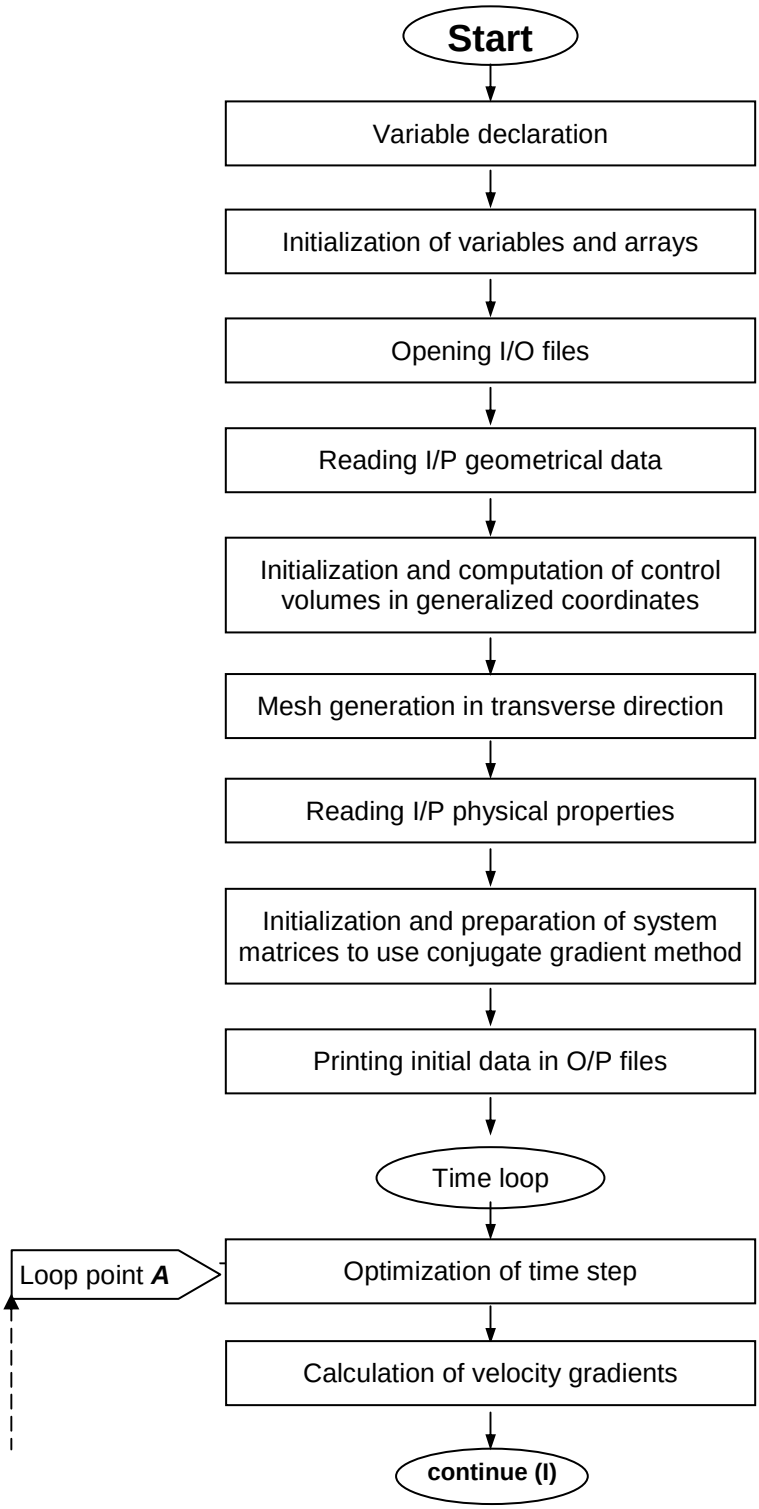
  Results show increasing lift coefficient with Reynolds number and decrease of the lift coefficient with Deborah number.

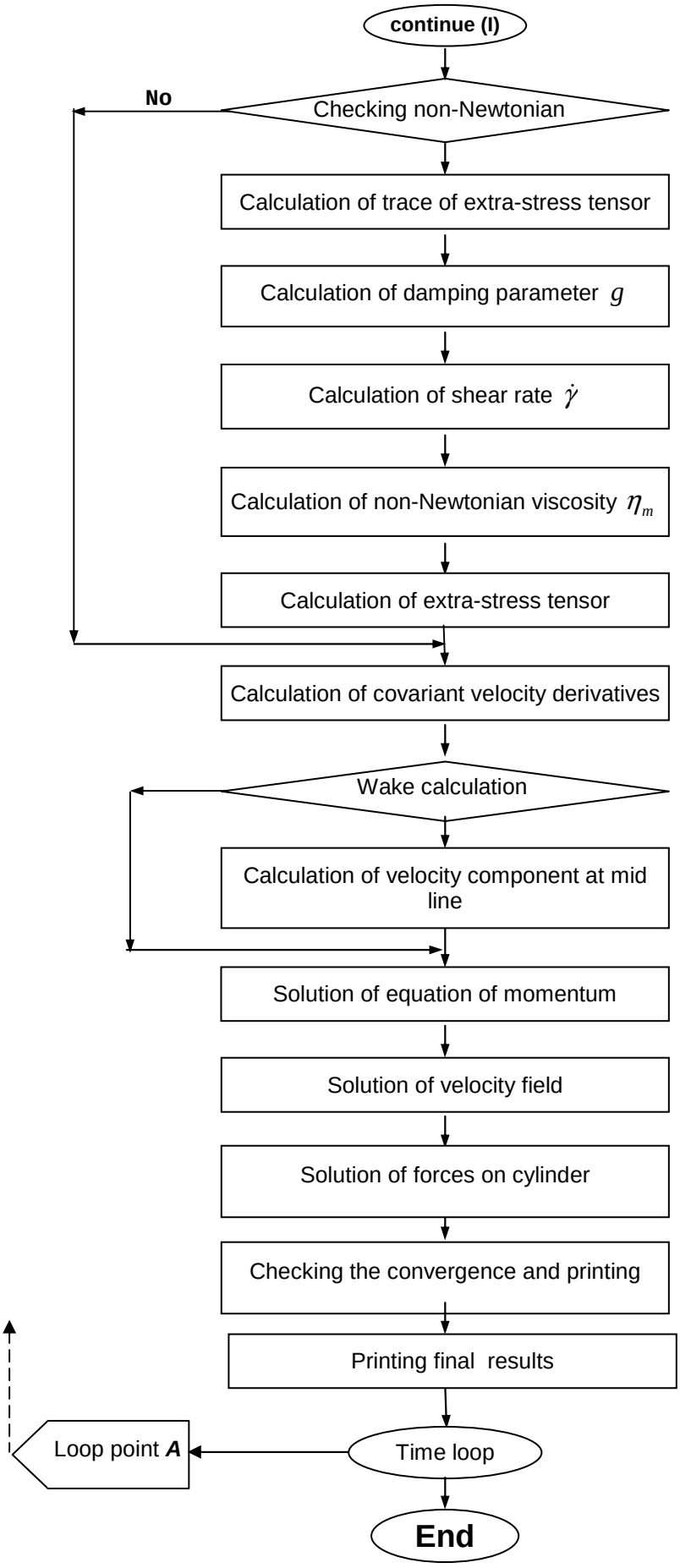
5.2. Perspectives

The following points are recommended for future work:

- Increasing the range of Deborah number range to exceed 0.25.
- Transferring the code to parallelized one to solve the 3D flow.
- Working with other more complex geometries.
- Coupling fluid mechanics problem to the structure of the obstacle to pass to the fluid-structure interaction.

APPENDIX: FLOWCHART OF THE DEVELOPED CODE




continue (I)
No
Checking non-Newtonian
Calculation of trace of extra-stress tensor
Calculation of damping parameter g
Calculation of shear rate $\dot{\gamma}$
Calculation of non-Newtonian viscosity η_m
Calculation of extra-stress tensor
Calculation of covariant velocity derivatives
Wake calculation
Calculation of velocity component at mid line
Solution of equation of momentum
Solution of velocity field
Solution of forces on cylinder
Checking the convergence and printing
Printing final results
Time loop
Loop point A
End

REFERENCES

1 **Phan-Thien N., Tanner R. I.,** "A new constitutive equation derived from network theory", *J. Non-Newtonian Fluid Mech.* (1977), Vol. 2, p. 353-365.

2 **Sumer B. M. & Fredsøe J**, "Hydrodynamics around cylindrical structures", *World Scientific*(2006), revised edition.

3 **Williamson C. H. K**., "Vortex dynamics in the cylinder wake", Annu. Rev. Fluid. Mech. 1996.28t477-53.

4 **Oliveira P.J., Pinho F.T., Pinto G.A**., "Numerical simulation of non-linear elastic flows with a general collocated finite-volume method", *J. Non-Newtonian Fluid Mech.* (1998), Vol. 79, p. 1–43.

5 **Phan-Thien N., Dou H.-S.**, "Viscoelastic flow past a cylinder: drag coefficient", *Comput. Methods Appl. Mech. Engrg.* (1999), Vol. 180, p. 243-266.

6 **Dou H.-S., Phan-Thien N.,** "The flow of an Oldroyd-B fluid past a cylinder in a channel: adaptive viscosity vorticity (DAVSS-ω) formulation", *J. Non-Newtonian Fluid Mech.* (1999), Vol. 87, p. 47-73.

7 **Behr M., Arora D., Coronado O.M. & Pasquali M.,** "GLS-type finite element methods for viscoelastic fluid flow simulation", *Computational Fluid and Solid Mechanics* (2005), p. 135-308.

8 **Sahin M. and Wilson H. J.,** "A semi-staggered dilation-free finite volume method for the numerical solution of viscoelastic fluid flows on all-hexahedral elements", *J. Non-Newtonian Fluid Mech.* (2007), Vol. 147, p. 79–91.

9 **Sahin M.,** "Apreconditioned semi-staggered dilation-free finite volume method for the incompressible Navier–Stokes equations on all-hexahedral elements", *Int. J. Numer. Methods Fluids* (2005), Vol. 49, p. 959–974.

10 **Dou H.-S. and Phan-Thien N.,** "Viscoelastic flow past a confined cylinder: Instability and velocity inflection", *Chemical Engineering Science* (2007), Vol. 62 p. 3909 – 3929.

11 **Rasmussen H. K**., "Time-dependent finite-element method for the simulation of three-dimensional viscoelastic flow with integral models*", J. Non-Newtonian Fluid Mech.* (1999), Vol. 84, p. 217-232.

12 **Caola A.E., Joo Y.L., Armstrong R.C., Brown R.A.,** "Highly parallel time integration of viscoelastic flows", *J. Non-Newtonian Fluid Mech.* (2001), Vol. 100, p. 191–216.

13 **Doering C. R., Eckhardt B., Schumacher J.**, "Failure of energy stability in Oldroyd-B fluids at arbitrarily low Reynolds numbers", *J. Non-Newtonian Fluid Mech.* (2006), Vol. 135, p. 92–96.

14 **Renardy M.,** "Short communication: Viscoelastic stagnation point flow in a wake", *J. Non-Newtonian Fluid Mech.* (2006), Vol. 138, p. 206–208.

15 **Phan-Thien N.,** "Squeezing a viscoelastic liquid from a wedge: an exact solution", *J. Non-Newtonian Fluid Mech.* (1984), Vol. 16(3), p. 329-345.

16 **Baaijens F., Selen S., Baaijens H., Peters G., Meijer H.,** "Viscoelastic flow past a confined cylinder of a low density polyethylene melt", *J. Non-Newtonian Fluid Mech.* (1997), Vol. 68, p. 173-203.

17 **Dou H., Phan-Thien N.,** "Parallelisation of an unstructured finite volume code with PVM: viscoelastic flow around a cylinder", J. *Non-Newtonian Fluid Mech.* (1998), Vol. 77, p. 21–51.

18 **Chauviere C. and Owens R.,** "A new spectral element method for the reliable computation of viscoelastic flow", *Computer methods in applied mechanics and engineering* (2001), Vol. 190(31), p. 3999-4018.

19 **Afonso A., Alves M. A., Pinho F. T. and Oliveira P. J.,** "Uniform flow of viscoelastic fluids past a confined falling cylinder", *Rheologica Acta* (2008), Vol. 47(3), p. 325-348.

20 **Xue S.-C., Phan-Thien N., R.I. Tanner,** "Numerical study of secondary flows of viscoelastic fluid in straight pipes by an implicit finite volume method", *J. Non-Newtonian Fluid Mech.* (1995), Vol. 59, p. 191-213.

21 **Yamamoto T., Ishiyama M., Nakajima M., Nakamura K., Mori N.,** "Three-dimensional viscoelastic flows through a rectangular channel with a cavity", *J. Non-Newtonian Fluid Mech.* (2003), Vol. 114, p. 13–31.

22 **Cruz D., Pinho F., Oliveira P.,** "Analytical solutions for fully developed laminar flow of some viscoelastic liquids with a Newtonian solvent contribution", *J. Non-Newtonian Fluid Mech.* (2005), Vol. 132, p. 28–35.

23 **Alves M., Oliveira P., Pinho F.,** "On the effect of contraction ratio in viscoelastic flow through abrupt contractions", *J. Non-Newtonian Fluid Mech*. (2004), Vol. 122, p. 117–130.

24 **Akyildiz F. T., Bellout H.,** " Viscoelastic Lubrication With Phan-Thein-Tanner Fluid (PTT)", *Journal of Tribology* (2004), Vol. 126.

25 **Sun J., Smith M.D., Armstrong R.C., Brown R.A.,** "Finite element method for viscoelastic flows based on the discrete adaptive viscoelastic stress splitting and the discontinuous Galerkin method: DAVSS-G/DG", *J. Non-Newtonian Fluid Mech.* (1999), Vol. 86, p. 281-307.

26 **Hulsen M. A., Fattal R., Kupferman R.,** "Flow of viscoelastic fluids past a cylinder at high Weissenberg number: Stabilized simulations using matrix logarithms", *J. Non-Newtonian Fluid Mech.* (2005), Vol. 127, p. 27–39.

27 **Oliveira P. J.,** "Method for time-dependent simulations of viscoelastic flows: vortex shedding behind cylinder", *J. Non-Newtonian Fluid Mech.* (2001), Vol. 101, p. 113–137.

28 **Lozinski A. and Chauvière C.,** "A fast solver for Fokker--Planck equation applied to viscoelastic flows calculations: 2D FENE model Source", *Journal of Computational Physics* (2003), Vol. 189(2), p. 607 – 625.

29 **Dou H.-S., Phan-Thien N.,** "Criteria of negative wake generation behind a cylinder", *Rheol Acta* (2004), Vol. 43, p. 203–209.

30 **Ogata S., Osano Y., and Watanabe K.,** "Effect of Surfactant Solutions on the Drag and the Flow Pattern of a Circular Cylinder", *AIChE Journal* (2006), Vol. 52(1), p. 16-37.

31 **Mompean G., Jongen T., Devillea M.O., Gatski T.B.,** "On algebraic extra-stress models for the simulation of viscoelastic flows*", J. Non-Newtonian Fluid Mech.* (1998), Vol. 79, p. 261-281.

32 **Mompean G.,** "On predicting abrupt contraction flows with differential and algebraic viscoelastic models", *Computers & Fluids* (2002), Vol. 31, p. 935–956.

33 **Helin L.,** "Développement de modèles algébriques explicites pour les fluides viscoélastiques", *Thesis – USTL,* (2006).

34 **Tanner R. I.,** "Engineering Rheology", *Oxford University Press* (2000), 2nd Edition.

35 **Phan-Thien N.,** "Understanding viscoelasticity: Basics of rheology", *Springer-Verlag Berlin Heidelberg,* (2002).

36 **Owens R. G. and Phillips T. N.,** "Computational rheology", *Imperial College Press,* (2002).

37 **Hulsen M.A., van Heel A.P.G., van den Brule B.H.A.A.,** "Simulation of viscoelastic flows using Brownian configuration fields*", J. Non-Newtonian Fluid Mech.* (1997), Vol. 70, p. 79-101.

38 **Matallah H., Townsend P., Webster M.F.,** "Recovery and stress-splitting schemes for viscoelastic flows", *J. Non-Newtonian Fluid Mech.* (1998), Vol. 75, p. 139–166.

39 **Fan Y., Tanner R.I., Phan-Thien N.** "Galerkin/least-square finite-element methods for steady viscoelastic flows", *J. Non-Newtonian Fluid Mech.* (1999), Vol. 84, p. 233-256.

40 **Fattal R., Kupferman R.,** "Time-dependent simulation of viscoelastic flows at high weissenberg number using the log-conformation representation*", J. Non-Newtonian Fluid Mech.* (2005), Vol. 126, p. 23–37.

41 **Coronado O. M., Arora D., Behr M. and Pasquali M.,** "Four-field Galerkin/least-squares formulation for viscoelastic fluids", *J. Non-Newtonian Fluid Mech.* (2006), Vol. 140(1-3), p. 132-144.

42 **Coronado O. M., Arora D., Behr M. and Pasquali M.,** "A simple method for simulating general viscoelastic fluid flows with an alternate log-conformation formulation", *J. Non-Newtonian Fluid Mech.* (2007), Vol. 147(3), p. 189-199.

43 **Alves M.A., Pinho F.T., Oliveira P.J.,** "The flow of viscoelastic fluids past a cylinder: finite-volume high-resolution methods", *J. Non-Newtonian Fluid Mech.* (2001), Vol. 97, p. 207–232.

44 **Sahin M., Owens R. G.,** "On the effects of viscoelasticity on two-dimensional vortex dynamics in the cylinder wake", *J. Non-Newtonian Fluid Mech.* (2004), Vol. 123, p. 121–139.

45 **Oliveira P. J., Miranda A. I.P.,** "A numerical study of steady and unsteady viscoelastic flow past bounded cylinders" *J. Non-Newtonian Fluid Mech.* (2005), Vol. 127, p. 51–66 .

46 **Wapperom P., Webster M.F.,** "Simulation for viscoelastic flow by a finite volume/element method ",*Comput. Methods Appl. Mech. Engrg.* (1999), Vol. 180, p. 281-304.

47 **Chauvière C. and Owens R. G.,** "A new spectrl element method for the reliable computation of viscoelastic flow", *Comput. Methods Appl. Mech. Engrg*. (2001), Vol. 190, p. 39999-4018.

48 **Chauvière C.,** "A first error indicator for micro–macro simulations of viscoelastic fluids having closed-form constitutive equations", *Comput. Methods Appl. Mech. Engrg.* (2002), Vol. 191, p. 5579–5594.

49 **Owens R. G., Chauvière C. and Philips T. N.,** "A locally-upwinded spectral technique (LUST) for viscoelastic flows", *Journal of Non-Newtonian Fluid Mechanics*(2002), Vol 108(1-3), p. 49-71.

50 **Shiang A.H., Lin J.C., Öztekin A., Rockwell D.,** "Viscoelastic flow around a confined circular cylinder: measurements using high-image-density particle image velocimetry", *J. Non-Newtonian Fluid Mech.* (1997), Vol. 73, p. 29-49.

51 **Cadot O. and Lebey M.,** "Shear instability inhibition in a cylinder wake by local injection of a viscoelastic fluid", *Physics of Fluids* (1999), Vol. 11(2).

52 **Cadot O. & KUMAR S.,** "Experimental characterization of viscoelastic effects on two- and three-dimensional shear instabilities", *J. Fluid Mech.* (2000), Vol. 416, p. 151-172.

53 **Cadot O.,** " Partial roll-up of a viscoelastic Kármán street ", *Eur. J. Mech. B – Fluids* (2001), Vol. 20, p. 145–153.

54 **Cressman J. R., Bailey Q., & Goldburg W. I.,** "Modification of a vortex street by a polymer additive", *Physics of Fluids* (2001), Vol. 13(4), p. 125-141.

55 **Coelho P.M., Pinho F.T.,** "Vortex shedding in cylinder flow of shear-thinning fluids I. Identification and demarcation of flow regimes", *J. Non-Newtonian Fluid Mech.* (2003), Vol. 110, p. 143–176.

56 **Coelho P.M., Pinho F.T.,** "Vortex shedding in cylinder flow of shear-thinning fluids II. Flow characteristics", *J. Non-Newtonian Fluid Mech.* (2003), Vol. 110, p. 177–193.

57 **Coelho P.M., Pinho F.T.,** "Vortex shedding in cylinder flow of shear-thinning fluids. III Pressure measurements", *J. Non-Newtonian Fluid Mech.* (2004), Vol. 121, p. 55–68.

58 **Pipe C.J., Monkewtiz P.A.,** "Vortex shedding in flows of dilute polymer solutions", *J. Non-Newtonian Fluid Mech.* (2006), Vol. 139, p. 54–67.

59 **Phan-Thien N., Tanner R. I.,** "A new constitutive equation derived from network theory", *J. Non-Newtonian Fluid Mech.* (1977), Vol. 2, p. 353-365.

60 **Phan-Thien N.,** "Squeezing a viscoelastic liquid from a wedge: an exact solution", *J. Non-Newtonian Fluid Mech.* (1984), Vol. 16 (3), p. 329-345.

61 **Pope S. B,** "The calculation of turbulent recirculating flows in general orthogonal coordinates", *J. Comp Phys* (1978), Vol. 2, p. 197-217.

62 **Magnaudet J., Rivero M. and Fabre J.,** "Accelerated flows past a rigid sphere or a spherical bubble. I: Steady straining flow", *J. of Fluid Mech.* (1995), Vol. 284, p. 97-135.

63 **Thais L., Mompean G. & Naji H.,** "Computation of flow past a circular cylinder using general orthogonal coordinates", *5th World Congress on Computational Mechanics WCCM V*, July 7-12, (2002) Vienna, Austria.

64 **Perera MGN and Walters K.** "Long-range memory effects in flows involving abrupt changes in geometry, Part I. Flows associated with L-shaped and T-shaped geometries", *J. Non-Newtonian Fluid Mech.* (1977), Vol. 2, p. 49–81.

65 **Mendelson MA, Yeh PW, Armstrong RC and Brown RA.** Approximation error in finite element calculation of viscoelasticfluid flows", *J. Non-Newtonian Fluid Mech.* (1982), Vol. 10, p. 31–54.

66 **Beris AN, Armstrong RC and Brown RA.** "Finite element calculation of viscoelastic flow in a Journal bearing: I, Small eccentricities", *J. Non-Newtonian Fluid Mech.* (1984), Vol. 16, p. 141–172.

67 **Hirsch C.,** "Numerical computation of internal and external: Fundamentals of computational fluid dynamics", *Elsevier*(2007), 2nd ed.

68 **Leonard, B. P.** "A stable and accurate convective modelling procedure based on quadratic upstream interpolation", *Comp. Meth. Appl. Mech. Engr.* (1979), Vol. 19, p. 58-98.

69 **Mompean G. & Deville M.,** "Unsteady finite volume simulation of Oldroyd-B fluid through a three-dimensional planar contraction", *J. Non-Newtonian Fluid Mech.* (1997), Vol. 72, p. 253-279.

70 **Persillon H., Braza M.,** "Physical analysis of the transition to turbulence in the wake of circular cylinder by thr,ee-dimentional Navier-Stokes simulation", *J. Fluid Mech*(1998), Vol. 365, p. 23-88.

71 **Versteeg H. K. and Malalasekera W.,** "An introduction to computational fluid dynamics: The finite volume method", *Longman Group Ltd.* (1995).

72 **Harlow F. H. and Welch J. E.,** "Numerical calculation of time-dependant viscous incompressible flow of fluid with free surfaces", *Phys. Fluids* (1965), Vol. 8, p. 2182-2189.

73 **Aris R.,** "Vectors, Tensors, and the Basic Equations of Fluid Mechanics", *Dover Publications* (1989), 2nd edition.

74 **Williamson C. H. K.,** "Vortex dynamics in the cylinder wake", *Annu. Rev. Fluid. Mech.* (1996),.p. 77-53.

75 **Thais L., Mompean G. & Naji H.,** "Computation of flow past a circular cylinder using general orthogonal coordinates", *5th World Congress on Computational Mechanics WCCM V, July 7-12,* (2002) Vienna, Austria.

76 **Ramšak M., Škerget L., Hriberšek M. & Žunič Z.,** "A multidomain boundary element method for unsteady laminar flow using stream function–vorticity equations" *Engineering Analysis with Boundary Elements* (2005), Vol. 29, p. 1–14.

77 **Liu C., Zheng X., and Sung C. H.,** "Preconditioned Multigrid Methods for Unsteady Incompressible Flows", *Journal of Computational Physics* (1998), Vol. 139, p. 35–57.

78 **Coutanceau, M. & Defaye, J. R.**, "Circular cylinder wake configurations: A flow visualization survey", *Appl. Mech.* (1991), Vol. 6, p. 255-305.

79 **McKinley G. H., Pakdel P., Oztekin A.,** "Rheological and geometric scaling of purely elastic instabilities", *J. Non-Newtonian Fluid Mech.* (1996), Vol. 67, p. 19-47.

80 **Joseph D., Funada T., Wang J.,** "Potential flows of viscous and viscoelastic fluids", *Cambridge University Press* (2008).